

Mechanical Engineering Department



The University of Sheffield

# **Experimental investigation of crack paths**

A thesis submitted for the degree of Doctor of Philosophy

By

**Mohammad Zanganeh**

November 2008

## **Acknowledgement**

First of all, thanks to the Almighty for the sustaining influence.

My special thanks go to my supervisors Dr Rachel Tomlinson and Prof John Yates who have made invaluable contributions towards this research. Their vision and patience have helped me stay in focus throughout this undertaking.

I would like to thank Dr Gavin Williams, Dr Erwin Hack, Dr João Quinta Da Fonseca and Prof Mike Sutton for their priceless help in some stages of this work. I wish to thank my colleagues in the Experimental Stress Analysis Group (Ahmad Kamil Hussain, Andrew Conway, Dr Richard Greene and William Cooke), as well as my other colleagues and friends Carlo Boldetti, Matthew Tsai, Han Tai, Ehsan Alborzi, Hassan Ghadbeigi, Reza Raufi, Pablo Lopez-Crespo, Frank Stolze, Hrishikesh Kapoor, Giovanni Lupica and Dr Reza Mofakhami for their help and discussions. I am also indebted to Mr Richard Kay for his continuous help in ESA laboratory.

I would like to extend these acknowledgements to my grandfather, Ghodrat, my parents Mohammad Hassan and Farah and my sister and brother Nikou and Mahdi for their support.

I am most grateful to the Universities UK organization for their award to pursue my PhD and Dr Richard Burguete from Airbus for providing the materials required for the manufacture of the specimens.

## Summary

The knowledge of crack path mechanism could improve the safety issues, design and finally reduce the cost of the maintenance or production of structures in aerospace and energy industries. However, the physical mechanism behind the crack path development is not still completely understood although many criteria have been developed to predict the crack path. It is even more challenging to predict the crack trajectory in areas such as multi site damage zones where there are interactions between cracks.

A study has been undertaken on sets of cracks with different interaction properties, both numerically, using a finite element (FE) method, and experimentally, using Thermoelastic Stress Analysis (TSA) where the effectiveness of three of the most common criteria was assessed. It was shown that the crack paths are not always repeatable as expected by FE models. It was found that the crack path criteria are capable of an acceptable prediction only in the early stages of the crack growth. Furthermore, the Stress Intensity Factors (SIF) only partially control the crack path and it has been recognised that the T-stress is one the influential parameters of the crack trajectory. Despite the vital role of T-stress, not only in directional stability problems but also in crack growth rate and the shape and size of the plastic zone ahead of the crack tip, little attention has been paid to experimentally determine the T-stress.

Therefore, based on both Muskhelishvili's and Williams' approaches, methodologies were developed to determine the SIF and the T-stress from both stress field and displacement data generated artificially and using a finite element method. These methodologies were successfully employed to experimentally determine the SIF and the T-stress for different types of notched and fatigue cracked specimens manufactured from Al 7010 T7651 using TSA and Digital Image Correlation (DIC) technique.

It was shown that the Muskhelishvili's approach is equivalent to the Williams' 2 terms stress solution for SIF determination. However, the 2 terms solution is not sufficient to determine the T-stress and, three or more terms are needed both from the stress and displacement fields. Results obtained from the stress field are numerically unstable if more than four terms are used. However, results obtained from the displacement field show more robustness with an increased number of terms.

# Contents

<b>EXPERIMENTAL INVESTIGATION OF CRACK PATHS</b> .....	<b>I</b>
<b>ACKNOWLEDGEMENT</b> .....	<b>II</b>
<b>SUMMARY</b> .....	<b>III</b>
<b>CONTENTS</b> .....	<b>IV</b>
<b>LIST OF FIGURES</b> .....	<b>VI</b>
<b>LIST OF TABLES</b> .....	<b>X</b>
<b>NOMENCLATURE</b> .....	<b>XI</b>
<b>CHAPTER 1 INTRODUCTION</b> .....	<b>1</b>
1.1    MOTIVATION OF THE RESEARCH.....	1
1.2    OBJECTIVE OF THE RESEARCH.....	3
1.3    THESIS LAYOUT.....	3
<b>CHAPTER 2 LITERATURE REVIEW</b> .....	<b>5</b>
2.1    CRACK TURNING CRITERIA: A HISTORICAL REVIEW.....	6
2.1.1 <i>Crack path direction</i> .....	6
2.1.2 <i>Directional stability</i> .....	9
2.2    OTHER IMPORTANT ASPECT OF T-STRESS.....	15
2.2.1 <i>T-stress and crack tip constraint</i> .....	15
2.2.2 <i>T-stress and fracture toughness</i> .....	17
2.2.3 <i>T-stress and failure assessment diagram (FAD)</i> .....	18
2.2.4 <i>T-stress and crack shape development and tunnelling</i> .....	20
2.2.5 <i>T-stress and fatigue crack growth rate</i> .....	21
2.3    NUMERICAL T-STRESS DETERMINATION.....	23
2.4    FULL FIELD EXPERIMENTAL TECHNIQUES FOR CRACK ANALYSIS.....	24
2.4.1 <i>Thermoelastic stress analysis</i> .....	26
2.4.2 <i>Digital image correlation</i> .....	34
2.4.3 <i>Summary</i> .....	39
2.5    CONCLUSION.....	40
<b>CHAPTER 3 INTERACTING CRACK PATHS</b> .....	<b>41</b>
3.1    FUNDAMENTALS OF THERMOELASTIC STRESS ANALYSIS.....	42
3.1.1 <i>Thermoelastic effect</i> .....	42
3.1.2 <i>Calibration of the thermoelastic signal</i> .....	43
3.1.3 <i>Thermoelastic signal processing</i> .....	44
3.1.4 <i>Acquired thermoelastic data</i> .....	45
3.2    EXPERIMENTAL STUDY.....	46
3.2.1 <i>Specimens</i> .....	46
3.2.2 <i>Loading</i> .....	50
3.2.3 <i>TSA equipment</i> .....	50
3.3    METHODOLOGY FOR EXTRACTING SIF FROM TSA DATA (FATCAT).....	54
3.3.1 <i>Mathematical model</i> .....	55
3.3.2 <i>Newton-Raphson method</i> .....	55
3.3.3 <i>Crack tip position</i> .....	56
3.3.4 <i>Data point selection</i> .....	57
3.4    FEM STUDY.....	58
3.4.1 <i>Numerical SIF calculation</i> .....	61
3.4.1.1    Displacement correlation technique.....	61
3.4.1.2    Modified crack closure integral technique (MCCI).....	62
3.4.1.3    J-integral technique.....	63

3.4.2	<i>Crack path prediction criteria</i> .....	64
3.4.2.1	Maximum tangential stress (MTS).....	64
3.4.2.2	Minimum strain energy density factor (S-min).....	65
3.4.2.3	Maximum energy release rate (G-max).....	65
3.4.3	<i>Initial analysis</i> .....	66
3.5	RESULTS AND DISCUSSION .....	68
3.6	CONCLUSION.....	77
<b>CHAPTER 4 T-STRESS DETERMINATION USING TSA .....</b>		<b>79</b>
4.1	METHODOLOGIES FOR T-STRESS AND SIF CALCULATION .....	80
4.1.1	<i>Muskhelishvili's and Williams' approaches: a comparative study</i> .....	80
4.1.2	<i>Mathematical description of the model</i> .....	83
4.2	INTERFACE.....	85
4.3	METHODOLOGY ASSESSMENT USING ARTIFICIAL DATA.....	86
4.3.1	<i>Williams' field with noise</i> .....	93
4.3.2	<i>Finite element stress field</i> .....	100
4.4	EXPERIMENTS .....	103
4.4.1	<i>Crack tip position</i> .....	107
4.4.1.1	Experiments to find the crack tip position .....	111
4.4.2	<i>T-stress and SIF determination</i> .....	118
4.5	DISCUSSION .....	124
4.6	CONCLUSION.....	126
<b>CHAPTER 5 T-STRESS DETERMINATION USING DIGITAL IMAGE CORRELATION .....</b>		<b>128</b>
5.1	DIC FUNDAMENTALS.....	129
5.1.1	<i>Displacement mapping</i> .....	130
5.2	METHODOLOGY .....	132
5.2.1	<i>Williams' approach</i> .....	132
5.2.2	<i>Muskhelishvili's approach</i> .....	134
5.3	METHODOLOGY ASSESSMENT USING ARTIFICIAL DATA.....	136
5.3.1	<i>Williams' field with noise</i> .....	140
5.3.2	<i>Finite element displacement field</i> .....	143
5.3.3	<i>Sensitivity to the crack tip position</i> .....	146
5.4	CRACK TIP POSITIONING AND THE NEWTON-RAPHSON METHOD.....	150
5.5	INTERFACE.....	153
5.6	EXPERIMENTAL RESULTS AND DISCUSSION .....	156
5.6.1	<i>Mixed mode experiments</i> .....	168
5.7	CONCLUSIONS.....	174
<b>CHAPTER 6 CONCLUSIONS AND FUTURE WORK .....</b>		<b>177</b>
6.1	OVERALL CONCLUSIONS .....	177
6.2	SUGGESTIONS FOR FUTURE WORK.....	178
<b>REFERENCES.....</b>		<b>183</b>

## List of Figures

FIGURE 2-1 EXAMPLES OF A) CLASS I AND B) CLASS II FRACTURES .....	10
FIGURE 2-2 DEFINITION OF FIRST AND SECOND STAGES OF KINKING IN A) CLASS I AND B) CLASS II [18].....	11
FIGURE 2-3 CRACK PATHS OBSERVED BY RADON <i>ET AL.</i> IN EXPERIMENTS ON BIAXIALLY STRESSED PMMA SHEETS [10] .....	12
FIGURE 2-4 THE NORMALIZED PLASTIC ZONE SIZES AND SHAPES OBTAINED FOR DIFFERENT T VALUES [24] .....	15
FIGURE 2-5 EFFECT OF T-STRESS ON FRACTURE TOUGHNESS (AFTER SHAH [34]) .....	18
FIGURE 2-6 THE R6 FAD DIAGRAM BEFORE CONSIDERING THE CONSTRAINT EFFECTS (AFTER AINSWORTH AND O'DOWD [37]) .....	19
FIGURE 2-7 THE R6 FAD DIAGRAM AFTER CONSIDERING THE CONSTRAINT EFFECTS (AFTER SHAH [34]) .....	20
FIGURE 2-8 TUNNELLING DEFINITION .....	21
FIGURE 2-9 FATIGUE CRACK GROWTH RATES OBTAINED FROM CT AND CN SPECIMENS IN WASPALOY AT 650°C [26] .....	22
FIGURE 2-10 NOMENCLATURE OF THE CARDIOID CURVE [78] .....	29
FIGURE 2-11 DERIVATION OF $S_0$ [78] .....	31
FIGURE 2-12 GRAPHICAL METHOD TO DETERMINE MODE I STRESS INTENSITY FACTOR FROM SPECKLE MEASUREMENTS [89].....	34
FIGURE 2-13 COMPARISON OF A) THEORETICAL AND B) EXPERIMENTAL VERTICAL DISPLACEMENT FIELD [90].....	36
FIGURE 2-14 J INTEGRAL DOMAIN (LEFT) [95] AND INTERACTION INTEGRAL DOMAIN (RIGHT) [96] .....	38
FIGURE 3-1 TSA APPARATUS .....	45
FIGURE 3-2 A) X, B) Y AND C) R IMAGE IN A TENSILE SPECIMEN.....	46
FIGURE 3-3 SPECIMEN DIMENSIONS .....	48
FIGURE 3-4 THE SHAPE OF THE GRAINS OF THE AL 7010 T7651 OBTAINED BY ANODIZING METHOD .....	49
FIGURE 3-5 STRESS FIELD AROUND THE CRACK TIPS FOR DIFFERENT VERTICAL OFFSET BETWEEN THE TWO SLITS.....	49
FIGURE 3-6 TSA EQUIPMENTS .....	51
FIGURE 3-7 THERMOELASTIC IMAGES FOR THE 5 DIFFERENT CRACK OFFSETS, SHOWING THE BEGINING (LEFT) AND END (RIGHT) OF CRACK GROWTH .....	52
FIGURE 3-8 POSITION OF STRAIN GAUGE ON THE SPECIMEN .....	53
FIGURE 3-9 A TYPICAL TSA SIGNAL USED FOR CALIBRATION.....	53
FIGURE 3-10 DATA COLLECTION IN FATCAT .....	54
FIGURE 3-11 DIFFERENT REGIONS OBSERVED IN STANLEY'S PLOT .....	58
FIGURE 3-12 CRACK GROWING PROCEDURE A) ORIGINAL CRACK AND MESH B)DELETING ELEMENTS C) CREATING NEW CRACK GEOMETRY D) RE-MESHING THE DELETED REGION .....	60
FIGURE 3-13 SINGULAR ELEMENTS AHEAD OF A CRACK .....	62
FIGURE 3-14 MESH CONFIGURATION USED FOR CCI AND MCCI A) BEFORE CRACK GROWTH B) AFTER CRACK GROWTH [116] .....	63
FIGURE 3-15 COMPARISON OF DIFFERENT CRITERIA TO CALCULATE THE CRACK INITIATION ANGLE $(\theta_c)$ FOR RANGE OF MODE MIXITY $M_E$ , WHERE $M_e = \frac{2}{\pi} \tan^{-1} \left( \frac{K_I}{K_{II}} \right)$ (AFTER [116]).....	66
FIGURE 3-16 PREDICTED CRACK PATH FOR 8MM VERTICAL OFFSET CRACKED SPECIMEN USING A) DISPLACEMENT CORRELATION B) MCCI C) J-INTEGRAL.....	67

FIGURE 3-17 COMPARISON BETWEEN THERMOELASTIC DATA, FINITE ELEMENT MODEL AND THE BROKEN SPECIMENS .....	69
FIGURE 3-18 LEFT AND RIGHT FATIGUE CRACK PATH COMPARISON USING THERMOELASTIC STRESS ANALYSIS (TSA) AND FINITE ELEMENT ANALYSIS (FRANC2D/L). (A) 0 MM OFFSET, (B) 8 MM OFFSET, (C) 16 MM OFFSET, (D) 32 MM OFFSET, (B) 48 MM OFFSET. THE INITIAL SLIT LENGTH IS NOT INCLUDED IN THE SCALE.....	71
FIGURE 3-19 LEFT AND RIGHT STRESS INTENSITY FACTORS ( $\Delta K_I$ AND $\Delta K_{II}$ ) USING THERMOELASTIC STRESS ANALYSIS (TSA) AND FINITE ELEMENT ANALYSIS (FRANC2D/L). (A) 0 MM OFFSET, (B) 8 MM OFFSET, (C) 16 MM OFFSET, (D) 32 MM OFFSET, (B) 48 MM OFFSET. THE INITIAL SLIT LENGTH IS NOT INCLUDED IN THE SCALE.....	73
FIGURE 3-20 COMPARISON OF THE CRACK PATHS AND TSA DATA OBTAINED BY REPEATING THE TEST FOR EACH OFFSET .....	74
FIGURE 3-21 FATIGUE CRACK PATH DETERMINED BY FRANC2D/L AND TSA, AS WELL AS THE MODE II STRESS INTENSITY FACTOR DETERMINED BY FATCAT FOR A SPECIMEN WITH 8 MM OFFSET CRACKS. THE SLIT LENGTH IS NOT INCLUDED IN THE CRACK LENGTH SCALE.....	75
FIGURE 3-22 (A) TSA IMAGE AND (B) ANSYS NON-LINEAR FE RESULTS FOR A SPECIMEN WITH 8 MM OFFSET CRACKS.....	76
FIGURE 3-23 FRACTURED SURFACE OF THE SPECIMEN WITH 8 MM OFFSET CRACKS .....	77
FIGURE 4-1 POINTS SELECTED FOR COMPARATIVE STUDY.....	81
FIGURE 4-2 MODE I (TOP) AND MODE II (BOTTOM) STRESS INTENSITY FACTORS FOR POINT A .....	81
FIGURE 4-3 MODE I (TOP) AND MODE II (BOTTOM) STRESS INTENSITY FACTORS FOR DATA POINTS B IN FIGURE 4-1 .....	82
FIGURE 4-4 NOTATION OF STRESS FIELD AROUND THE CRACK TIP.....	84
FIGURE 4-5 THE GRAPHICAL INTERFACE .....	87
FIGURE 4-6 TYPICAL OUTPUT OF THE INTERFACE FOR WILLIAMS ALGORITHM .....	88
FIGURE 4-7 SUM OF PRINCIPAL STRESS DISTRIBUTION (IN PA) IN CASE 1 .....	89
FIGURE 4-8 CONVERGENCE CURVE FOR CASE 1.....	89
FIGURE 4-9 SUM OF PRINCIPAL STRESS DISTRIBUTION (IN PA) IN CASE 2 .....	90
FIGURE 4-10 CONVERGENCE CURVE FOR CASE 2.....	90
FIGURE 4-11 SUM OF PRINCIPAL STRESS DISTRIBUTION (IN PA) IN CASE 3.....	91
FIGURE 4-12 CONVERGENCE CURVE FOR CASE 3.....	91
FIGURE 4-13 SUM OF PRINCIPAL STRESS DISTRIBUTION (IN PA) IN CASE 1B .....	94
FIGURE 4-14 CONVERGENCE CURVE FOR CASE 1B .....	94
FIGURE 4-15 SUM OF PRINCIPAL STRESS DISTRIBUTION (IN PA) IN CASE 1C .....	95
FIGURE 4-16 CONVERGENCE CURVE FOR CASE 1C .....	95
FIGURE 4-17 SUM OF PRINCIPAL STRESS DISTRIBUTION (IN PA) IN CASE 2B .....	96
FIGURE 4-18 CONVERGENCE CURVE FOR CASE 2B .....	96
FIGURE 4-19 SUM OF PRINCIPAL STRESS DISTRIBUTION (IN PA) IN CASE 2C .....	97
FIGURE 4-20 CONVERGENCE CURVE FOR CASE 2C .....	97
FIGURE 4-21 SUM OF PRINCIPAL STRESS DISTRIBUTION (IN PA) IN CASE 3B .....	98
FIGURE 4-22 CONVERGENCE CURVE FOR CASE 3B .....	98
FIGURE 4-23 SUM OF PRINCIPAL STRESS DISTRIBUTION (IN PA) IN CASE 3C .....	99
FIGURE 4-24 CONVERGENCE CURVE FOR CASE 3C .....	99
FIGURE 4-25 FE MODEL CREATED IN ABAQUS.....	101
FIGURE 4-26 CONVERGENCE CURVE FOR FE DATA .....	101
FIGURE 4-27 TYPICAL INSTABILITY USING EXPERIMENTAL DATA AND MORE THAN 3 TERMS IN WILLIAMS' SOLUTION.....	103
FIGURE 4-28 SPECIMEN DIMENSIONS: (A) DCB (B) CRUCIFORM (C) DOUBLE EDGE CRACKED (DEC) SPECIMEN .....	105

FIGURE 4-29 THERMOELASTIC IMAGES FOR THE DIFFERENT CASES USED TO VALIDATE THE T-STRESS DETERMINATION METHOD (SEE TABLE 4-5).....	106
FIGURE 4-30 PURE MODE I ( $K_I = 6 \text{ MPa}\cdot\text{m}^{0.5}$ ) (A) WITHOUT T-STRESS AND (B) WITH $T = -10 \text{ MPa}$	109
FIGURE 4-31 TYPICAL PHASE SIGNAL ALONG A LINE TAKEN THROUGH A CRACK TIP AND CO-LINEAR WITH THE CRACK [88].....	111
FIGURE 4-32 Y-IMAGE AND SIGNAL PROFILE FOR A DCB SPECIMEN WITH A NOTCH .....	113
FIGURE 4-33 Y-IMAGE AND SIGNAL PROFILE FOR A CRUCIFORM SPECIMEN WITH A NOTCH .....	114
FIGURE 4-34 PHASE IMAGE FOR A FATIGUE CRACK IN A DCB SPECIMEN .....	116
FIGURE 4-35 IMAGE OF A STEEL RULE USED FOR GEOMETRICAL CALIBRATION OF THE IMAGE .....	117
FIGURE 4-36 IMAGE CAPTURED USING A CCD CAMERA TO MEASURE THE CRACK LENGTH.....	117
FIGURE 4-37 DEFINITION OF DISTRIBUTION .....	118
FIGURE 4-38 DATA POINTS DISTRIBUTION FOR DIFFERENT $D$ VALUES (A) $D=1$ (B) $D=2$ (C) $D=10$ .	119
FIGURE 4-39 EFFECT OF DISTRIBUTION ON RANGE OF T-STRESS AND SIF .....	120
FIGURE 4-40 EFFECT OF NUMBER OF POINTS ON THE DETERMINED T-STRESS AND SIF .....	120
FIGURE 4-41 COMPARISON OF ABAQUS, TWO AND THREE TERMS WILLIAMS' AND MUSKHELISHVILI'S SOLUTIONS FOR A) $\Delta T$ -STRESS B) $\Delta K_I$ AND C) $\Delta K_{II}$ . SEE FIGURE 4-29 FOR THE THERMOELASTIC IMAGES.....	122
FIGURE 4-42 COMPARISON BASED ON CRACK TIP FOUND BY GA/DS AND Y/PHASE-IMAGE TECHNIQUES USING THREE TERMS WILLIAMS' SOLUTION: A) $\Delta T$ -STRESS B) $\Delta K_I$ AND C) $\Delta K_{II}$ . SEE FIGURE 4-29 FOR THE THERMOELASTIC IMAGES .....	123
FIGURE 5-1 SCHEMATIC VIEW OF THE DIC EQUIPMENT .....	129
FIGURE 5-2 CONCEPT OF DIGITAL IMAGE CORRELATION .....	131
FIGURE 5-3 STRESS STATE AHEAD OF A CRACK TIP .....	133
FIGURE 5-4 DISPLACEMENT FIELD U (LEFT) AND V (RIGHT) FOR (A) CASE 1, (B) CASE 2 AND (C) CASE 3 DEFINED IN TABLE 5-1 (ALL IN MM).....	138
FIGURE 5-5 CONVERGENCE CURVES FOR A) CASE 1, B) CASE 2 AND C) CASE 3 (SEE ALSO TABLE 5-1 AND FIGURE 5-3) .....	139
FIGURE 5-6 DIFFERENT LEVELS OF NOISE INTRODUCED IN VERTICAL DISPLACEMENT FIELD (V) AND HORIZONTAL DISPLACEMENT FIELD (V) FOR DIFFERENT CASES AS MENTIONED IN TABLE 5-3 .....	141
FIGURE 5-7 CONVERGENCE CURVE FOR A) CASE 1B, B) CASE 1C, C) CASE 2B, D) CASE 2C, E) CASE 3B AND F) CASE 3C (SEE TABLE 5-3 AND FIGURE 5-6 FOR THE DATA).....	142
FIGURE 5-8 FE MODEL CREATED IN ABAQUS .....	143
FIGURE 5-9 CONVERGENCE CURVE FROM FE DATA .....	144
FIGURE 5-10 CONVERGENCE CURVES FOR FE DATA; COMPENSATED FOR RIGID BODY MOTION .....	145
FIGURE 5-11 EFFECT OF UNCERTAINTY IN THE HORIZONTAL CRACK TIP POSITION .....	147
FIGURE 5-12 EFFECT OF UNCERTAINTY IN THE VERTICAL CRACK TIP POSITION.....	148
FIGURE 5-13 EFFECTS OF FILTERING AND THRESHOLD VALUE ON CRACK LENGTH A) NO FILTER B) MEDIAN FILTER C) MEDIAN FILTER AND 0.003 AS THE THRESHOLD VALUE D) MEDIAN FILTER AND 0.15 AS THE THRESHOLD VALUE .....	150
FIGURE 5-14 GRAPHICAL INTERFACE (SEE FIGURE 5-15 FOR DETAILS) .....	154
FIGURE 5-15 CONTROL PANEL OF THE GRAPHICAL INTERFACE .....	155
FIGURE 5-16 DCB SPECIMEN DIMENSIONS IN MM .....	156
FIGURE 5-17 TYPICAL CORRELATED DISPLACEMENT FIELDS OBTAINED AROUND A CRACK USING DIC .....	157
FIGURE 5-18 QUALITY OF FITTED DISPLACEMENT FIELD A) HORIZONTAL AND B) VERTICAL AND C) VARIATION OF T-STRESS AND SIF VERSUS NUMBER OF WILLIAMS' SOLUTION TERMS FOR THE 1MM FATIGUE CRACK UNDER 0.5 TO 1.5 kN LOADING CONDITION.....	161

FIGURE 5-19 QUALITY OF FITTED DISPLACEMENT FIELD A) HORIZONTAL AND B) VERTICAL AND C) VARIATION OF T-STRESS AND SIF VERSUS NUMBER OF WILLIAMS' SOLUTION TERMS FOR THE 4MM FATIGUE CRACK UNDER 0.5 TO 1.5 kN LOADING CONDITION .....	162
FIGURE 5-20 QUALITY OF FITTED DISPLACEMENT FIELD A) HORIZONTAL AND B) VERTICAL AND C) VARIATION OF T-STRESS AND SIF VERSUS NUMBER OF WILLIAMS' SOLUTION TERMS FOR THE 8MM FATIGUE CRACK UNDER 0.5 TO 1.5 kN LOADING CONDITION .....	163
FIGURE 5-21 QUALITY OF FITTED DISPLACEMENT FIELD A) HORIZONTAL AND B) VERTICAL AND C) VARIATION OF T-STRESS AND SIF VERSUS NUMBER OF WILLIAMS' SOLUTION TERMS FOR THE 15MM FATIGUE CRACK UNDER 0.5 TO 1.5 kN LOADING CONDITION .....	164
FIGURE 5-22 COMPARISON OF A) STRESS INTENSITY FACTORS AND B) T-STRESSES DETERMINED USING ABAQUS, 3 TERMS WILLIAMS (W3), 15 TERMS WILLIAMS (W15) AND NEWTON-RAPHSON METHOD FOR 0.5 TO 1.5 kN LOAD RANGE .....	165
FIGURE 5-23 COMPARISON OF A) STRESS INTENSITY FACTORS AND B) T-STRESSES DETERMINED USING ABAQUS, 3 TERMS WILLIAMS (W3), 15 TERMS WILLIAMS (W15) AND NEWTON-RAPHSON METHOD FOR 0.5 TO 3 kN LOAD RANGE .....	166
FIGURE 5-24 COMPARISON BETWEEN A) STRESS INTENSITY FACTORS AND B) T-STRESS OBTAINED USING ONLY VERTICAL DISPLACEMENT FIELD (V) AND USING BOTH HORIZONTAL AND VERTICAL DISPLACEMENT FIELDS (U AND V) .....	167
FIGURE 5-25 CENTRALLY CRACKED SPECIMEN AND MIXED MODE GRIPS .....	169
FIGURE 5-26 MODIFICATIONS IN THE HOLES OF THE GRIPS .....	170
FIGURE 5-27 BOLTED SPECIMEN .....	170
FIGURE 5-28 FEM MODEL USED IN SIMULATIONS .....	170
FIGURE 5-29 A) MODE I , B) MODE II AND C) T-STRESS FOUND IN A CENTRALLY CRACK SPECIMEN UNDER MIXED MODE LOADING CONDITIONS .....	171
FIGURE 5-30 NON-SYMMETRIC BOUNDARY CONDITION .....	173
FIGURE 5-31 EFFECT OF ASYMMETRIC BOUNDARY CONDITIONS ON T-STRESS AND SIF .....	173
FIGURE 5-32 FITNESS QUALITY FOR 30° LOADING ANGLE .....	174
FIGURE 5-33 T-STRESS DETERMINED BY EXCLUDING THE POORLY FITTED REGIONS SURROUNDING THE CRACK FLANKS .....	175
FIGURE 6-1 THERMAL SPECKLES .....	179
FIGURE 6-2 CORRELATED VERTICAL DISPLACEMENT FIELD .....	180
FIGURE 6-3 CORRELATED VERTICAL STRAIN FIELD .....	180
FIGURE 6-4 THERMAL SPECKLES IN A HIGHER RESOLUTION .....	181
FIGURE 6-5 CORRELATED VERTICAL DISPLACEMENT IN A HIGHER RESOLUTION .....	181
FIGURE 6-6 CORRELATED VERTICAL STRAIN FIELD IN A HIGHER RESOLUTION .....	182

## List of Tables

TABLE 3-1 MATERIAL PROPERTIES OF AL 7010 T7651 .....	47
TABLE 3-2 AL 7010 T7651 CHEMICAL COMPOSITION% .....	47
TABLE 3-3 VALUES OF VERTICAL OFFSET (2B) AND LOADING CONDITIONS FOR DIFFERENT SPECIMENS .....	50
TABLE 3-4 CALIBRATION FACTORS UNDER DIFFERENT CONDITIONS .....	51
TABLE 4-1 THE SIF AND THE T-STRESS USED IN EACH CASE .....	88
TABLE 4-2 CHANGE IN T-STRESS AND SIF DUE TO CHANGE IN CRACK TIP POSITION .....	92
TABLE 4-3 DESCRIPTION OF DIFFERENT CASES .....	93
TABLE 4-4 VALUES OF T-STRESS AND SIF IN FE MODEL .....	101
TABLE 4-5 EXPERIMENTAL DETAILS FOR THE SPECIMENS USED IN THE T-STRESS AND SIF DETERMINATION .....	104
TABLE 4-6 COMPARISON BETWEEN THE Y/PHASE IMAGE AND THE GA/DS TECHNIQUES TO FIND THE LOCATION OF THE NOTCH TIP (IN PIXELS) .....	112
TABLE 4-7 COMPARISON BETWEEN THE Y/PHASE IMAGE AND THE GA/DS TECHNIQUES TO MEASURE THE FATIGUE CRACK LENGTH (IN MM) .....	115
TABLE 5-1 THE SIF AND THE T-STRESS USED IN EACH CASE .....	136
TABLE 5-2 SIF USING MUSKHELISHVILI'S APPROACH .....	137
TABLE 5-3 DESCRIPTION OF THE NOISE INTRODUCED INTO THE DIFFERENT CASES.....	140
TABLE 5-4 VALUES OF T-STRESS AND SIF IN FE MODEL .....	143
TABLE 5-5 CHANGE IN CRACK TIP POSITION USING NEWTON-RAPHSON METHOD .....	159

## Nomenclature

$A$	Thermoelastic calibration factor
$A_N, B_N$	Coefficient of Fourier series
$C_{j,k}, D_{j,k}$	
$E_{j,k}, F_{j,k}$	
$a_1$	Coefficient of first term of Williams' stress solution expansion
$a_2$	Constant term of Williams' stress solution expansion
$a_n, b_n$	Coefficient of higher terms of Williams' stress solution
$C$	Correlation factor
$C_P$	Specific heat at constant pressure
$C_\varepsilon$	Specific heat at constant strain
$d$	Distribution
$E$	Module of elasticity
$F$	Nodal force to close the crack tip
$f$	Auxiliary load
$G_I, G_{II}$	Mode I and Mode II energy release rate
$G(x,y), H(x,y)$	Grey scale light intensities
$g, p$	Error functions
$i$	Square root of -1
$J$	$J$ integral
$K_I$	Mode I stress intensity factor
$K_{II}$	Mode II stress intensity factor
$K_{IC}$	Mode I fracture toughness

$K_{IIc}$	Mode II fracture toughness
$L_r$	Applied load over plastic collapse load
$M_e$	Mode mixity
$O$	Order symbol
$P$	Applied load
$P_L$	Plastic collapse load
Re, Im	Real and imaginary part operator
$r, \theta$	Notation for polar coordinate system
$S$	Magnitude of thermoelastic signal
$SE$	Strain energy density factor
$T$	T-stress
$T_i$	Traction vector
$t$	Absolute temperature
$u, v$	Horizontal and vertical displacements
$W$	Strain energy
$w$	Strain energy density
$x, y$	Notation for Cartesian coordinate system
$x^*, y^*$	Mapped Cartesian coordinate system
$z$	Notation for complex coordinates in the physical plane
$\alpha$	Linear thermal expansion coefficient
$\Delta$	Notation for range operator
$\delta q$	Heat exchange with environment
$\varepsilon_{ij}$	Strain tensor
$\varepsilon_{zz}$	Out of plane strain

$\zeta$	Complex coordinate in mapping plane
$\kappa_c$	Fracture toughness ratio
$\mu$	Shear modulus
$\nu$	Poisson's ratio
$\rho$	Density
$\sigma_{ij}$	Stress tensor
$\sigma_{0x}$	Non singular term of Williams' stress solution
$\sigma_{\theta\theta}$	In plane tangential stress in polar coordinate system
$\sigma_{r\theta}$	In plane shear stress in polar coordinate system
$\sigma_{xx}, \sigma_{yy}$	In plane normal stress in $x$ and $y$ direction in Cartesian coordinate system
$\tau_{xy}$	In plane shear stress in Cartesian system
$\Phi(z), \Omega(z), \Psi(z)$	Complex stress functions
$\varphi(z), \psi(z)$	Complex stress function in integral form
$\omega(z)$	Mapping function
$\partial$	Notation for partial derivative

# **Chapter 1**

## **Introduction**

### **1.1 Motivation of the research**

Since the first attempts to mathematically model fracture early in the twentieth century, there has been impressive progress in this field of science. However, despite the extensive amount of research undertaken in this area, there are many problems which are not well understood. For example, the physical mechanism behind the crack path development is still somewhat mysterious [1].

Crack turning as a mechanism to improve the failure safety and damage tolerance of aerospace structures has been recognised as a potentially important crack arrest mechanism. Therefore, better understanding of this phenomenon could lower the cost and increase the freedom and confidence in aerospace programs [1].

Crack trajectory is also an important issue in aging aircraft structures where the multi-site damage could be developed. In assessment of multi-site damage and damage tolerant structures it is important to predict the way the crack is growing at each instant of the process. It should be known if the crack is growing in a self similar manner or is going to kink or bifurcate [2].

The complete solution of the problems above is the answer of a more general question of why a crack grows in a direction that it does. Many engineers and scientists have tried to answer this question and therefore many criteria have been developed so far.

It may be assumed theoretically that the crack path is predictable, but even if the loading is such that straight mode I crack growth could be expected for symmetry reasons, the path might be directionally unstable [3]. Generally speaking, it is not easy to predict the crack path and there are discussions about criteria that can control the direction in which a crack goes.

Traditionally in linear elastic fracture mechanics it is assumed that the state of the strain and stress field ahead of the crack tip can be characterized by a single parameter, called the stress intensity factor. However, it has been observed that there many circumstances in which this single parameter is not sufficient to characterize the strain field ahead of the crack tip. Directional stability of the cracks is one of these circumstances. The so-called T-stress, which is defined as a constant stress acting parallel to crack extension direction, has been used by many authors to interpret the directional stability problems.

Such a potential effect of the T-stress in crack path stability problems can be used in turning the crack in desired directions. For example from a damage tolerance point of view it is desirable for the crack to be as parallel as possible to the stiffeners. Since the more T-stress, the sharper the crack is likely to turn [1], higher T-stress around the stiffeners could help in turning the crack in those regions.

Despite the vital role of T-stress not only in directional stability problems but also in the initiation angle of fracture and consequently the apparent fracture toughness, crack growth rate, crack tip constraints, crack closure, and the shape and size of the plastic zone ahead of the crack tip, little attention has been paid to experimentally determining the T-stress.

This motivated the author to pursue this research with the following objective.

## 1.2 Objective of the research

Understanding the behaviour of mixed mode cracks in general, and the path of such cracks in particular, requires a combination of high quality experimental data and observations as well as robust physically based models.

Therefore, the objectives of the research were:

- Investigating the ability of some of the existing criteria to predict the crack path numerically, using a finite element method, and experimentally, using Thermoelastic Stress Analysis (TSA).
- Determining methodologies to determine the T-stress and stress intensity factor using experimental techniques of thermoelastic stress analysis and Digital Image Correlation (DIC).

## 1.3 Thesis layout

Therefore, this thesis is concerned with experimental investigation of crack paths and determining the T-stress and stress intensity factor using advanced experimental methods particularly thermoelastic stress analysis and digital image correlation techniques.

Chapter two is a literature review of the previously mentioned topics in this chapter, i.e. crack direction prediction, directional stability, importance of the T-stress and experimental techniques used in fracture mechanics studies.

In Chapter three, first the basic concepts of the thermoelastic stress analysis technique are discussed, since it has been used as the main experimental method to explore the crack path in this research. Then, the interaction of cracks and corresponding paths of the cracks in five sets of double edge cracked specimens with different vertical offsets are investigated experimentally and numerically. Mixed mode stress intensity factors as well as moving crack tip positions are determined using the thermoelastic stress analysis technique and a finite element method. At the end of this chapter a comparison has been made between the experimental results and the finite element data and the reasons for the observed differences are explored.

In Chapter four, first two major mathematical models to describe the crack tip stress field are compared. Then a methodology is proposed to extract the T-stress from the sum of the principal stress field, i.e. the output of the thermoelastic stress analysis technique. This methodology first is assessed using artificial data, finite element data and finally experimental data.

In Chapter five, a similar approach as in Chapter four is used. However, in this chapter the T-stress and stress intensity factors are extracted from displacement data obtained from digital image correlation technique.

Finally, in Chapter six a conclusion is made based on the results gained in previous chapters and some guidelines are presented for future work.

## **Chapter 2**

### **Literature Review**

The crack path problem has been studied extensively within the last half century. Various theories based on different concepts have been developed to rationalize the crack path behaviour. These theories will be reviewed in this chapter with the focus on the criteria which have had a major impact on the matter. The crack path is not always directionally stable. This problem has also been addressed by many authors that have led to different definitions and consequently different solutions to the problem. These points of view will also be covered in this chapter. It will be shown that the T-stress is an influential parameter in crack path and directional stability problems. However, this parameter is traditionally ignored in fracture mechanics studies. It will be shown that the T-stress not only affects the crack paths but also can change the size of the plastic zone, fatigue crack growth rate and many other parameters. Several numerical techniques have been developed to determine the T-stress. However, less attention has been paid to the experimental determination of the T-stress. Both numerical and experimental techniques available to determine the T-stress and stress intensity factors will also be reviewed briefly in this chapter.

## 2.1 Crack turning criteria: A historical review

### 2.1.1 Crack path direction

In 1920, Griffith, in his classic paper on rupture, demonstrated that potential energy must be released when a crack propagates [4]. In 1961, Barenblatt and Cherepanov [5-7] introduced the local symmetry criterion which says that the crack moves smoothly and selects the trajectory in such a manner that only normal separation takes place at its end. Almost at the same time, in 1963, Erdogan and Sih [8] based on Barenblatt's finiteness of stress on the crack tip assumption, showed that the crack grows in a direction normal to the maximum tension at the tip of the crack and this growth releases the maximum of energy. Referring to their experiments they concluded that in ideal brittle materials, the so called "sliding" and "tearing" modes of crack extension do not take place. The mode of fracture seems to be always a crack opening mode [8]. The latter conclusion is almost equivalent to the local symmetry criterion. These are the basis of two of the most popular crack path criteria, i.e. maximum tangential stress criterion as a crack kinking criterion and pure mode I crack growth as a general crack path criterion.

In 1974 Sih [9], developed the Minimum Strain Energy Density criterion (S-criterion). It is based on the local density of the elastic energy field in the crack tip region. According to this criterion the crack grows in a direction along which the strain energy density factor is a minimum. The instability occurs when the minimum strain energy factor reaches a critical value.

In a non uniform stress field the cracks generally follow a curved path. In a brittle homogeneous isotropic material the path where the cracks propagate is the one in which in the local stress field ahead of crack tip is of a mode I type. It means that the crack prefers to grow in a direction that there is no mode II stress intensity factor. Since the other mixed mode crack propagation criteria (such as the maximum tangential stress and the Sih's minimum strain energy density factor, all predict that under mixed mode loading conditions,  $K_{II} \neq 0$ , the crack will kink from the original crack direction. It seems that the local symmetry criterion is in

contradiction with these criteria. However, where the crack extends in a continuous curved path, all these criteria yield the same results, which is the crack propagation is along the vanishing mode II stress intensity factor direction [10].

It is true that mode II crack propagation is very rare on a laboratory scale because mode I growth usually takes over. However, such a mode II growth is often observable at earth-quake slipping [11]. Melin [11] investigated the conditions for mode II instead of mode I growth with respect both to confining pressure and relevant material characteristics. She assumed that mode II growth, if it appears, proceeds in a direction that maximizes the mode II stress intensity factor. She found that a high confining pressure promotes mode II growth. Furthermore, she described the role of the material by the ratio,  $\kappa_c = K_{IIc}/K_{Ic}$ . If  $\kappa_c$ , is around 0.38-0.81 or smaller, mode II seems to be preferred whenever there is a confining pressure. If  $\kappa_c = K_{IIc}/K_{Ic}$  is around unity or larger, mode I is preferred if the pressure is smaller than the shear stress.

All the previously mentioned criteria are based on the continuum mechanics concept which disregards the molecular or micro structure of the material and presumes that there is no gap or empty space in the material. However, the local conditions ahead of the crack tip have a vital role in the crack growth mechanism. Micro-separation directly depends on these local conditions. The direction and intensity of the local fields are the parameters which determine the formation and growth of the cracks. Hence, the crack grows in a direction where an increase in mode I or mode II stress intensity factor is dictated not along a path in which a combination of mode I and mode II stress intensity factors reaches an extreme value [3]. However, it does not appear that the crack *always* grows in the pure mode I. As is shown by Shirmohammadi [12] and later in this current work, a crack does not necessarily grow in the vanishing mode II or pure mode I direction.

These early continuum mechanics based criteria were for perfectly elastic stresses in homogenous continua under static loadings and were validated against brittle fracture tests. Since stress intensity factor is a good characterizing parameter it is common [13] to base the fatigue crack paths studies on brittle fracture models. However, plasticity and microstructure could modify crack behaviour in both

fracture and fatigue. Therefore, the continuum mechanics based criteria should be modified to consider the effects of plastic zone size and microstructure. This has been done by introducing the concept of the process zone in the calculation.

For example, the maximum tangential stress criterion can be modified by calculating the maximum tangential stress at a critical or characteristic distance from the crack tip. However, finding a characteristic length applicable for both brittle and ductile failure is the most difficult part of the problem. The characteristic distance of twice the grain size was introduced by Ritchie *et al.* [14]. As an alternative the size of plastic zone was used as the critical distance by Streit and Finnie [15]. The latter case will be discussed further in the next section where the directional stability is reviewed. Such a treatment, especially the Ritchie *et al.* work, which is known as RKR model for brittle materials, is basis of the newly introduced local approach to fracture and damage mechanics which can be applied for brittle, ductile and creep fracture. This research area, particularly developing appropriate constitutive models is very active and open at the moment [16].

As another interesting work regarding the crack propagation, the research of Pook [13] can be mentioned. He used the concept of chaos theory to explain the behaviour of crack propagation. He drew to our attention that since the conditions for mode I branch crack are not completely understood, any metallurgical discontinuities or pre-crack front curvature may influence the crack tip surface deformation. In chaos theory terms the mode I branch crack formation has a chaotic behaviour which strongly depends on the initial conditions.

The focus of previous review was mostly on the criteria which have had the major influence on the matter. The author refers the reader for supporting research and some contradictory observations for these criteria to reference [17].

In crack path prediction, intuitively, one may anticipate that at least under pure mode I loading in a symmetric specimen the crack grows in a self similar manner and continues the initial direction of the original crack. However, even under such a condition the crack does not necessarily follow such a straight line. This is because of the fact that the crack may not be directionally stable [13]. This led to the development of second order criteria by considering other influential

parameters than the stress intensity factors such as T-stress. The matter of directional stability and the parameters affecting the directional stability are discussed in the following section.

### 2.1.2 Directional stability

In 1965, Cotterell [4], based on the observations in fractured paths of centrally cracked specimen and double cantilever specimens, divided the fractured paths into two classes of fracture. Firstly, in class I in which the crack path tends to return to its original path after initial deviation from the ideal path. For example in a symmetrically loaded, centrally cracked specimen (Figure 2-10) the symmetric line of the specimen is the ideal path of the crack propagation. Even if the crack is inclined in the plate the crack will kink towards the line of symmetry of the specimen. On the other hand, in class II fractures no tendency exists for the crack to return to the ideal path, see Figure 2-1(b). He drew the conclusion that rather than the global symmetry line of the specimen, the line of local symmetry of maximum principal stress is a highly probable path for macroscopic growth. This coincides with the maximum tangential stress criterion, because in the absence of higher order terms of the Williams' solution, the maximum tangential stress occurs in the same direction of zero shear stress and the tangential stress is the maximum principal stress as well.

Later, in 1966, Cotterell tried [18] to justify the behaviour observed in class II fractures. He stated that in a perfect isotropic elastic solid a crack will grow in the direction where the maximum energy is released or the principal stress is maximum. However, flaws or microscopic anisotropy in real materials may influence the crack path deviation from ideal path. Particularly, if these irregularities are cumulative, the crack may grow in a class II type of fracture. To consider these irregularities, he used the expanded form of the stress distribution at the crack tip as a power series. He used the two term solution, in which the first term ( $a_1$ ), determines the initiation of fracture in a brittle material and is proportional to the stress intensity factor, and the second term ( $a_2$ ) a transverse stress parallel to the crack face. He concluded that this transverse stress controls the stability of the crack direction.

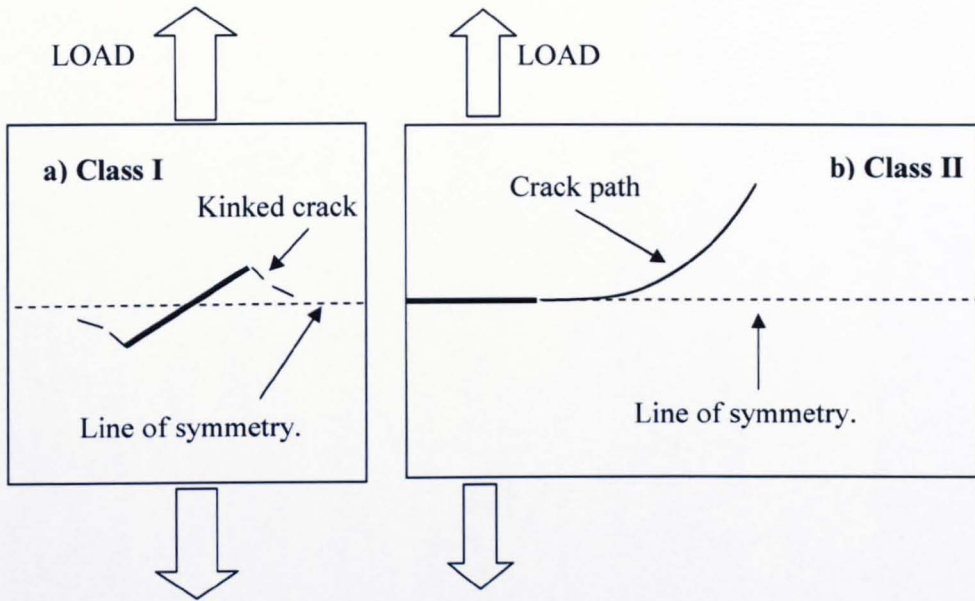


Figure 2-1 Examples of a) Class I and b) Class II fractures

Cotterell assumed that the ideal direction for crack growth, when the stress distribution is symmetrical, is along the symmetric line. By defining  $d\theta$  and  $d\phi$  as the first and second stages of kinking (see Figure 2-2), using the singular term of Williams' solution for shear stress and considering the shear stress as zero to find the maximum principal axis, the relationship between  $d\theta$  and  $d\phi$  was found as follows,

$$d\phi = \left[ 1 - \frac{4}{\pi} \left( \frac{a_2}{a_1} \right) \sqrt{\frac{s}{l}} \right] d\theta \quad 2-1$$

where  $l$  is the original length of the crack and  $s$  is the length of the kinked crack. It is evident that at any stage of crack growth, if the sign of the second term ( $a_2$ ) is negative,  $d\phi > d\theta$  and the crack path has tendency to return to its original path and it will propagate in a zig-zag manner. But if the second term is positive the path does not return to the original path and behaves as a class II fracture type.

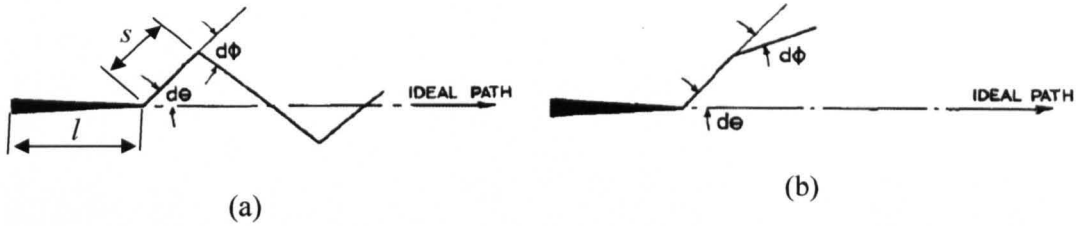


Figure 2-2 Definition of first and second stages of kinking in a) Class I and b) Class II [18]

The previous derivations were for the case of straight or kinked crack. In another attempt in 1980, Cotterell and Rice [10] found an approximate analytical solution for both mode I and mode II stress intensity factors for the tips of semi-infinite and slightly curved or kinked cracks. In contrast to the previous work which was based on the maximum principal stress criterion, this time they introduced a perturbation in the solution found for the mode II stress intensity factor. They used the pure mode I crack growth criterion and made the perturbed solution equal to zero. They showed that for a mode I uniform slow crack growth, the straight crack path is stable when the stress acting parallel to the crack tip in the second term of the stress distribution expansion (T-stress),  $T$ , is negative and is unstable when  $T > 0$ . Their results were in agreement with their previous work [18] and the work of Radon *et al.* [19] as shown in Figure 2-3.

It may be observed in Figure 2-3 that for  $R < 1$  ( $T < 0$ ) the crack path is a straight line, however, for the rest of the cases the crack paths deviate from the straight line. These are so called directionally unstable cracks.

In 1983, Melin [20] criticised the definition presented by Cotterell and Rice [10], i.e. that the crack path is directionally unstable if the vertical distance of the crack tip from the ideal path is increasing as the crack grows. She stated that the crack instability should be defined as unstable if the vertical distance of the crack tip from the ideal path divided by the length of the crack is increasing as the crack grows. In other words if the angle formed by the straight line between the crack tip and the original crack direction eventually decreases, then the crack growth the crack is directionally stable. This prevails if  $\sigma_x^\infty < \sigma_y^\infty$ , [21]. However, the only difference between this definition and the Cotterell's definition is in the case

where the crack grows parallel to the ideal path. A counter example for the proposed criterion is the case of a double cantilever beam (DCB) where  $\sigma_x^\infty = 0$  but the crack path is directionally unstable in both her definition and Cotterell's definition. She also questioned the range of applicability of the Cotterell and Rice approach and stated that their solution is valid only up to a crack growth for which the tangent angle is still of the same order as the one originally imposed by the disturbance. She also went further and questioned the reliability of using T-stress as a criterion for the prediction of directional stability [22]. She stated that the T-stress criterion can not be applied for all situations. For example, in the case of an array of collinear cracks under remote mode I loading, directional stability always prevails and does not depend on the T-stress. In her belief it is more reliable to use the maximum principal stress criterion than the T-stress as a criterion for directional stability.

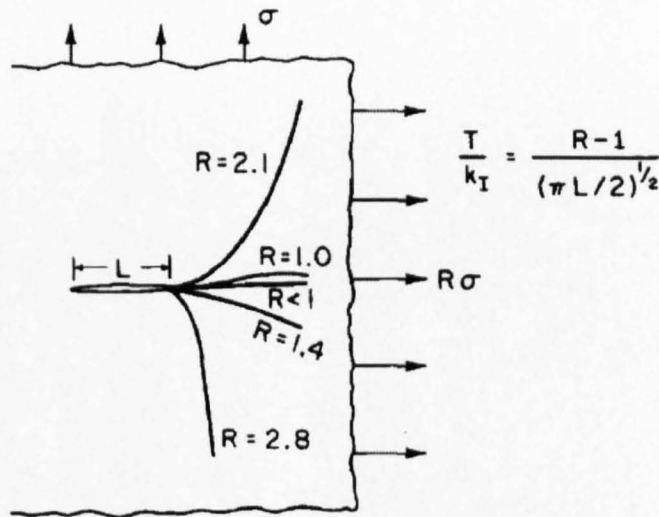


Figure 2-3 Crack paths observed by Radon *et al.* in experiments on biaxially stressed PMMA sheets [10]

The author also believes that it is not possible to use the T-stress nor any other local parameter to predict the directional stability of the whole path of the crack. Because, for example the T-stress in a centrally cracked specimen is negative for short cracks (here a short crack means one with a crack length to width ratio of less than 0.25) which means that the crack path should be directionally stable for

the whole range of crack growth. However, as the crack grows the T-stress becomes positive which means that the crack path is becoming unstable, according to the T-stress criterion. This shows that by knowing the T-stress only at the beginning of the crack growth it is not possible to say that the crack path will be stable or unstable. The crack path might change due to geometrical changes in the specimen or getting close to the boundaries of the specimen which in turn may change the sign or magnitude of the T-stress. However, it does *not* mean that the crack path is not affected by the T-stress. Erdogan and Sih [8] neglect the T-stress in their solution and Cotterell and Rice [10] used the pure mode I crack growth criterion. However, by using the Erdogan and Sih criterion and considering the higher order terms, the effect of T-stress in crack path will be revealed.

The stress distribution near the crack tip is written in the polar coordinate system as follows,

$$\begin{aligned}\sigma_{\theta\theta} &= \frac{1}{\sqrt{2\pi r}} \cos \frac{\theta}{2} \left( K_I \cos^2 \frac{\theta}{2} - \frac{3}{2} K_{II} \sin \theta \right) + T \sin^2 \theta + O(r^{1/2}) \\ \sigma_{r\theta} &= \frac{2}{2\sqrt{2\pi r}} \cos \frac{\theta}{2} [K_I \sin \theta + K_{II} (3 \cos \theta - 1)] - T \sin \theta \cos \theta + O(r^{1/2})\end{aligned}\quad 2-2$$

Ignoring the T-stress results in equality of the maximum principal stress criterion ( $\sigma_{r\theta} = 0$ ), and the maximum tangential stress criterion ( $\partial\sigma_{\theta\theta}/\partial\theta = 0$ ). However, these are not equal if the T-stress is considered [15]. For a pure mode I case considering  $\partial\sigma_{\theta\theta}/\partial\theta = 0$  leads to,

$$\frac{-3K_I}{4\sqrt{2\pi r}} \sin \theta \cos \frac{\theta}{2} + 2T \sin \theta \cos \theta = 0 \quad 2-3$$

Obviously, one of the solutions of this equation is  $\theta=0$ . As the sufficient condition, to make sure that  $\theta=0$  corresponds to the maximum of tangential stress, the second derivative of the tangential stress should be negative at  $\theta=0$ ,

$$\partial^2\sigma_{\theta\theta}/\partial\theta^2 < 0. \text{ This condition gives } 2T < \frac{3K_I}{4\sqrt{2\pi r}}.$$

Since  $K_I$  is a positive parameter, this condition always prevails if  $T < 0$ . For a non-negative value of  $T$ , this condition only holds if,

$$r \geq r_o = \frac{9}{128\pi} \left( \frac{K_I}{T} \right)^2 \quad 2-4$$

which means for the radii  $r$  less than  $r_o$  (defined by 2-4) or a negative T-stress, the crack grows in a straight line no matter what the magnitude of the T-stress is. However, for the radii greater than  $r_o$  and non-negative T-stress the crack will deviate from the plane of symmetry based on the following equation,

$$\theta = \pm \cos^{-1} \left[ \frac{3K_I}{32T\sqrt{2\pi r}} + \sqrt{\left( \frac{3K_I}{32T\sqrt{2\pi r}} \right)^2 + \frac{1}{2}} \right] \quad 2-5$$

It means that for a pure mode I case, the Cotterell and Rice treatment is partially valid. The stability (crack growth in a straight line) can be achieved even with positive T-stress values. It should be noted that the above derivations were for a pure mode I; in mixed mode conditions the relationship of T-stress and other parameters becomes more complicated and therefore the Cotterell and Rice treatment may not be easily applicable.

Using the above concept Streit and Finnie [15] introduced another stability criterion. In this criterion the crack path is stable if the critical radius  $r_c$  ahead of the crack is less than  $r_o$ . After exploring the microstructural parameter such as grain size they could not correlate the critical radius with microstructural dimensions. However, a close relationship was found between critical radius and size of plastic zone especially with the Larsson and Carlsson [23] plastic zone estimation.

What attracts one's attention is that there are many different definitions for directional stability. It is not possible to talk about the directional stability without considering a criterion for crack path direction. It seems what has been used in literature is the mode I crack growth or the equivalent vanishing mode II stress intensity factor and the maximum tangential stress. It means that in all the previously discussed criteria, the stress intensity factor which is an elastic parameter is considered as the governing parameter in crack growth problems. Regarding the T-stress as a controlling parameter in crack directional stability it should be mentioned that it might be used as a necessary condition for crack stability/instability but it can not be used as the only parameter to predict

instability. As was shown earlier, the T-stress could highly influence the crack path. However, in this treatment the size of plastic zone is also influential. So, it seems that the effects of crack tip plasticity as well as plastic strains ahead of the crack tip should also be considered.

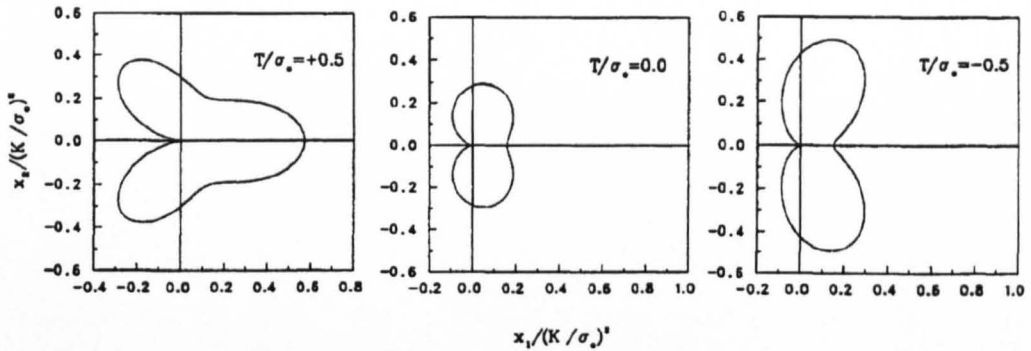


Figure 2-4 The normalized plastic zone sizes and shapes obtained for different T values [24]

Figure 2-4 shows the normalized plastic zone size and the shape of the plastic zone obtained under different T-stress values applied. As it is observed in Figure 2-4 and discussed further in the next section the T-stress can significantly affect the size of plastic zone. Therefore, to investigate the crack path, in addition to the stress intensity factors, the T-stress and size of plastic zone should be considered.

## 2.2 Other important aspect of T-stress

As previously mentioned, apart from the role of T-stress in directional stability problems a considerable amount of research has been undertaken to investigate the effect of both magnitude and sign of the T-stress in rationalizing various phenomena observed in fracture mechanics applications. These include the effect of T-stress on crack tip constraint and the size of plastic zone, the role of T-stress in fatigue crack growth, crack tunnelling, fracture toughness and even in failure assessment diagrams. These are briefly reviewed in this section.

### 2.2.1 T-stress and crack tip constraint

When a tensile load is applied to a specimen a transverse contraction is observed in the specimen. If the tensile stress is high enough to produce plasticity in the

specimen this transverse contraction becomes larger due the fact that the volume is constant during the plastic deformation. In a thick specimen, under plane strain conditions, the elastically loaded material away from the crack tip works as a constraint and prevents such a contraction ahead of crack tip. On the other hand in a thin specimen, under plane stress conditions, such a constraint does not exist and the material can contract freely and produce an out of plane deformation [25].

The concept of using out of plane deformation as a constraint or using the plane stress/strain transition idea has often been used to justify the phenomena observed in fracture mechanics. However, the out of plane constraint does not seem enough to rationalize a broad range of situations. So, a more general constraint parameter is needed to explain the intricate nature of crack tip constraint, which is a combination of in plane and out of plane constraints [26].

The T-stress as a measure of the in plane crack tip constraint was first used by Larsson and Carlsson [23] and later by Rice [27]. By performing elastic-plastic finite element simulations using the boundary layer formulation for different geometries, they found different plastic zone sizes and shapes for the same level of applied stress intensity factor. They managed to verify their results by using a modified boundary layer formulation (using two parameters of the asymptotic approach, namely stress intensity factor and T-stress).

This two-parameter approach later was used by Betegon and Hancock [28] and the T-stress was used as measure of crack tip constraint in a mode I loading condition. They showed that the elastic field can be described by the stress intensity factor and a biaxiality parameter which is the T-stress normalized by the mode I stress intensity factor. Similarly, in large scale yielding  $J$  and  $T$  can be used to characterize the elastic-plastic field ahead of the crack tip. Later, the  $J$ - $T$  concept has been extended to fully yielded conditions by proposing the  $J$ - $Q$  two-parameter approach by O'Dowd and Shih [29]. The crack tip constraint effect in mode II has also been investigated by Ayatollahi *et al.* [30].

As a summary, in a loose constraint cracked specimen the T-stress has a negative value and the normal stress field ahead of the crack tip is not fully characterized by the HRR field. On the other hand in a cracked specimen where the T-stress

does not exist or it has a positive value the stress field can be estimated by HRR approach [30].

It should be noted that the T-stress or using a two-parameter approach should not be overextended as a universal constraint parameter. This parameter together with other known constraint parameters like the crack closure and triaxiality (which is defined as the hydrostatic mean stress to the Von Mises effective stress) can give an insight to a better explanation of the fracture mechanics problems.

## 2.2.2 T-stress and fracture toughness

Based on the linear elastic fracture mechanics approach a crack extends or fracture happens when the stress field ahead of the crack reaches a critical value. Since in the single parameter LEFM it is assumed that the stress field is totally defined by the stress intensity factor; the fracture occurs when the stress intensity factor reaches the critical value which is called fracture toughness. It is assumed in LEFM that the fracture toughness is independent of the geometry and only depends on the material [31]. This parameter is usually determined by using a three point bending or a compact tension standard specimen under plane strain conditions and the results are used for other configurations. This material independency is only limited to a range of geometries and loading conditions.

Shih and German [32] explored the size requirement needed for characterizing the crack tip in an edge cracked bar subjected to bending and in a centre cracked panel and single cracked panel subjected to tensile loads. Their finite element study showed that the proposed size requirement by ASTM is adequate to ensure a valid toughness characterization of the crack tip region in the cracked bend bar and compact specimen or configurations where the uncracked ligament is subjected primarily to bending. However the specimen dimensions will have to be considerably larger to ensure a valid characterization in centre-cracked panels and similar configurations where the ligament is subjected primarily to tension. Later, in an experimental study done by Hancock *et al.* [33] on different specimens (centre cracked, single edge cracked and three point bending specimens) made from the same material it was revealed that the plane strain toughness in different geometries are considerably different, as was observed by Shih and German [32].

To explore this problem they used the two-parameter approach and they managed to justify the obtained results based on the effect of T-stress. They found that the geometries which show a positive T-stress (like single edge crack or compact tension specimens) exhibit a geometry independent fracture toughness. On the other hand a negative T-stress, which occurs in centre cracked specimens, makes the fracture toughness dependent on the geometry of the specimen and as shown in Figure 2-5, a negative T-stress increases the fracture toughness compared to zero or positive T-stress levels.

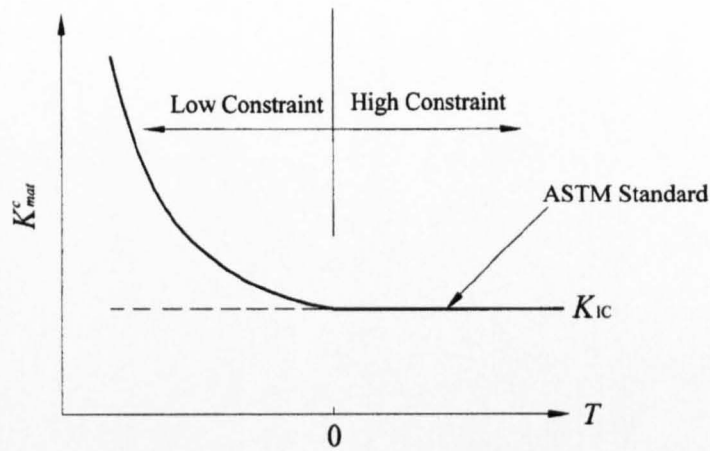


Figure 2-5 Effect of T-stress on fracture toughness (after Shah [34])

### 2.2.3 T-stress and failure assessment diagram (FAD)

There has been a substantial effort to develop a procedure to assess the structural integrity of the material not only based on fracture mechanics concepts but also considering the effect of plasticity in structures. The failure assessment diagram (FAD) was first introduced by Dowling and Townley [35] in 1975. Then the first procedure was published by the Central Electricity Generating Board in the UK and it became popular all over the world. Since then it has been published and revised many times under the name of the *R6 procedure* [36].

Figure 2-6 shows the R6 FAD diagram with no allowance for constraint. The vertical axis includes the fracture mechanics criteria of the diagram. It says that

the linear elastic stress intensity factor  $K$  should be less than the fracture toughness of the material  $K_{mat}$ .

$$K_r = \frac{K}{K_{mat}} \leq 1 \quad 2-6$$

The horizontal axis which contribute to the plastic collapse criterion is defined as,

$$L_r = \frac{P}{P_L} \leq L_r^{\max} \quad 2-7$$

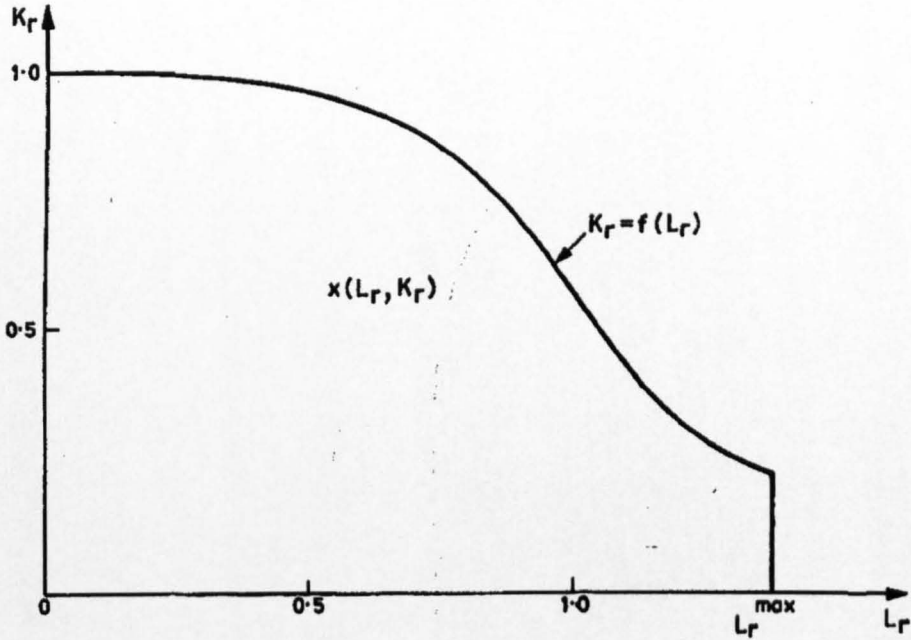


Figure 2-6 The R6 FAD diagram before considering the constraint effects (after Ainsworth and O'Dowd [37])

in which,  $P$  is the applied load and  $P_L$  is the plastic collapse load corresponding to the yield stress.  $L_r^{\max}$  is the average of the yield strength of the material and ultimate tensile strength of the material, divided by the yield strength, which is 1 for non-hardening material, and greater than 1 in general.

The FAD diagram which accounts for the interaction of both the aforementioned criteria, predicts a safe region for point  $(L_r, K_r)$  if this point lies in the region where

$$K_r \leq f(L_r) \quad 2-8$$

in which  $f(L_r) = \sqrt{J_e / J}$  and  $J_e$  and  $J$  come from elastic and elastic plastic analysis respectively. Consideration of the effect of the T-stress in the FAD was introduced by Ainsworth and O'Dowd [37] and continued by Bilby *et al.* [38] and Ainsworth *et al.* [39]. This work lead to publication of the SINTAP (Structural Integrity Assessment Procedures for European Industry). To consider the constraint effect, equation 2-8 was modified to  $K_r \leq \frac{J}{J_e} \frac{K_{mat}^c}{K_{mat}}$  where,  $K_{mat}^c$  is a constraint-dependent toughness. The constraint modified FAD is shown in Figure 2-7.

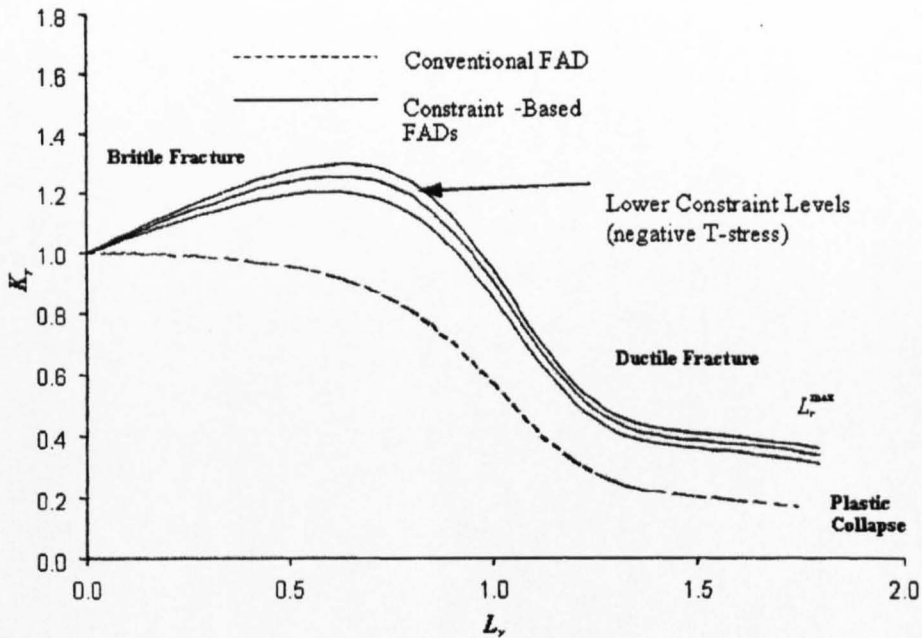


Figure 2-7 The R6 FAD diagram after considering the constraint effects (after Shah [34])

As it is observed in the constraint based FAD, decreasing the constraint level increases the safe region or in other words makes it less conservative.

## 2.2.4 T-stress and crack shape development and tunnelling

A simple observation of the fracture surface of a specimen reveals that no matter what the crack propagation path is, usually the crack front grows faster in the centre than the edge surface of the specimen. Therefore, the crack front takes the

shape of a curve rather than a straight line normal to the edge of the specimen as shown in Figure 2-8. This phenomenon is called tunnelling [31].

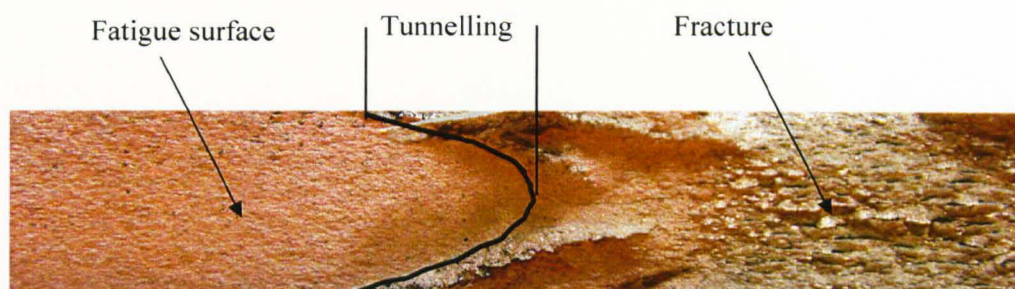


**Figure 2-8 Tunnelling definition**

In a study conducted by Zhao *et al.* [40] on corner cracked specimens (CN) it was observed that the crack grows faster in the mid plane than the surface leading to a tunnelling effect. To investigate the reason behind this phenomenon they used a 3D finite element model to simulate the crack front condition. The stress intensity factor was found both on the surface and in the mid plane of the specimen. However, the calculated stress intensity factors in the mid plane were lower than the ones in the surface which obviously shows that the stress intensity factor solely can not be used to explain this phenomenon because the region with lower stress intensity factors seem to have grown faster! Therefore, they determined the T-stress as well and they found that the T-stress in the mid plane is higher than the T-stress on the surface which shows the crack front is more constrained in the mid plane and this increases the growth rate in the mid plane.

### **2.2.5 T-stress and fatigue crack growth rate**

As reported by Tong [26], a remarkable difference was observed in the fatigue crack growth rate measured in CN and CT specimens made from Waspaloy and tested at 650°C, Figure 2-9. These were consistent with the results from a previous study [41] on nickel-based alloys at 200°C.

To see if such a behaviour was due to high temperature or specimen geometry, Tong [26] conducted a similar experiment on PM alloy, U720Li, at room temperature. A similar trend was observed for the fatigue crack growth at room temperature and led to the conclusion that the specimen geometry is responsible for such a trend.

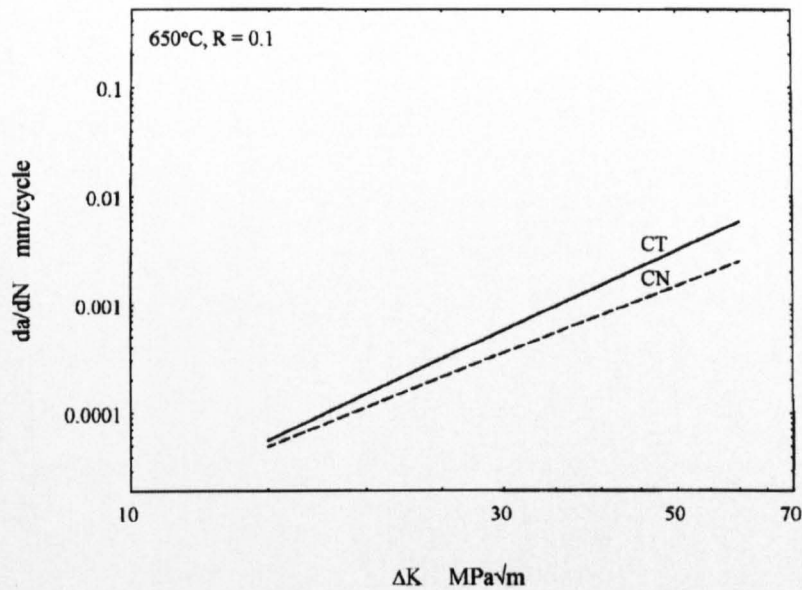


Figure 2-9 Fatigue crack growth rates obtained from CT and CN specimens in Waspaloy at  $650^{\circ}C$  [26]

To examine the effect of specimen geometry on fatigue crack growth, she used CT, single-edge tension (SENT) and CCT specimens made from mild steel with the same thickness and similar initial crack lengths and loaded in such a way that similar  $\Delta K$  was applied to all the specimens. The lowest fatigue crack growth rate was found in CCT specimens which was almost consistent with SENT specimens particularly in higher  $\Delta K$ . However, it was observed that the rate was much higher in CT specimens.

Crack closure phenomena could not be used to explain these discrepancies. Crack closure is more likely to happen in the threshold region but the differences in the CN and CT crack growth rate was negligible in that region and became higher as the  $\Delta K$  increased. Therefore, the T-stress based crack tip constraint concept was

used to rationalize the discrepancies. It was seen that as the crack grows the net difference in the T-stress in different specimen geometries increases which is in harmony with the difference found in fatigue crack growth rates measured from different type of specimens. Comparable negative values of T-stress in CCT and SENT specimens can also explain the comparable results obtained for these cases. The positive T-stress, which confines the plastic zone size of the crack tip, in CT specimens explains the faster crack growth compared to CCT and SENT specimens.

### **2.3 Numerical T-stress determination**

Many different methods have been proposed to evaluate the T-stress specimens and structures. The purpose of this section is to briefly review the numerical methods available for T-stress determination because these ideas might be applicable in experimental studies as well. The only method which will be discussed in more detail is that currently used in ABAQUS. Results from this method will be used later for comparison with the experimental results in chapters 4 and 5.

The first studies regarding the numerical calculation of the T-stress goes back to the work of Larson and Carlson [23] in 1973. Based on the difference of normal stress acting parallel to the crack face and the traditional boundary layer formulation (which does not account for the T-stress) they managed to determine the T-stress numerically. This method was later called the stress substitution method [42]. Since then many other methods have been proposed. Among these are the Leever and Radon [43] variational formulation of William's solution, Kfoury [44] T-stress determination based on J integral, the weight function method [45], the interaction integral method [46], the line spring method [47], Green's function method [48], the nodal displacement method [49] and the stress difference method [50]. Among these numerical methods, the integral techniques seem to be more reliable because they avoid the stress singularity near crack tip.

ABAQUS employs an interaction integral [46, 51]. In this technique an auxiliary load is applied to the crack front and the  $J$  integral is calculated for the total field,

$J_{total}$ , (total field means field due to application of the actual load plus the auxiliary load), actual field  $J_{actual}$  and auxiliary field  $J_{auxiliary}$ . The interaction integral is defined as  $I = J_{total} - J_{actual} - J_{auxiliary}$ . It can be shown that T-stress can be determined as [46],

$$T = \frac{E}{f(1-\nu^2)}(I + \nu\epsilon_{zz}) \quad 2-9$$

where,  $f$ , is the magnitude of the auxiliary load,  $E$  and  $\nu$  are modulus of elasticity and Poisson's ratio.

All the previously mentioned techniques were numerical techniques. In the next section experimental methods used in crack analysis in general and SIF and T-stress in particular are reviewed.

## 2.4 Full field experimental techniques for crack analysis

There are many full field experimental techniques which provide the displacement and strain/stress fields. These include photoelasticity and thermoelastic stress analysis which provide stress fields and geometric moiré, moiré interferometry, electronic speckle pattern interferometry and digital image correlation which provide displacement fields. By knowing the displacement or stress field ahead of a crack, the characterizing parameters of the crack tip can be derived. Due to the improvements made in digital technology these techniques can be used in almost real time applications. Each of these techniques has its own benefits and drawbacks [52].

Photoelasticity is one the oldest full field experimental techniques. This technique provides a full field map of difference of principal stresses on the surface of the specimen. Using transmission photoelasticity to determine the fracture parameters goes back to the work of Post [53] in 1954, and Post and Wells [54] in 1958, where the static and dynamic stress field ahead an edge crack were investigated.

At the same time Irwin [55] in a discussion made on the work of Post and Wells extended the work to mode I stress intensity factor determination in the presence of the constant term of Williams' solution. In this method only a single fringe was used in calculation and a slight error in measuring the corresponding radial and

angular distance of the fringe introduced considerable errors in calculated mode I stress intensity factor.

This approach was modified later by Bradley and Kobayashi [56] for two fringes and up to 20 points for mixed mode cracks by Sanford and Dally [57]. In the latter work, in contrast to the previous works, all three fracture parameters namely, mode I and mode II stress intensity factor and the constant non-singular stress (T-stress), were determined using an overdeterministic method and Williams two term solution.

As an alternative, the work of Nurse and Patterson [58] can be mentioned, in which the Muskhelishvili complex stress function and the Fourier series were utilized to determine the stress intensity factors in mixed mode conditions using an overdeterministic method. Recently, in 2008, in the spirit of this work and ignoring the conformal mapping approach used in that work, Christopher *et al.* [59, 60] developed a method to determine the stress intensity factor as well as the T-stress but only under mode I loading conditions. The feasibility of photoelasticity has also been examined in crack closure studies [61] and fatigue crack growth problems [62].

Photoelasticity is a fantastic full field experimental technique. However, the transmission form of photoelasticity needs a transparent specimen which means it can not be used for non transparent components (eg. metals) unless an epoxy model is used instead, which of course in this case the microstructural effects are ignored. On the other hand if reflection photoelasticity is used a birefringent coating is needed and therefore in case of growing cracks it can not be used unless the crack path is known in advance. It needs to be mentioned that data cannot be recorded at the edge of the coating due to Poisson's ratio mismatch. This also limits its usefulness [63]. Another drawback of photoelasticity in fatigue crack studies is the fact that most of the photoelastic resins (except polycarbonate) are too brittle to be able to grow fatigue cracks on them.

Moiré is another full field technique which provides contour maps of in plane displacements based on interference of two gratings. Similar studies have been carried out using moiré technique to determine pure mode I stress intensity factors

[64, 65], mixed mode stress intensity factors [66], dynamic fracture studies [67] and crack closure measurements [68, 69]. The same approaches have been used to extract the stress intensity factors from displacement data obtained from Electronic Speckle Pattern Interferometry (ESPI) for pure mode I [65, 70] and mixed mode loading [71].

The Moiré technique is a very accurate method for displacement measurement. However, it needs a reference grating and a specimen grating which should be bonded to the specimen. This makes this technique cumbersome to use and also vulnerable in situations where debonding is probable between the grating and specimen surface such as at the high strain gradient at a crack tip. ESPI on the other hand does not need a time consuming surface preparation. However, it requires expensive equipment. The main disadvantage of ESPI is high sensitivity of the technique to environmental vibrations. This makes it very hard to be used in the vicinity of a test machine and it limits the application ESPI to the laboratories. For further comparison between these experimental techniques author refers the reader to Olden's work [72].

In the last few years, thermoelastic stress analysis and digital image correlation have been used to measure crack tip strains and displacements. Minimal surface preparation is required in these techniques. Unlike reflection photoelasticity and moiré technique where a coating or grating has to be bonded to the surface, only using a painted or an abraded surface of the component is sufficient in these techniques. They also can be used on real specimens and are not sensitive to environmental vibration which makes these techniques suitable to be used in real industrial situations. Application of these two techniques in fracture mechanics studies is reviewed in more detail in the following sections.

#### **2.4.1 Thermoelastic stress analysis**

Thermoelastic stress analysis is an experimental technique which works on measuring the minute temperature changes induced on the surface of a specimen due to the applied load. As the output this technique yields a signal which under certain conditions which will be discussed in the following chapter is proportional to the sum of principal stresses on the surface of the specimen.

The high sensitivity and resolution of thermoelastic stress analysis (TSA) equipment and, in particular, the non-contacting nature of the TSA technique come together to offer a very attractive novel approach in fracture mechanics studies [73]. The first attempts to use this technique in fracture mechanics problems was recognized by Stanley and Chan [74] in 1985. After that many studies were done to characterize the stress field ahead of the crack quantitatively by determining the stress intensity factors from the thermoelastic images. For example, Stanley and Chan [75], used the mixed mode Williams' solution and considered only the first term of the expansion for a point with radial distance,  $r$ , and angular distance,  $\theta$ , from the crack tip. They managed to establish a relationship between the thermoelastic signal ( $S$ ) and the sum of principal stresses and consequently between thermoelastic signal and variation of stress intensity factors ( $\Delta K_I$  and  $\Delta K_{II}$ ) as follows,

$$AS = \frac{2\Delta K_I}{\sqrt{2\pi r}} \cos \frac{\theta}{2} - \frac{2\Delta K_{II}}{\sqrt{2\pi r}} \sin \frac{\theta}{2} \quad 2-10$$

in which  $A$  is the calibration factor.

In a pure mode I case,  $\Delta K_{II} = 0$ , by replacing  $r$  with  $y/\sin\theta$  and differentiating with respect to  $\theta$ , they observed that the maximum signal,  $S_{max}$ , occurs in  $\theta=60^\circ$ . Therefore, the vertical distance from the crack plane,  $y$ , can be related to the mode I stress intensity factor and  $S_{max}$  as follows,

$$y = \left( \frac{3\sqrt{3}K_I^2}{4\pi A^2} \right) \frac{1}{S_{max}^2} \quad 2-11$$

This means if the vertical distance from the crack tip is plotted versus the inverse square of the maximum thermoelastic signal, the range of the stress intensity factor can be found from the slope of the curve as follows,

$$\Delta K_I = \sqrt{\frac{4\pi A^2 slope}{3\sqrt{3}}} \quad 2-12$$

This graphical method was used to investigate the pure mode I stress intensity factor in a centrally cracked specimen subjected to a uniaxial load. The results were found to be within less than 5% different of the theoretical values. This difference was mainly explained by the presence of plastic strains ahead of crack

tip. This method was extended by them [76] to pure mode II conditions and similar formula was found,

$$y = \left( \frac{3\sqrt{3}K_{II}^2}{4\pi A^2} \right) \frac{1}{S_{\max}^2} \quad 2-13$$

However, in the pure mode II case the experimental results were found to have a 30% difference from the theoretical values. In spite of the reported difference between experimental and theoretical results, this methodology has the advantage that the results are independent of the crack tip position.

The Stanley approach is mainly based on the assumption that the relationship between  $y$  and the inverse square of the maximum thermoelastic signal is linear as can be seen in equations 2-11 and 2-13. However, this assumption is only valid when the pure stress intensity factors are applied or in other words, the T-stress is absent. If in equation 2-10 the T-stress,  $T$ , is considered and the same procedure is repeated it readily can be shown that for pure mode I with presence of T-stress,

$$y = \frac{3\sqrt{3}\Delta K_I^2}{4\pi A^2} \frac{1}{S_{\max}^2} + \frac{\Delta T(2AS_{\max} - \Delta T)}{A^2 S_{\max}^2 - \Delta T AS_{\max} + \Delta T} \quad 2-14$$

and for pure mode II with presence of T-stress,

$$y = \frac{3\sqrt{3}\Delta K_{II}^2}{4\pi A^2} \frac{1}{S_{\max}^2} + \frac{\Delta T(2AS_{\max} - \Delta T)}{A^2 S_{\max}^2 - \Delta T AS_{\max} + \Delta T} \quad 2-15$$

Obviously, these equations are not linear any more. Therefore, in the presence of the T-stress the linearity assumption is invalid and the methodology is confined to the application where no T-stress exists.

Later, in 1996, and based on Stanley's graphical treatment, Stanley and Dulieu-Smith [77] proposed another graphical technique to measure mixed mode stress intensity factors and the non-singular term of Williams' solution (T-stress). They rewrote equation 2-10 in the form of

$$A(S + S_0) = \frac{2\Delta K_I}{\sqrt{2\pi r}} \cos \frac{\theta}{2} - \frac{2K_{II}}{\sqrt{2\pi r}} \sin \frac{\theta}{2} \quad 2-16$$

in which  $S_0 = \sigma_{0,x} / A$  represents the effect of the non-singular term or T-stress.

By defining

$$C_1 = \tan\left(\frac{3\theta_{\max}}{2} + \beta\right) = \frac{\Delta K_I}{\Delta K_{II}} \quad 2-17$$

$$C_2 = A^2(S + S_0)\sqrt{2\pi\Sigma/3} = \Delta K_I^2 + \Delta K_{II}^2$$

where  $\theta_{\max}$  is either  $\theta_{\max 1}$  or  $\theta_{\max 2}$  as shown in Figure 2-10 and  $\Sigma$  is the area surrounded by the cardioid. They found

$$\Delta K_I = C_1 \sqrt{\frac{C_2}{1+C_2}}$$

$$\Delta K_{II} = \sqrt{\frac{C_2}{1+C_2}} \quad 2-18$$

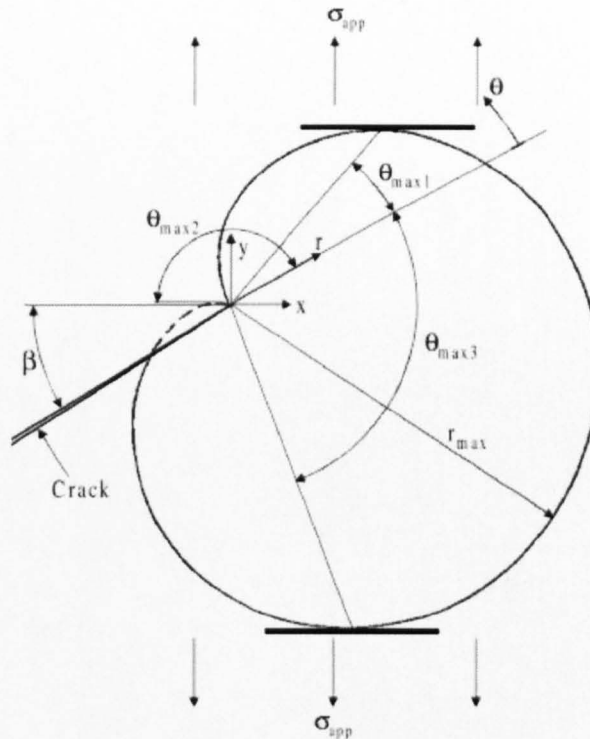


Figure 2-10 Nomenclature of the cardioid curve [78]

In this method for a certain value of  $S$ , the cardioid is constructed graphically and then  $C_1$  and  $C_2$  are determined and finally stress intensity factors can be calculated. It should be noted that  $S_0$  in equation 2-17 is determined from thermoelastic data gained from a horizontal scan line from the crack tip and using equation 2-16.

This technique, like the previous techniques, is a graphical technique but unlike the previously mentioned techniques requires the position of the crack tip. Unfortunately no experimental results were presented in this paper to support the methodology. However, later in 2000, inspired by the graphical cardioid method, Dulieu-Barton *et al.* [78] developed a computer code (FACTUS) to determine stress intensity factors from thermoelastic data. They rearrange the equation 2-16, as follows,

$$(r_m + c) = \frac{\Delta K_I^2 + \Delta K_{II}^2}{A^2(S + S_0)^2} [1 + \cos(\theta + 2\varphi)] \quad 2-19$$

in which  $\tan \varphi = \Delta K_{II} / \Delta K_I$  and  $r_m$  is the measured value of  $r$  and  $c$  and accounts for the uncertainties in measuring  $r$ . They chose three values of  $S$  at equal intervals along the crack scanning line, as shown in Figure 2-11. Thus,

$$(r_{m2} + c) - (r_{m1} + c) = (r_{m3} + c) - (r_{m2} + c) \quad 2-20$$

By putting equation 2-19 in equation 2-20,

$$\frac{1}{(S_1 + S_0)^2} + \frac{1}{(S_3 + S_0)^2} = \frac{1}{(S_2 + S_0)^2} \quad 2-21$$

This equation can be solved to find  $S_0$ . Three values for  $S_0$  were found using this equation. It was reported that two of them were more than the applied nominal stress and were neglected. The other one was chosen as the right value for the  $S_0$ . By knowing  $S_0$ ,  $\Delta K_I$  and  $\Delta K_{II}$  can be determined using equations 2-17 and 2-18. To validate the code they used artificial data and they found that for  $S_0$  values less than 25% of the nominal signal this method gives poor results for  $S_0$ . They used a centrally cracked specimen for different mode mixity (different  $\beta$  angles) and they found both stress intensity factor and the non-singular term. Up to 13% error for pure mode I cases and up to 30% error was reported for the calculated stress intensity factors using this methodology. Such a difference might be due to the fact that they ignored the effect of  $S_0$ . For a mode I case it is well known [31] that for a centre cracked specimen the magnitude of the non-singular term is of the order of magnitude of the applied stress (it also depends on the dimensions of the plate and the crack but it only makes a few percent difference). So, the expected non-singular term is much bigger than 25% of nominal stress and it is expected that this methodology be able to predict the non-singular term accurately.

However, the value found for  $S_0$  for such a case was about 10% of the applied nominal stress which is not consistent with analytical studies [31]. Therefore in the rest of their experiments  $S_0$  was ignored and the stress intensity factors were determined. As mentioned before such an omission might be the source of errors observed in stress intensity factor results using this methodology.

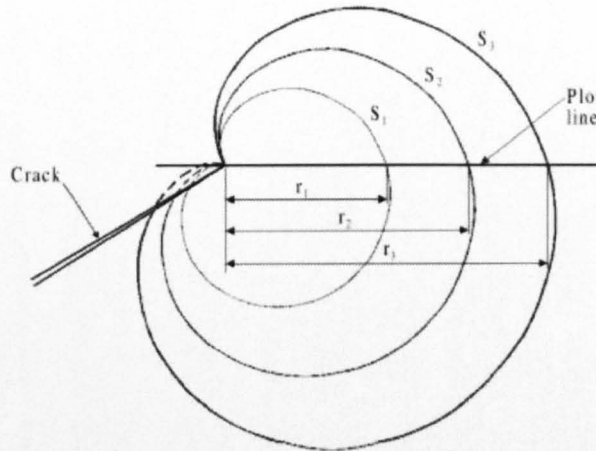


Figure 2-11 Derivation of  $S_0$  [78]

Using the same idea Dulieu-Barton and Worden [79] upgraded the FACTUS program and tried to fit the experimental data to the cardioid model. However, later Worden *et al.* [80] questioned the applicability of the cardioid model.

Based on the fact that the cardioid approach (single term Williams' approach) is not always dominant, Lesniak and Boyce [81] used up to 4 terms of the Williams' solution. A set of data points were selected from a window surrounding the crack tip and the area affected by crack tip plasticity or non-adiabatic conditions were removed from the data set. Then a least square method was used to determine the stress intensity factors. It was shown that for pure mode I cases increasing the number of terms reduces the difference observed with the theoretical values from 20% (for the single term approach) to 3% (for the 4 terms approach).

To investigate the accuracy of the least squares method Ju *et al.* [82] simulated pure mode I and mixed I and II modes numerically using a finite element method

for linear elastic and plane stress conditions. In their approach the sum of principal stresses was determined using up to 6 terms of the Williams' expansion. The  $J$  integral was calculated numerically by averaging the  $J$  values found for four different contours surrounding the crack tip. The sum of principal stress data was used in the least squares method and the stress intensity factors were determined. Finally the  $J$  integral results were compared with  $(\Delta K_I^2 + \Delta K_{II}^2)/E$  using the stress intensity factors gained from the least squares method. It was observed that using too many terms of Williams' solution introduced numerical truncation errors and finally decreased the accuracy of the calculated stress intensity factors. It was suggested that using three or four terms of Williams' solution for the sum of principal stresses can improve the calculated stress intensity factors.

All the previously mentioned methods to find the crack tip field characterizing parameters were based on Williams' solution. Basically in Williams' solution a stress function (Airy stress function) which automatically satisfies both equilibrium and compatibility equation is estimated. This stress function must satisfy the boundary conditions as well. As a result the Williams' solution is formed for the stress and displacement fields. The Airy stress function is a non complex function. As an alternative, in a general elasticity problem it has been shown by Muskhelishvili [83] that the state of stress (and displacement) field is also definable by two complex analytical function.

$$\begin{aligned}\sigma_{xx} + \sigma_{yy} &= 4 \operatorname{Re}[\Phi(z)] \\ \sigma_{yy} - \sigma_{xx} + 2i\tau_{xy} &= 2[\bar{z}\Phi'(z) + \Psi(z)]\end{aligned}\tag{2-22}$$

If these two complex analytical functions are given, then the stress (and displacement) fields can be fully defined. Rather than guessing these functions and determining the stress (and displacement) field, Nurse and Patterson [58] used a general form of Fourier series with unknown coefficients ( $A$ ,  $B$ ,  $a$  and  $b$ ) for these stress functions,

$$\begin{aligned}\Phi(\zeta) &= \sum_{N=0}^{\infty} A_N \zeta^{2N} + \sum_{m=1}^{\infty} \frac{a_m}{\zeta^{2m}} \\ \Psi(\zeta) &= \sum_{N=0}^{\infty} B_N \zeta^{2N} + \sum_{m=1}^{\infty} \frac{b_m}{\zeta^{2m}}\end{aligned}\tag{2-23}$$

in which  $\zeta$  is a known function of  $z$ .

By satisfying the boundary conditions and fitting the experimental data gained from photoelasticity they managed to find the unknown coefficients. By knowing these coefficients, then the stress field and consequently the stress intensity factors may be determined.

Based on this idea Tomlinson *et al.* [84] proposed an alternative method to determine the stress intensity factors in mixed mode I and II conditions. However, in this case the sum of principal stresses obtained from the thermoelastic signal was used as the experimental data. A Newton-Raphson iteration combined with the least squares approach was used to fit the Muskhelishvili's approach. The crack tip was found by inspection. The differences reported in mode I stress intensity factors were almost in the same range as the previous methods. However, improvements were observed in the mixed-mode results. Such a difference might be attributed to the uncertainties in crack tip position or the area where the data points are collected. Diaz [85] implemented the Tomlinson method in a computer code (FATCAT). Moreover, he considered the position of the crack tip as an unknown in the equations and used the Downhill-Simplex method to solve the equations and fit the experimental data in Muskhelishvili's approach. He also used a Genetic Algorithm (GA) optimization to locate the crack tip. Although this method works in many situations, this method depends on the data point selection. Besides, the results found from the GA and the Downhill-Simplex methods did not always agree with each other.

A similar approach to the Tomlinson approach was also used by Lin *et al.* [86] for orthotropic composites which of course can be used for isotropic materials as well. Compared to Tomlinson's approach, in this method a different general form of stress functions and a different conformal mapping were used. In this technique the J integral was used to determine the stress intensity factors. In artificially generated data with 10% noise in pure mode I conditions the determined stress intensity factors showed at least 3% difference. In real data, however, up to -15% difference from theoretical values was observed. The interesting point about this technique is that the data are not required to be collected from the region close to the crack tip. Therefore, the effect of local plasticity or non-adiabatic conditions ahead of the crack tip can be ignored.

The aim of the review was to identify the main approaches which have been used in fracture mechanics applications and quantifying the characteristic parameters in stress fields ahead of the crack using thermoelastic stress analysis. Many other works can be found in the literature, such as crack growth rate [87] and crack closure studies [88]. However, most of these studies are just applications of the aforementioned approaches.

To summarise, it was shown that all previous methods using TSA for stress intensity factor calculations are based on either Williams' stress solution or the Muskhelishvili's complex formulation. However, lack of direct comparison of these two approaches in the same stress conditions is noted. It is also evident that despite a huge amount of work having been done regarding the SIF determination, little attention has been paid into the T-stress determination using thermoelastic stress analysis. In the following chapters both Williams' solution and Muskhelishvili's approach are directly compared and a methodology to determine the T-stress from the thermoelastic data is also presented.

## 2.4.2 Digital image correlation

One of the earliest works to determine fracture parameters from displacement data is the work of Evans and Luxmoore [89] in 1974, in which a graphical method (Figure 2-12) was proposed to determine mode I stress intensity factor.

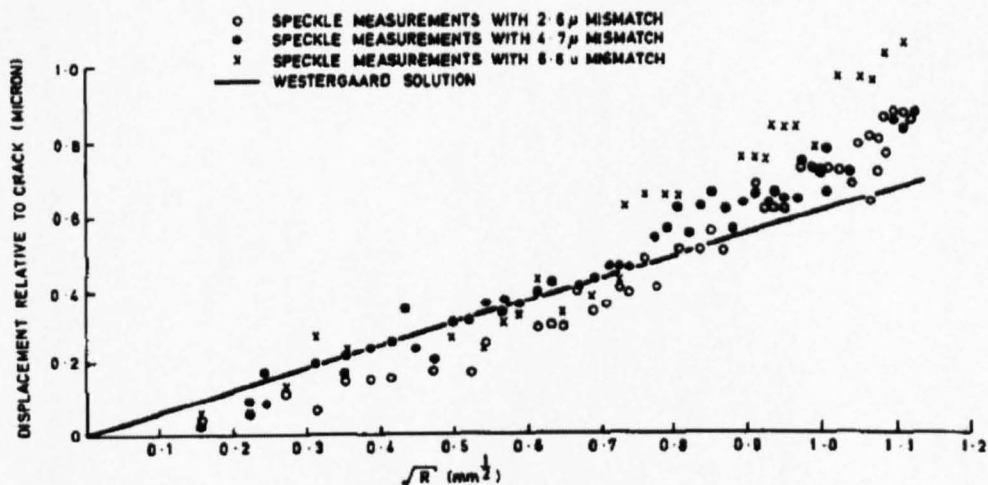


Figure 2-12 Graphical method to determine mode I stress intensity factor from speckle measurements [89]

The displacement perpendicular to the crack face was plotted versus the root of radial distance from the crack tip along  $\theta=90^\circ$ . Since the slope of the best fit line is proportional to the mode I stress intensity factor, by finding the slope, the mode I stress intensity factor was determined. However, in this work the displacement field was obtained from a laser speckle method. The first attempt to determine the stress intensity factor using image correlation was the work of McNeil *et al.* [90] in 1987. In this work they used C-shape specimens and 3-point bending specimens and only the pure mode I loading condition was examined. Digital image correlation was applied and the displacement field was obtained. To extract the stress intensity factor, the vertical displacement field (displacement normal to the crack face) was employed and the data in the horizontal direction were ignored. This means that this method is restricted to pure mode I conditions. An error function was defined based on the difference between the experimental displacement field and the Williams' solution. The minimum of the error function was found by taking the partial derivative of the function with respect to the unknown coefficients and equalling it to zero. The stress intensity factor was considered as an unknown coefficient in this equation and it was determined using a least squares method. The crack tip was found by calculating the defined error function by varying the crack tip position for a few pixels. The corresponding position to the minimum of this error function was considered as the crack tip. However, the calculated mode I stress intensity factors were relatively scattered compared to ASTM results they used as the reference. These errors might be due to ignoring the horizontal data and less accurate image correlation algorithms that were employed in that early stage of developing the technique. This can be observed in Figure 2-13 by comparing the vertical displacement field found using digital image correlation (b) and theoretical solution (a) where a noticeable amount of difference is observed particularly in cracked area.

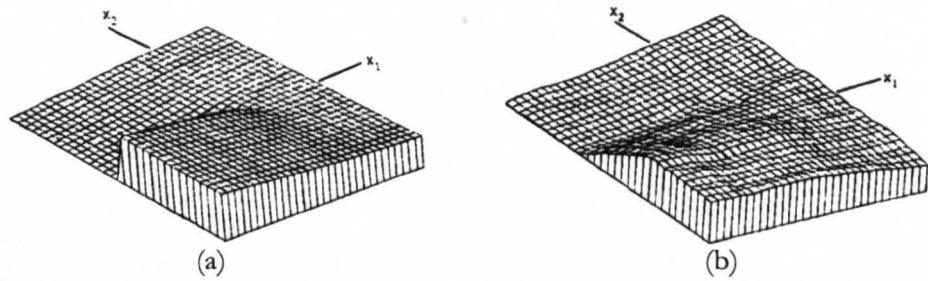


Figure 2-13 Comparison of a) Theoretical and b) Experimental vertical displacement field [90]

This methodology was extended by Durig *et al.* [91] to mixed mode crack studies. However, they used up to 20 terms of the Williams' solution. Similar tests were also conducted using photoelasticity and the results compared with the image correlation technique. A good agreement was found for mode I stress intensity factors, however, mode II stress intensity factors were slightly different and not as good as mode I results. However, again in this work and the same as the previous work [90] the crack tip positions were calculated by trial and error and minimizing the defined error function. Using the idea of the error function but considering the position of the crack tip as unknowns in the equations, Hild and Roux [92] managed to find an optimized crack tip position and stress intensity factors. Although their method was developed for mixed mode conditions, their experiments were conducted under almost pure mode I conditions. Almost at the same time, based on the method of Durig *et al.* [91], Yoneyama *et al.* [93] used the crack tip coordinates as two unknowns in the displacement field equations. They used up to 20 terms of the Williams' solution as the mathematical model and used an iterative Newton-Raphson technique to solve the nonlinear system of equations. Using the Cartesian coordinate system they could not find a converged value for stress intensity factors and they tried to use the polar coordinate system instead. However, the reason simply lies in the fact that they only used the vertical displacement field when they used the Cartesian form of the equations. Obviously ignoring the effect of horizontal displacements particularly in cases where the mode II stress intensity factor is strong can easily make the solution unstable. This was corrected in their next work [94]. Mixed mode stress intensity factors were determined by adopting the convergent value of the solution by increasing the

number of Williams' solution terms. It was shown that using higher-order terms of the Williams' solution helps the estimation of the stress intensity factors.

It should be noted that there are some other methods that do not need the knowledge of the crack tip position. Among these techniques, the J integral method [95] and the interaction integral technique [96] can be mentioned. Basically in all the previously mentioned methods the stress intensity factors were directly inferred from the output of digital image correlation which is a displacement field. However, as it was discussed the determined stress intensity factors are affected by the uncertainties in crack tip position. Additionally, the effect of the rigid body translations should be compensated to get reasonable results for the stress intensity factors. On the other hand in the J integral and interaction integral techniques as long as the crack tip is included in the integration domain (Figure 2-14), these methods are not affected by the crack tip position.

However, in both of these techniques the stress field (rather than displacement field) is needed to determine the integrals. Since the experimental displacement field always comes with some level of noise, the experimental displacement data do not completely satisfy the equilibrium equations and consequently this reduces the accuracy of the stress and strain analysis [97]. Therefore, it is almost impossible to get the stress and strain data from raw experimental displacement data [98]. Basically, determination of the stress/strain field from the displacement data requires numerical differentiation which is extensively sensitive to the noise in the data. Therefore, the data should be smoothed before doing the differentiation operation. Although this reduces the random errors in the data, it introduces systematic errors in the derivations [95]. Thus, it is true that these techniques do not need the crack tip position but in using them or generally in problems where the stress/strain are obtained from displacement field, filtering and smoothing or in general signal processing plays an important role and can reduce or increase the error in the determined parameters.

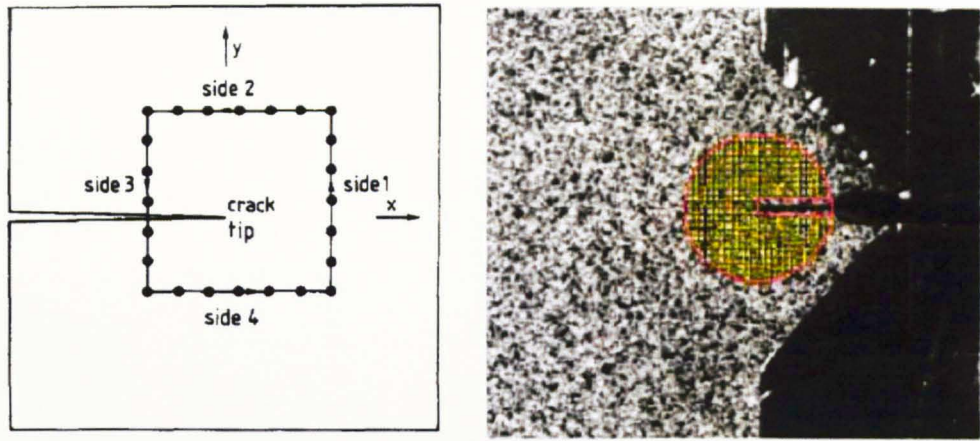


Figure 2-14 J integral domain (left) [95] and Interaction integral domain (right) [96]

All the previously reviewed methods were based on using the Williams' solution. For an alternative method the works of Shterenlikht *et al.* [71] and Lopez-Crespo [99] can be mentioned. In the former the strain fields were determined using the displacement data and the stress intensity factors were extracted using the Muskhelishvili's approach which previously had been used for photoelastic studies [58]. However, in the latter the displacement fields were directly written in the form of a Fourier series and using Muskhelishvili's approach the stress intensity factors were determined. This technique will be discussed further in chapter 5.

Although there is considerable amount of work regarding the stress intensity factor calculations, less attention has been paid to the T-stress determination using image correlation. To the author's knowledge only the works of Abanto-Bueno and Lambros [100, 101] and Carroll *et al.* [102] can be mentioned in this regard. In the former work, unlike most of the previously mentioned work, only one term and two terms of Williams' solution and only vertical displacements were used to extract the stress intensity factors and T-stress in homogeneous and Functionally Graded Materials (FGM). Although they determined the T-stress, the focus of their work was mostly in determining the stress intensity factors and exploring the effects of the presence of T-stress on the determined stress intensity factors. Therefore, no comparison was made between the calculated T-stress with other resources and the accuracy of the determined T-stresses was not investigated. The

same approach was used by Carroll *et al.* [102]. The T-stress was found for a pure mode I loading condition in a single edge crack case. Value of -110 MPa was found for the T-stress and compared to the value of -60 MPa reported by Anderson [103] which shows almost 100% difference. However, since the value of the T-stress is only reported for one case, it is hard to criticize their technique.

For completeness, the non full field and non-optical work of Maleski *et al.* [104] should also be mentioned. They used strain gauges to determine the T-stress under mode I loading conditions. They used the Williams' solution and investigate using two or three terms of the expansion. Data was collected from one and two strain gauges respectively bonded at 60 and 120 degree from the crack faces and away from the area where out of plane displacement exists. Their technique was only validated under mode I conditions. The position of the strain gauges will change with respect to the crack face as the crack grows or kinks and the sensitivity of this technique to the gauge position makes the results unrealistic in these situations. However, their technique, the normal stress difference technique, which was originally proposed by Yang and Ravi-Chandar [50] might be extendable to photoelasticity applications or techniques where the stress components or differences can be extracted experimentally.

### 2.4.3 Summary

Different experimental techniques and their application in fracture mechanics problems were reviewed. It was shown that in both full field stress techniques (such as photoelasticity and TSA) and displacement techniques (such as Moiré, ESPI and DIC) two approaches based on Williams' solution or Muskhelishvili's stress function approach have been used. Although some techniques do not require the crack tip position, in most of the techniques the crack tip position can influence the determined crack tip characteristic parameters. It was shown that in most of the works only stress intensity factors have been determined and the T-stress has been ignored or has not been determined. In cases where it has not been ignored only the effects of the presence of the T-stress on the calculated stress intensity factors have been investigated. There are few publications where the T-stress has been determined, however, the determined T-stresses were not accurate

or their accuracy was not explored. Therefore in this current work both TSA and DIC techniques have been used as the experimental techniques and methodologies have been developed to determine the T-stress and stress intensity factors accurately. Moreover, both Muskhelishvili's and Williams' approaches have been implemented in the calculations and a comparative study has been undertaken to compare these two approaches.

## **2.5 Conclusion**

The crack path problem and various theories to predict the crack paths in homogeneous materials were discussed. It was shown that even under pure mode I loading the crack path is not stable and it might be directionally unstable. Different criteria to justify this directional stability was reviewed and it was found that the T-stress and the plastic zone ahead of crack tip as well as other elastic parameters are highly influential in crack path problems. Thus in the next chapter the feasibility of three of the most popular crack path criteria are examined experimentally in interacting cracks field using thermoelastic stress analysis technique and numerically using finite element method.

The importance of the T-stress as a crack tip constraint was discussed. It was observed that not only is the T-stress influential in crack path problems but also it affects the crack growth rate, fracture toughness and tunnelling phenomenon that occurs in fatigue and fracture applications. It was shown that many numerical methods have been developed to determine the T-stress numerically in the literature. However, less attention has been paid to experimental determination of the T-stress and most of the works are limited to merely stress intensity factor determinations. This motivates the author to develop methodologies to determine the T-stress as well. Based on potential of the TSA and DIC in fatigue and fracture applications, these two experimental techniques were selected and methodologies have been developed which will be discussed in the following chapters.

## **Chapter 3**

# **Interacting crack paths**

The aim of this chapter is to investigate the ability of some of the most common existing criteria to predict the crack path in more realistic situations where more than one crack exists in the field of study.

In real structures such as the dove tail part of a turbine blade or the multi site damage regions in aircraft structure the failure can happen due to growth of more than one crack. The interaction of these cracks may have an effect on crack growth rate as well as the path each of cracks may follow. Analytical work assumes symmetry or the cracks growing at the same time. However, real cracks do not do this and the results may diverge from the expected behaviour. This makes the experimental study of a great importance. However, there are relatively few experimental studies regarding the interaction of cracks. Therefore, a study has been undertaken on sets of cracks with different interaction properties, numerically, using a finite element method, and experimentally, using Thermoelastic Stress Analysis (TSA).

The first part of this chapter is dedicated to the experimental study conducted. In this part, the specimens, test conditions and methodology to analyse the

experimental data are explained. The second part of the chapter describes the procedure used and assumptions made in finite element modelling. Various aspects of the theoretical background applied in the simulations are also reviewed. At the end of the chapter, the experimental and numerical results are compared and the corresponding uncertainties are discussed.

### 3.1 Fundamentals of Thermoelastic Stress Analysis

Thermoelastic stress analysis is an experimental technique which has become more popular since the full field surface temperature measurement has become more practical due to development of infrared detectors. This technique is based on the thermoelastic effect and measurement of the surface temperature changes of the order of  $0.001^{\circ}\text{C}$  experienced by a material subjected to changes in the volume.

#### 3.1.1 Thermoelastic effect

The thermoelastic effect is the temperature change induced by the deformation of a continuum. It can be shown [105] that for elastically deformed continuum under a reversible process,

$$dt = \frac{t}{\rho C_{\epsilon}} \frac{\partial \sigma_{ij}}{\partial t} d\epsilon_{ij} + \frac{\delta q}{C_{\epsilon}} \quad 3-1$$

where,  $t$  is absolute temperature,  $dt$  is the change in temperature,  $C_{\epsilon}$  is the specific heat at constant strain,  $\delta q$  is the heat exchange with environment,  $\rho$  is the density of the body,  $\sigma_{ij}$  is the tensor of stress change and  $\epsilon_{ij}$  is the tensor of strain change.

Now by using stress-strain-temperature relations for homogeneous isotropic materials and neglecting the effect of temperature on the Lamé elastic constants, for an adiabatic process it can be shown that [105],

$$\Delta t = -t_0 \frac{\alpha}{\rho C_p} \Delta \sigma_{kk} \quad 3-2$$

where,  $\alpha$  is the linear thermal expansion coefficient of the material,  $\rho$  is density and  $C_p$  is the specific heat at constant pressure.

Equation 3-2 is the main relationship in thermoelastic stress analysis. It should be noted that this equation has been derived for isotropic homogenous materials for elastic deformation under an adiabatic process with the assumption that the Lamé elastic constants do not vary in the range of temperature change.

The magnitude of temperature change induced by stress is just a few hundreds of a degree Celcius depending on the material properties. To have better feeling about the temperature changes induced due to the stress let us consider the temperature change that occurs as the result of applying 1 MPa stress to a carbon steel with following material properties [73] with the ambient temperature of 25 °C.

$$\left. \begin{array}{l} \alpha = 11.3 \times 10^{-6} \text{ K} \\ \rho = 7850 \text{ kg/m}^3 \\ C_p = 480 \text{ J/kg.K} \end{array} \right\} \longrightarrow \Delta t = -8.937 \times 10^{-4} \text{ K} \quad 3-3$$

This minute temperature change can be sensed by modern infrared detectors.

Although equation 3-2 is the main thermoelastic equation, it is usually used in its working form shown below,

$$AS = \Delta \sigma_{kk} \quad 3-4$$

in which the range of first invariant of the stress tensor ( $\Delta \sigma_{kk}$ ) has been correlated to the output signal of the camera ( $S$ ) with a calibration factor ( $A$ ).

### 3.1.2 Calibration of the thermoelastic signal

The captured thermoelastic images have their own units which are dependent on the apparatus used and temperature fluctuations. To convert these units to something more familiar like units of stress the corresponding calibration factor should be determined. Referring to the equations 3-2 and 3-3, this calibration factor is dependent on the reference temperature of the specimen, radiometric characteristics of the infrared sensors, material properties and surface emissivity of the specimen.

To calibrate the thermoelastic signals, the signal is measured for a known quantity, stress for example, should be known. There are many different techniques to do the calibration [73, 106], but one of the most commonly used

methods is bonding a strain gauge rosette at the back of a plane specimen where the corresponding thermoelastic signal from the front of the specimen can be obtained. It should be noted that due to the nature of thermoelastic stress analysis the applied load is cyclic (see equations 3-2 and 3-4 where variations of the stress are related to variations of the temperature), so when the strain gauges are to be used only the values of strain/stress in two extremes of loading cycle is needed.

According to equation 3-4 as the sum of principal stresses is an invariant parameter, the direction of the orthogonal rosette is not important, by substituting the strain using the Hooke's law in equation 3-4 we will have,

$$\frac{E}{1-\nu} \Delta \epsilon_{kk} = AS \quad 3-5$$

where,  $E$  is the modulus of elasticity,  $\nu$  is poisson's ratio,  $A$  is calibration factor,  $S$  thermoelastic signal and  $\Delta \epsilon_{kk}$  is the difference of sum of principal strains at point of interest. By rearranging equation 3-5, calibration factor can be calculated as follows,

$$A = \frac{1}{S} \frac{E}{1-\nu} \Delta \epsilon_{kk} \quad 3-6$$

### 3.1.3 Thermoelastic signal processing

What an infrared detector senses is a combination of the photon flux emitted from surface of the body, background noise as well as reflection from other sources. So, to extract the meaningful data from the output signal, the output signal of the detector needs to be processed.

In order to filter the background noise from the thermoelastic signals, the output signal of detectors is compared with a reference signal. The reference signal is a signal proportional to the load amplitude with the same frequency as the load in the case of constant amplitude loading. The reference signal can be obtained through a function generator that derives the loading machine, a strain gauge, load cell, a displacement transducer, an accelerometer or a position transducer.

The IR signal and reference signal are acquired and fed simultaneously to an electronic signal-processing device, where a computer algorithm compares the thermal image to the corresponding reference signal, and mathematically refines

the image to yield a meaningful measure of temperature variation arising due to elastic strains induced in response to the cyclic applied load[107].

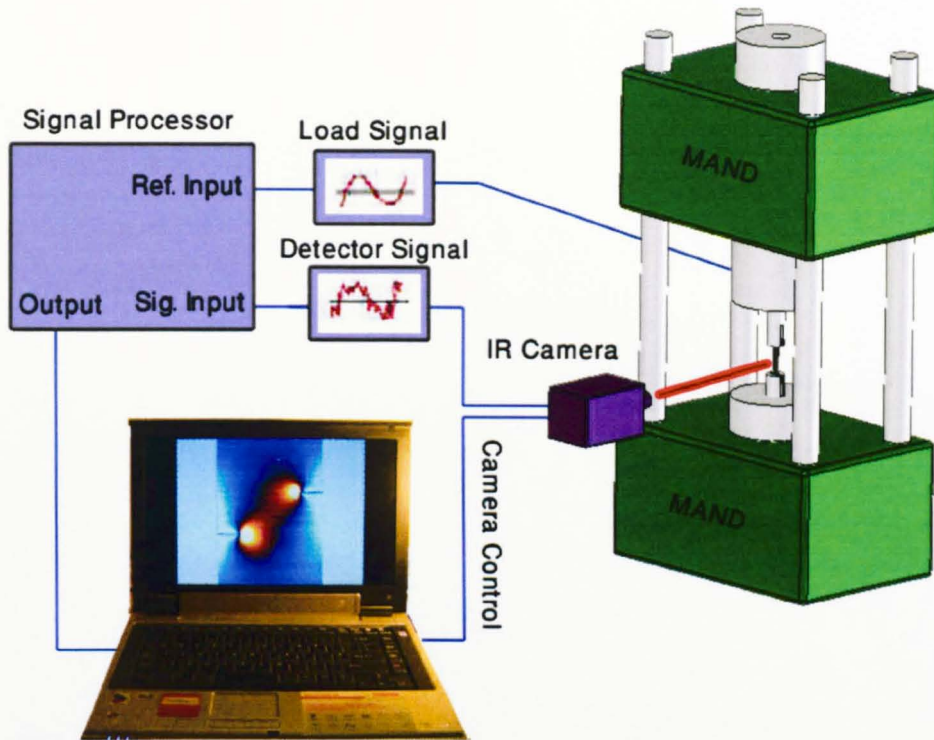


Figure 3-1 TSA apparatus

### 3.1.4 Acquired thermoelastic data

Using a Deltatherm system (either 1400 or 1500 series), the acquired data is either a DC image which is a static image showing only absolute temperatures or an AC image which is a differential thermal image that shows temperature variations over time. AC images are used to measure thermoelastic effect, while DC images are used only when the absolute temperatures themselves are of primary interest.

The information in AC images is presented as a vector through four different images. R-image, which is the magnitude of IR signal and express the variation of temperature in the target specimen. Phase-image, refers to the relative timing between the reference signal and the temperature variation in the target specimen. X-image (Figure 3-2(a)), and Y-image (Figure 3-2(b)) are the projection of R-image (Figure 3-2(c)) in X and Y axes of a given coordinate system.

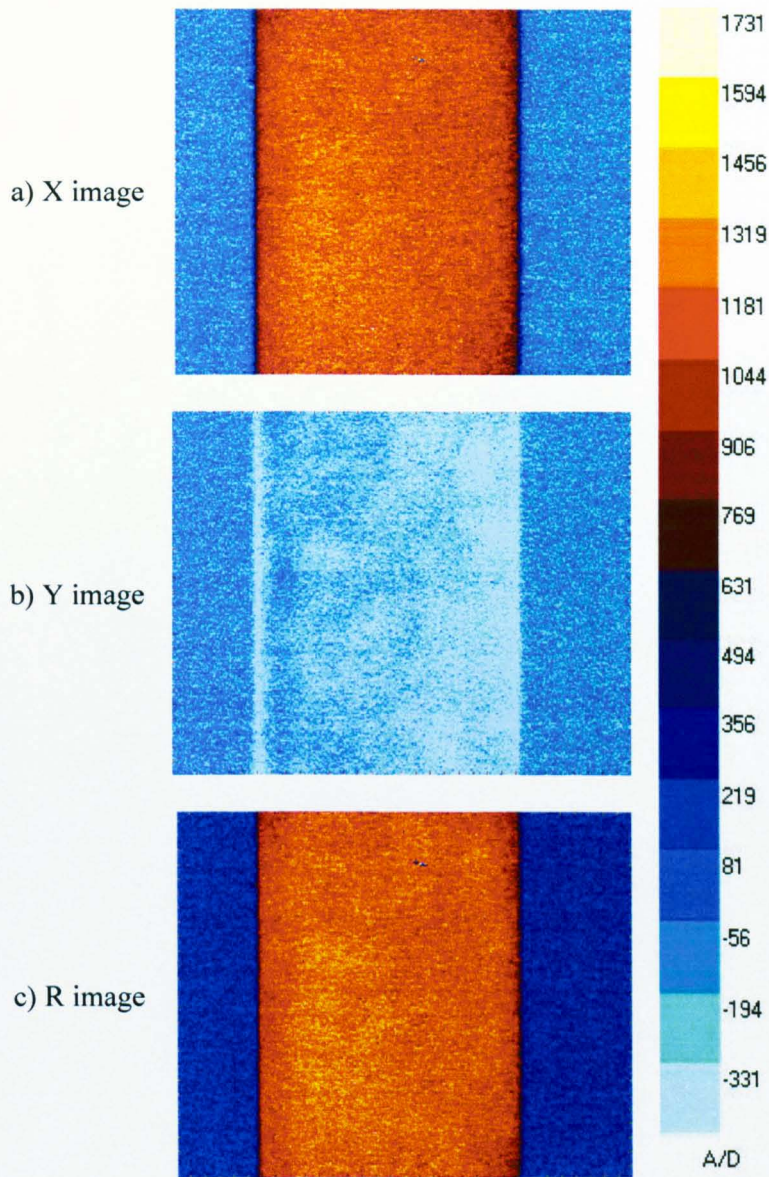


Figure 3-2 a) X, b) Y and c) R image in a tensile specimen

## 3.2 Experimental study

### 3.2.1 Specimens

Offset double edge slit fatigue specimens were manufactured to explore the trajectory and crack tip stress states of a pair of interacting fatigue cracks. Dimensions of the specimen are shown in Figure 3-3.

The specimens 6mm thick, 40mm wide and 250mm long were machined from a plate of 7010 T7651 aluminium alloy. Material properties and composition are listed in Table 3-1 and Table 3-2.

**Table 3-1 Material Properties of Al 7010 T7651**

$E$ [GPa]	$\nu$	Proof Stress (0.2) [MPa]	Tensile Strength [MPa]	$K_{IC}$ [MPa $\sqrt{m}$ ]	
				L-T	T-L
73	0.33	450	522	25	24

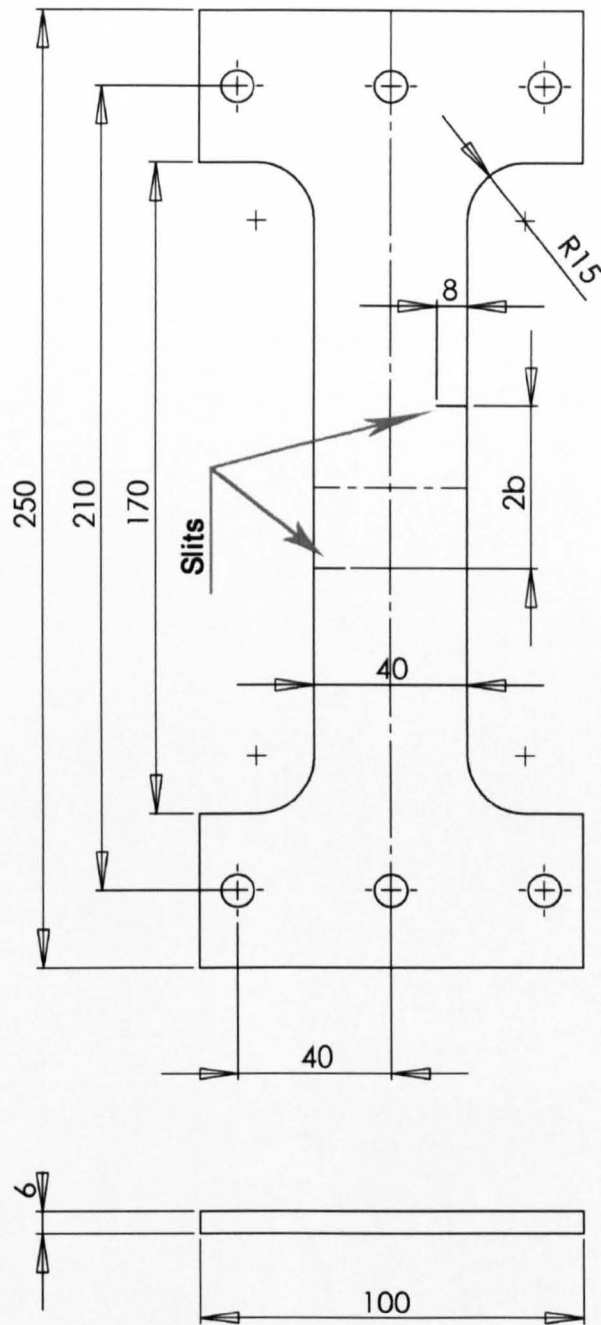
The specimens were cut along the rolling direction of the plates. The rolling direction was found out by cutting 15mm  $\times$  10mm samples from different plates of material. They were polished to 1 $\mu$ m using diamond paste and then anodized [108] using Baker's reagent (4ml HBF<sub>4</sub> 48%, 200ml ionized water) to reveal the grains and find the rolling direction. The result for one of the samples is shown in Figure 3-4.

Two slits, each 8mm long, were electric discharge machined using 0.3mm diameter wire on opposite sides of the specimens (see Figure 3-1).

Before machining the slits different models were created using ANSYS 5.4 [109]. As it is common in FE crack modelling, quarter point singular elements were used in elastic conditions (this will be more discussed in Section 3.4). It was found that for 2b values more than 48mm the two slits have no interaction with each other (Figure 3-5).

**Table 3-2 Al 7010 T7651 Chemical Composition%**

Element	Si	Fe	Cu	Mn	Mg	Cr	Ni	Zn	Ti	Zr	Others		Al
											each	total	
<b>Min</b>	-	-	1.5	-	2.1	-	-	5.7	-	0.1	-	-	Rem
<b>Max</b>	0.12	0.15	2.0	0.10	2.60	0.05	0.05	6.70	0.06	0.16	0.05	0.15	



All dimensions are in mm

Figure 3-3 Specimen dimensions

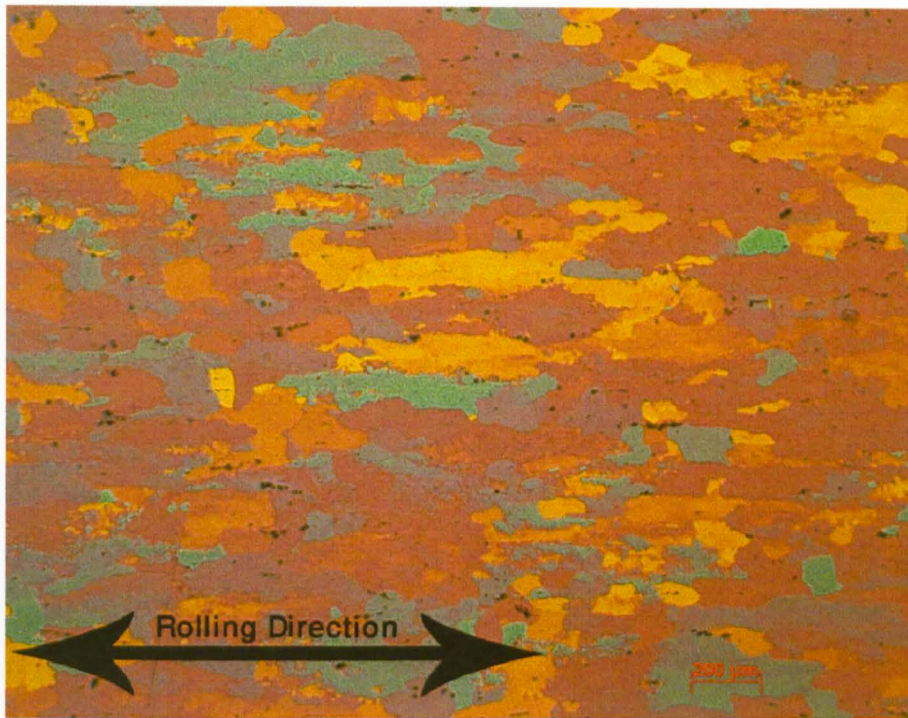


Figure 3-4 The shape of the grains of the Al 7010 T7651 obtained by Anodizing Method

Therefore, the vertical offset between the two cracks (namely,  $2b$  in Figure 3-3) was set at 0, 8, 16, 32 and 48mm for the series of tests conducted.

One face of each specimen was painted with a thin coat of matt black paint (RS type 496-782) to provide a surface of uniform and known emissivity.

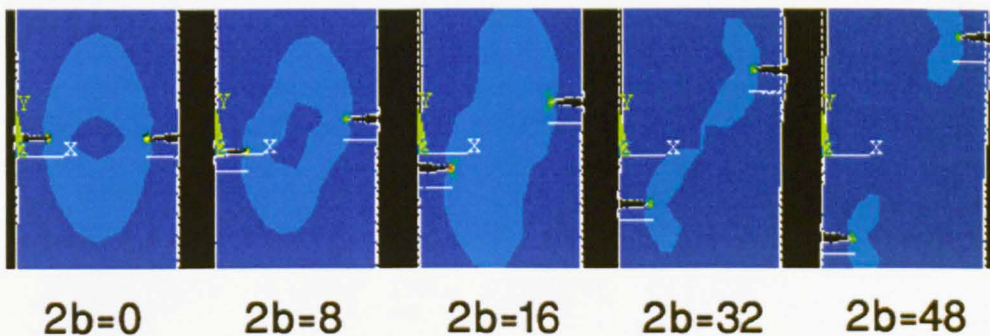


Figure 3-5 Stress field around the crack tips for different vertical offset between the two slits

### 3.2.2 Loading

The specimens were loaded through the pins located 210 mm apart (Figure 3-3). Fatigue tests were conducted under load control at a frequency of 20 Hz, a range of 3.6 kN and a mean load of 14.4 kN for the 0 and 8 mm offset specimens (No. 4 and No. 5 specimens, respectively) and a range of 3.5 kN and a mean load of 8.5 kN for the remaining three specimens (i.e. specimen No. 6, 7 and 8). The load range was reduced since considerable crack growth rate was observed in the first two tests. These loads have been summarised in Table 3-3.

The frequency was chosen to be sufficiently high for adiabatic conditions to be attained in the material ahead of the crack tip. By doing so, we ensure that the thermoelastic signal contains information about the sum of the elastic principal stresses from which the mode I and mode II stress intensity factor ranges can be evaluated.

**Table 3-3 Values of vertical offset (2b) and loading conditions for different specimens**

<b>Specimen No.</b>	4	5	6	7	8
<b>2b [mm]</b>	0	8	16	32	48
<b>Mean load [kN]</b>	14.4	14.4	8.5	8.5	8.5
<b>Load Range [kN]</b>	3.6	3.6	3.5	3.5	3.5

### 3.2.3 TSA equipment

The TSA equipment loading machine and the specimen are shown in Figure 3-6. A Deltatherm 1550 instrument manufactured by Stress Photonics Inc. was used to gather thermoelastic data from the matt black surface. As it can be seen in Figure 3-7 the quality of the images, particularly ahead of the crack tips, are good at the beginning but as the cracks grow some saturation is observed. So, to have a better image quality, different iris values for the IR camera which give different calibration factors were used throughout the subsequent tests.

A single rosette strain gauge (Tokyo Sokki Kenkyujo Co., 1 mm,  $120 \pm 0.5\Omega$ ) was bonded to a similar specimen in a region of uniform and known elastic stress to provide a calibration for the thermoelastic data. Figure 3-8 shows the position of

the strain gauge on the specimen and Figure 3-9 shows a typical TSA signal obtained for calibration.

Table 3-4 shows different calibration factors used for calibrating the TSA signals under different iris values, integration time and temperature. As it can be seen in Table 3-4, the change of ambient temperature of the order of one or two degrees, does not considerably affect the calibration factor. However, the calibration factor changes almost linearly with the changes in electronic iris value.

**Table 3-4 Calibration factors under different conditions**

<b>Electronic iris %</b>	<b>Integration Time [Sec.]</b>	<b>Temperature [C]</b>	<b>Calibration Factor (A)</b>	<b>Applicable specimen No.</b>
47	20	21	0.005	5, 6, 7, 8
37	40	21	0.006	4
37	20	22.1 to 24.1	0.005	3, 9 to 21
27	20	22.1 to 24.1	0.007	3, 10, 12
20	20	22.1 to 24.1	0.010	3, 9 to 21
15	20	22.1 to 24.1	0.013	3, 12
10	20	22.1 to 24.1	0.020	9 to 21

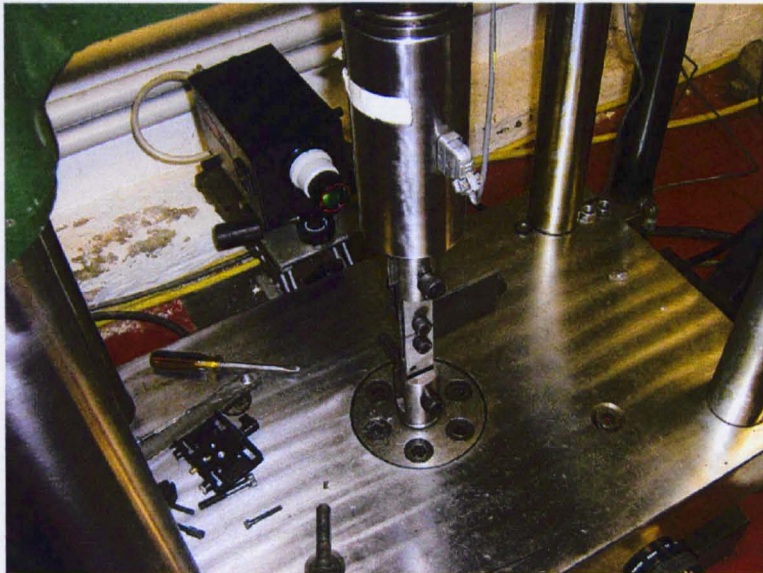


**Figure 3-6 TSA equipments**

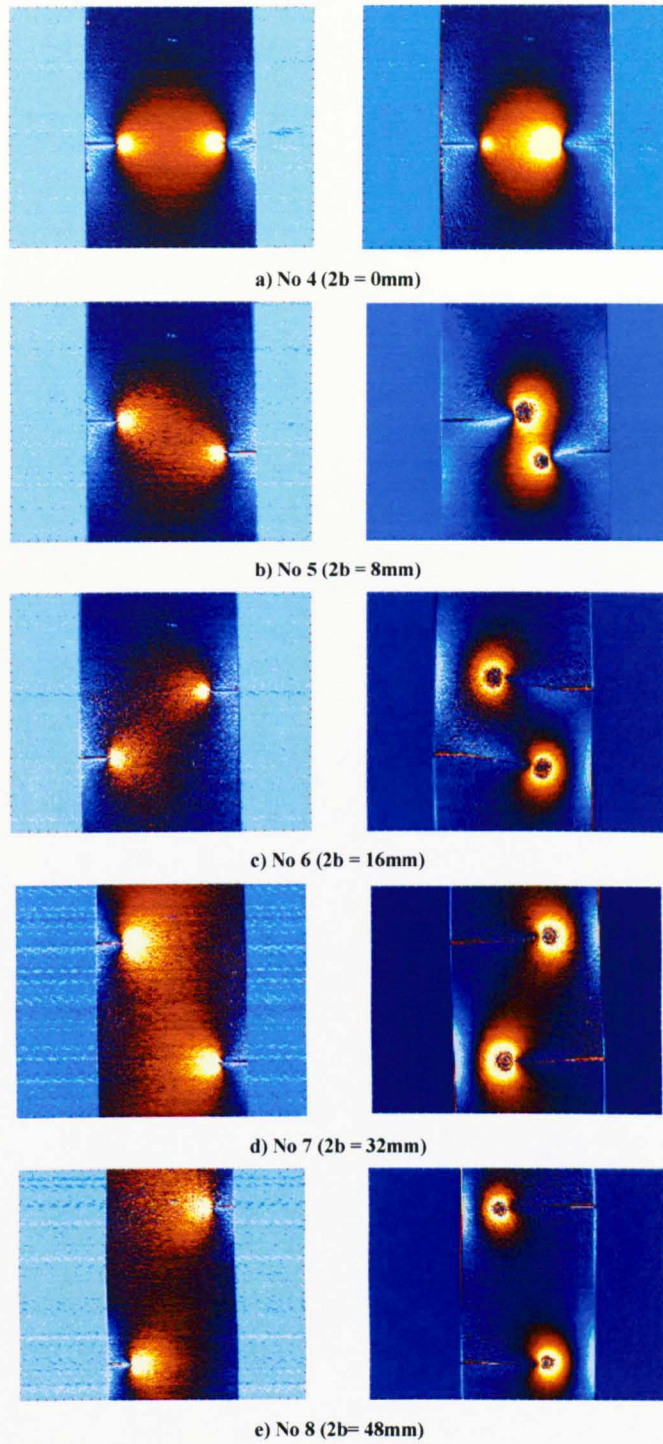


**Figure 3-7** Thermoelastic images for the 5 different crack offsets, showing the beginning (left) and end (right) of crack growth

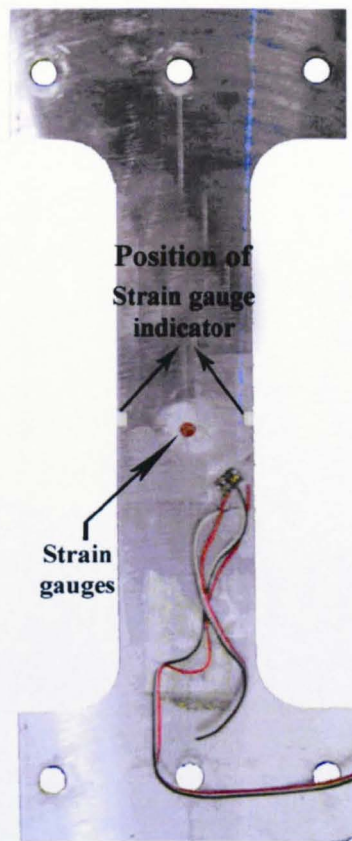


Figure 3-8 Position of strain gauge on the specimen

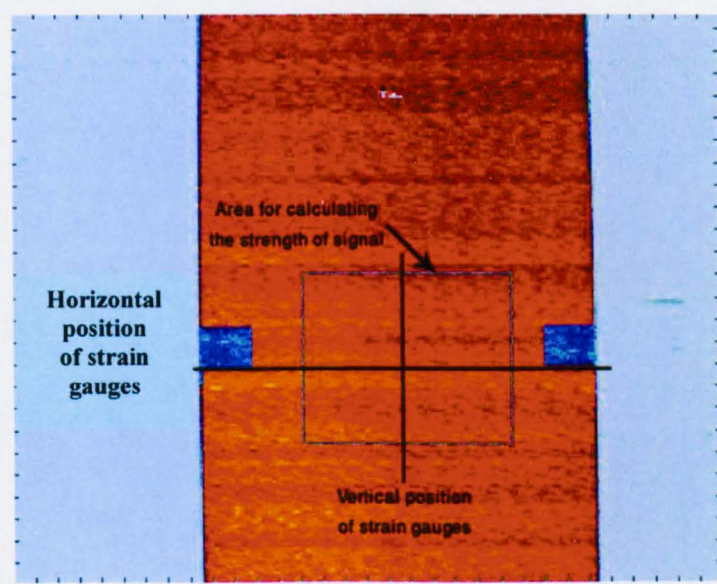


Figure 3-9 A typical TSA signal used for calibration

### 3.3 Methodology for extracting SIF from TSA data (FATCAT)

The crack tip position and the mode I and mode II stress intensity factor ranges occurring in the specimen were evaluated using the FATCAT software [85]. This software was developed at The University of Sheffield by Diaz [85] and was further modified and improved during the current research as described in chapter 4.

After choosing a position in the thermoelastic image the software collects experimental data points in the thermoelastic image from the region dominated by the crack tip stress field. Then it uses the collected data points (see Figure 3-10) to fit a mathematical model to the experimental data in order to describe the stress field ahead of the crack tip and finally uses the resultant fitting equation to determine the stress intensity factor range. The procedure, mathematical model used in fitting algorithm and the data collected are explained in the following section.

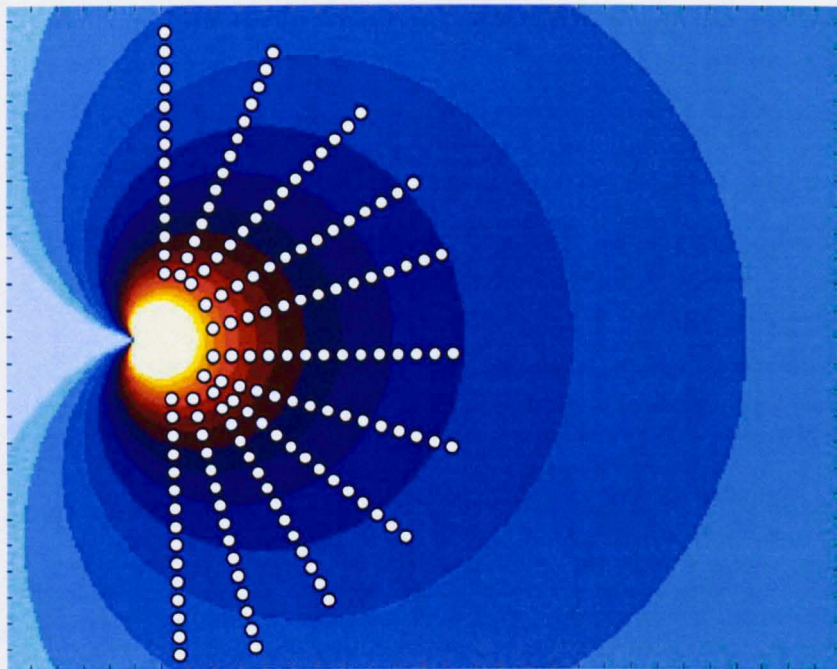


Figure 3-10 Data collection in FATCAT

### 3.3.1 Mathematical model

Muskhelishvili's approach [83] is used in FATCAT as the mathematical model of the crack tip stress field. Based on this approach for the general problem of elasticity the state of stress can be found using two analytic complex functions  $\Phi$  and  $\Omega$

$$\begin{aligned}\sigma_{yy} &= \text{Re}[\Phi(z)] + 2y \text{Im}[\Phi'(z)] + \text{Re}[\overline{\Omega}(z)] \\ \sigma_{xx} &= 3 \text{Re}[\Phi(z)] - 2y \text{Im}[\Phi'(z)] - \text{Re}[\Omega(\bar{z})] \\ \tau_{xy} &= -2y \text{Re}[\Phi'(z)] + \text{Im}[\overline{\Omega}(z)] - \text{Im}[\Phi(z)]\end{aligned}\quad 3-7$$

in which,  $z = x + iy$ , and bar sign is the conjugation operator. Therefore, range of the principal stress sum or in TSA terms,  $AS$ , can be found as

$$AS = \Delta(\sigma_{xx} + \sigma_{yy}) = 4 \text{Re}[\Phi(z)] \quad 3-8$$

Stress intensity factor can be determined as [110],

$$\Delta K_I - i\Delta K_{II} = \lim_{z \rightarrow 0} 2\sqrt{2\pi z} \Phi(z) \quad 3-9$$

So, the problem is reduced to finding  $\Phi(z)$ . This was done by Nurse and Patterson [58] using a general form of Fourier series for  $\Phi$  and  $\Omega$ . By satisfying the boundary conditions using the assumed stress functions they found

$$\Phi(\zeta) = A_0 + \frac{A_0 + \bar{A}_0 + \bar{B}_0}{\zeta^2 - 1} + \sum_{N=1}^{\infty} \left[ \left( \frac{2N}{\zeta^{2N}} \right) \left( \frac{\zeta^2 + 1}{\zeta^2 - 1} \right) \bar{A}_N - \frac{\bar{A}_N}{\zeta^{2N}} - \frac{\bar{B}_N}{\zeta^{2N}} + A_N \zeta^{2N} \right] \quad 3-10$$

where  $A$  and  $B$  are generally constant complex numbers and are unknown.

Relation between  $z$  and  $\zeta$  is defined as,

$$\zeta = \frac{z}{a} + \sqrt{\left( \frac{z}{a} \right)^2 - 1} \quad 3-11$$

where  $a$  represents the crack length. Now, by solving equation 3-8 to find  $A$  and  $B$  unknowns in equation 3-10 and finally using equation 3-9 stress intensity factor ranges ( $\Delta K_I$  and  $\Delta K_{II}$ ) can be determined. To solve this equation the Newton-Raphson method in FATCAT was used. This method is explained in the following section.

### 3.3.2 Newton-Raphson method

With no doubt, the Newton-Raphson or Newton-Fourier iterative method is one of the most popular techniques used to solve the initial value problems. In stress

intensity factor calculations it was first used by Sanford and Dally [57] to determine SIF from photoelastic fringes. Then it was used to extract SIF based on Muskhelishvili's approach both from photoelastic data [58] and thermoelastic data [84].

The Newton-Raphson method extrapolates the local derivatives to find an estimate for a root based on the Taylor expansion as follows,

$$(g_i)_{l+1} = (g_i)_l + \frac{\partial(g_i)_l}{\partial A_N} \Delta A_N + \frac{\partial(g_i)_l}{\partial B_N} \Delta B_N \quad 3-12$$

in which,  $l$  is the iteration number and  $\Delta A_N$  and  $\Delta B_N$  modify the previous values of  $A_N$  and  $B_N$ . By defining  $g_i = AS_i - 4 \operatorname{Re}[\Phi(z_i)]$  and comparing with equation 3-8, it is evident that  $g_i = 0$  and equation 3-12 can be written as

$$-(g_i)_l = \frac{\partial(g_i)_l}{\partial A_N} \Delta A_N + \frac{\partial(g_i)_l}{\partial B_N} \Delta B_N \quad \text{or in matrix notation} \quad 3-13$$

$$[g] = -[J][\Delta]$$

in which,

$$[g] = \begin{bmatrix} g_1 \\ \vdots \\ g_i \end{bmatrix}, [\Delta] = \begin{bmatrix} \Delta \operatorname{Re}(A_N) \\ \Delta \operatorname{Im}(A_N) \\ \Delta \operatorname{Re}(B_N) \\ \Delta \operatorname{Im}(B_N) \end{bmatrix} \quad 3-14$$

$$[J] = \begin{bmatrix} \frac{\partial g_1}{\partial \operatorname{Re}(A_N)} & \frac{\partial g_1}{\partial \operatorname{Im}(A_N)} & \frac{\partial g_1}{\partial \operatorname{Re}(B_N)} & \frac{\partial g_1}{\partial \operatorname{Im}(B_N)} \\ \vdots & \vdots & \vdots & \vdots \\ \frac{\partial g_i}{\partial \operatorname{Re}(A_N)} & \frac{\partial g_i}{\partial \operatorname{Im}(A_N)} & \frac{\partial g_i}{\partial \operatorname{Re}(B_N)} & \frac{\partial g_i}{\partial \operatorname{Im}(B_N)} \end{bmatrix}$$

So,  $[\Delta]$  can be determined using a least squares method. The procedure is repeated for a fixed tolerance or number of iterations. In FATCAT code, 10 iterations have been used for the calculations.

### 3.3.3 Crack tip position

To find the crack tip from TSA data two methods have been implemented in FATCAT, to reduce the operator dependency on the results. The first method is considers the crack tip coordinates as two unknowns in the equations and solves the equations to determine both Fourier series coefficients and crack tip positions

using a Downhill Simplex method [85, 111]. This method was not used here because it is sometimes required to be run many times to get close to an acceptable result [85, 112].

The other method based on Genetic Algorithm (GA) optimization was used to find the crack tip. To do so, a point in the image was used as an initial value for GA. Then the crack tip position found using GA was used in the Newton-Raphson algorithm to find the stress intensity factors.

### 3.3.4 Data point selection

Data points are selected from the region dominated by the crack tip stress field where the linear elastic region surrounding the crack tip and the effect of the through thickness stress is negligible. This method is based on the method described by Diaz *et al.* [88]. In this method the linear region is identified by using Stanley's plot [113]. In pure mode I loading conditions, Stanley *et al.*, observed that the maximum thermoelastic signal,  $S_{max}$ , occurred at the  $60^\circ$  angle with respect to the crack. Taking into account this condition in Williams' stress solution and considering only the singular term of the solution they found the vertical distance from the crack tip,  $y$ , is linearly proportional to the inverse square of the maximum thermoelastic signal in a line parallel to the crack in the distance of  $y$  from the crack.

$$y = \left( \frac{3\sqrt{3}\Delta K_I^2}{4\pi A^2} \right) \frac{1}{S_{max}^2} \quad 3-15$$

By plotting equation 3-15 for a real thermoelastic image, three different regions are observed, as in Figure 3-11.

In region A, no linearity is observed. It is due to lack of adiabatic conditions because of plastic deformation due to the high stress gradient at the crack tip. Region C is the region where the proposed mathematical model is not valid because the mathematical model assumes that the singular term is dominant. Region B is the region of linear behaviour and the mathematical model prevails. Consequently, data points were selected from region B. As it was mentioned in the literature review (section 2.4.1), such a linear behaviour is not always

observed. In such a condition the same range of data points were used in the calculations.

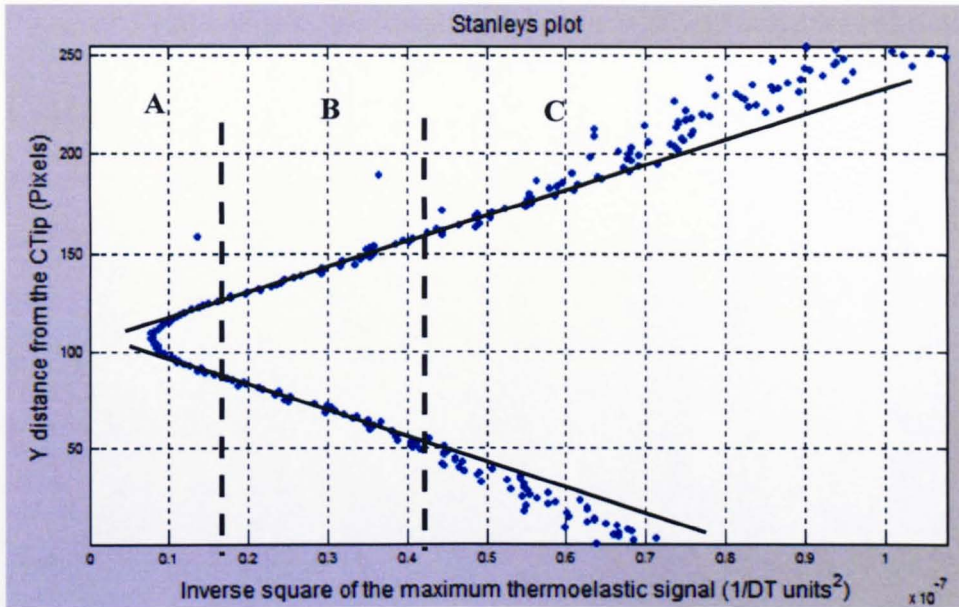


Figure 3-11 Different regions observed in Stanley's plot

### 3.4 FEM study

The FRANC2D/L finite element package [114] was used to predict the likely path of the cracks for each of the offset conditions. FRANC2D/L uses eight or six node elements with a quadratic shape function. These elements work well in elastic simulations and are capable of being used in fracture mechanics modelling where the stress singularity ahead of the crack tip can be modelled by moving the side nodes to the quarter point positions in elastic solutions.

The crack growth modelling was performed as follows. First, the stress intensity factors were determined from the FE results before the start of crack growth. The Displacement Correlation (DC) technique, Modified Crack Closure Integral (MCCI) technique and the J-integral technique were used to determine the stress intensity factors. These techniques will be reviewed briefly in the next section. Then the crack kink angle was determined using three of the most common crack path prediction criteria available which will be discussed later on in section 3.4.1.

These criteria have been developed for brittle fracture crack paths. However, they can be used in fatigue crack path prediction as well [13].

After determining the kink angle the mesh around the crack tip was deleted, Figure 3-12(a), and the geometry was modified by extending the crack geometry to move the crack tip in the direction of the predicted kink, Figure 3-12(b). The area was re-meshed, Figure 3-12(c), and above procedure was repeated until the crack(s) reach close to the boundary of the specimen. To explore the effect of the crack extension size in each increment, the increment was changed from 5mm to 1mm, in 1mm steps, and the crack paths were compared. No difference was observed between 2mm and 1mm cases and therefore 2mm crack extension were used in the simulations.

In elastic modelling of the crack region using singular elements a very fine mesh is not needed. However, it is recommended [109] that to get a reasonable result, the singular element size should be at least than  $1/8^{\text{th}}$  of the crack length in radial direction. This size is  $1/2$  of the crack length in each crack increment recommended by Swenson and James [114]. To determine the uncertainty introduced due to the size of the singular elements, the mode I stress intensity factor was determined using 2 singular elements per crack extension length and then the element was modified to have 4 and 8 singular elements per crack extension length. No difference was observed between the 2 and 4 element cases and there was only 0.05% difference with the 8 element case. So two elements were used along the crack extension which is also in agreement with Sutton *et al.* [115].

In circumferential direction an element is needed at least every  $40^{\circ}$  [109] or  $45^{\circ}$  [114]. The results are not so sensitive to this number and using more elements (smaller angles) does not introduce a noticeable difference in the results. For example the difference in the mode I stress intensity factor using one element in every  $45^{\circ}$  and  $22.5^{\circ}$  is only 0.2%. Therefore, one element in every  $45^{\circ}$  was used in the simulations.

It is noteworthy to mention that the quarter point singular elements are only valid for elastic simulation where the singularity is in the order of  $1/\sqrt{r}$  for the stress field. In cases where the stress field singularity is in the order of  $1/r$  the element

mid nodes should be moved to half point positions. Besides, only 8 node elements without collapsed nodes in the crack tip are recommended. However, in large strain analysis or in cases where the stress singularity has a general form of  $r^{-1}$ , none of the above singularities are applicable and only a very fine mesh is the feasible solution [103].

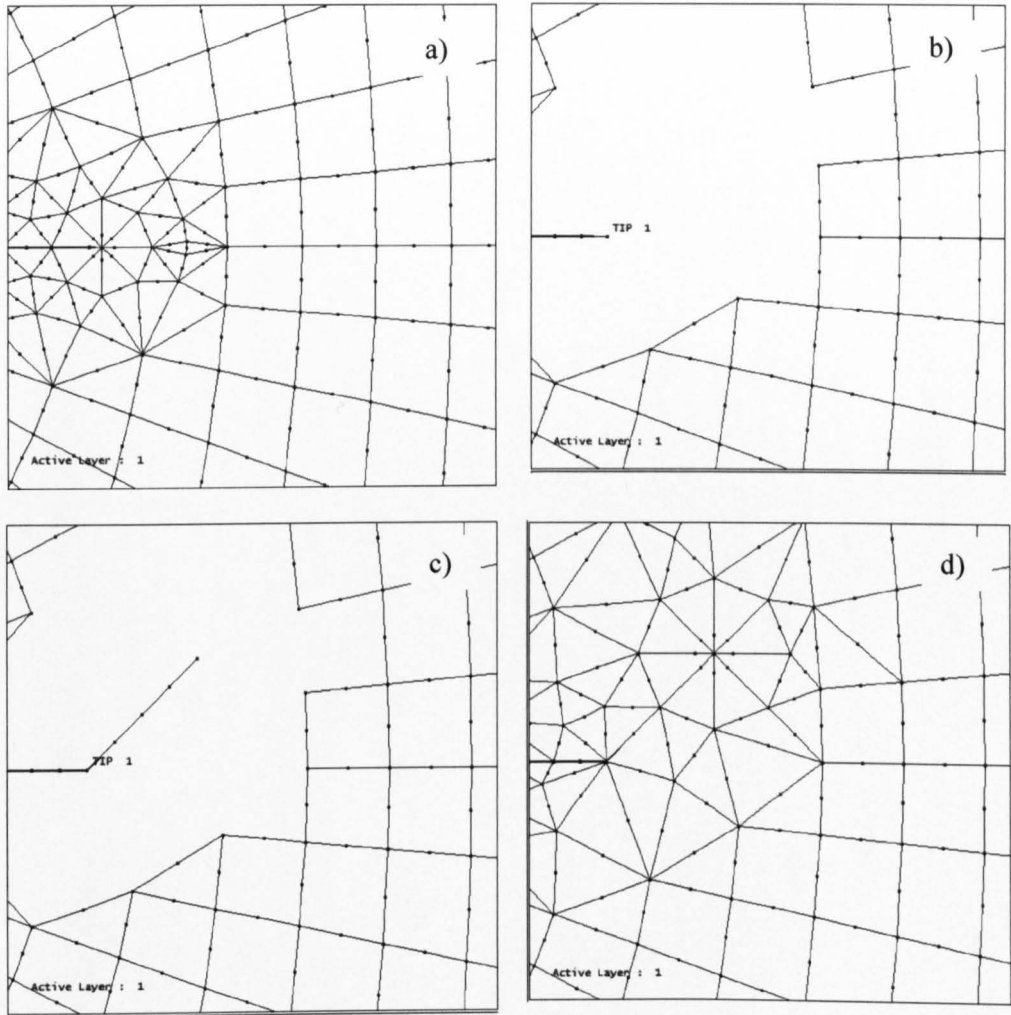


**Figure 3-12 Crack growing procedure a) original crack and mesh b) deleting elements c) creating new crack geometry d) re-meshing the deleted region**

### 3.4.1 Numerical SIF calculation

As mentioned before, to extract the stress intensity factors from the finite element local field information, three numerical techniques were used which are briefly explained here.

#### 3.4.1.1 Displacement correlation technique

The Displacement Correlation technique is based on correlation of the FE determined displacement field with the theoretical values.

Using the Williams' asymptotic solution and ignoring all the non-singular terms, the theoretical plane strain displacement field can be written as equation 3-16. where,  $K$  is the SIF,  $r$  and  $\theta$  are radial and angular distance from crack tip, and  $\nu$  and  $\mu$  are material constants for plane strain conditions. In plane stress conditions,  $\nu = \nu / (1 + \nu)$ .

$$\begin{aligned} u &= \frac{K_I}{\mu} \sqrt{\frac{r}{2\pi}} \cos \frac{\theta}{2} \left( 1 - 2\nu + \sin^2 \frac{\theta}{2} \right) + \frac{K_{II}}{\mu} \sqrt{\frac{r}{2\pi}} \sin \frac{\theta}{2} \left( 2 - 2\nu + \cos^2 \frac{\theta}{2} \right) \\ v &= \frac{K_I}{\mu} \sqrt{\frac{r}{2\pi}} \sin \frac{\theta}{2} \left( 2 - 2\nu - \cos^2 \frac{\theta}{2} \right) - \frac{K_{II}}{\mu} \sqrt{\frac{r}{2\pi}} \cos \frac{\theta}{2} \left( 1 - 2\nu + \sin^2 \frac{\theta}{2} \right) \end{aligned} \quad 3-16$$

Thus, for a quarter point singular element, as shown in Figure 3-13, the theoretical difference between the upper and lower faces of the crack can be determined using equation 3-16 and using  $\theta = 180^\circ$  for the upper face and  $\theta = -180^\circ$  for the lower face,

$$\begin{aligned} u_{upper} - u_{lower} &= \frac{4K_{II}}{\mu} \sqrt{\frac{r}{2\pi}} (1 - \nu) \\ v_{upper} - v_{lower} &= \frac{4K_I}{\mu} \sqrt{\frac{r}{2\pi}} (1 - \nu) \end{aligned} \quad 3-17$$

The FEM solution for this type of element can be derived [116] as,

$$v_{upper} - v_{lower} = [4(\nu_2 - \nu_4 + \nu_5 - \nu_3)] \sqrt{\frac{r}{r_3}} + [4(\nu_2 - \nu_4) - 2(\nu_5 - \nu_3)] \frac{r}{r_3} \quad 3-18$$

where the indices represent the node numbers as shown in Figure 3-13. By correlating equation 3-18 and equation 3-17 for vertical displacement,  $K_I$  can be determined as follows,

$$K_I = \frac{\mu\sqrt{2\pi}}{4(1-\nu)\sqrt{r_3}} \quad 3-19$$

An analogous procedure can be used to determine  $K_{II}$ .

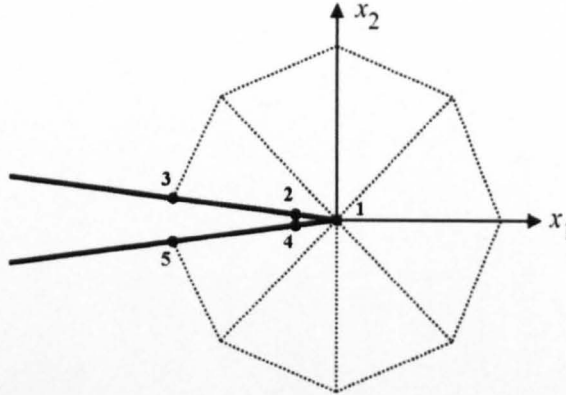


Figure 3-13 Singular elements ahead of a crack

#### 3.4.1.2 Modified crack closure integral technique (MCCI)

The Crack Closure Integral technique (CCI) was first proposed by Rybicki and Kanninen [117]. This technique is based on Irwin's contention which says in a  $\Delta C$  extension process of a crack the absorbed energy in the process is equal to the work needed to close the crack to its original length. Writing this statement for a linear element yields [117],

$$G_I = \frac{1}{2\Delta L} F_y^c (v^c - v^d) = \frac{K_I^2}{E} \alpha \quad 3-20$$

$$G_{II} = \frac{1}{2\Delta L} F_x^c (u^c - u^d) = \frac{K_{II}^2}{E} \alpha$$

where  $G_I$  and  $G_{II}$  are the energy release rates,  $F$  is the nodal force to close the crack tip, and  $u$  and  $v$  are the horizontal and vertical displacements for nodes  $c$  and  $d$ , respectively (as shown in Figure 3-14).  $\alpha=1$  for plane stress and  $(1-\nu^2)$  for plane strain conditions.

Based on CCI, the potential energy is calculated from two analyses before and after crack growth. In the modified version (MCCI), it is assumed that the  $\Delta L$  is

sufficiently small and in this case,  $v^c = v^a$ ,  $u^c = u^a$ ,  $v^d = v^b$  and  $u^d = u^b$ . Therefore, SIF can be determined as

$$K_I = \sqrt{\frac{E}{2\alpha\Delta L} F_y^c (v^a - v^b)}$$

$$K_{II} = \sqrt{\frac{E}{2\alpha\Delta L} F_x^c (u^a - u^b)}$$
3-21

which means only by one analysis, the SIF and energy release rate can be determined.

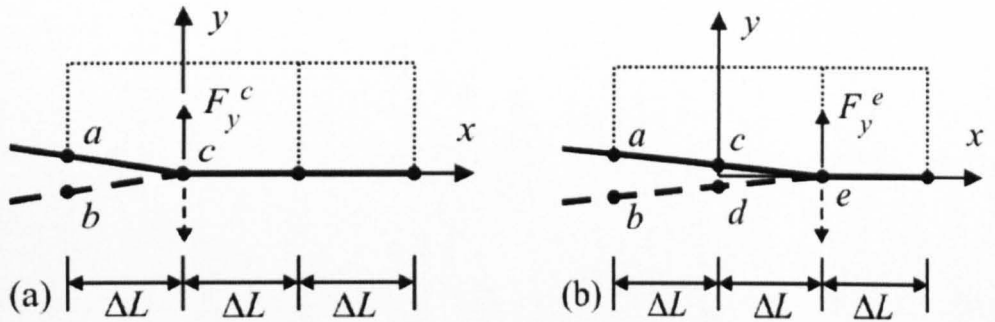


Figure 3-14 Mesh configuration used for CCI and MCCI a) before crack growth b) after crack growth [116]

### 3.4.1.3 *J*-integral technique

$J$  is a path independent line integral which is defined as  $J = \int_{\Gamma} \left( w dy - T_i \frac{\partial u_i}{\partial x} ds \right)$  in

which  $w$  is the strain energy density,  $T_i$  are components of the traction vector,  $u_i$  are displacement vector components, and  $ds$  is a length increment along the contour  $\Gamma$ .

$J$  is definable in both linear and non-linear materials. In elastic conditions it is equivalent to the energy release rate. So, by determining the integral in elastic conditions the SIF and energy release rate can be calculated. The only problem is that how mixed mode stress intensity factors can be extracted from  $J$ . To do so both strain field and displacement field can be decomposed to symmetric and anti-symmetric parts and the corresponding SIF and energy release rate can be determined as follows.

$$\begin{aligned}\sigma &= \sigma_{sym} + \sigma_{anti-sym} = \frac{\sigma + \bar{\sigma}}{2} + \frac{\sigma - \bar{\sigma}}{2} \\ u &= u_{sym} + u_{anti-sym} = \frac{1}{2} \left\{ \begin{matrix} u + \bar{u} \\ v - \bar{v} \end{matrix} \right\} + \frac{1}{2} \left\{ \begin{matrix} u - \bar{u} \\ v + \bar{v} \end{matrix} \right\}\end{aligned}\quad 3-22$$

where, the bar sign shows transpose operation. Then the energy release rate and stress intensity factors can be determined. Thus:

$$\begin{aligned}G_I &= J_I = J(u_{sym}, \sigma_{sym}) = \frac{K_I^2}{E} \alpha \\ G_{II} &= J_{II} = J(u_{anti-sym}, \sigma_{anti-sym}) = \frac{K_{II}^2}{E} \alpha\end{aligned}\quad 3-23$$

### 3.4.2 Crack path prediction criteria

An extensive amount of work has been done related to the crack path prediction [17]. However, most of the studies are focused on the crack initiation criteria. These types of criteria are applicable in FE simulations provided that they are applied incrementally with the extension of the crack.

Among the available first order criteria to predict the initial kink angle of the cracks, three of the most popular ones, which are implemented in FRANC2D/L, are briefly explained here.

#### 3.4.2.1 Maximum tangential stress (MTS)

The maximum tangential stress criterion which has been proposed by Erdogan and Sih [8], states that the crack grows in the radial direction where the tangential stress,  $\sigma_{\theta\theta}$ , is maximum. The corresponding  $\theta$  is defined as  $\theta_c$ . In mathematical terms,

$$\sigma_{\theta\theta} = \frac{1}{\sqrt{2\pi}} \cos \frac{\theta}{2} \left( K_I \cos^2 \frac{\theta}{2} - \frac{3}{2} K_{II} \sin \theta \right) \quad 3-24$$

By considering,  $\frac{\partial \sigma_{\theta\theta}}{\partial \theta} = 0$ , and  $\frac{\partial^2 \sigma_{\theta\theta}}{\partial \theta^2} < 0$ ,

$$\theta_c = 2 \tan^{-1} \left[ \frac{1 - \sqrt{1 + 8(K_{II}/K_I)^2}}{4(K_{II}/K_I)} \right] \quad 3-25$$

### 3.4.2.2 Minimum strain energy density factor (*S-min*)

The minimum strain energy density factor criterion has been proposed by Sih [9]. He showed that the strain energy ( $W$ ) stored in an element with the area of ( $A$ ) can be expressed as,

$$\frac{dW}{dA} = \frac{1}{r} (a_{11}k_1^2 + 2a_{12}k_1k_2 + a_{22}k_2^2) = \frac{1}{r} SE \quad 3-26$$

in which  $a_{ij}$  ( $i, j = 1, 2$ ) are functions of  $\theta$  and elastic constants.  $k_i$  is proportional to stress intensity factors,  $k_i = K_i/\sqrt{\pi}$  ( $i = I, II, III$ ), and  $SE$  is defined as the strain energy density factor.

The criterion states that the initial crack growth occurs in the direction along which the strain energy density factor is minimum, i.e.

$$\frac{\partial S}{\partial \theta} = 0, \text{ and } \frac{\partial^2 S}{\partial \theta^2} > 0.$$

### 3.4.2.3 Maximum energy release rate (*G-max*)

The maximum energy release rate criterion was first proposed by Hussain *et al.* [118]. They showed that the energy release rate  $G$  under plane stress condition can be expressed as,

$$G = \left( \frac{4}{E} \right) \left( \frac{1}{3 + \cos^2 \theta} \right)^2 \left[ K_I^2 (1 + 3 \cos^2 \theta) + 4K_I K_{II} \sin 2\theta + K_{II}^2 (9 - 5 \cos^2 \theta) \right] \quad 3-27$$

The criterion states that the initial crack growth occurs in the direction along which the energy release rate is a maximum, i.e.  $\partial G/\partial \theta = 0$ , and  $\partial^2 G/\partial \theta^2 < 0$ .

Figure 3-15 shows is a comparison of crack initiation angle predicted with the three different criteria for the whole range of mode mixity.

These criteria show the most difference in pure mode I conditions, whereas by increasing the mode mixity this difference decreases.

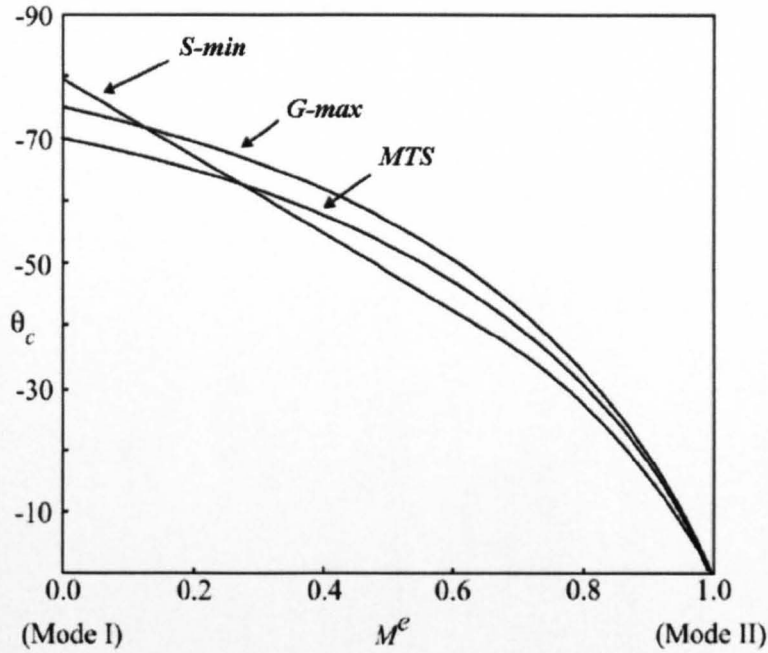


Figure 3-15 Comparison of different criteria to calculate the crack initiation angle ( $\theta_c$ ) for

range of mode mixity  $M^e$ , where  $M^e = \frac{2}{\pi} \tan^{-1} \left( \frac{K_I}{K_{II}} \right)$  (after [116])

### 3.4.3 Initial analysis

In this regard and for the 8mm vertical offset cracked specimen, the DC, MCCI and J integral methods were used to determine the stress intensity factors. Additionally, the aforementioned common crack path prediction criteria, i.e. MTS, S-min and G-max criteria were used as the crack turning criteria.

Figure 3-16 shows the comparison of the predicted crack paths using the aforementioned methods and criteria. The predicted trajectory varies slightly according to the different techniques used in the calculation of stress intensity factors and the crack turning criterion chosen. Although there are no major discrepancies, which are in agreement with Bittencourt *et al.* [119], there are small differences in the crack paths predicted, especially in the case where the cracks are initially only slightly offset.

Therefore, the paths found by using the MTS turning criterion were used for experimental comparison and the J integral method was used to evaluate the stress intensity factors for the rest of cases.

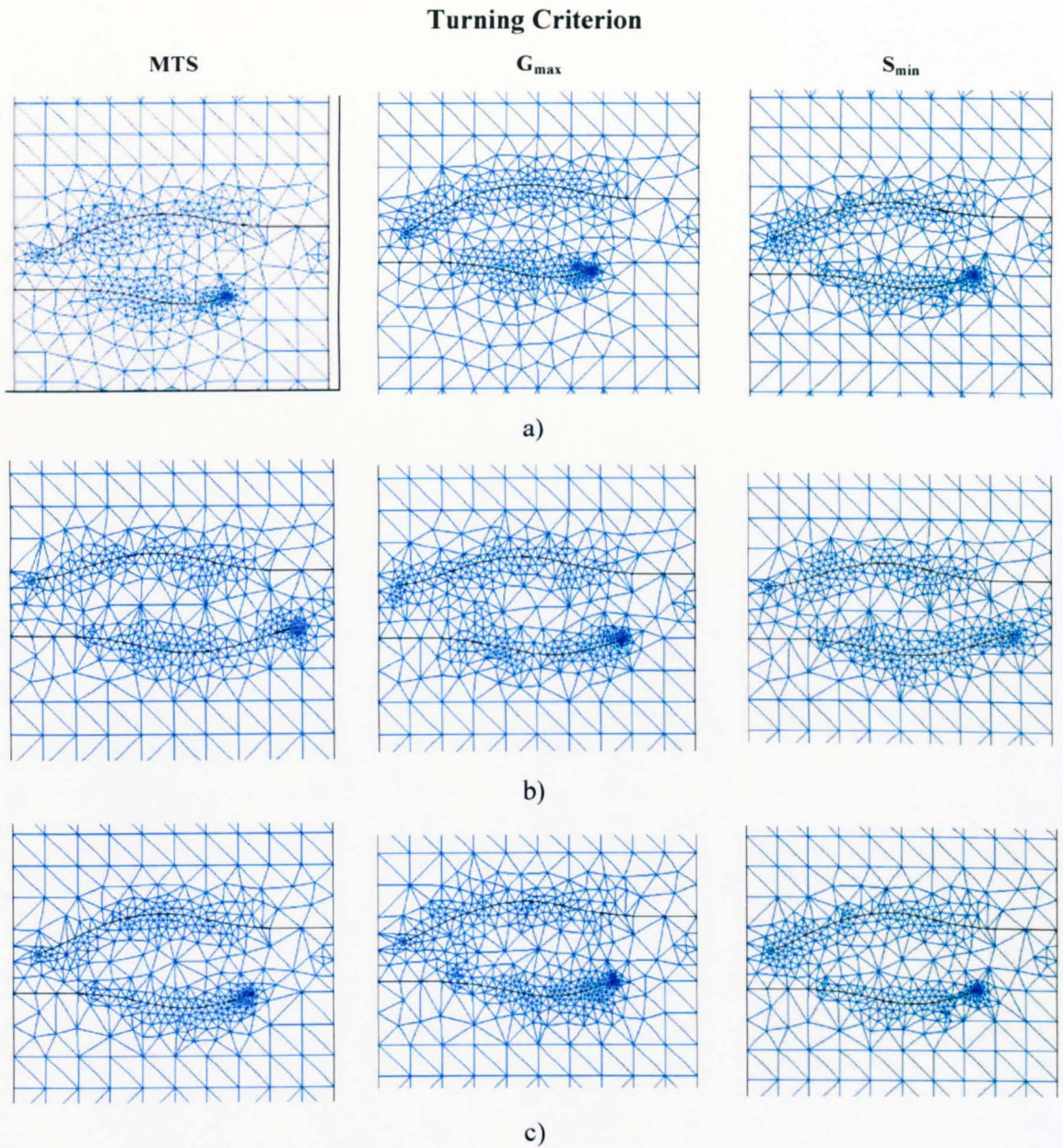


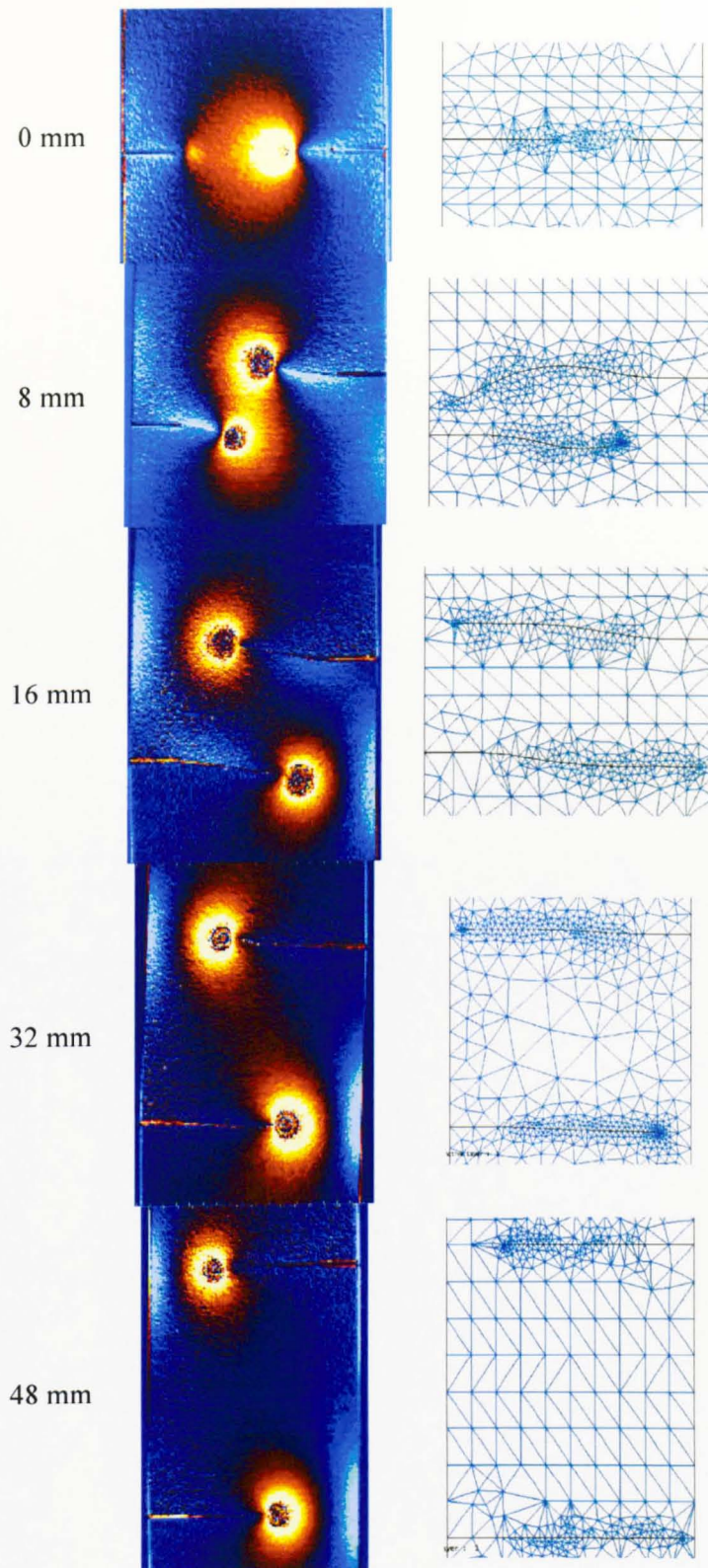
**Figure 3-16 Predicted crack path for 8mm vertical offset cracked specimen using a) Displacement Correlation b) MCCI c) J-integral**

### 3.5 Results and discussion

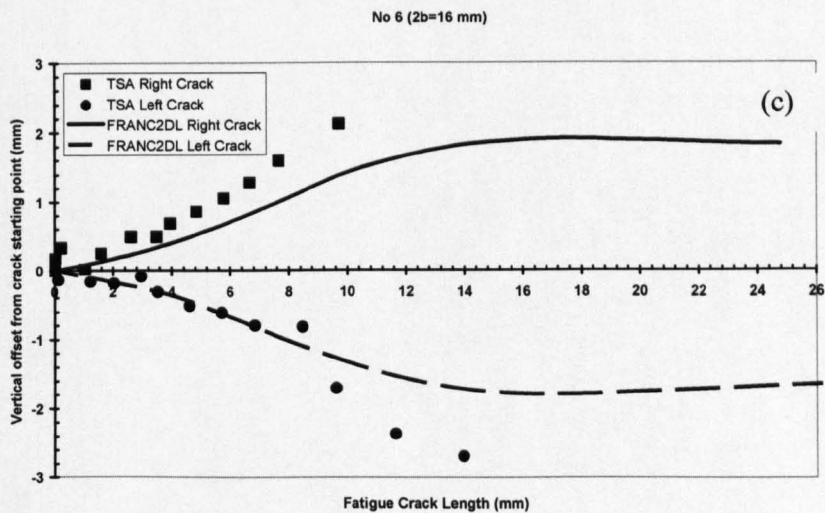
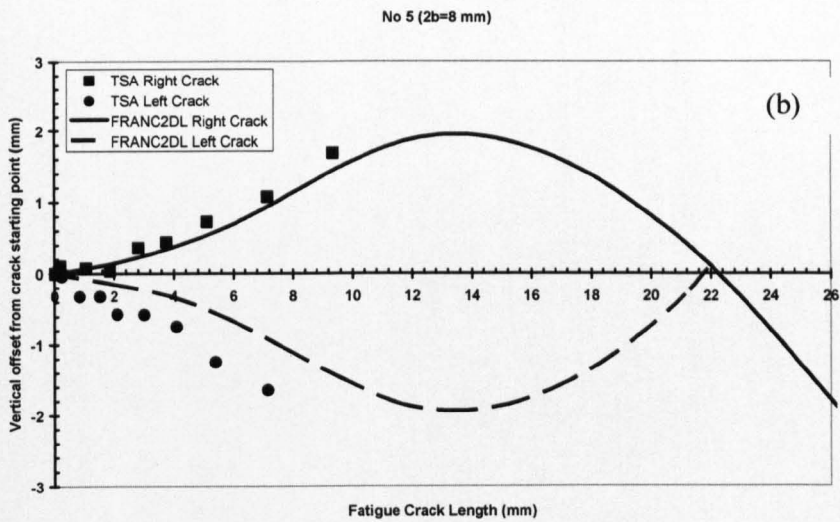
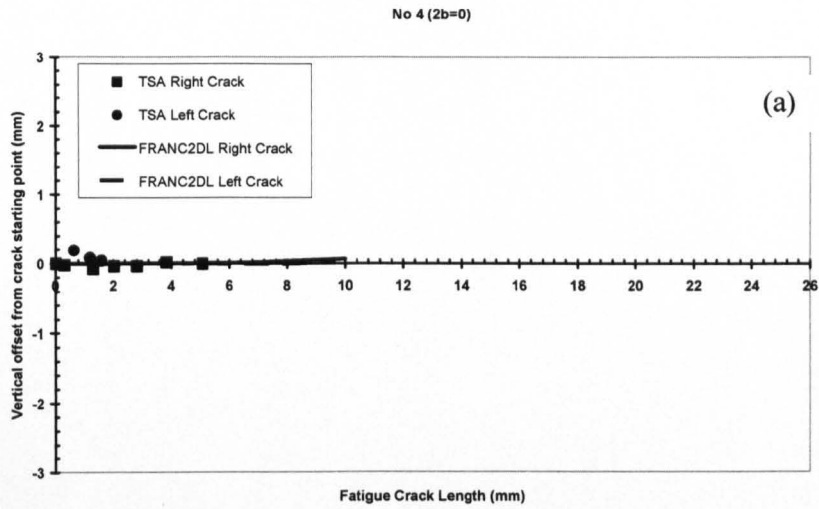
A qualitative comparison between the thermoelastic and the finite element data for the 5 different crack offsets is made in Figure 3-17. The experimental crack paths are very similar to those predicted by the finite element method. This is relatively surprising since the numerical simulations assume that both the left and right hand cracks start growing at the same time. In practice, the creation of a growing fatigue crack from the tip of the spark machine slit takes a different number of cycles in every case, and the cracks do not grow symmetrically as can be observed in the thermoelastic data from the 0 mm offset in Figure 3-17(a) where the right hand crack grew faster than the left hand one.

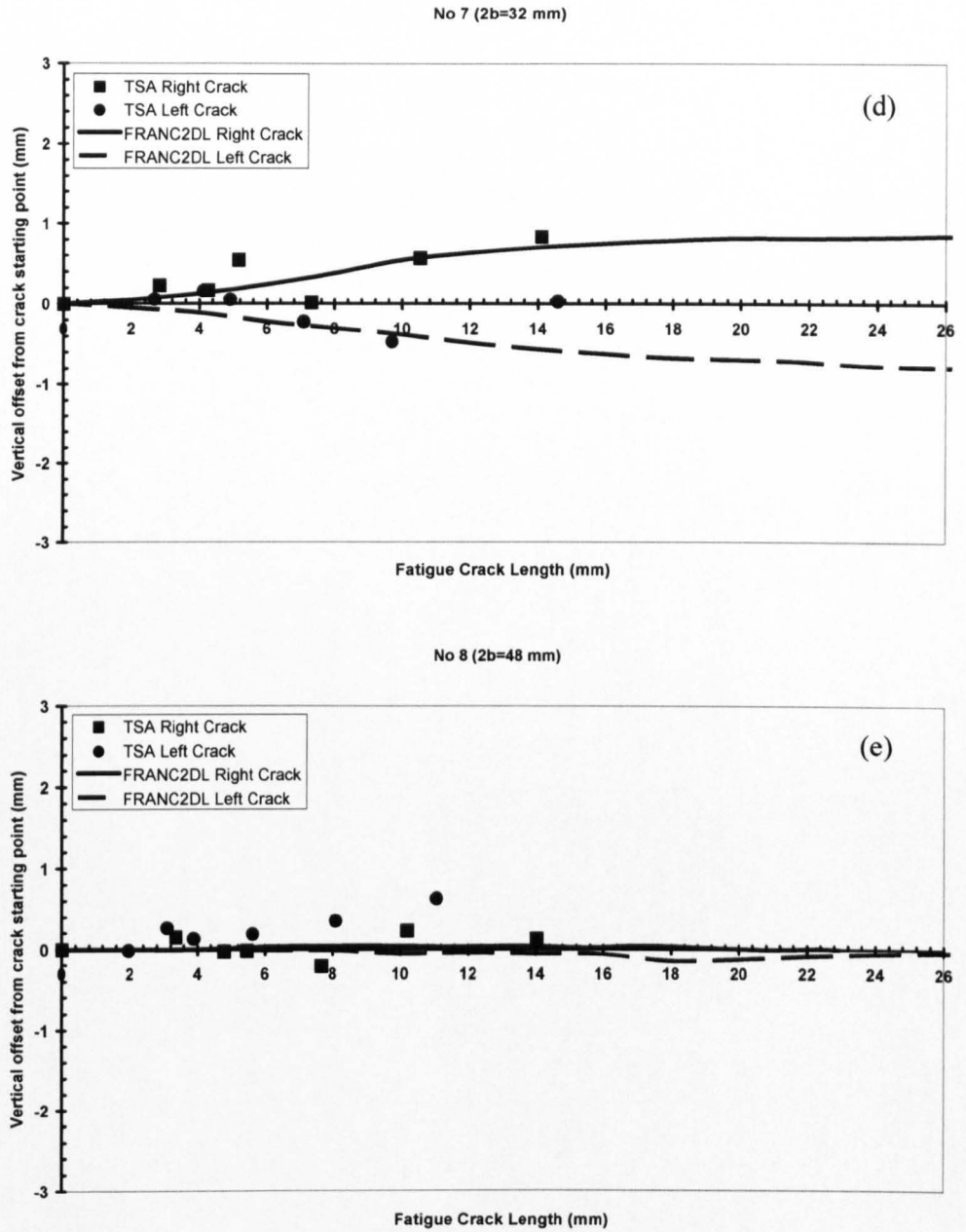
Quantitative comparisons are made in Figure 3-18 and Figure 3-19. The crack tip positions throughout the tests were located from the thermoelastic data using the GA implemented in FATCAT and compared with the positions predicted by the FRANC2D/L finite element package for offsets of 0, 8, 16, 32 and 48 mm respectively in Figure 3-18. Results are more consistent in early stages of the crack growth, however, as the crack grows the differences between experimental and numerical results are accumulated.

The values of  $\Delta K_I$  derived from the FRANC2D/L analysis, Figure 3-19, are quite consistent with the experimental results. The stress intensity factor ranges found using the thermoelastic data have been established [87] to be from the true, or effective, conditions at the crack tip, and therefore incorporate the effects of crack closure and crack face friction. That is why the experimental values of  $\Delta K_I$  are found to be slightly smaller than those predicted by the finite element technique in cases where almost a symmetrical crack growth is observed from left and right cracks (see Figure 3-19(b) to Figure 3-19(e). However, the asymmetry of the crack growth completely swamps any subtle closure effects that may occur. In the zero offset case, for example, in Figure 3-19 the  $\Delta K_I$  of the right hand crack is much larger than that of the left hand crack since it started growing sooner and grew much longer than the left hand crack. It should be noted, as an aside, that mostly, the mode II stress intensity factor ranges are approximately zero, as expected and as predicted by the numerical simulations. But is it always like this?

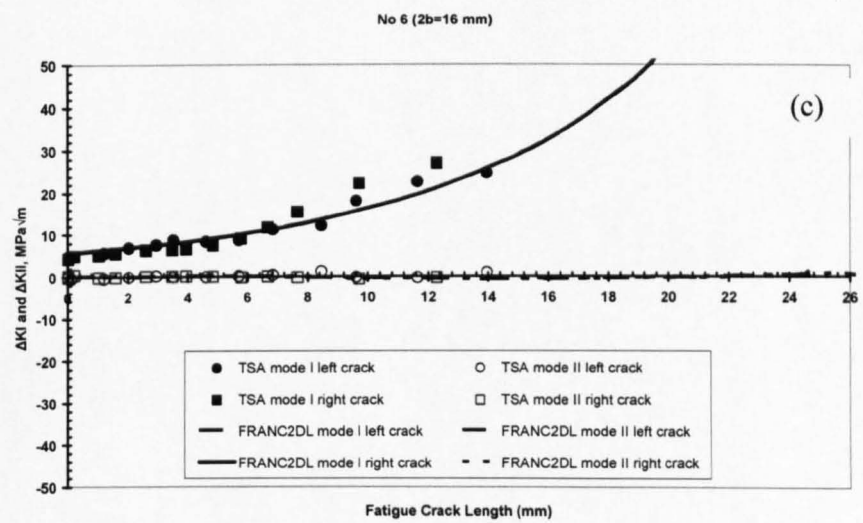
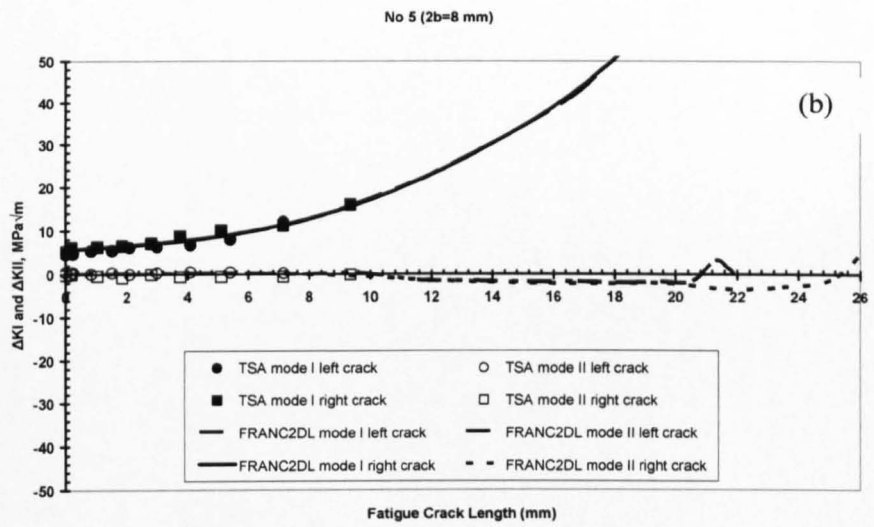
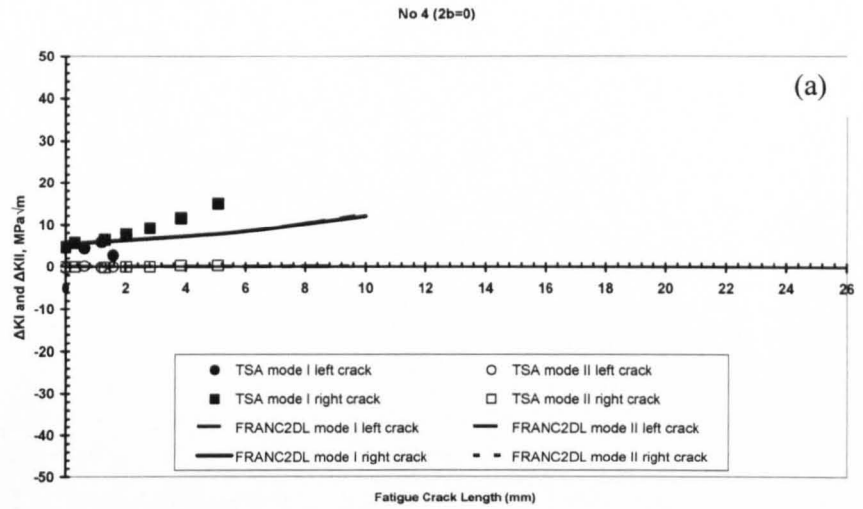


**Figure 3-17 Comparison between thermoelastic data, finite element model and the broken specimens**





**Figure 3-18** Left and right fatigue crack path comparison using Thermoelastic Stress Analysis (TSA) and finite element analysis (FRANC2D/L). (a) 0 mm offset, (b) 8 mm offset, (c) 16 mm offset, (d) 32 mm offset, (e) 48 mm offset. The initial slit length is not included in the scale.



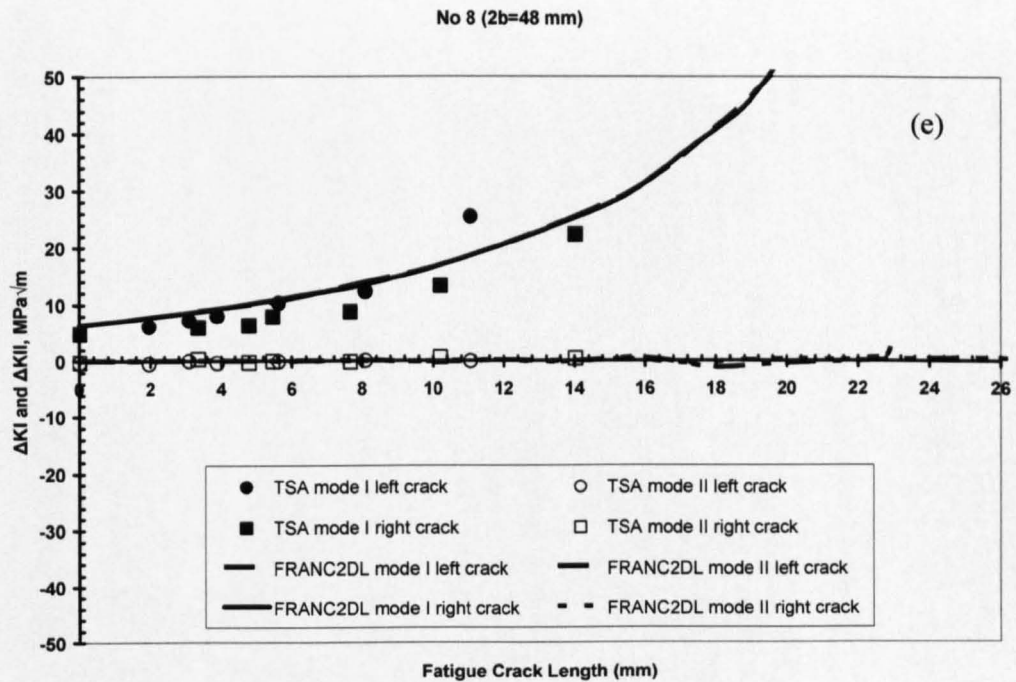
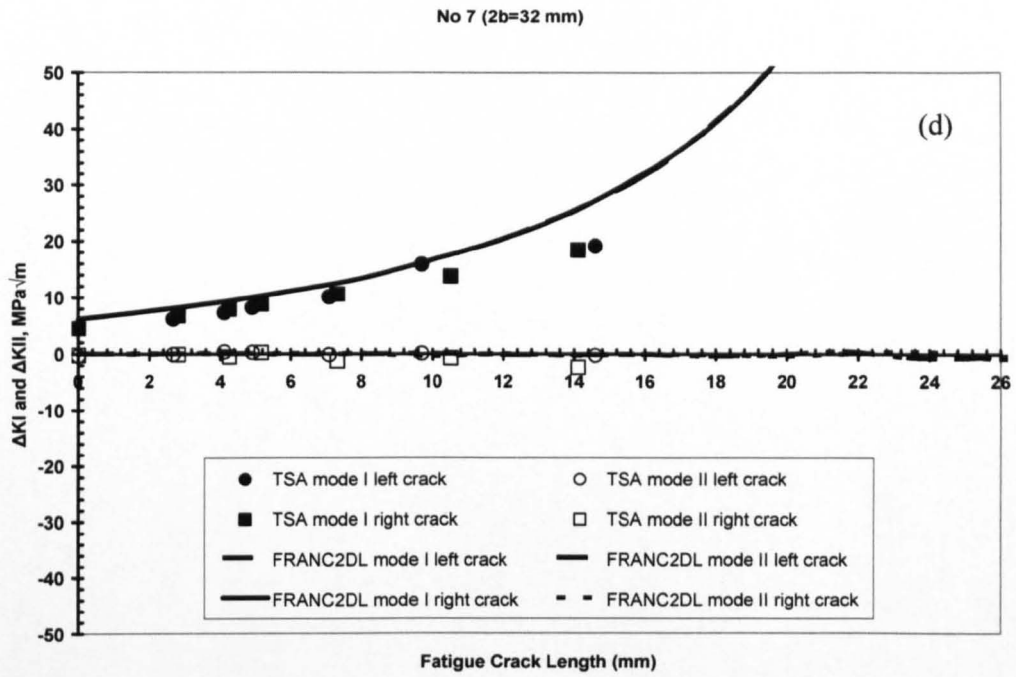
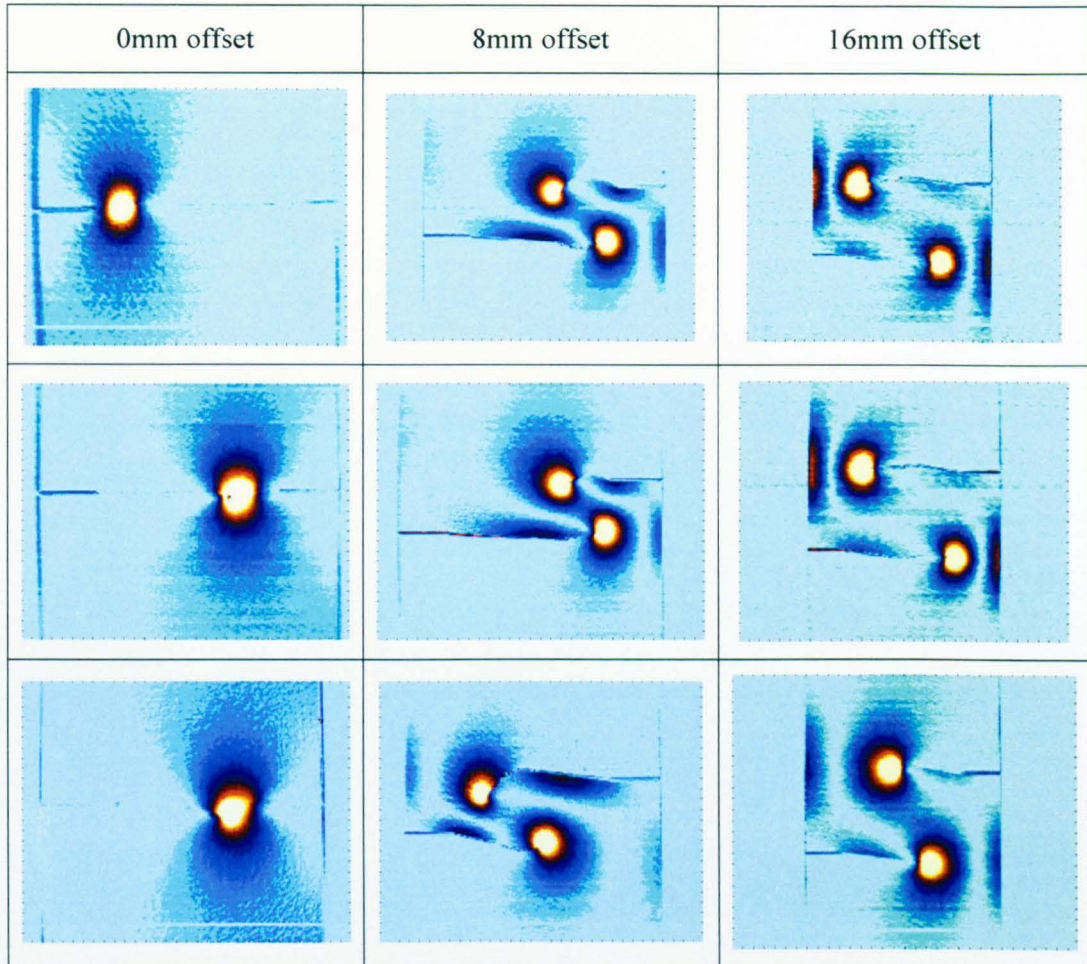


Figure 3-19 Left and right stress intensity factors ( $\Delta K_I$  and  $\Delta K_{II}$ ) using Thermoelastic Stress Analysis (TSA) and finite element analysis (FRANC2D/L). (a) 0 mm offset, (b) 8 mm offset, (c) 16 mm offset, (d) 32 mm offset, (e) 48 mm offset. The initial slit length is not included in the scale.



**Figure 3-20 Comparison of the crack paths and TSA data obtained by repeating the test for each offset**

To answer this question the tests were repeated for 0mm offset, 8mm offset and 16mm offset cases. Three specimens were tested for each case. Besides, to increase the fatigue crack length in the specimens, the load was reduced to a range of 3kN and mean of 4kN. The results are qualitatively compared in Figure 3-20.

It is observed that the crack paths are not highly repeatable. It becomes worse in cases where the interaction field is stronger. For example, as it is observed from Figure 3-21, in the early stages of crack growth the TSA crack paths agree with the predicted paths by FEM (FRANC2D/L). This is because of the fact that in the early stage of crack growth the cracks followed the path where the mode II stress intensity factor is practically zero. However, there are some regions, shown in

Figure 3-21, where a significant mode II stress intensity factor is noticeable. It is exactly in these regions where the deviation of the predicted crack paths from the experimental crack path is observed.

As can be observed in the TSA image in Figure 3-22(a) there are regions on the crack flanks where non-uniform stresses appear, which could be due to contact between the crack faces. Therefore the possibility of crack face contact and the extent of plasticity at the crack tip were explored using non-linear finite element analysis. An elastic plastic finite element model was developed in ANSYS which reproduced the crack path observed experimentally.

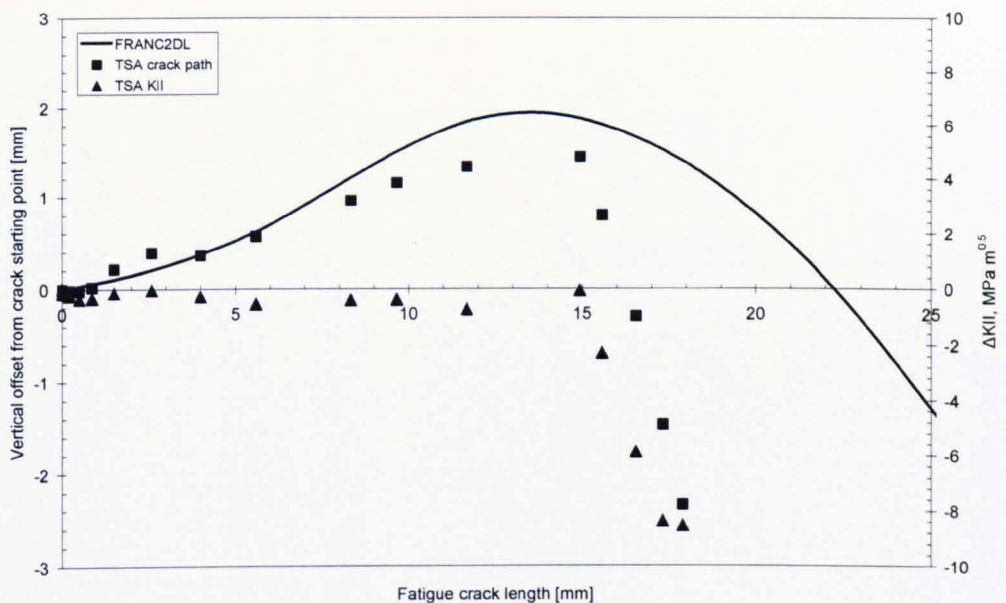


**Figure 3-21 Fatigue crack path determined by FRANC2D/L and TSA, as well as the mode II stress intensity factor determined by FATCAT for a specimen with 8 mm offset cracks. The slit length is not included in the crack length scale.**

A fine mesh using 8 node elements was used to model the region ahead of the crack tip and a bihardening model was used for material behaviour modelling. In Figure 3-22(b) are presented the sum of principal strains in the specimen obtained from FE analysis. As is well known, the sum of principal strains is proportional to the thermoelastic signal. By comparing the two Figure 3-22(a) and Figure 3-22(b) it can be seen that the results from the finite element analysis show a very similar

pattern of dilatational strain, particularly in areas along the crack flanks. Since the numerical model showed that there was no contact between the crack faces, it is concluded that the strains, and hence stresses, observed on the crack flanks were due to bending of the ligament of the material between the two cracks. Examination of the fracture surface, Figure 3-23, does not show any evidence of crack face contact or rubbing and confirms this conclusion.

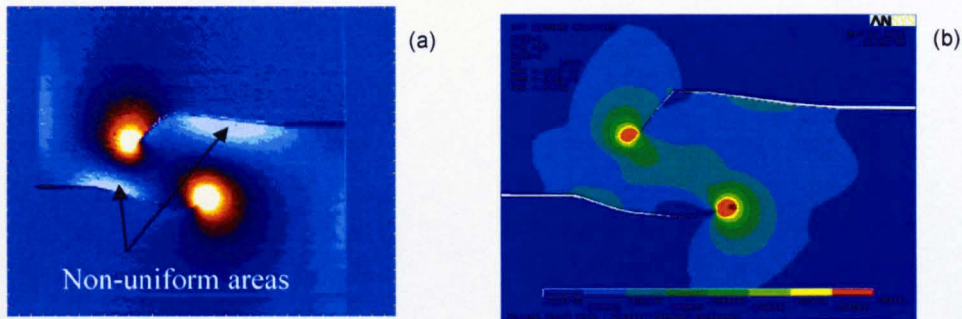


**Figure 3-22 (a) TSA image and (b) ANSYS non-linear FE results for a specimen with 8 mm offset cracks**

Although the sum of the principal strains in both images in Figure 3-22 are similar in the crack tip region, it seems that the contours in the TSA image around the crack tip have twisted from the crack plane more than is observed in the FE analysis. This was investigated by observing the fracture surfaces as it was suspected to be due to crack tunnelling.

When the fracture surface was examined, shear lips were observed at the end of crack growth (Figure 3-23) which indicated a transition from tensile to shear fracture in the region where the plastic strains increase significantly. These coincide exactly with the point where the crack path deviated from the modelling predictions and where the high values of  $\Delta K_{II}$  were observed. It is recognised that three-dimensional modelling would provide further insight into the crack propagation. The fact that only surface data may be recorded is a limitation of the thermoelastic technique, but no non-destructive techniques can monitor the internal crack front as it propagates. Modern thermoelastic apparatus used here allows data collection in near real time, which offers the potential of using

experimental and numerical techniques together from which valuable information can be obtained. From these experiments it appears that the single parameter elastic stress field, as characterized by the stress intensity factor, may be only partially controlling the crack path.

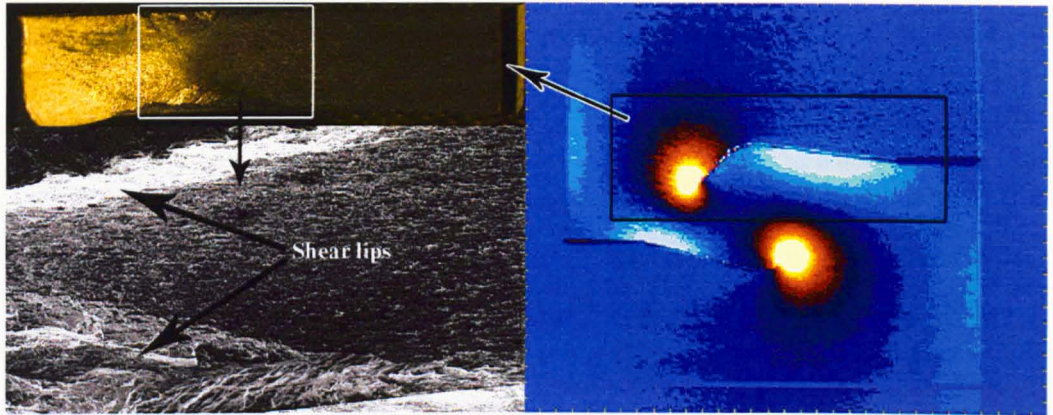


Figure 3-23 Fractured surface of the specimen with 8 mm offset cracks

### 3.6 Conclusion

The interaction of cracks with different offsets was investigated experimentally and numerically. It was shown that the crack paths are not always repeatable as expected in FE models. It was found that the crack path criteria are only capable of an acceptable prediction only in early stage of the crack growth and generally the stress intensity factors only partially control the crack path. It is highly expected that some other parameters should be considered as well. If Broberg's [3] assertion is correct, and it is the directionality of the plastic strain field that governs the crack path, then we should be seeking ways of measuring plastic strains directly. If Cotterell and Rice [10] assertion is correct, then the T-stress needs to be determined experimentally. Moreover, as it was mentioned in section 2.2, the T-stress directly affects the plastic strain ahead the crack tip and there is an interaction between the T-stress and plastic strain. Therefore, it is believed that determining both of these parameters experimentally could offer some further insight into the trajectory of fatigue cracks.

Recent developments in experimental mechanics offer an opportunity to explore the hypothesis that the direction of fatigue crack paths may be governed more strongly by a combination of T-stress, stress intensity factor as well as directionality of crack tip plasticity rather than solely by the magnitude of the elastic stress field.

It is suggested that the latest developments in image correlation techniques and differential thermography may provide a route to quantitative evaluation of T-stress and the non-linear strains fields around a crack tip.

Digital image correlation is capable of capturing both elastic and inelastic displacement field. On the other hand thermorlastic stress analysis, as the name suggests, is an elastic technique. Therefore, the difference between the parameters determined using TSA and DIC can potentially provide the opportunity to separate the elastic and inelastic field ahead of the crack. Thus, the following chapters are dedicated to developing methodologies and tools to experimentally determine the T-stress and stress intensity factors from both TSA and DIC.

## **Chapter 4**

# **T-stress determination using TSA**

The aim of this chapter is to develop a methodology to determine the T-stress from the experimental data obtained from TSA images. In process of determining the T-stress, stress intensity factors will also be determined.

This chapter starts with a brief review of analytical solutions available for the description of the crack dominant stress field and will be followed by a comparative study between these methodologies.

Then the methodology chosen for this work is explained and it is assessed using artificial and finite element data. It will also be employed in T-stress and SIF determination using thermoelastic stress analysis experimental data.

## 4.1 Methodologies for T-stress and SIF calculation

One of the most important issues in experimentally determining crack parameters is choosing an appropriate mathematical description of the stress field to which the experimental data are fitted.

As mentioned in the literature review (chapter 2), there two general approaches in characterizing the stress field using TSA. The first one is Muskhelishvili's complex stress functions [83] and the second one is Williams' solution for the crack tip stress field [120]. It can be shown analytically that for a certain stress function Muskhelishvili's approach and Williams' solution yield the same stress distribution for the same boundary conditions [121]. However, it is believed by some authors [58] that Muskhelishvili's approach can consider the effect of actual boundary conditions in experimental studies. Williams' solution, on the other hand, is an asymptotic expansion and the optimum number of terms that should be used to get a reasonable result from experimental data is still not fully understood.

In this chapter both Muskhelishvili's and Williams' approach will be used in the same experimental situation. The study will focus on developing a methodology to determine the T-stress.

### 4.1.1 Muskhelishvili's and Williams' approaches: a comparative study

To compare these two approaches a TSA image was chosen and the data were collected from two different data points (data points A and B as shown in Figure 4-1). These points were chosen randomly. The stress intensity factors were calculated from Muskhelishvili's approach, using a Newton-Raphson solver [85]. Williams' single parameter solution and Williams' two parameter solution were also used and the comparison was made between the results of these solutions. The Williams' approach will be discussed in details in section 4.1.2.

Obviously the stress intensity factors calculated here do not represent the stress intensity for the crack tip because the data have been chosen from random regions. However, the stress intensity factors can be used as matter of comparison between Muskhelishvili's and Williams' approaches. In the proposed

Muskhelishvili' approach a mapping function is used to map the crack to a circle. This mapping function is a function of a length parameter or a geometry factor. The Fourier analysis in Muskhelishvili's approach is more accurate for large value of this geometry factor [58]. By increasing the value of geometry factor the results converge to a value which should be considered as the output of the algorithm. The results of the comparison are shown in Figure 4-2 and Figure 4-3.

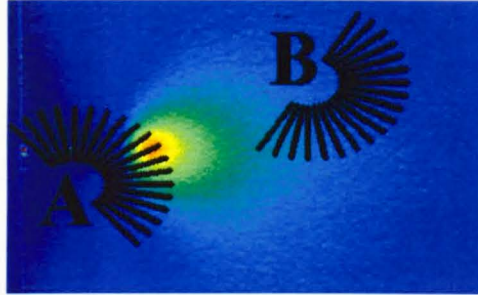


Figure 4-1 Points selected for comparative study

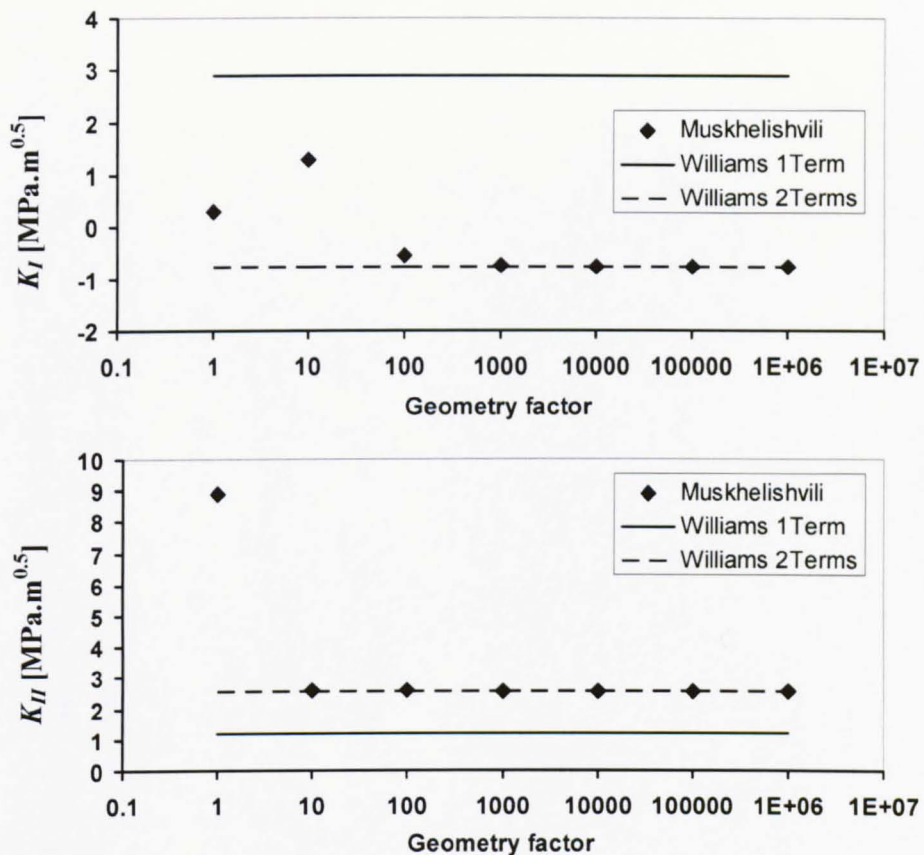


Figure 4-2 Mode I (top) and mode II (bottom) stress intensity factors for point A

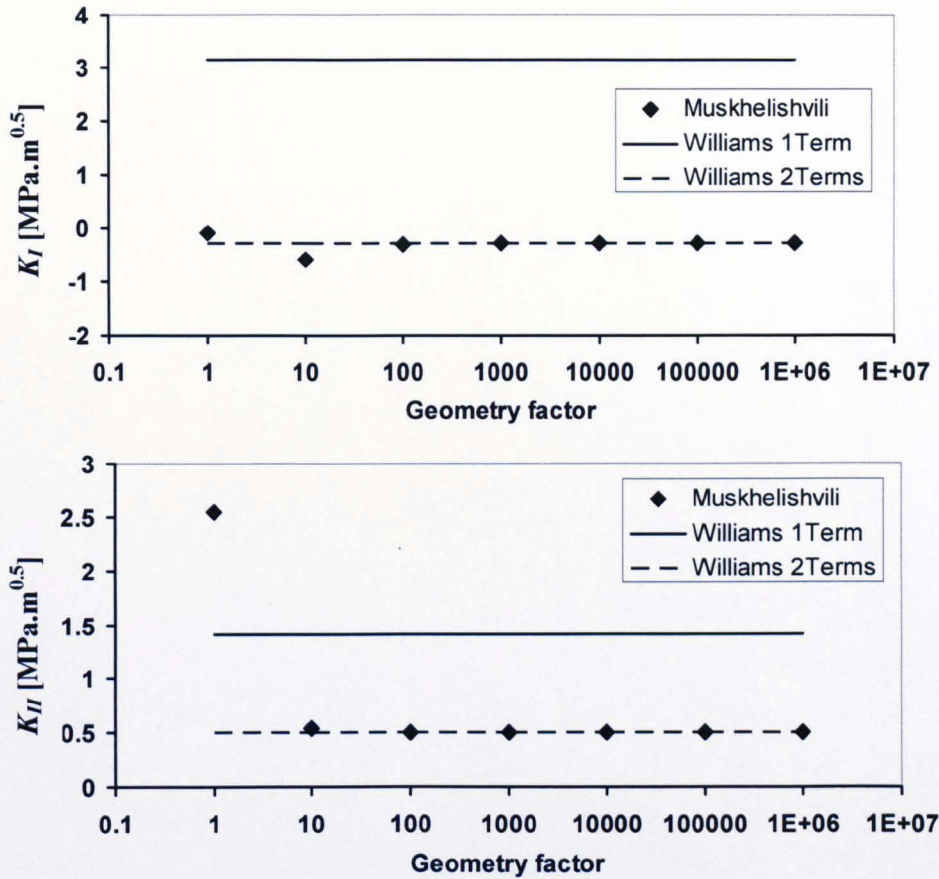


Figure 4-3 Mode I (top) and mode II (bottom) stress intensity factors for data points B in Figure 4-1

It is observed from Figure 4-2 and Figure 4-3 that the output of Muskhelishvili's algorithm is completely different from the single term Williams' solution. However, both mode I and II stress intensity factors obtained from Muskhelishvili's approach converge to the values obtained from Williams' 2 term solution when the geometry factor is increased. In other words no matter where the data points are collected both Muskhelishvili and Williams' 2 term solution yield the same result if a large value of the geometry factor is used. Therefore, it can be concluded that the stress function proposed by Nurse and Patterson [58] which was extended for TSA [84] and implemented in FATCAT [85] yield equivalent results to the 2 terms solution of Williams. Additionally it should be noted that the T-stress can not be extracted from Nurse and Patterson [58] stress function.

The definition of the T-stress is based on Williams' solution. However, is this two terms approach sufficient for T-stress *and* stress intensity factor determination? The answer to this question will be explored in the next section using higher order terms of the Williams' solution.

#### 4.1.2 Mathematical description of the model

Based on Williams' approach the stress field ahead of a crack can be expressed as an infinite series. In a plane mixed mode I and II condition this stress field is expressed as equations 4-1 and 4-2 [116, 120].

Mode I :

$$\begin{cases} \sigma_{xx} = \sum_{n=1}^{\infty} \frac{n}{2} r^{\frac{n}{2}-1} a_n \left\{ \left[ 2 + \frac{n}{2} + (-1)^n \right] \cos \left[ \left( \frac{n}{2} - 1 \right) \theta \right] - \left( \frac{n}{2} - 1 \right) \cos \left[ \left( \frac{n}{2} - 3 \right) \theta \right] \right\} \\ \sigma_{yy} = \sum_{n=1}^{\infty} \frac{n}{2} r^{\frac{n}{2}-1} a_n \left\{ \left[ 2 - \frac{n}{2} - (-1)^n \right] \cos \left[ \left( \frac{n}{2} - 1 \right) \theta \right] + \left( \frac{n}{2} - 1 \right) \cos \left[ \left( \frac{n}{2} - 3 \right) \theta \right] \right\} \\ \tau_{xy} = \sum_{n=1}^{\infty} \frac{n}{2} r^{\frac{n}{2}-1} a_n \left\{ \left( \frac{n}{2} - 1 \right) \sin \left[ \left( \frac{n}{2} - 3 \right) \theta \right] - \left[ \frac{n}{2} + (-1)^n \right] \sin \left[ \left( \frac{n}{2} - 1 \right) \theta \right] \right\} \end{cases} \quad 4-1$$

and,

Mode II :

$$\begin{cases} \sigma_{xx} = -\sum_{n=1}^{\infty} \frac{n}{2} r^{\frac{n}{2}-1} b_n \left\{ \left[ 2 + \frac{n}{2} - (-1)^n \right] \sin \left[ \left( \frac{n}{2} - 1 \right) \theta \right] - \left( \frac{n}{2} - 1 \right) \sin \left[ \left( \frac{n}{2} - 3 \right) \theta \right] \right\} \\ \sigma_{yy} = -\sum_{n=1}^{\infty} \frac{n}{2} r^{\frac{n}{2}-1} b_n \left\{ \left[ 2 - \frac{n}{2} + (-1)^n \right] \sin \left[ \left( \frac{n}{2} - 1 \right) \theta \right] + \left( \frac{n}{2} - 1 \right) \sin \left[ \left( \frac{n}{2} - 3 \right) \theta \right] \right\} \\ \tau_{xy} = \sum_{n=1}^{\infty} \frac{n}{2} r^{\frac{n}{2}-1} b_n \left\{ \left( \frac{n}{2} - 1 \right) \cos \left[ \left( \frac{n}{2} - 3 \right) \theta \right] - \left[ \frac{n}{2} - (-1)^n \right] \cos \left[ \left( \frac{n}{2} - 1 \right) \theta \right] \right\} \end{cases} \quad 4-2$$

where,  $\sigma_{xx}$  and  $\sigma_{yy}$  are the stresses in the  $x$  and  $y$  directions, respectively.  $\tau_{xy}$  is the shear stress in  $xy$  plane.  $r$  and  $\theta$  are distance and angle from crack tip to the point of interest as shown in Figure 4-4.  $a$  and  $b$  are constants which are proportional to the stress intensity factors and the T-stress using equation 4-3.

$$\begin{aligned} K_I &= a_1 \sqrt{2\pi} \\ K_{II} &= -b_1 \sqrt{2\pi} \\ T &= 4a_2 \end{aligned} \quad 4-3$$

As was shown in previous chapters, the TSA signal is proportional to sum of principal stresses. Therefore, using equations 4-1 and 4-2 the thermoelastic signal ( $S$ ) for a single point can be related to the sum of principal stresses as follows,

$$AS = \Delta(\sigma_{xx} + \sigma_{yy}) = \sum_{n=0}^{\infty} 2nr^{\frac{n}{2}-1} \left\{ \Delta a_n \cos \left[ \left( \frac{n}{2} - 1 \right) \theta \right] - \Delta b_n \sin \left[ \left( \frac{n}{2} - 1 \right) \theta \right] \right\} \quad 4-4$$

where,  $A$  is the thermoelastic calibration factor.

By defining  $f_n^m(r, \theta)$  and  $g_n^m(r, \theta)$  as in equation 4-5 and writing equation 4-4 in matrix form for  $m$  data points,  $S$  will be related to  $a_n$  and  $b_n$  as in equation 4-6.

$$f_n^m(r, \theta) = \frac{2n}{A} r_m^{\frac{n}{2}-1} \cos \frac{(n-2)\theta}{2} \quad 4-5$$

$$g_n^m(r, \theta) = \frac{2n}{A} r_m^{\frac{n}{2}-1} \sin \frac{(2-n)\theta}{2}$$

$$\begin{Bmatrix} S_1 \\ \vdots \\ S_m \end{Bmatrix} = \begin{bmatrix} f_1^1 \cdots f_n^1 & g_1^1 \cdots g_n^1 \\ \vdots & \vdots \\ f_1^m \cdots f_n^m & g_1^m \cdots g_n^m \end{bmatrix} \begin{Bmatrix} a_1 \\ \vdots \\ a_n \\ b_1 \\ \vdots \\ b_n \end{Bmatrix} \quad \text{or simply } [S]_{m \times 1} = [f]_{m \times 2n} [a]_{2n \times 1} \quad 4-6$$

If equation 4-6 is solved the T-stress and the SIF can be determined using equation 4-3.

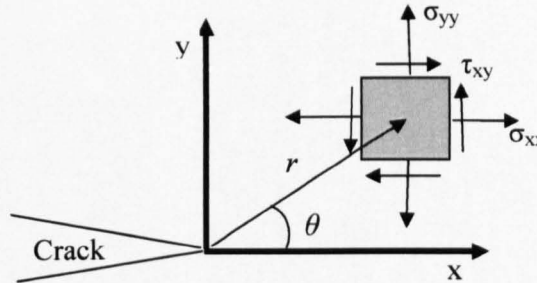


Figure 4-4 Notation of stress field around the crack tip

Since the number of data points obtained from a TSA image is always more than twice the number of terms usually used in the expansion, equation 4-6 is an over-determined system of equations. Mathematically, many different methods are available to solve a linear over-determined system of equations. The method used

in this work is a least squares technique based on determining the Moore-Penrose pseudoinverse [122] of  $[f]$ . This method is less sensitive to the rank deficiencies that may happen in solving the over-determined system of equations [122].

## 4.2 Interface

To analyse the TSA images the algorithm and the graphical interface which was developed originally by Diaz [85] was modified to determine the T-stress as well. It only works based on Muskhilishvili's approach and only determines the stress intensity factors. In the new version, the code is capable of determining the T-stress as well. Furthermore, it can determine the stress intensity factor using up to  $n$  terms of Williams' expansion. The previous version had been designed only for DT 1000 and DT 1500 Deltatherm camera series. The new version is able to read the output file of the DT 1410 Deltatherm camera as well.

Figure 4-5 shows the graphical interface and its sections. In block A by pressing the *Filename* button a .dt1 file can be opened. It should be noted that the file should be in an ASCII format. This preference can be set when the images are captured. Alternatively, the images can be saved as ASCII format in the Deltavision software.

In block B both the image scale and the TSA calibration factor are set. The crack length (geometry factor) should be set to a large number, like  $1 \times 10^6$ , if the Muskhelishvili's approach is being used (as discussed in section 4.1.1) but the Williams' solution does not depend on this parameter. Pixels/mm is the geometrical calibration factor of the image and the calibration constant is the calibration factor ( $A$ ) for the thermoelastic image. The rest of the boxes in this block are for information only, and are not used in the subsequent calculations.

To be able to avoid the regions affected by non-adiabatic conditions ahead of the crack tip the properties of data points collecting mask can be set in block C and D.

In block D, crack tip position which is used as the datum of the coordinate system can also be set.

Sometimes it might be necessary to correct the phase shift in the TSA images. This can be done in the DeltaVision software that comes with the Deltatherm camera or in block E in FATCAT.

Since finding the crack tip position from TSA images involves some difficulties, in block F the manually set crack position in block D can be optimized using Genetic Algorithm (GA).

In block G the methodology to determine the stress intensity factor can be set. Among the methods available in the pop-up menu in this block, only Williams' method is capable of determining both the T-stress and the SIF. *Nterms* in this block represents the number of terms used in each method.

By pressing the *Calculate SIF* in all algorithms, except Williams, the calculated SIF are shown in the boxes provided. The results using Williams algorithm appear as separate figures as a convergence curve for both T-stress and SIF as well as a table filled with the corresponding numerical values as shown in Figure 4-6.

Blocks H and I show the intensity of the TSA signal of the selected image along horizontal and vertical lines passing through the point where the mouse pointer is.

Block J shows the image. Block K shows the Stanley's plot (as explained in section 2.4.1) and in block L the type of image and camera can be set.

### 4.3 Methodology assessment using artificial data

To explore the reliability of the methodology and the code another subroutine was developed to produce artificial data in TSA file format legible for the modified FATCAT code. In this subroutine the artificial sum of principal stress field is created using equation 4-7 which means the higher terms of Williams' equation have been omitted.

$$S = (\sigma_{11} + \sigma_{22}) = \frac{2}{\sqrt{2\pi r}} K_I \cos \frac{\theta}{2} - \frac{2}{\sqrt{2\pi r}} K_{II} \sin \frac{\theta}{2} + T \quad 4-7$$

in which,  $S$  is equivalent to thermoelastic signal,  $\sigma_{11}$  and  $\sigma_{22}$  are the principal stresses at the point of interest with distance,  $r$ , and angle,  $\theta$ , from the crack tip. Obviously, in equation 4-7 the calibration factor has been considered as unity.

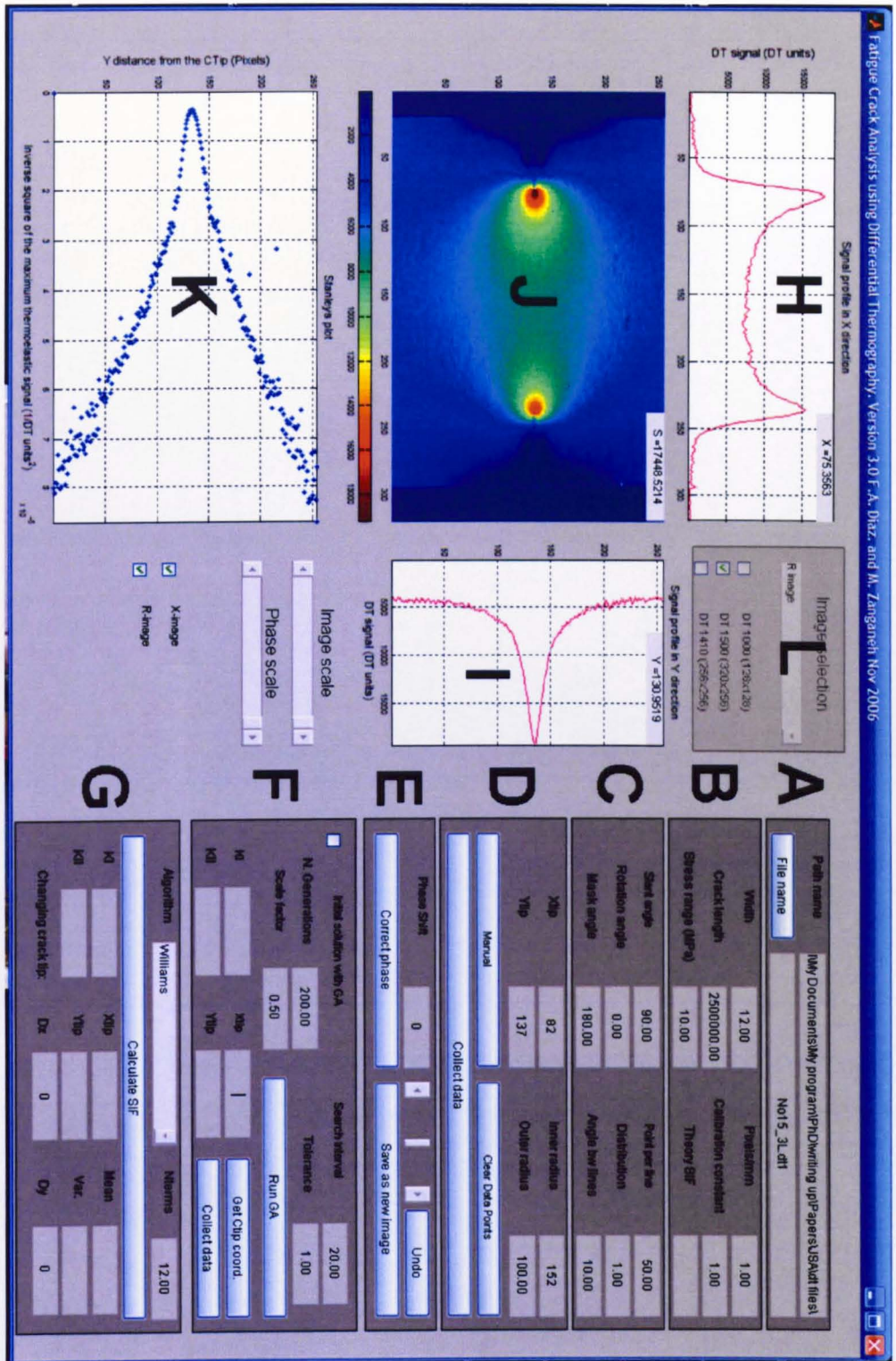


Figure 4-5 The graphical interface

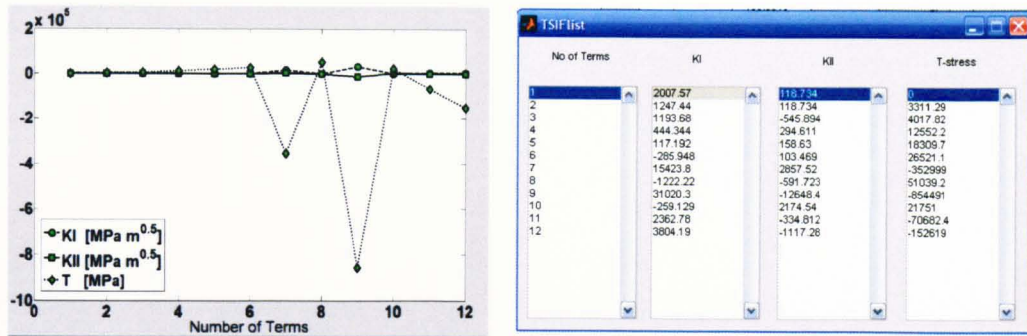


Figure 4-6 Typical output of the interface for Williams algorithm

To consider different situations three different conditions were investigated using the artificial data. First, a case in pure mode I was examined then a mixed mode condition was created by introducing mode II effects in artificial data. At the end T-stress was also entered in the data. Table 4-1 shows the SIF and T-stress used in each case.

Table 4-1 The SIF and the T-stress used in each case

Case No.	Description	$K_I$ [MPa m <sup>0.5</sup> ]	$K_{II}$ [MPa m <sup>0.5</sup> ]	$T$ [MPa]
1	Pure mode I	6	0	0
2	Mixed mode I & II	6	2	0
3	General plane stress	6	2	10

The following figures (Figure 4-7 to Figure 4-12) show the sum of principal stress distribution and the convergence curve gained for up to 10 terms of Williams' solution for each of the 3 cases.

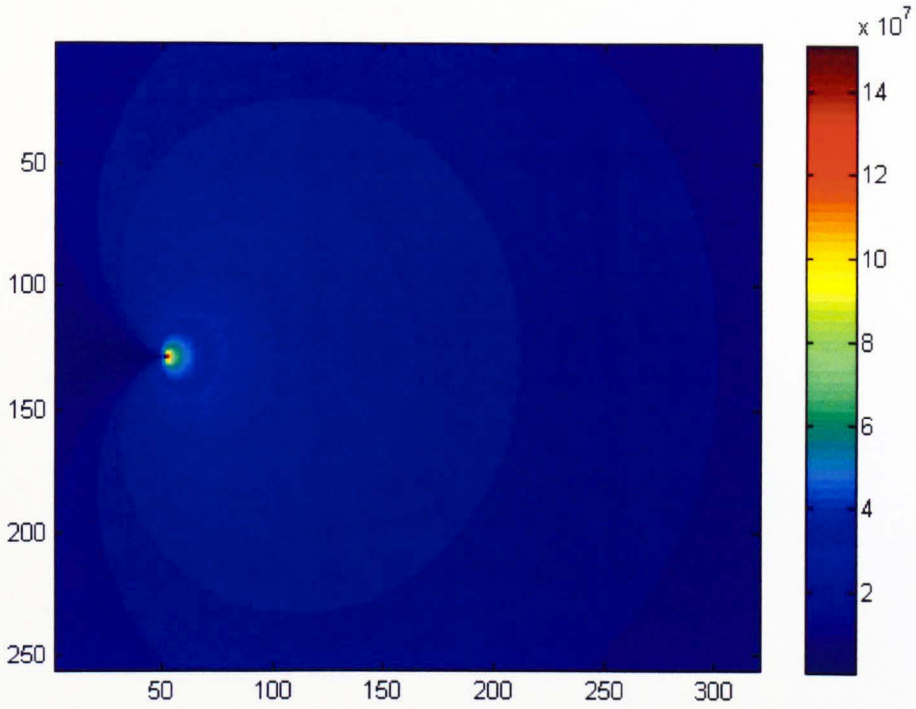


Figure 4-7 Sum of principal stress distribution (in Pa) in case 1

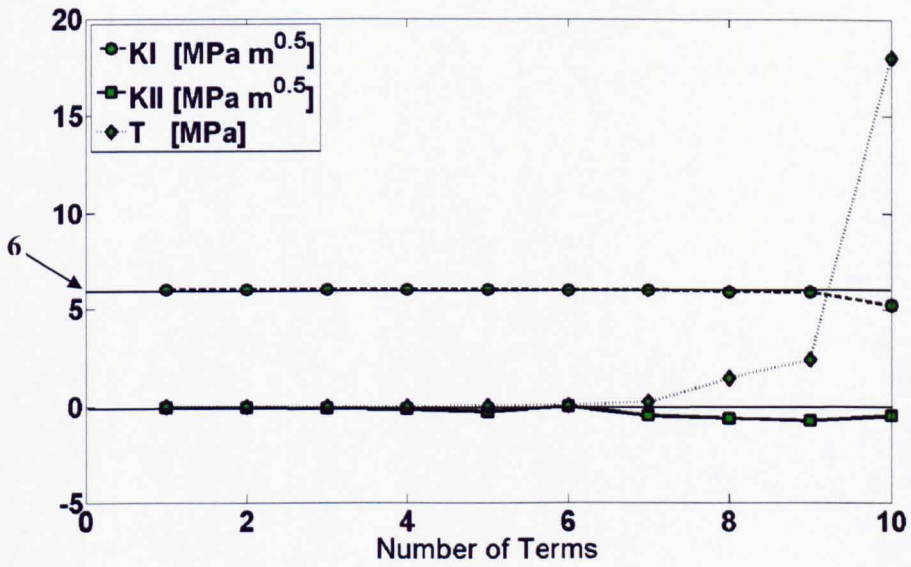


Figure 4-8 Convergence curve for case 1

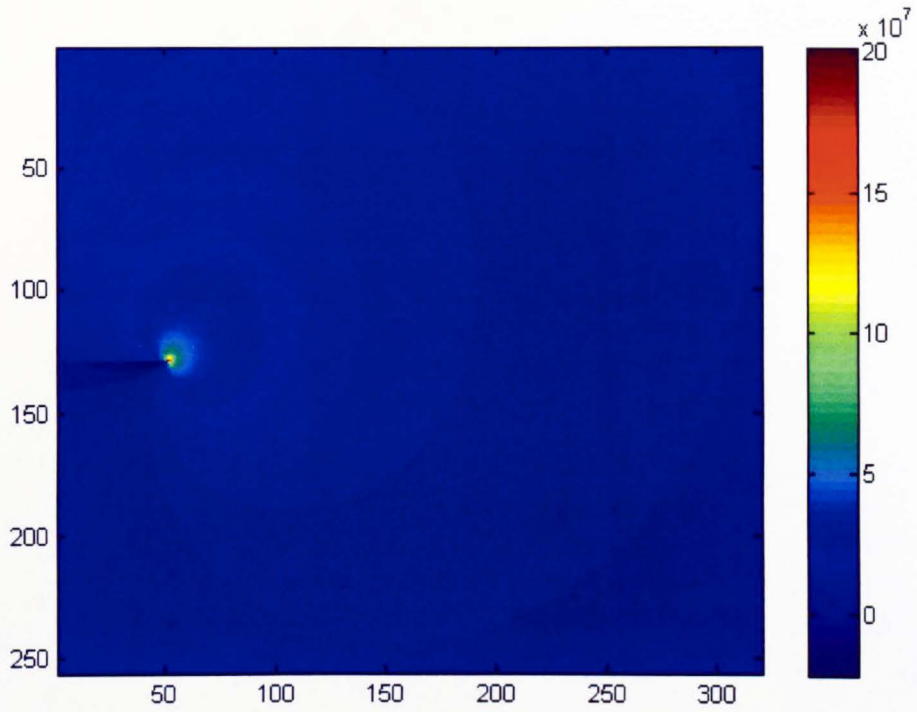


Figure 4-9 Sum of principal stress distribution (in Pa) in case 2

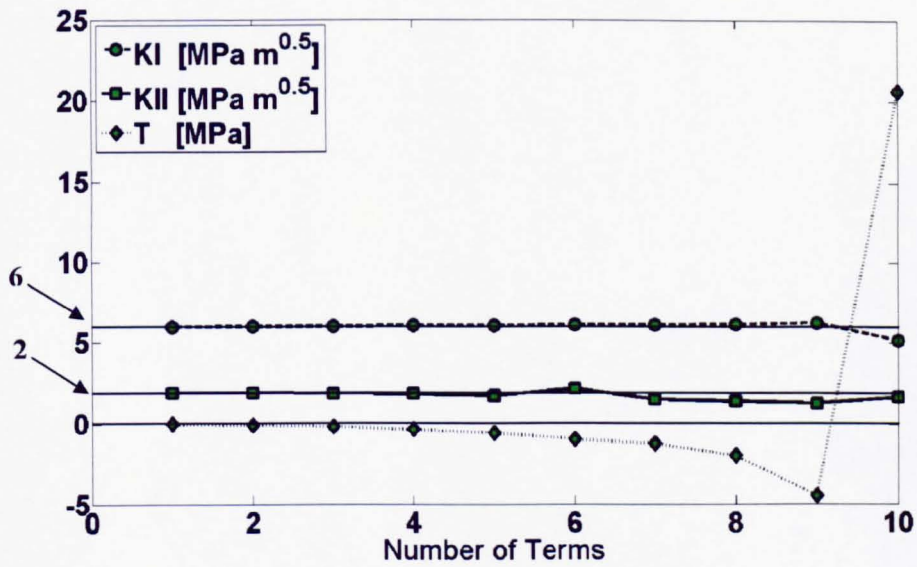


Figure 4-10 Convergence curve for case 2

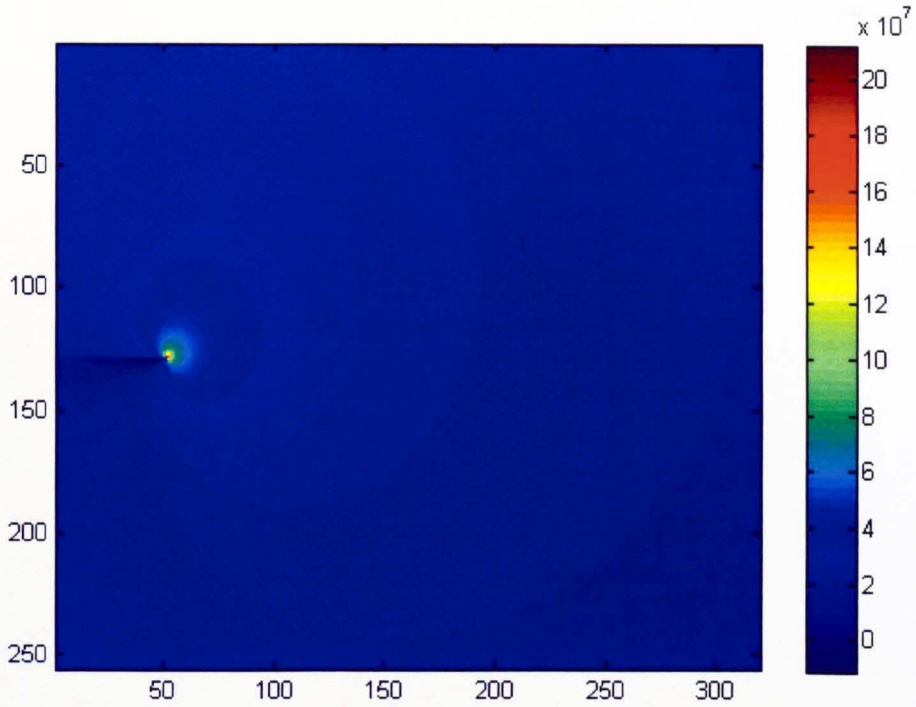


Figure 4-11 Sum of principal stress distribution (in Pa) in case 3

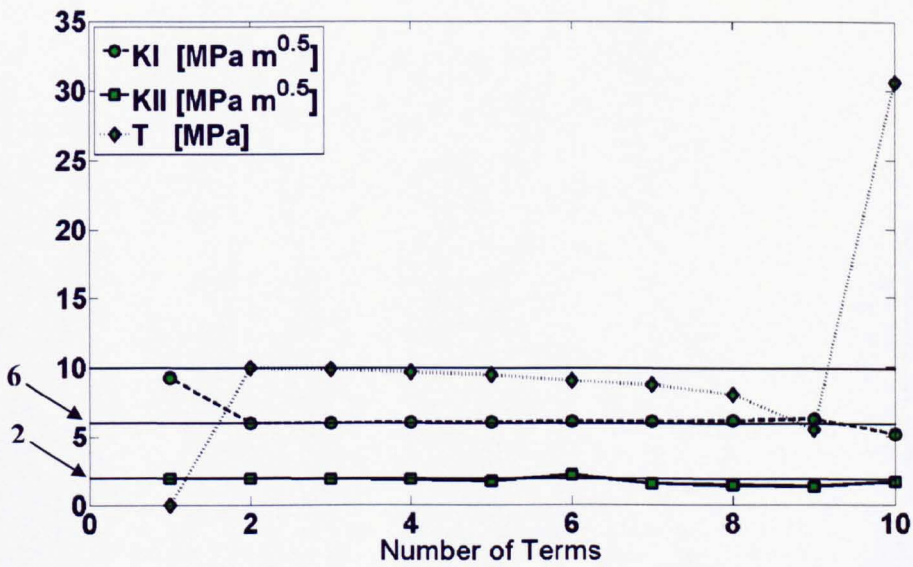


Figure 4-12 Convergence curve for case 3

In all the above cases it is observed that  $K_I$  is not so sensitive to the number of terms up to 9 terms. In other words the  $K_I$  solution is numerically stable up to 9

terms. However, numerical instability starts after the 9<sup>th</sup> term. It is also observed that using more than one term of Williams' solution does not introduce any advantage in  $K_I$  determination in cases 1 and 2 where there is no T-stress in the stress field ahead of the crack. However, in case 3 where the T-stress exists, more than one term must be used for  $K_I$  determination otherwise significant error is introduced (see Figure 4-12).

Compared to  $K_I$ ,  $K_{II}$  and  $T$  are more affected by the number of terms.  $K_{II}$  is quite stable using up to 4 terms of the expansion and starts fluctuating when more than 5 terms are used. The behaviour of the  $T$  convergence curve is quite similar to  $K_{II}$  convergence curve. However, the  $T$  convergence curve shows a decreasing behaviour after the second term, however, this is not significant up to the 4<sup>th</sup> term.

Normally in real thermoelastic images it is difficult to locate the crack tip position and it may consist of a few pixels error in locating the crack tip. To study the effect of crack tip position on T-stress and SIF results, case 3 was used as a basis. The crack tip was moved  $\pm 2$  pixels in the x direction and the T-stress and SIF were calculated for 2, 3 and 4 terms of the expansion. Results are shown in Table 4-2.

It is observed from Table 4-2 that underestimating the crack length increases the SIF and decreases the T-stress by a few percentage. However it is the other way round if the crack length is overestimated. It is also revealed that using a higher number of terms makes the equations more sensitive to the crack position. Therefore, it can be concluded that the lower the number of terms is used the more robust the solution will be. Now the question is that how many terms is adequate to accurately determine the T-stress and SIF? To be able to answer this question it is useful to study the effect of noise.

**Table 4-2 Change in T-stress and SIF due to change in crack tip position**

$\Delta x$	2 terms			3 terms			4 terms		
	$\% \Delta K_I$	$\% \Delta K_{II}$	$\% \Delta T$	$\% \Delta K_I$	$\% \Delta K_{II}$	$\% \Delta T$	$\% \Delta K_I$	$\% \Delta K_{II}$	$\% \Delta T$
-2	4.3	3.3	-6.5	6.3	6.6	-18.7	12.3	-232.0	-49.0
-1	2.2	1.6	-3.3	3.1	3.2	-9.3	6.0	51.7	-24.0
1	-2.2	-1.6	3.5	-3.1	-3.2	9.2	-5.8	98.9	22.9
2	-4.5	-3.2	7.1	-6.2	-6.3	18.3	-11.3	-25.1	44.7

It should be noted that the studied examples are all ideal cases and there is no noise in the data. To explore the effect of noise in the data different levels of Gaussian noise were introduced in the artificial data. This is explored in the next section.

### 4.3.1 Williams' field with noise

To explore the effect of noise on the determined T-stress and SIF, different levels (10% and 30%) of noise were uniformly introduced into the artificial data. Different cases have been outlined in Table 4-3.

Table 4-3 Description of different cases

Case No.	Description	$K_I$ [MPa m <sup>0.5</sup> ]	$K_{II}$ [MPa m <sup>0.5</sup> ]	$T$ [MPa]
1b	Pure mode I 10% noise	6	0	0
1c	Pure mode I 30% noise	6	0	0
2b	Mixed mode I & II 10% noise	6	2	0
2c	Mixed mode I & II 30% noise	6	2	0
3b	General plane stress 10% noise	6	2	10
3c	General plane stress 30% noise	6	2	10

Figure 4-13 to Figure 4-24 show the sum of the principal stress distribution and the convergence curves gained for up to 5 terms of Williams' solution.

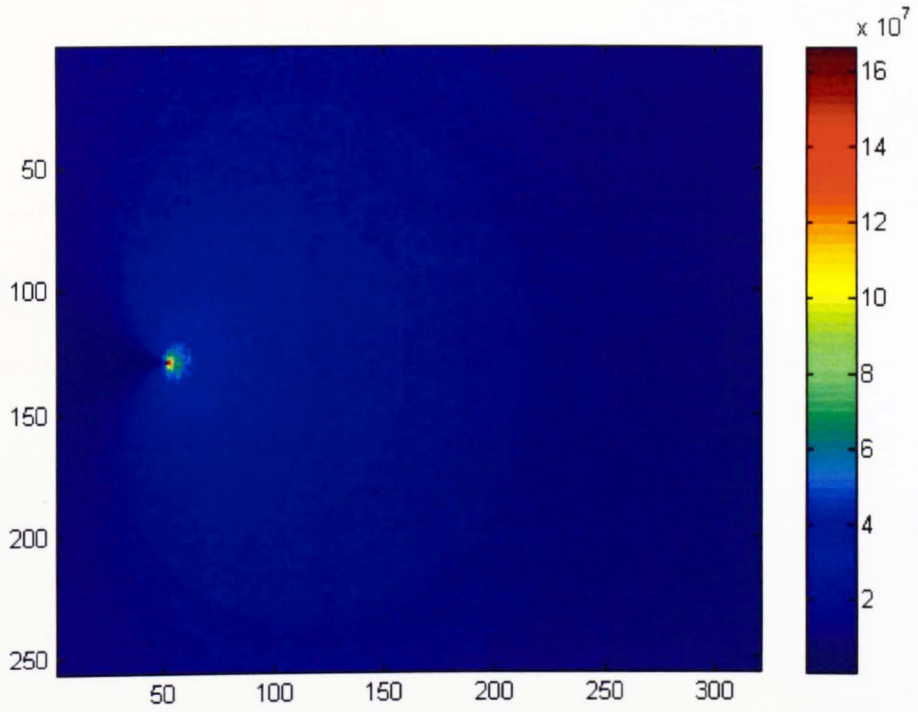


Figure 4-13 Sum of principal stress distribution (in Pa) in case 1b

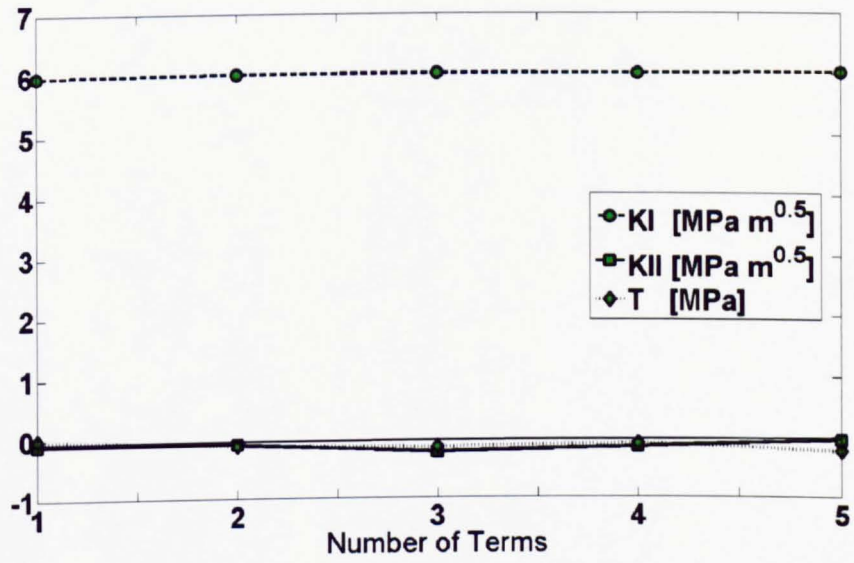


Figure 4-14 Convergence curve for case 1b

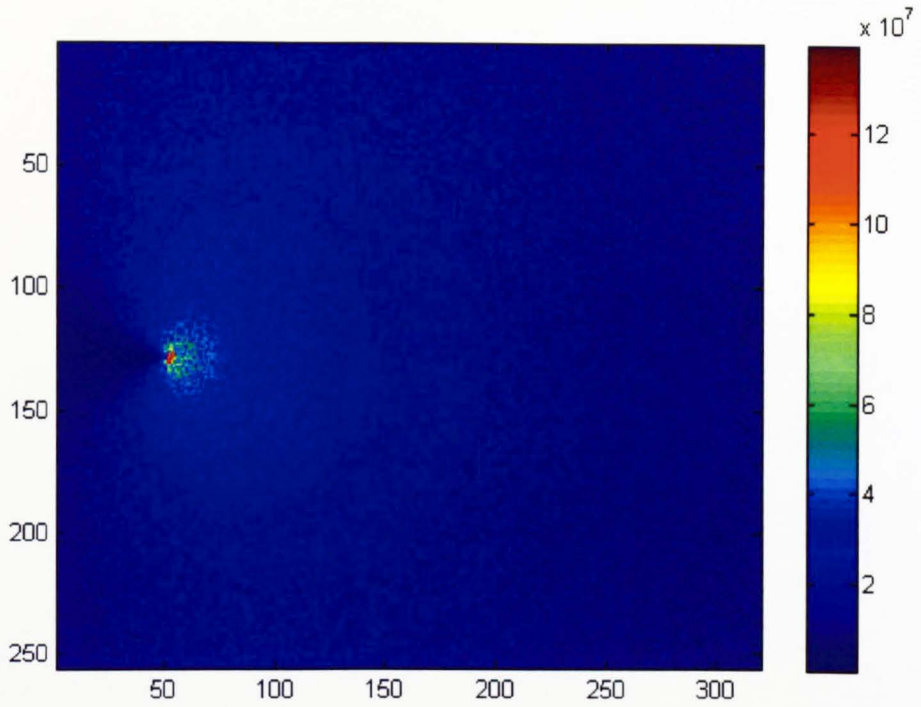


Figure 4-15 Sum of principal stress distribution (in Pa) in case 1c

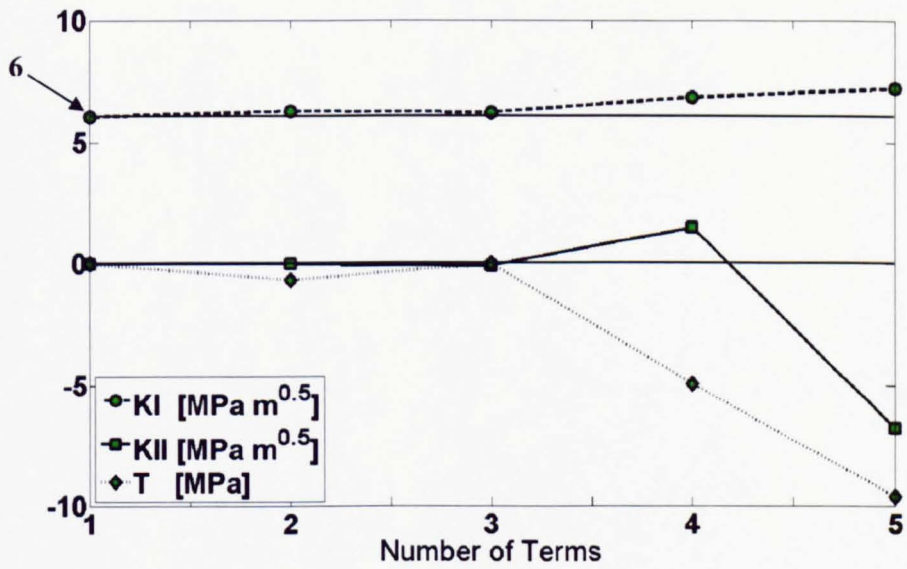


Figure 4-16 Convergence curve for case 1c

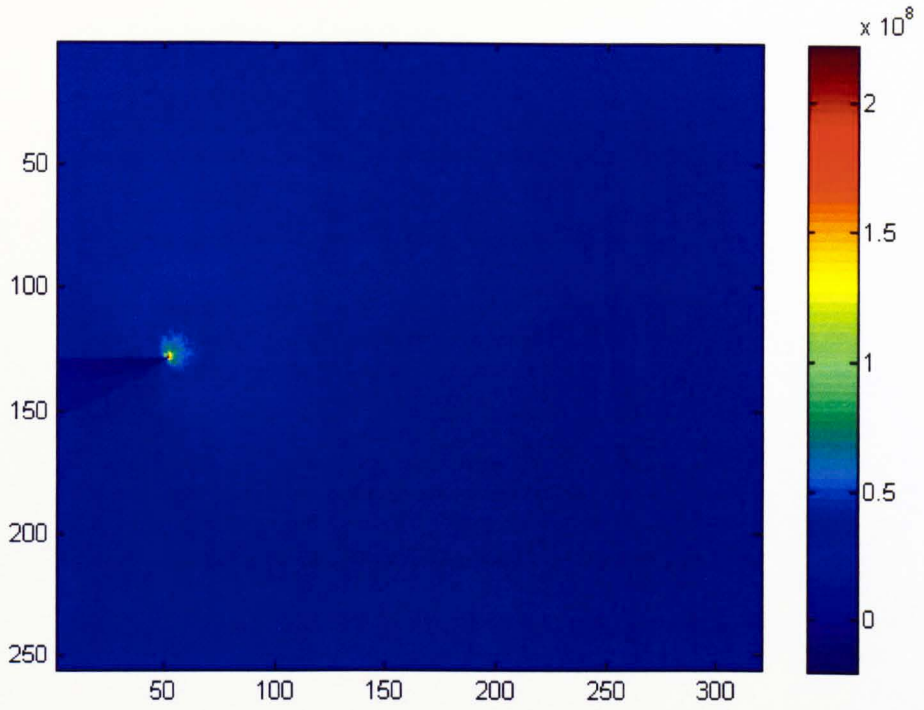


Figure 4-17 Sum of principal stress distribution (in Pa) in case 2b

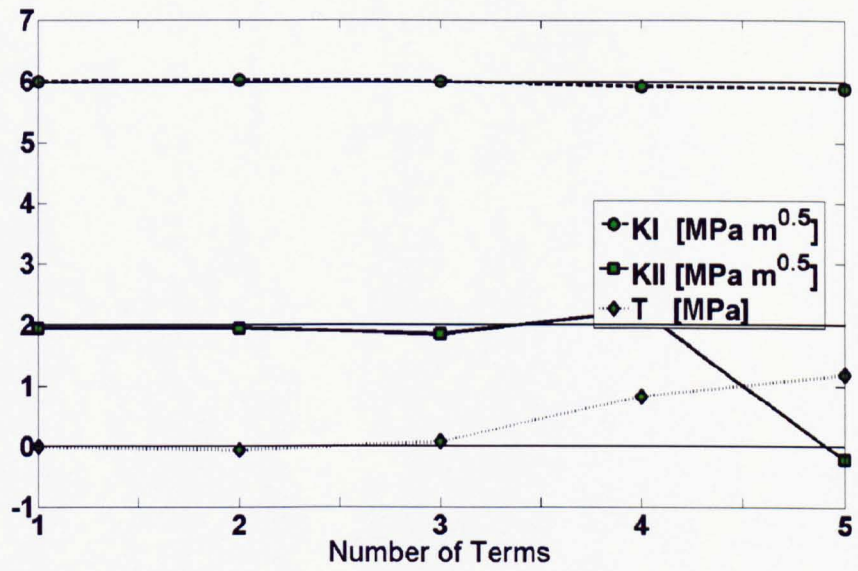


Figure 4-18 Convergence curve for case 2b

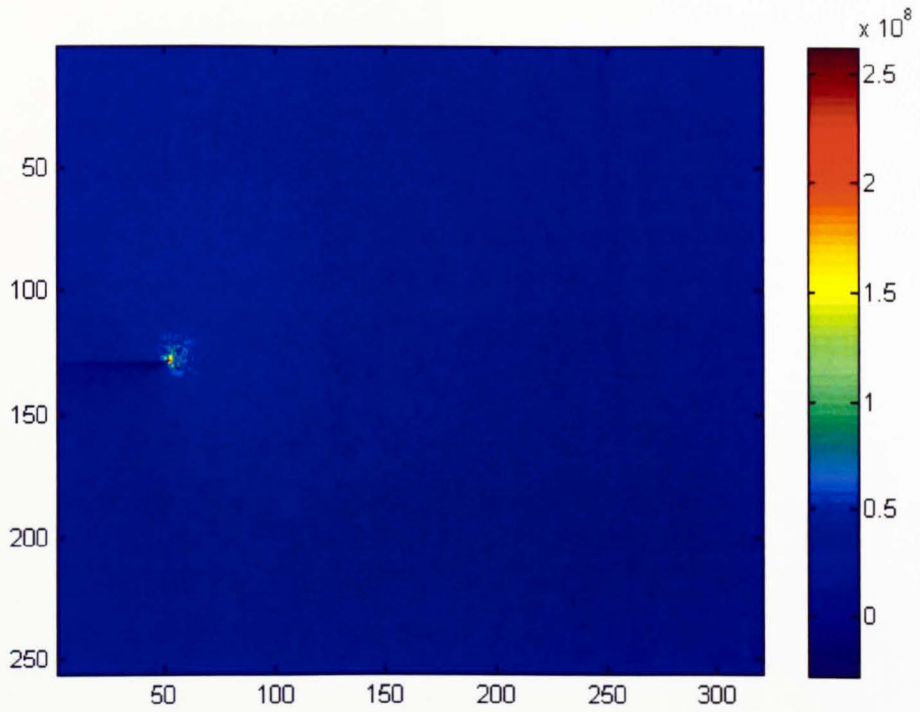


Figure 4-19 Sum of principal stress distribution (in Pa) in case 2c

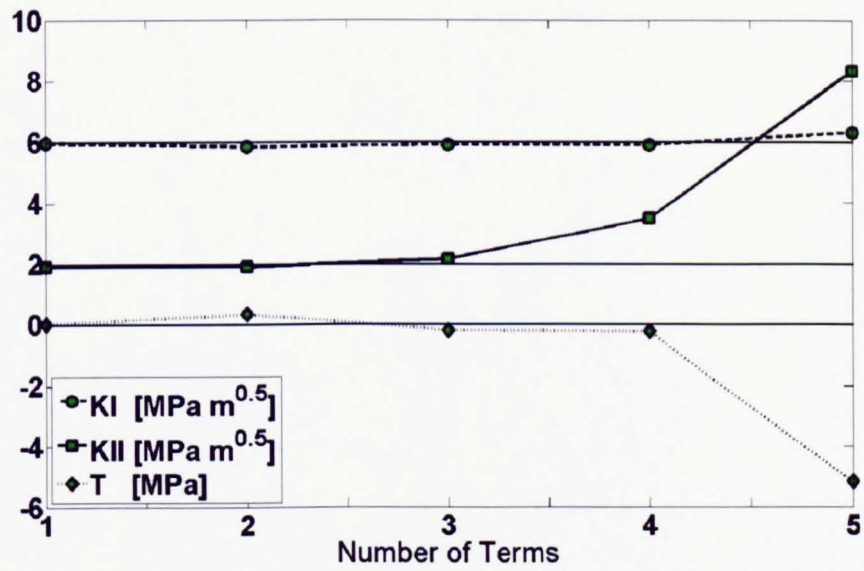


Figure 4-20 Convergence curve for case 2c

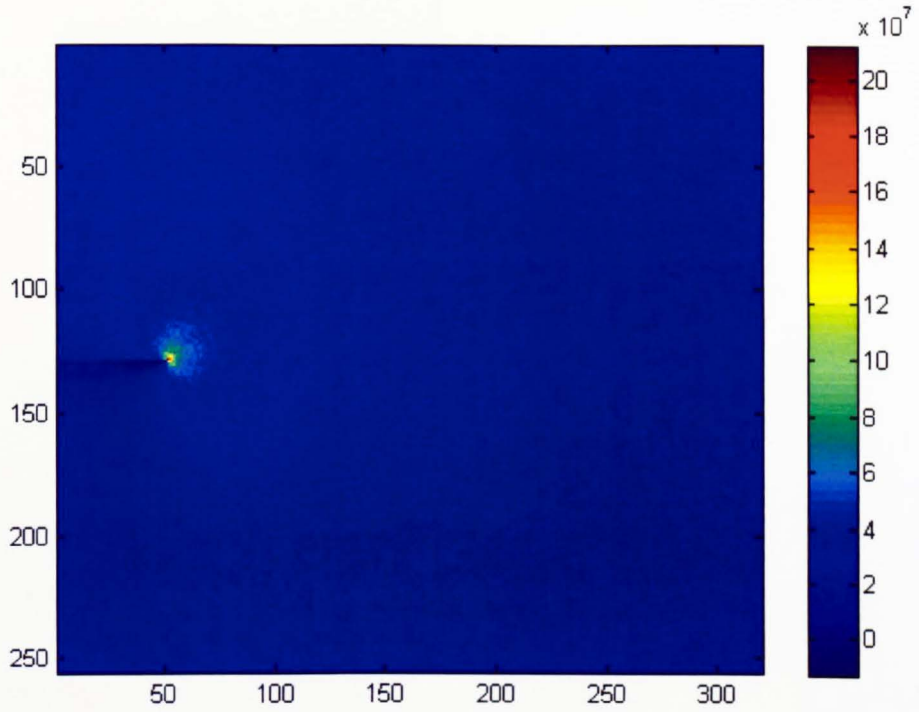


Figure 4-21 Sum of principal stress distribution (in Pa) in case 3b

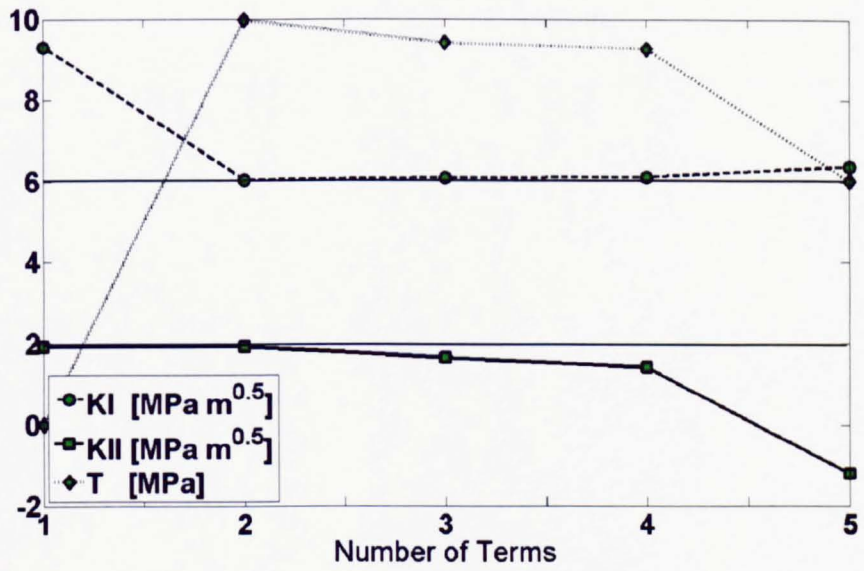


Figure 4-22 Convergence curve for case 3b

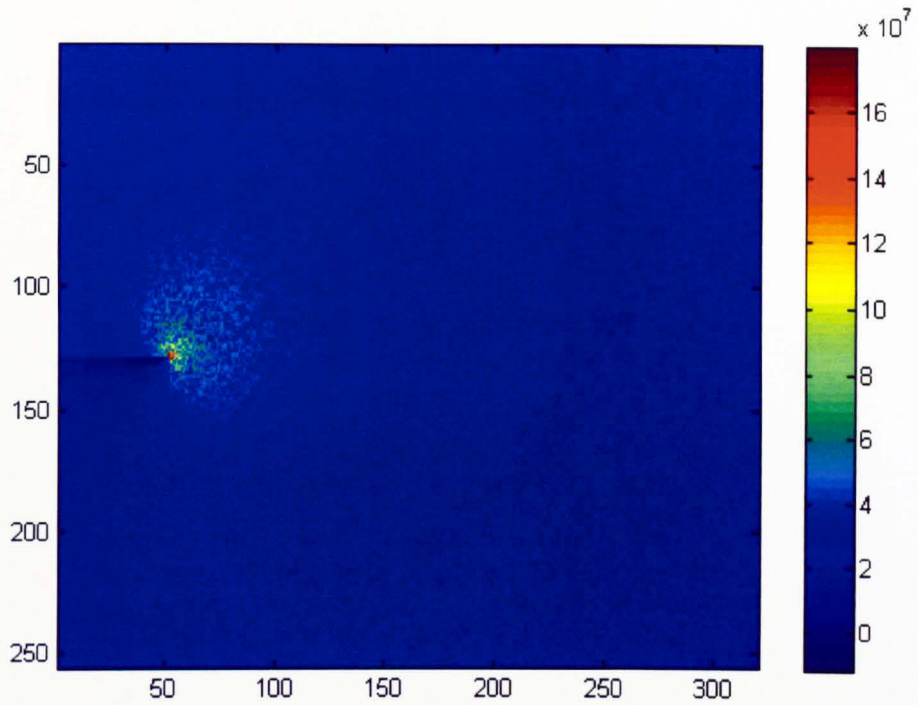


Figure 4-23 Sum of principal stress distribution (in Pa) in case 3c

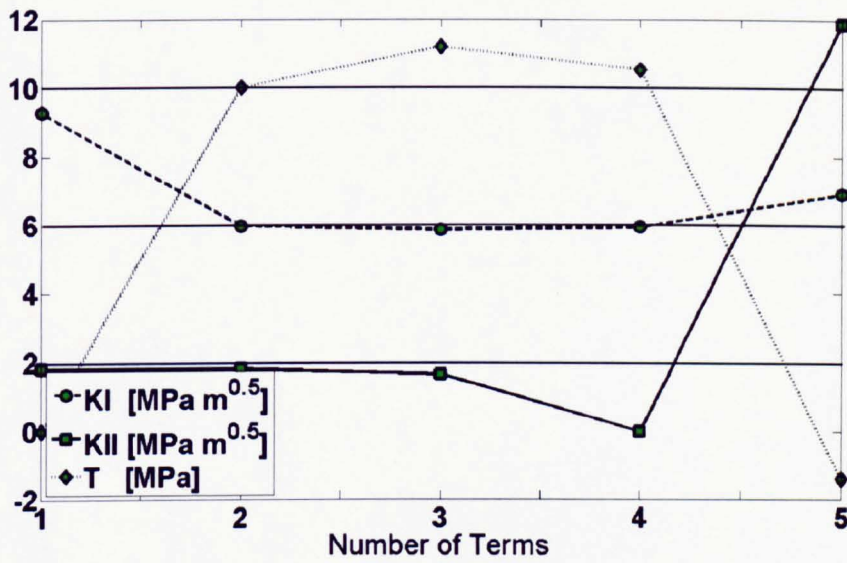


Figure 4-24 Convergence curve for case 3c

As it can be seen, in all the figures, results have been shown from one up to only 5 terms of Williams' solution. This is because of the fact that in most of the cases

the results became so unstable that showing more terms of the solution prevents an appropriate scaling of the figures and it makes the fluctuations of the curves not visible. Therefore, only 5 terms of the expansion were shown in the graphs.

Similar to the noise free data,  $K_I$  values in the noisy artificial data are more stable than  $K_{II}$  and  $T$  and only a slight variation is observed by increasing the number of terms. On the other hand,  $K_{II}$  and  $T$  show more sensitivity to the number of terms in noisy artificial data. Increasing the level of noise in the data increases the chance of numerical instability in lower number of terms. For example see Figure 4-14 in which only 10% noise is introduced and both stress intensity factors and the  $T$ -stress are quite stable up to 5 terms. However, increasing the level of noise to 30% (Figure 4-16) make the mode II stress intensity factor and the  $T$ -stress unstable after using more than 3 terms.

In majority of cases numerical instability happens if more than 4 terms of the solution are used. Besides, using the 4<sup>th</sup> term can introduce a slight error in the calculations. Therefore, from the above results it can be pointed out that for determining the  $T$ -stress the minimum number of terms that can be used by this methodology is 2 terms and the maximum is 3 or 4 terms.

In the case of  $T$ -stress, specifically, it is observed the second term gives more accurate results compare to the 3<sup>rd</sup> term. However, this might be only because of creating the stress field based on only two terms of the Williams' solution. So, to investigate this matter a more realistic model for producing the artificial data is needed. This is explored in the next section using a finite element model.

### **4.3.2 Finite element stress field**

To create more realistic artificial data, a DCB model was created in ABAQUS as shown in Figure 4-25. The values of  $K_I$ ,  $K_{II}$  and  $T$  gained from the simulation in ABAQUS are shown in Table 4-4. ABAQUS uses the J integral method for stress intensity factor determinations and an interaction integral method to determine the  $T$ -stress as discussed in sections 3.4.1.3 and 2.3, respectively. A code was developed to transfer the nodal data as well as the principal stresses from ABAQUS to the Williams' solver.  $K_I$ ,  $K_{II}$  and  $T$  were determined as in the

previous 3 case studies and the output of the Williams solver is shown in Figure 4-26.

Table 4-4 Values of T-stress and SIF in FE model

$K_I$ [MPa m <sup>0.5</sup> ]	$K_{II}$ [MPa m <sup>0.5</sup> ]	$T$ [MPa]
6.85	0	27.77

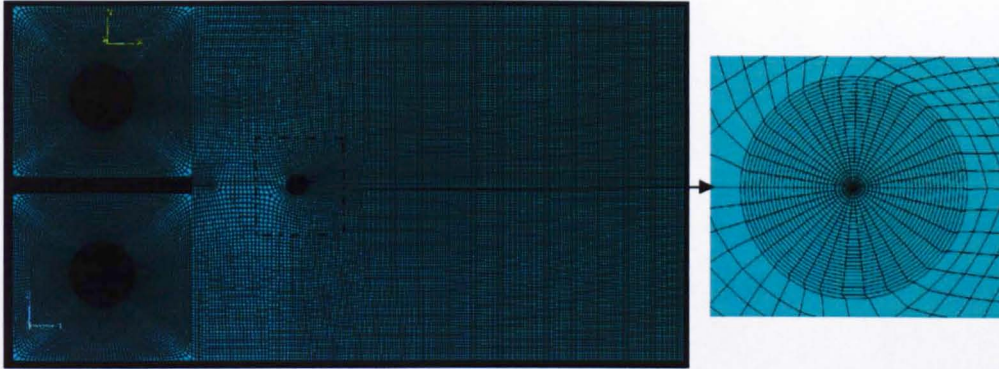


Figure 4-25 FE model created in ABAQUS

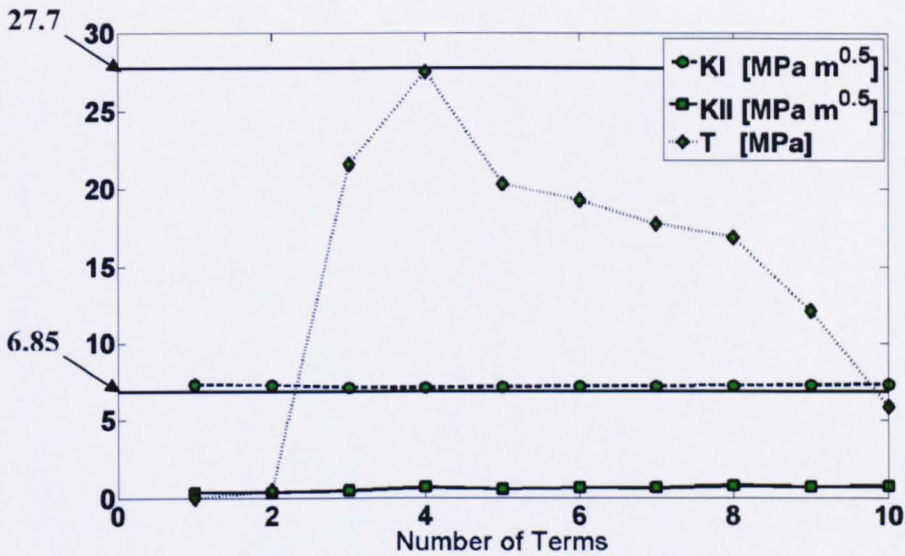


Figure 4-26 Convergence curve for FE data

As it was expected, since the FE data are noise free, like the noise free cases (case 1 to case 3) increasing the number of terms does not significantly affect the results obtained for  $K_I$  and  $K_{II}$ . However, the T-stress trend with respect to number of terms has a different story. In all the previous artificial case studies, T-stress

values obtained from 2, 3 and 4 terms were almost at same level, and even 2 terms showed less error than the other terms. As was stated earlier, this was due using only 2 terms of the expansion in producing the artificial data, whereas the FE results for T-stress shows that in a more realistic model using only 2 terms of the expansion introduces significant error in the calculated T-stress. However, this error is negligible in SIF calculations.

In summary, from previous discussions it can be concluded that using only one term of the expansion is not capable of determining the T-stress. Also, in SIF calculations the number of terms used needs careful consideration because in the cases where T-stress is not negligible errors may be introduced in the calculated SIF. Using 2 terms of the expansion looked promising in the artificial data. However, when the FE data were used it was found that the 2 terms methodology is not adequate to give accurate results for T-stress. Solutions based on more than 4 terms of solution are numerically unstable, especially where more noise exists. These results are consistent with the findings of Lesniak and Boyce [79] and Ju *et al.* [80] where an instability was observed using more than 4 terms of the Williams' solution in artificial data (see section 2.4.1 for more details).

Although a 4 terms solution, like a 3 terms solution, gives acceptable results in most of the artificially generated cases (and even better results for the T-stress using finite element data), as shown in Figure 4-27 using real experimental data showed a highly unstable results for mode II stress intensity factors and the T-stress when more than 3 terms of the Williams' solution is used.

The 3 terms solution is less sensitive to potential uncertainties regarding the crack tip positioning and other possible uncertainties happen in the experimental results. Besides, the 3 terms solution is faster as it uses less computing resources. Therefore, a 3 terms solution is more likely to be the optimum number of terms that can be used to determine the T-stress from experimental TSA data.

In the next section a series of experiments have been conducted to assess the feasibility of this methodology to determine the T-stress and stress intensity factor from experimental thermoelastic data.

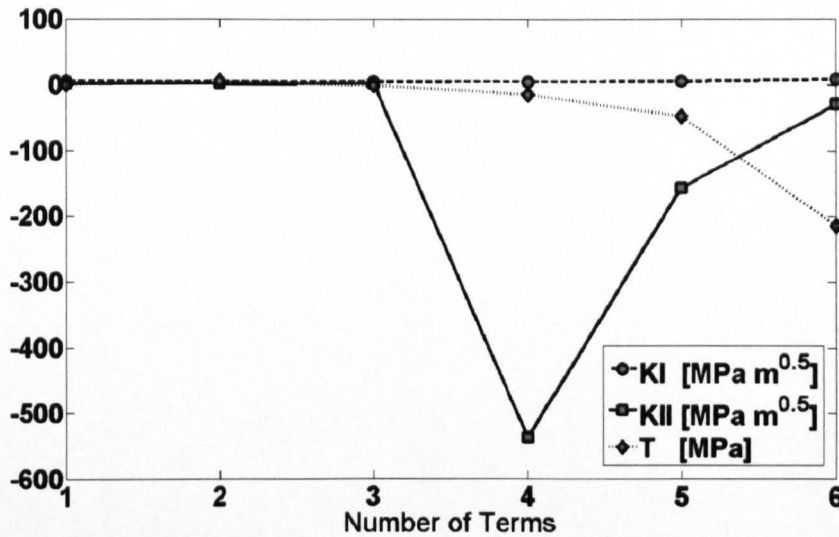


Figure 4-27 Typical instability using experimental data and more than 3 terms in Williams' solution

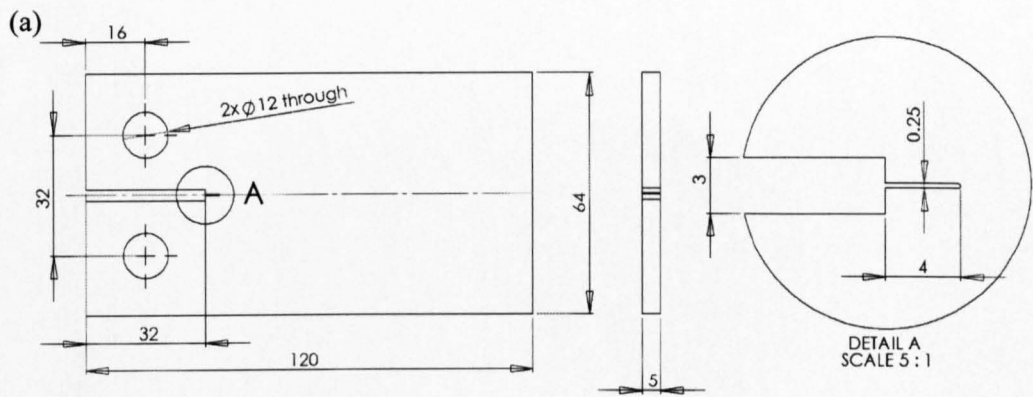
#### 4.4 Experiments

Different loading conditions were used in order to determine the T-stress and SIF using the proposed methodology. These loading conditions include: pure mode I in a double cantilever beam (DCB) specimen where the T-stress is expected to be positive; mixed mode I and II in cruciform specimens under biaxial loading where the T-stress is expected to be zero; and interacting crack tip fields (double edge cracked specimens) where the T-stress is expected to have a negative value for the configuration used. The dimensions of the specimens are shown in Figure 4-28 and Table 4-5 details the specimens, crack lengths, and loading conditions.

A 100 kN MAND hydraulic test machine was used to load the specimens in all cases except cases 3 and 4 where a 100 kN Denison Mayes Biaxial Testing Machine was used to apply the load. It should also be noted that the cruciform specimens were tested before by Tomlinson and Marsavina [123] and their data were reprocessed using this current methodology.

**Table 4-5 Experimental details for the specimens used in the T-stress and SIF determination**

Case No.	Type	Material	Notch length [mm]	Fatigue crack length [mm]	Freq. [Hz]	Loading [kN]	
						$\Delta F_x$	$\Delta F_y$
1	DCB	Al 7010	4	0	25	0	0.5to1.5
2	DCB	Al 7010	4	2.42	25	0	0.5to1.5
3	Cruciform	150M36 steel	9	0	8	0.3to10.3	0.1to10.1
4	Cruciform	150M36 steel	9	0	8	0.1to5.0	0.1to14.7
5	DEC 0 offset Left crack	Al 7010	8	0	20	0	1 to 7
6	DEC 0 offset Right crack	Al 7010	8	0	20	0	1 to 7



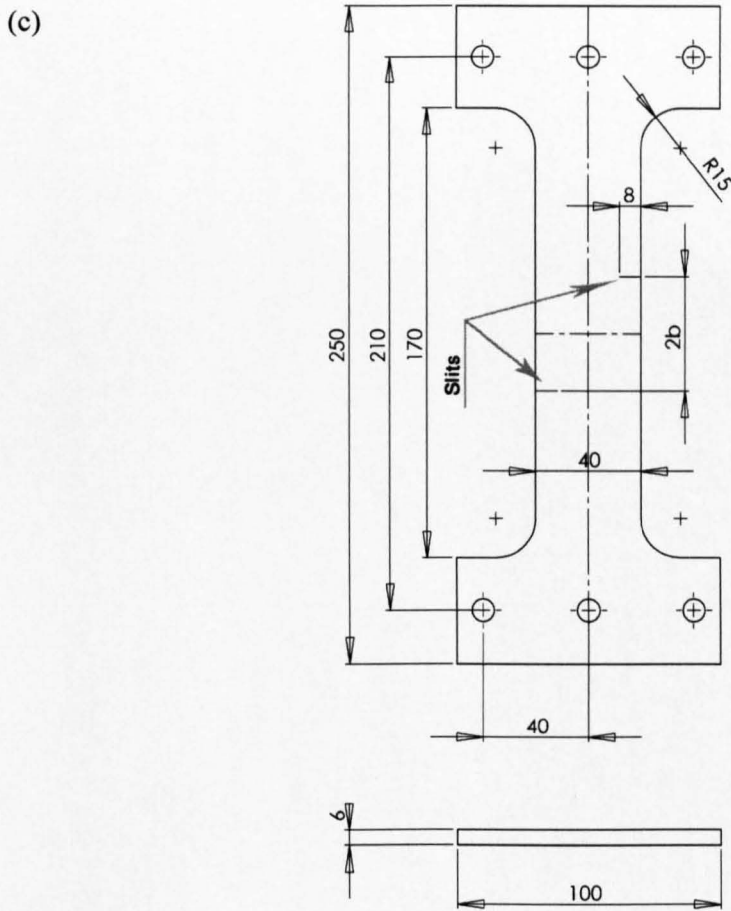
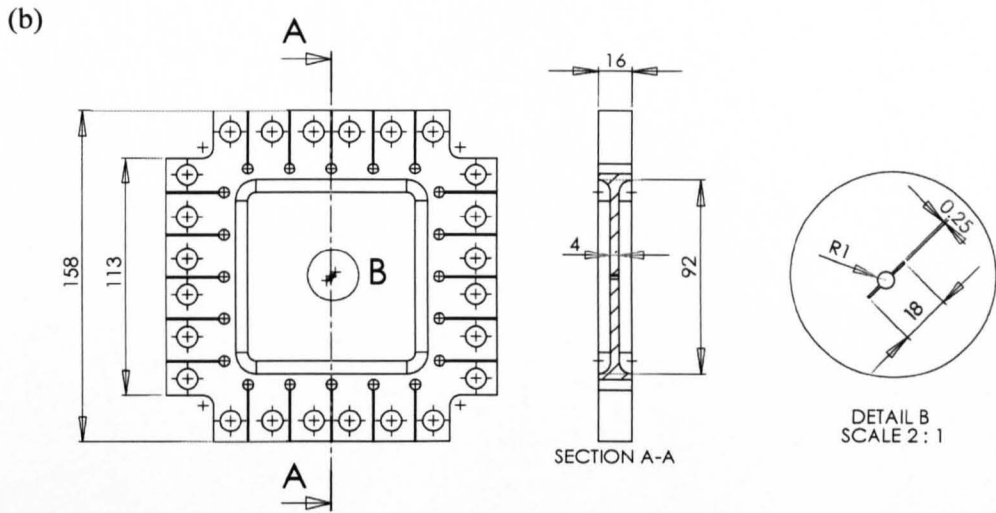
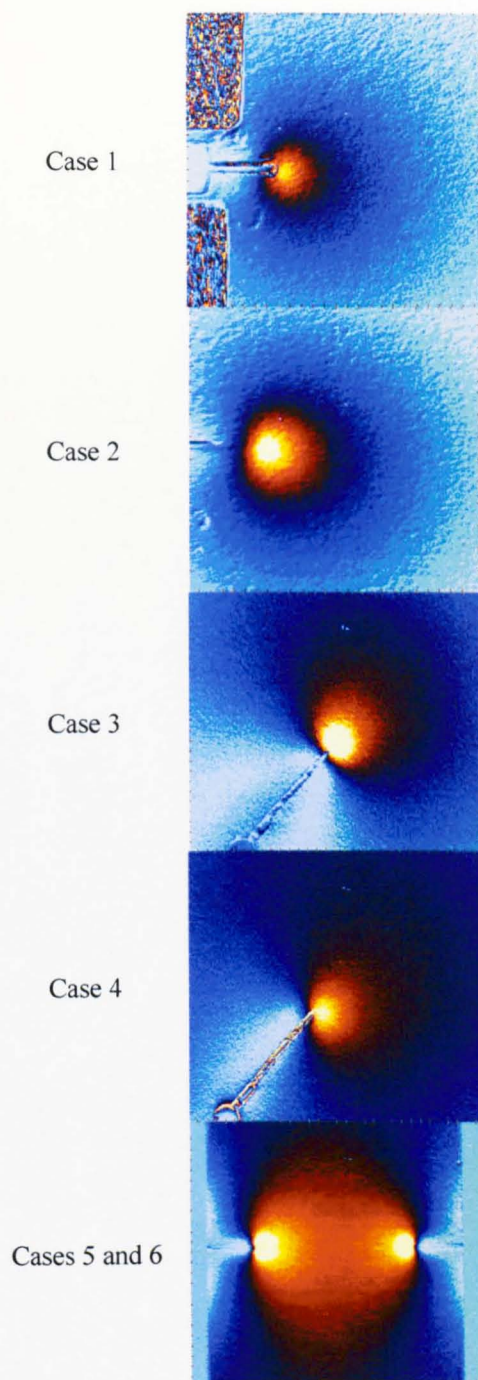


Figure 4-28 Specimen dimensions: (a) DCB (b) Cruciform (c) Double edge cracked (DEC) specimen

Figure 4-29 shows the qualitative results gained from thermoelastic stress analysis for the different cases given in Table 4-5.



**Figure 4-29** Thermoelastic images for the different cases used to validate the T-stress determination method (see Table 4-5)

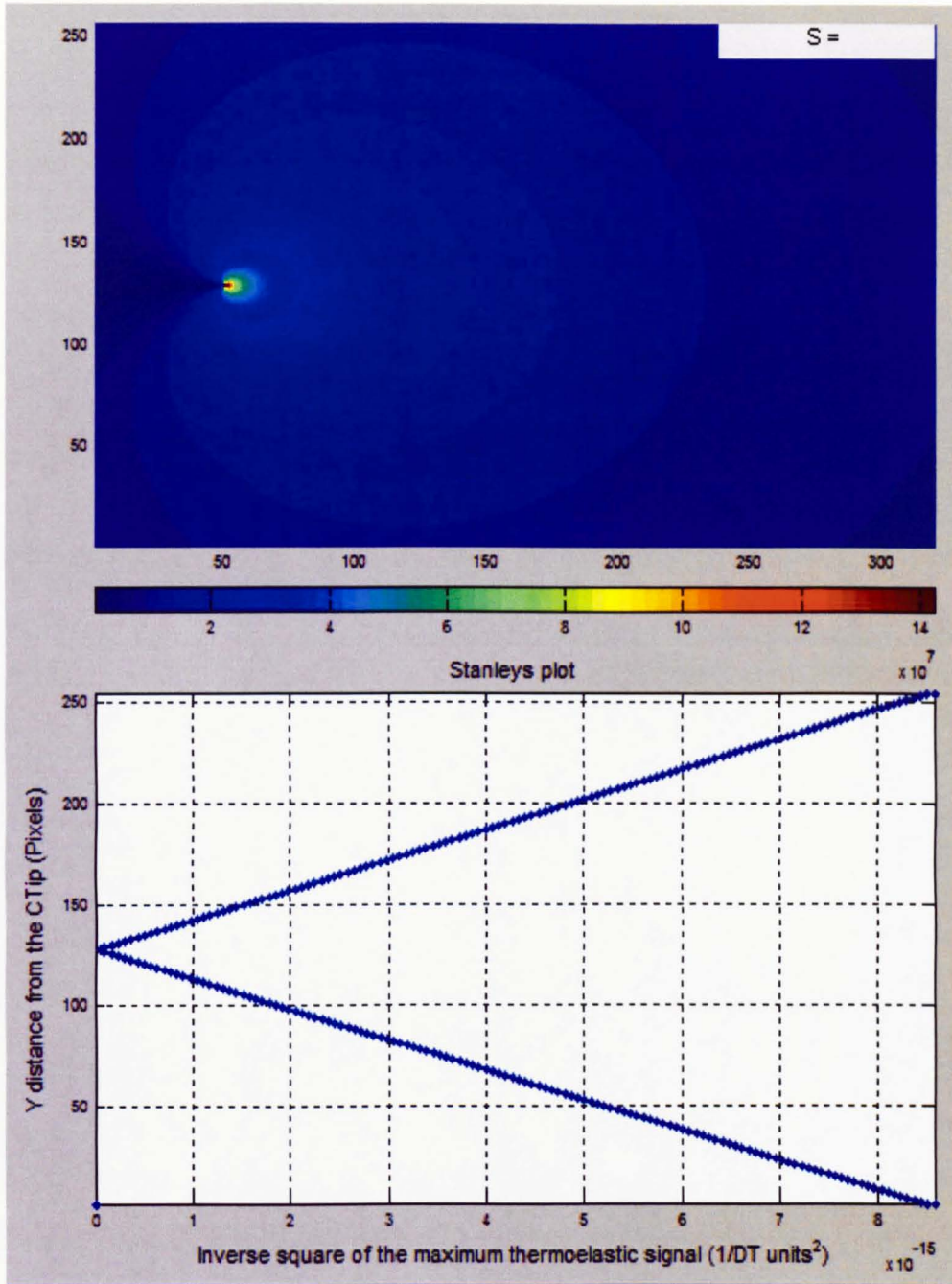
In parallel with the experiments, the finite element method, ABAQUS/CAE, was used to find the stress intensity factors and T-stress. In order to check the accuracy of the numerical analysis, a uniaxial tensile model was generated for a centre-cracked large plate with  $a/w=0.08$  and  $w/h=1$ , in which  $a$  is the crack length,  $w$  is width of specimen and  $h$  is height of specimen. The T-stress was determined for a range of loads and compared to an analysis published by Fett [124]. The results showed only 0.6% difference when compared to the published data. A double-edge-cracked rectangular plate ( $a/w=0.4$  and  $h/w>1.5$ ) was also modelled using FE. In this case T-stress results were about 2% different from those in reference [124]. Therefore it was considered that the FE method could be used as a datum for the experiments.

#### 4.4.1 Crack tip position

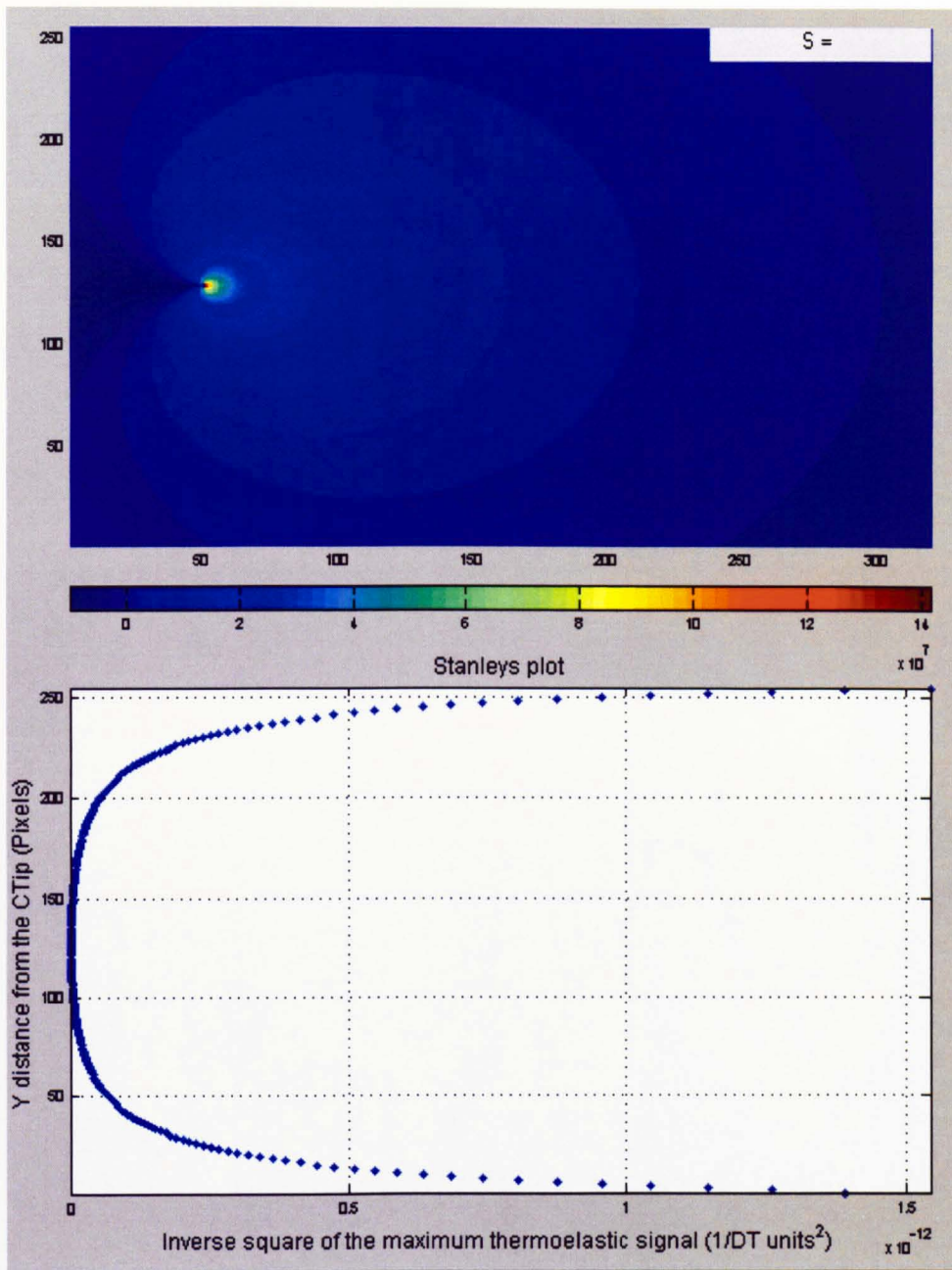
It has been shown in the work of Diaz *et al.* [88] in determining the SIF from TSA data that locating the crack tip within the field of data has a significant influence on the calculated value. This is because the coordinate systems for full field data collection and processing are generally relative to the crack tip (see equation 4-1). As mentioned before, it is of interest to note, however, that early publications [75, 76] on this topic presented a method for SIF determination which does not require an accurate knowledge of the crack-tip position. However, since the effect of T-stress has been ignored in these publications (see equations 2-10 to 2-15), it is not possible to use that method in the presence of T-stress. To have a better illustration of this, Stanley's plot has been drawn in Figure 4-30 in a pure mode I (with  $K_I = 6 \text{ MPa}\sqrt{\text{m}}$ ) case with  $T = 10 \text{ MPa}$  and without presence of T-stress.

Obviously, the presence of the T-stress does not affect the generated TSA contours; however, the T-stress causes the Stanley's plot to be curved (see Figure 4-30). Thus, the linearity assumption which is the base of the Stanley's method will not be valid in presence of T-stresses. In other words equations 2-11 and 2-12 are no longer valid and a full field method must be used instead of the linear fit method to obtain stress intensity factor. Therefore a good method is needed to find

the crack tip. In addition it should be noted that the *T*-stress can not be found using Stanley's method.



(a)



(b)

Figure 4-30 Pure mode I ( $K_I = 6 \text{ MPa}\cdot\text{m}^{0.5}$ ) (a) without T-stress and (b) with  $T = -10 \text{ MPa}$

Several different methods have been proposed so far to find the crack tip position from thermoelastic images [78, 88, 125]. The TSA image can be presented as a vector with magnitude (R-image) and phase (which is the phase shift between the

TSA signal and the reference signal); or as the projection of the vector in X (X-image) and Y (Y-image) directions in the Cartesian coordinate system, where the X image is the in-phase image and the Y-image is the out-of-phase image. Most of the proposed methods use the magnitude of the thermoelastic signal (the X or R image) to estimate the position of the crack tip. Recently Diaz *et al.* [88] attempted to overcome the problem of locating the crack tip by including the crack tip coordinates as two additional variables in the optimization process to calculate the Fourier series coefficients in the Muskhelishvili approach using a downhill simplex (DS) method. As an alternative, a genetic algorithm (GA) was also used to find an initial value for the downhill simplex method to solve the same problem. However, both of these methods are based on numerical techniques rather than any physical basis and are very slow and depend on the data points selected. Therefore an alternative method is proposed in here to locate the position of the fatigue crack tip from thermoelastic images using the out of phase signal.

The concept of using the thermoelastic phase image to find the approximate location of the crack tip was first proposed by Diaz *et al.* [88]. Figure 4-31 shows the phase signal along a line taken through a crack tip and co-linear with the crack and is typical for all fracture problems observed. They divided the phase image into three different regions. Region A is the region where the adiabatic condition prevails and the thermoelastic signal and the load signal are in phase. They defined region B as a region where there is a higher gradient of stress and the out of phase signal indicates that the adiabatic condition is lost. They assigned region C as an indication of heat generation due to plasticity ahead of the crack tip. So, point O was adopted as an *estimation* for the crack tip and used as an initial value for their GA/DS method to solve for the SIFs and the optimised crack tip position.

It is reasonable that the phase shift around the crack tip is due to a high stress gradient and plasticity ahead of the crack tip. However, since the size of plastic zone ahead of the crack tip, especially at the early stages of crack growth, is the order of the resolution of the camera and the highest stress gradient still exists in the crack tip, it is postulated that the phase image should have an extreme value at the crack tip rather than zero. As Euler says “*Nothing at all happens in the*

universe in which there does not shine out some principle of maximum and minimum, wherefore there is absolutely no doubt but that all happenings in the universe may be determined from final effects by a method of maxima or minima quite as successfully as from actual causes themselves" [116]. So, it is more likely for the actual crack tip to be at point P and therefore experiments were performed to investigate this hypothesis. It should be noted that the location of Point P can be determined equally well using either the thermoelastic Y image or the phase image since both show the same out of phase characteristics.

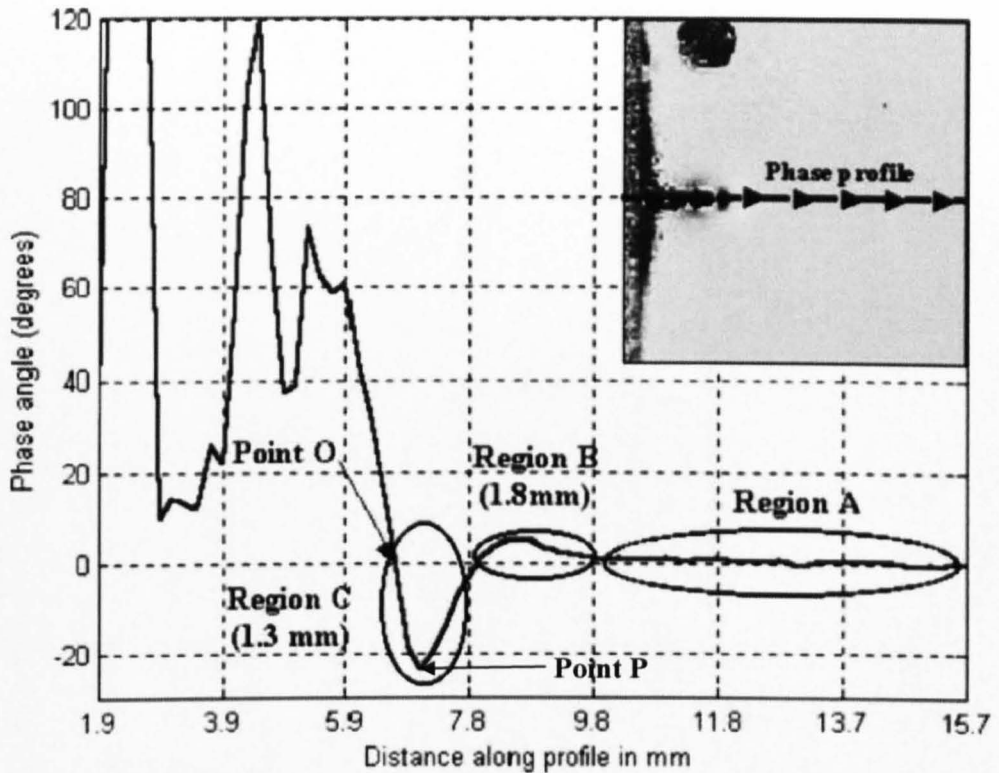


Figure 4-31 Typical phase signal along a line taken through a crack tip and co-linear with the crack [88]

#### 4.4.1.1 Experiments to find the crack tip position

To investigate the applicability of using point P as the crack tip position in the TSA images, TSA data were recorded from notch tips from five different specimens since locating a notch tip from a TSA image by visual inspection is

straightforward (compared to a fatigue crack tip). The specimens used were a DCB specimen and four cruciform specimens with different notch lengths (see Figure 4-28 and Table 4-5 for geometry). The coordinates of the notch tips in each of the TSA images were found using the Y/Phase image technique, and again the GA/DS method, and these were compared with the notch location found by visual inspection.

**Table 4-6 Comparison between the Y/Phase image and the GA/DS techniques to find the location of the notch tip (in pixels)**

Specimen Type	Notch location using Visual method		Y/Phase image Technique		GA/DS	
	x	y	X	y	x	y
DCB	80	119	81	118	75.3	118.2
Cruciform	154	101	155	101	157.1	97.2
Cruciform	128	102	129	103	132.2	102.5
Cruciform	136	102	136	101	139.1	99.8
Cruciform	137	102	135	101	135.1	99.1

Figure 4-32 and Figure 4-33 show the Y-image for a DCB and a cruciform specimen respectively. In these figures a plot of the Y-image signal versus both horizontal and vertical directions have been plotted. These plots show a similar pattern to that observed in Figure 4-31. However, it can be seen that in the DCB specimen point O is totally out of the notch tip area. This is a bit better for the cruciform specimen in which point O is closer estimate of the notch tip in the horizontal direction but not in the vertical direction. However, point P is a closer estimate of the notch tip. These values are shown quantitatively in Table 4-6 and compared with the values found by GA/DS technique. The Y-phase image results are in good agreement with the notch tip locations found visually.

The GA/DS technique is highly affected by the point selected as the initial guess for the algorithm, the data collection procedure, the number of iterations for the algorithm and some other issues such as, the number of generations, tolerance and many other parameters which always exist in optimization algorithms. Sometimes, this randomly makes the results obtained from the algorithm highly

accurate and sometimes poor. Thus this reduces the repeatability of the whole procedure.

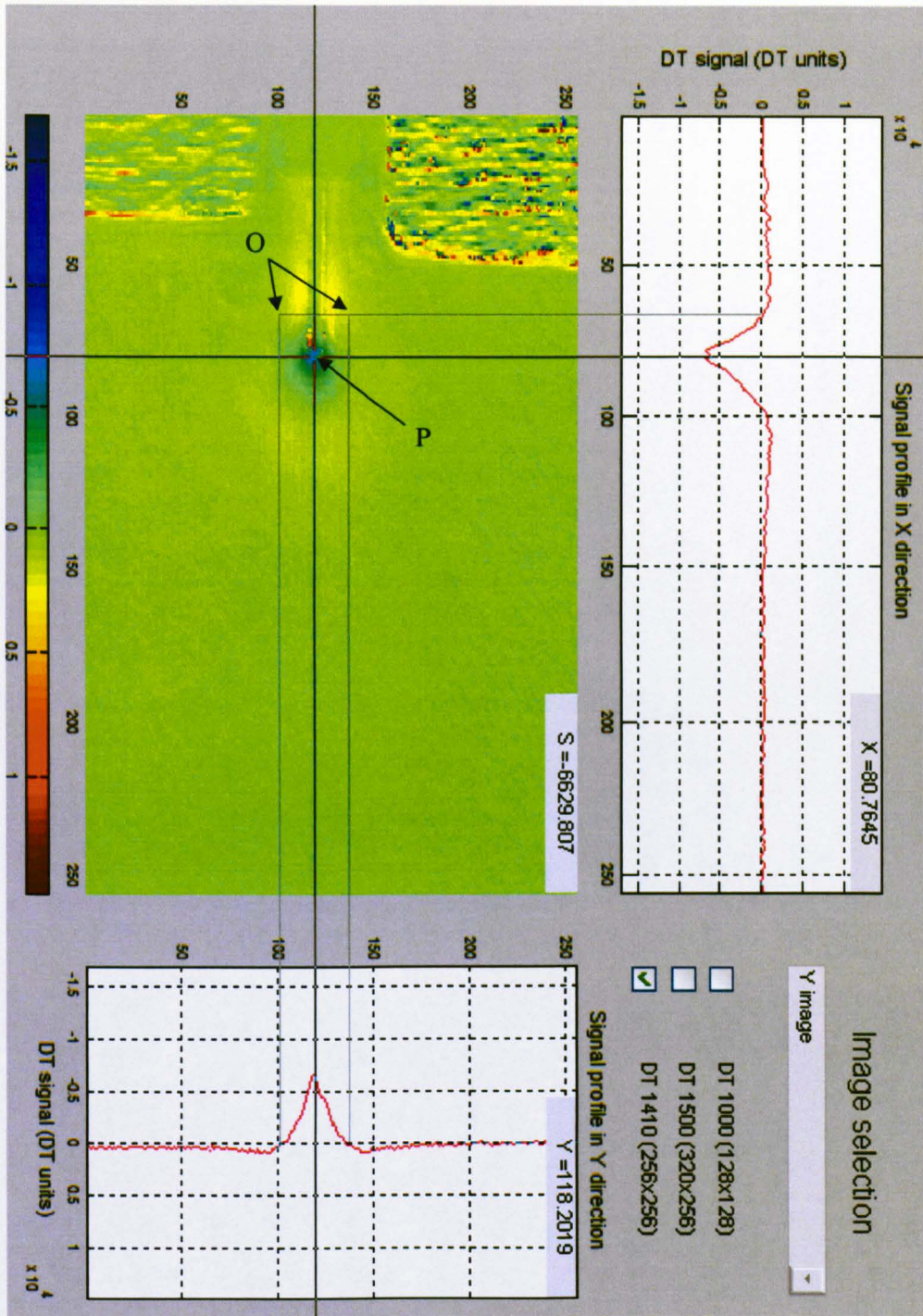


Figure 4-32 Y-image and signal profile for a DCB specimen with a notch

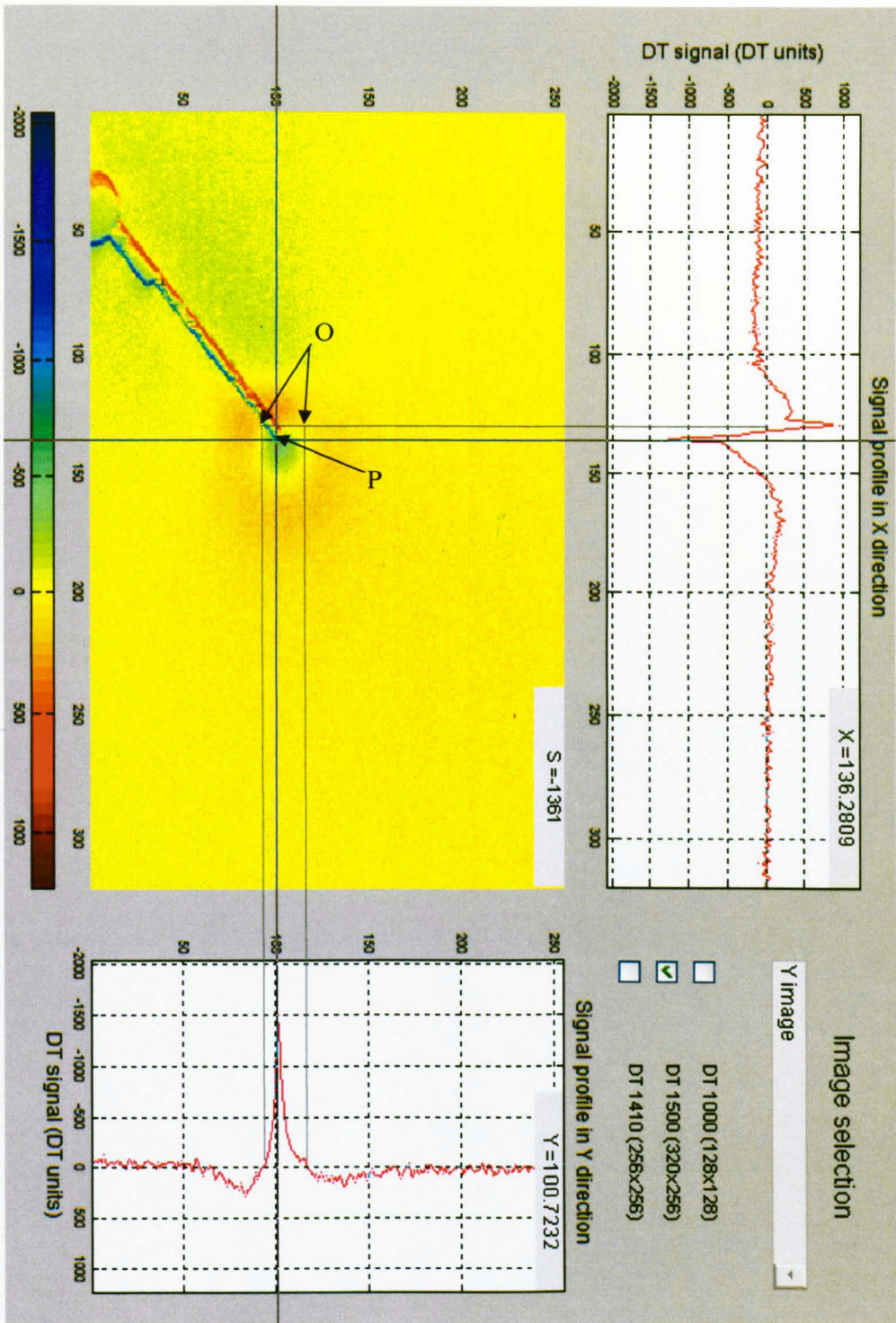


Figure 4-33 Y-image and signal profile for a Cruciform specimen with a notch

Further TSA data were collected by growing a fatigue crack in DCB specimens. Figure 4-34 shows the phase image for a typical case with a fatigue crack. By looking at the image, the horizontal position of the crack tip based on the proposed technique is found as  $x=85$  pixels. To measure the crack length the notch tip should also be found which is  $x=51$  pixels. The difference of these two values, which is 34 pixels, is the fatigue crack length. To geometrically calibrate the phase image an image was taken from a steel rule in the same plane as the specimen as shown in Figure 4-35. This gives a geometrical calibration factor of 14.22 pixels per mm. By using this calibration factor the crack length was  $34/14.22=2.391$ mm.

The crack lengths were also measured using a travelling microscope. Just for the matter of better illustration a CCD camera was used to take an image of the crack as shown in Figure 4-36. In this case the crack length was found as 2.42mm. The same procedure was repeated for other lengths of cracks. The obtained results are compared with the crack tip found using Y/Phase technique and GA/DS in Table 4-7.

**Table 4-7 Comparison between the Y/Phase image and the GA/DS techniques to measure the fatigue crack length (in mm)**

Crack length measured using microscope	Y/Phase image		GA/DS	
	crack length	%difference with microscope measurements	crack length	%difference with microscope measurements
0.65	0.703±0.15	-15% to 31%	0.82±0.15	3% to 49%
1.39	1.47±0.15	-5% to 16%	0.562±0.15	-70% to -49%
2.42	2.391±0.15	-7.5% to 5%	2.069±0.15	-21% to -8%

The measured crack lengths using Y/Phase image method are in range 5% to 31% difference with the measured crack lengths using travelling microscope. This shows a good improvement compared to 3% to 70% difference range using the GA/DS technique.

It is worthy to note that the concept of the crack tip is only valid in linear elastic fracture mechanics. In reality there is not such a definite definition for the crack tip particularly for ductile materials where the mechanism of crack growth is more

based on the nucleation of voids ahead of crack tip. In these cases the concept of process zone is more likely to be used instead of the crack tip [126].

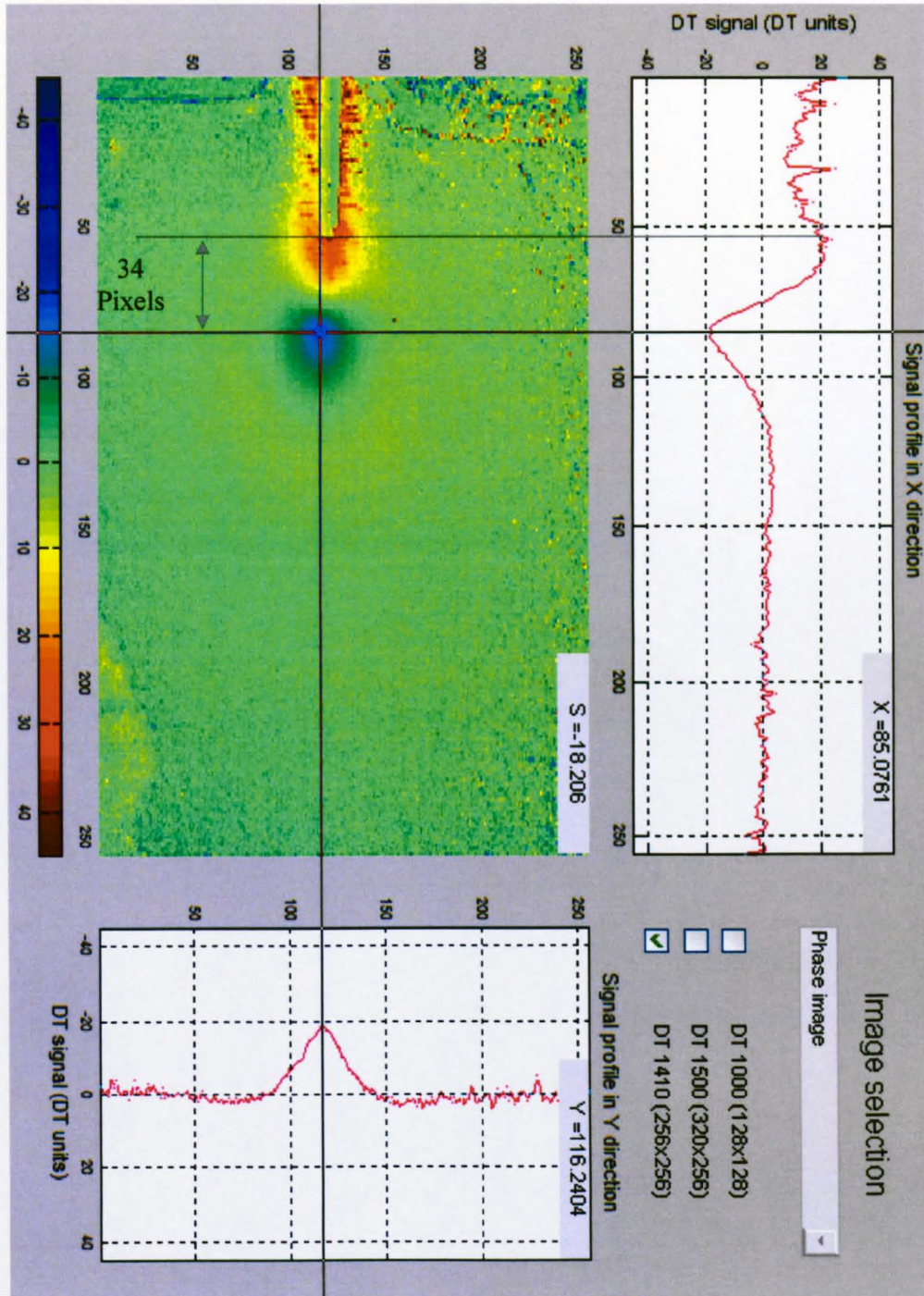


Figure 4-34 Phase image for a fatigue crack in a DCB specimen

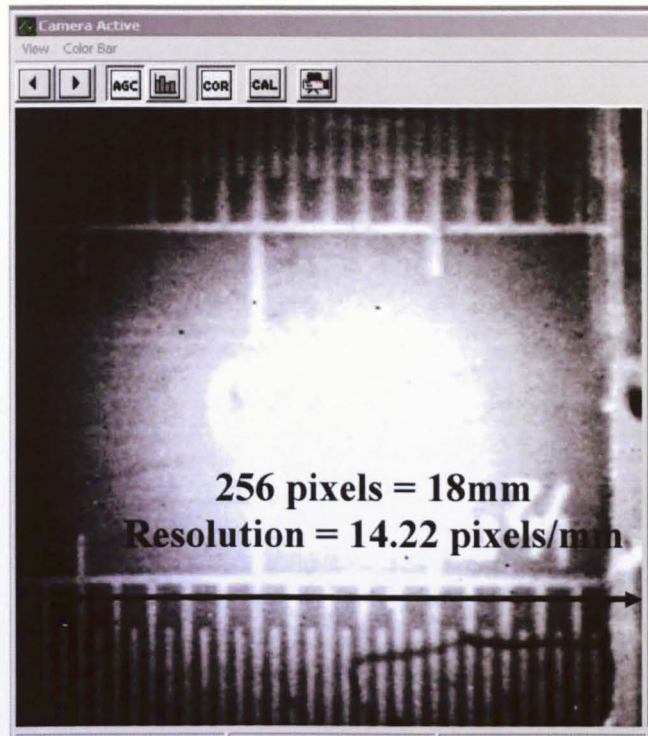


Figure 4-35 Image of a steel rule used for geometrical calibration of the image

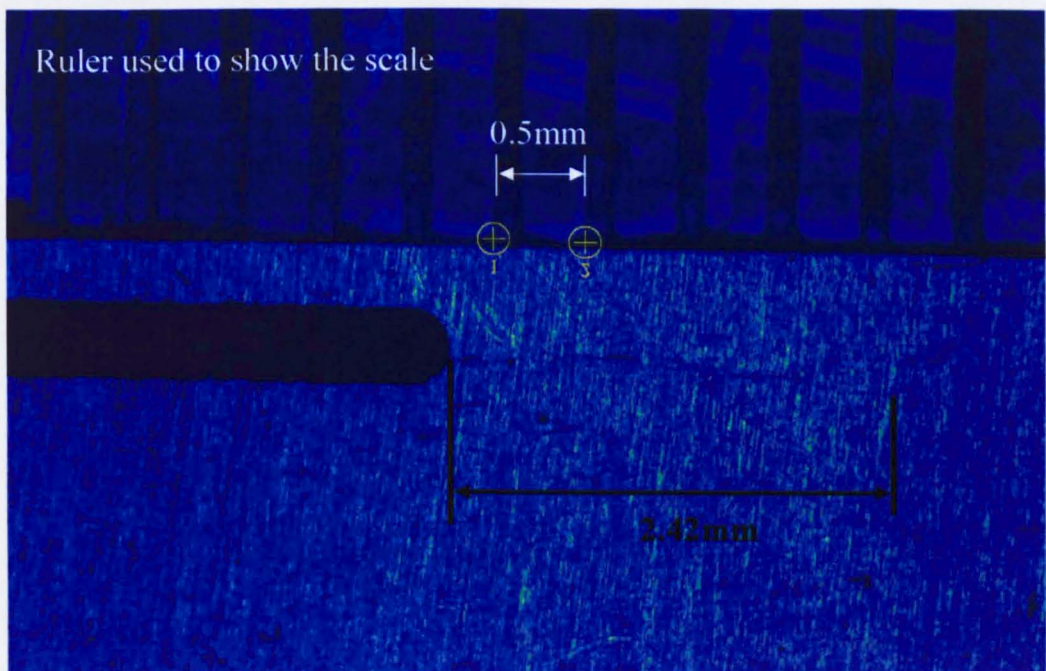


Figure 4-36 Image captured using a CCD camera to measure the crack length

#### 4.4.2 T-stress and SIF determination

The crack tip positions were found using the Y/Phase image technique as described in previous section. Data points were taken from the linear elastic region surrounding the crack tip, where the effect of the through thickness stress is negligible, using a data collection method described by Tomlinson and Marsavina [123] with some modifications in the distribution of data points around the crack tip. The distribution is defined as  $d=d_2/d_1=d_3/d_4=d_{n-1}/d_{n-2}$  (Figure 4-37).

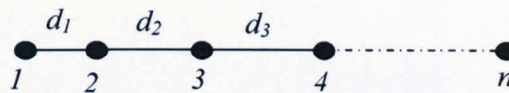
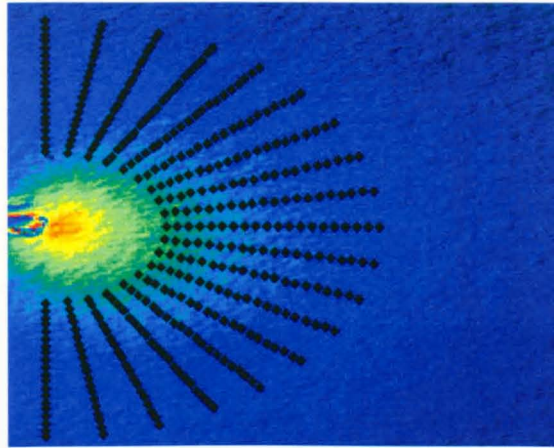


Figure 4-37 Definition of distribution

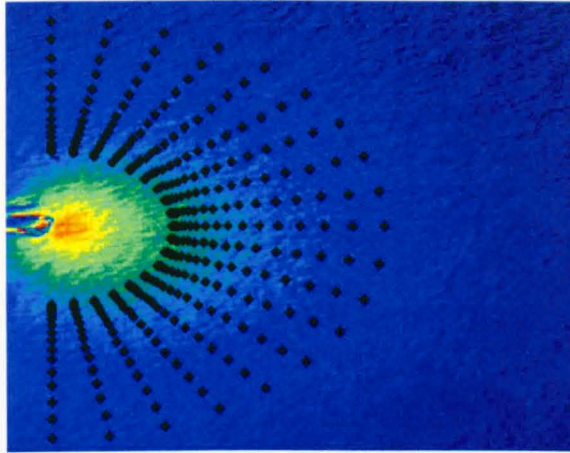
Imagine  $n$  data points along a line as shown in Figure 4-37. Thus uniform, equally spaced, distribution is equivalent to  $d=1$ . First for a DCB specimen (case no.1 in Table 4-5) the T-stress and SIF were determined using a uniform distribution of data points along the radial direction (Figure 4-38). To explore the effect of distribution, the distribution was increased until no significant change in the values of the T-stress was observed. This is shown in Figure 4-39.

The results were compared to the finite element simulation results. It was found that increasing the distribution number does not significantly change the SIF. However, looking at the T-stress results, it is evident that by increasing the distribution number the results converge to the FEM results. It is true that the SIF values are slightly different from FEM results but in comparison to the significant improvement in T-stress results this difference is negligible.

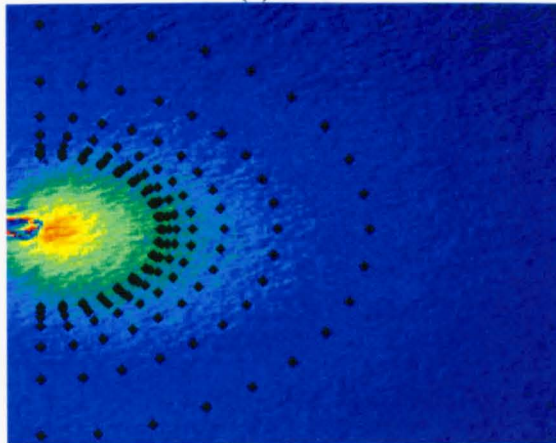
To explore the influence of the number of points in each radial line on the results, a range of 10 to 70 data points were used in each line. Results are shown in Figure 4-40.



(a)  $d=1$



(b)  $d=2$



(c)  $d=10$

Figure 4-38 Data points distribution for different  $d$  values (a)  $d=1$  (b)  $d=2$  (c)  $d=10$

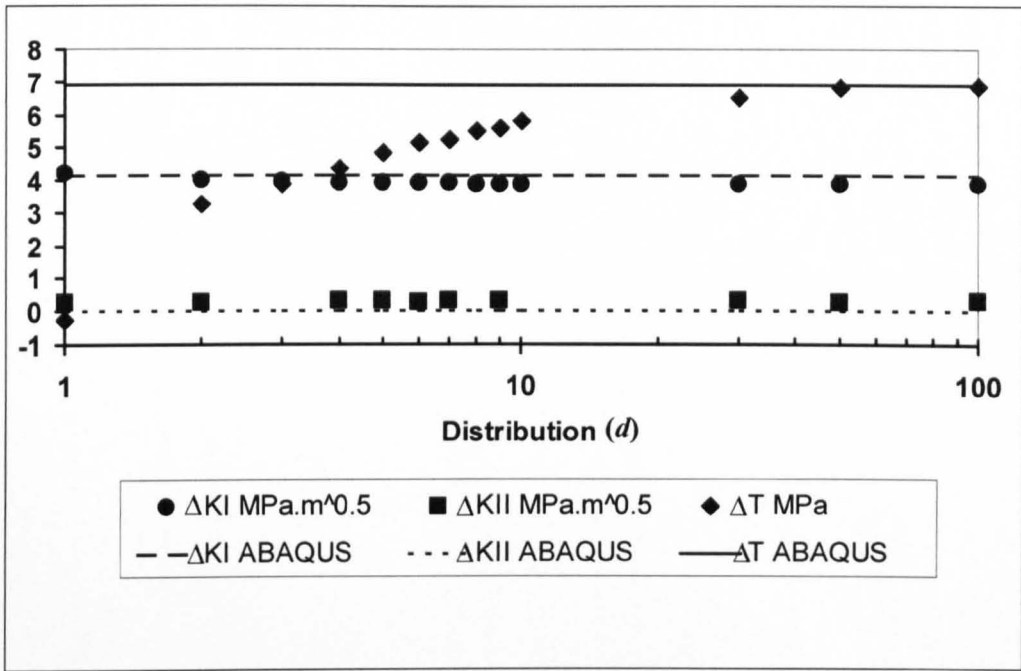


Figure 4-39 Effect of distribution on range of T-stress and SIF

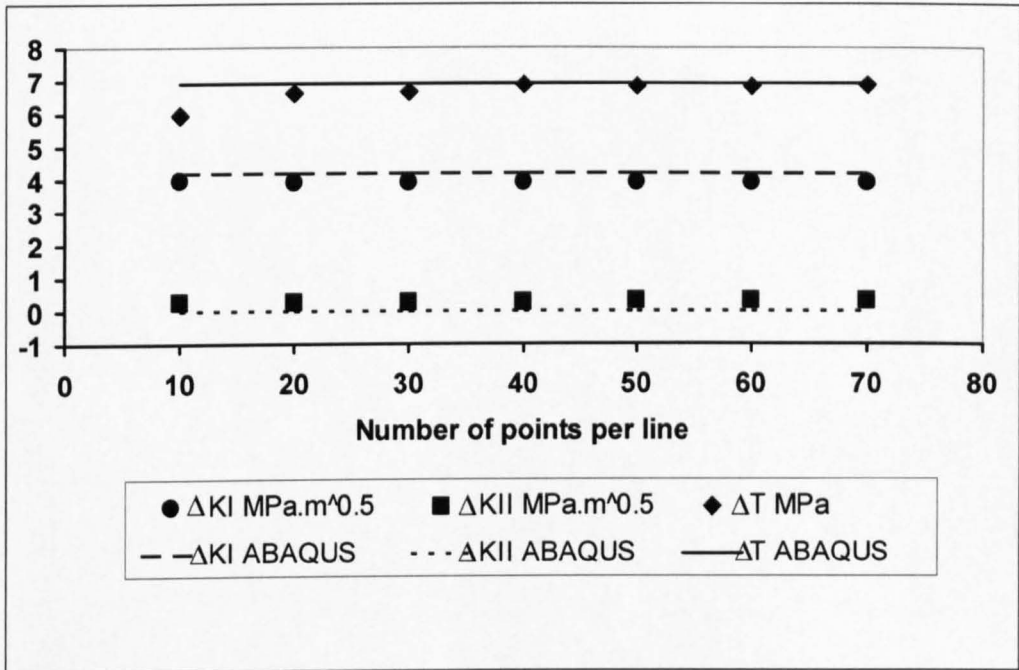


Figure 4-40 Effect of number of points on the determined T-stress and SIF

It is observed that the number of points does not noticeably affect the SIF. It is almost the same for the T-stress in which for more than 40 points the results converge.

Therefore for the rest of the cases, a distribution of  $d=100$  and 70 data points per line were used to determine the T-stress and SIF.

A comparison between the numerical simulation and experimental results is shown in Figure 4-41. This shows the effect of using two terms of Williams' solution, and three terms of Williams' solution, on  $\Delta K_I$ ,  $\Delta K_{II}$  and  $\Delta T$ -stress. The stress intensity factor results are also compared with those determined using the Muskhelishvili approach. The effect of crack tip location found by means of the Y/Phase image technique and the GA/DS technique on the determined stress intensity factors and T-stress is shown in Figure 4-42. A comparison is made between those results and the finite element results. Results for the GA/DS technique shown in the Figure 4-42 were obtained by finding point O as the initial estimation for the crack tip location. Then this crack tip was optimized using a GA. Then the optimized crack tip location was used as the initial value for the DS algorithm to find the crack tip. Using this crack tip, the T-stress and SIF were calculated using the Williams' three terms solution.

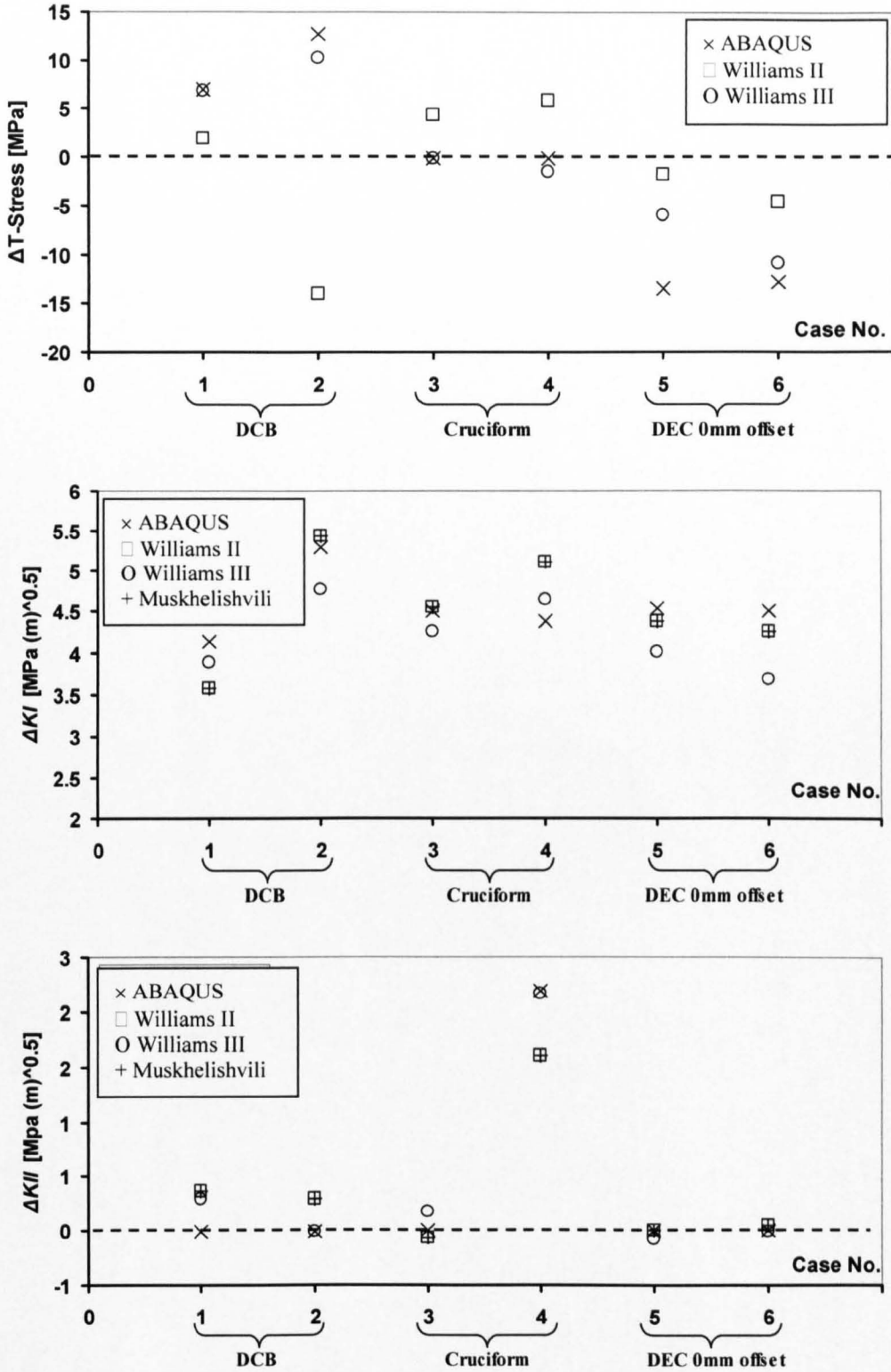


Figure 4-41 Comparison of ABAQUS, two and three terms Williams' and Muskhelishvili's solutions for a)  $\Delta T$ -stress b)  $\Delta K_I$  and c)  $\Delta K_{II}$ . See Figure 4-29 for the thermoelastic images

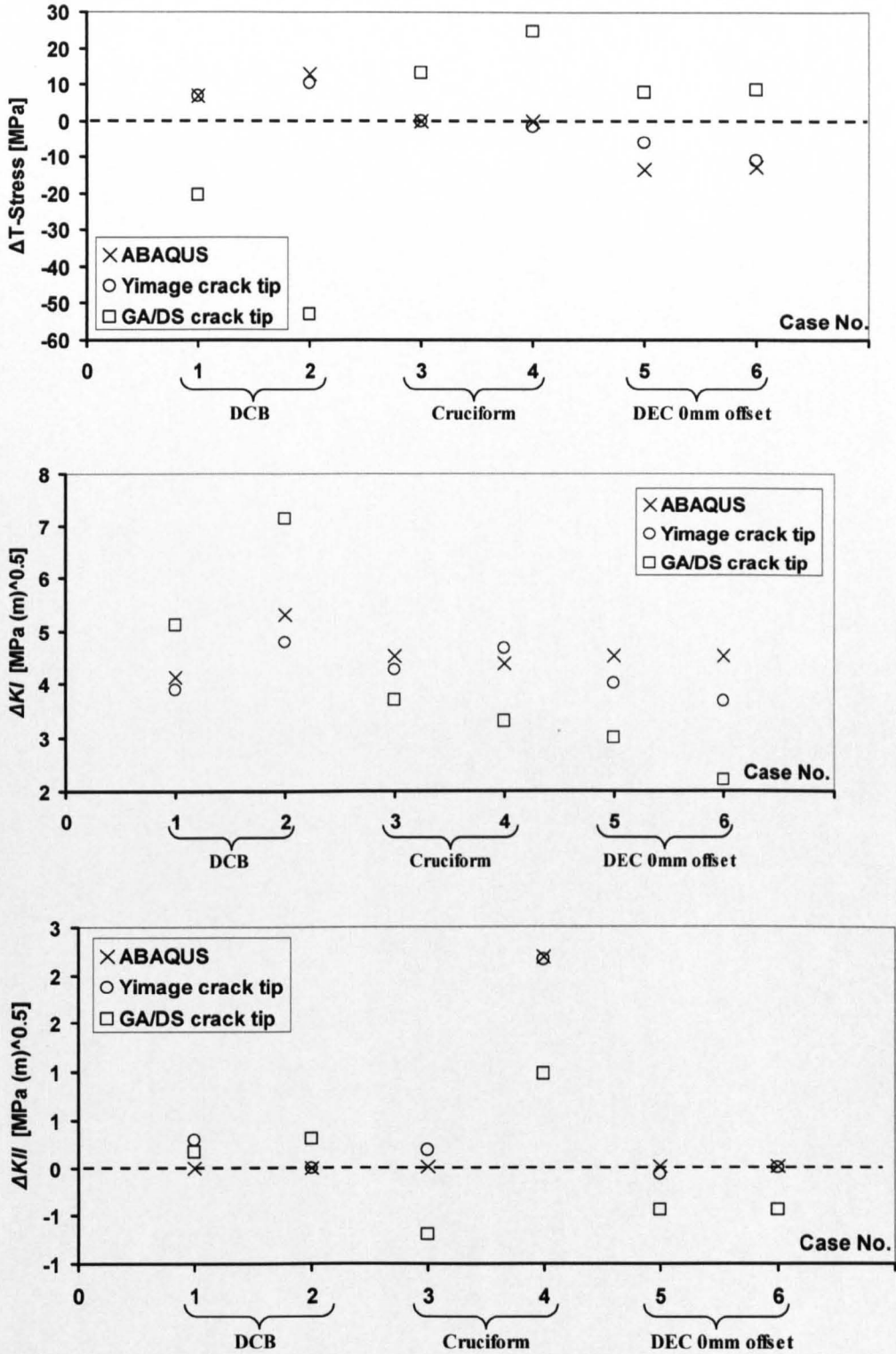


Figure 4-42 Comparison based on crack tip found by GA/DS and Y/phase-image techniques using three terms Williams' solution: a)  $\Delta T$ -stress b)  $\Delta K_I$  and c)  $\Delta K_{II}$ . See Figure 4-29 for the thermoelastic images

## 4.5 Discussion

The main area of investigation during this research was to establish how many terms of the Williams' equations (equations 4-1 and 4-2) were needed to determine the T-stress accurately using TSA data. This was done first by using noise free artificial data, artificial data with different noise levels and finite element stress data. It was shown that using two terms of the expansion looked promising in the artificial data. However, when the FE data were used it was found that two terms were not adequate to give accurate results for T-stress. Solutions based on more than 4 terms of the solution were numerically unstable, especially where more noise exists. Although a four terms solution, like a three terms solution gives acceptable results in most of the numerically generated cases and even better results for the T-stress using finite element data, the 4 terms solution were highly unstable in real experimental TSA data. Therefore, it was postulated that the three terms solution might be the optimum number of terms that can be used to determine the T-stress from experimental TSA data. This was experimentally investigated by comparing the experimentally determined T-stress for a range of 6 different test conditions to corresponding values determined from Finite Element analysis. The FEA was used as a datum since the FEA methodology was found to give results comparable for T-stress to previously published data for standard specimens [124]. It can be seen in Figure 4-41(a) that the FEA compares well with the experimentally determined T-stress using three terms of Williams' equations but using only two terms introduces considerable differences, in terms of magnitude.

One of the reasons that the non-singular (i.e. T-stress) term found by Dulieu-Barton *et al.* [78, 125] did not agree with the analytical solution may be that their method is based on using only two terms of Williams' solution which is shown in Figure 4-41(a) to be insufficient. However, using the third term as well to determine the T-stress significantly improves the results when compared with the numerical solution in majority of the majority of the cases considered.

In addition to using William's solution to determine the stress intensity factors, the Muskhelishvili solution [84, 88] was also used and it was found that the

results determined using this formulation coincide exactly with the results using two terms of the Williams's solution as shown in Figure 4-2, Figure 4-3 and Figure 4-41(b and c). It can be observed from Figure 4-41(b) that the mode I stress intensity factor determination using up to three terms of Williams's solution shows comparable results to those obtained using two terms in all cases. It was considered, however, that for the mode II stress intensity factor determination (Figure 4-41(c)) using three terms in Williams's equations gives a marginally better comparison to the FEA results than using only two terms.

Thus using the Muskhelishvili or two terms of Williams's solution does not introduce a significant error when compared to a three terms solution in SIF determination, but the use of these terms affects the T-stress results noticeably in terms of magnitude and sign. Therefore it is recommended that three terms of Williams's solution should be used for T-stress determination from thermoelastic data.

It can be seen in Figure 4-32, Table 4-6 and Table 4-7 that the Y/Phase image technique is more reliable than the GA/DS technique in finding the crack tip from thermoelastic images when compared to a manual/visual method. It is considered that the GA/DS method may be improved by using a more sophisticated objective function in the optimization method or increasing the number of iterations. The effect of using these different methods on SIF and T-stress determination was explored. The Y/Phase image technique as well as GA/DS technique was used with three terms of Williams' solution to determine the SIF and T-stress and the results are shown in Figure 4-42. It can be observed that for the SIF determination, Figure 4-42(b) and (c), the proposed Y/Phase image technique does give results which are closer to the FEA values than the GA/DS technique.

It also seems that the T-stress results, Figure 4-42(a) are sensitive to the crack tip position. The crack tips found using the GA/DS introduce significant errors both in sign, (e.g. cases 1 and 2), and magnitude, (e.g. case 3), of the determined T-stresses. As discussed in the Literature Review (chapter 2), in addition to the magnitude [33], the sign of T-stress is also crucial in crack directional stability

problems [10]. It is therefore important that the experimental technique should be able to determine the sign and magnitude of the T-stress properly.

The proposed Y/Phase technique can be implemented in such a way that eliminates the need for an operator to locate the crack tip. Also this technique is fast and does not need a large amount of memory and CPU resources. Consequently it has the potential to be used in a fully automated system to monitor fatigue crack paths during tests and to determine the corresponding parameters, SIF and T-stress, in almost real time conditions.

## 4.6 Conclusion

T-stress and stress intensity factors have been determined from the thermoelastic data using up to three terms of Williams' formulation with a least squares technique. The Muskhelishvili technique has also been used to determine the stress intensity factors only. The results have been compared to finite element simulations. It has been shown that Muskhelishvili and the two term Williams' solutions both give the same results and are sufficient to determine stress intensity factors accurately. However, the two term Williams' solution is not sufficient to determine the T-stress accurately and the results for T-stress using this model are dissimilar to those predicted by the finite element method. It has been shown that using up to three terms of the Williams' solution makes it possible to determine T-stress but more terms than 3 gives unstable solution.

A new technique was proposed to find the crack tip from thermoelastic images based on the Y or Phase image. It has been shown that this technique is much more reliable than the other technique attempted, especially in T-stress determination and it has a great potential to be used in fully automatic and real time fatigue crack tip monitoring applications.

The data used in this chapter were based on the TSA technique which yields the sum of the principal stress field. As it was discussed, the sum of the principal stress field shows numerical instability with an increase in the number of terms of Williams' solution fitted to the experimental or even numerically generated data. This numerical instability occurs especially when more than 3 terms of the

expansion are used. Although the T-stress can be determined using the 3 terms Williams' solution, such a numerical instability questions the robustness and reliability of the results obtained from the sum of the principal stress field using thermoelastic stress analysis. Therefore in the next chapter the robustness of another popular technique in fracture mechanics applications is explored. The T-stress and stress intensity factors are determined using the displacement field obtained by digital image correlation.

## **Chapter 5**

# **T-stress determination using digital image correlation**

The aim of this chapter is to develop a methodology to determine the T-stress from the experimental data obtained from digital image correlation. In process of determining the T-stress, stress intensity factors will also be determined.

First, the fundamentals of Digital Image Correlation (DIC) are explained. An interface is designed to process the image correlation output. This was done using both Muskhelishvili's and Williams' approaches based on displacement fields. These methodologies were assessed using artificial data, noisy artificial data and finite element data and the T-stress and stress intensity factors determined.

Experiments were also conducted on both notches and fatigue cracks. In the pure mode I case a notched DCB specimens were used. T-stress and stress intensity factors were determined and a fatigue crack was grown from the tip of the notch and the above procedure repeated after different stages of fatigue crack growth. The experiments were extended to mixed mode loading conditions and the results are compared with numerically simulated results using the finite element method.

## 5.1 DIC fundamentals

Like geometric moiré, moiré interferometry, holographic interferometry, and electronic speckle pattern interferometry (ESPI), digital image correlation (DIC) is also a full field technique which is used to measure the crack tip in-plane and out of plane displacement fields. However, in terms of the equipments required DIC is much simpler than the other techniques. This technique only needs a digital camera or a CCD camera and a computer to process the captured images. Normally the natural white light provides sufficient illumination. However depending on the application some artificial illumination may be needed. Figure 5-1 shows the equipment used typically in DIC technique to measure the displacement field.

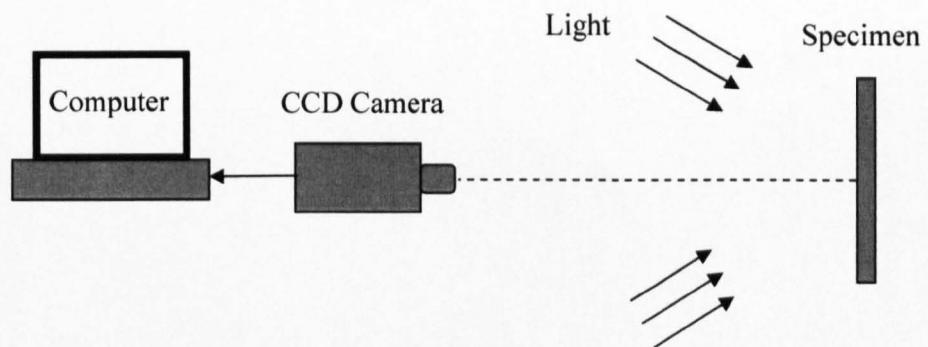


Figure 5-1 Schematic view of the DIC equipment

DIC is based on the mathematical correlation of the change in intensity characteristics of sequential digital images captured from the surface of the specimen while it undergoes deformation. In this technique the grey scale pattern of the surface is compared before (reference image) and after (deformed image) applying the deformation to the specimen.

To be able to compare two images a random pattern of speckles is needed on the surface of the specimen. To recognize this pattern mathematically, the intensity of light of each pixel in the reference and deformed images can be traced and the displacement vector can be determined. However, practically it is not possible to recognize every single pixel on the image. At least  $3 \times 3$  pixels are needed for one

recognizable feature [127]. Therefore, the images are divided into sub images and the correlation is performed for each of these sub images. These sub images are usually called a *subset* or *interrogation window*.

It should be noted that in such a division the average of intensity of light throughout the subset is used in the correlation process. In other words it is assumed that all the features in each subset have the same displacement. This assumption requires the subset to be as small as possible for accurate displacement measurement. On the other hand more features in a subset increase the accuracy of the correlation process, because the average intensity is obtained from a higher number of pixels. Thus, a too small a subset includes fewer features and consequently may decrease the accuracy of the correlated results. Therefore, finding the optimum size of subset depends on the image properties (such as feature/speckle size and resolution) and sometimes a trial and error process is needed to get the proper interrogation window size.

To produce a speckle pattern on the specimen different methods can be used. Sometimes the surface roughness of the material is enough to produce a suitable pattern. Glass or emery paper can be used to scratch the surface of the specimen and make a random pattern [99]. Alternatively, the speckles can be produced by spraying paint which makes a contrast to the specimen colour on the surface of the specimen, or even using copy machine toner to produce the speckles. Such a pattern is enough in macro digital image correlation applications, however, in micro scale applications more attention should be paid to producing the patterns and the speckle size.

### 5.1.1 Displacement mapping

Assume that a point P in the reference image with an  $x$  and  $y$  coordinate system is mapped into point  $P^*$  in deformed image with an  $x^*$  and  $y^*$  coordinate system (Figure 5-2). The mapping can be performed as

$$\begin{aligned}x^* &= x + u(x, y) \\ y^* &= y + v(x, y)\end{aligned}\tag{5-1}$$

To find the displacement fields, the vertical,  $v$ , and horizontal,  $u$ , displacements can be approximated using the Taylor series around a point  $P(x_o, y_o)$  as

$$\begin{aligned}
 x^* &= x_0 + u_0 + \frac{\partial u}{\partial x} \Delta x + \frac{\partial u}{\partial y} \Delta y + \frac{1}{2} \frac{\partial^2 u}{\partial x^2} \Delta x^2 + \frac{1}{2} \frac{\partial^2 u}{\partial y^2} \Delta y^2 + \frac{\partial^2 u}{\partial x \partial y} \Delta x \Delta y \\
 y^* &= y_0 + v_0 + \frac{\partial v}{\partial x} \Delta x + \frac{\partial v}{\partial y} \Delta y + \frac{1}{2} \frac{\partial^2 v}{\partial x^2} \Delta x^2 + \frac{1}{2} \frac{\partial^2 v}{\partial y^2} \Delta y^2 + \frac{\partial^2 v}{\partial x \partial y} \Delta x \Delta y
 \end{aligned}
 \tag{5-2}$$

in which  $\Delta x = x - x_0$  and  $\Delta y = y - y_0$ .

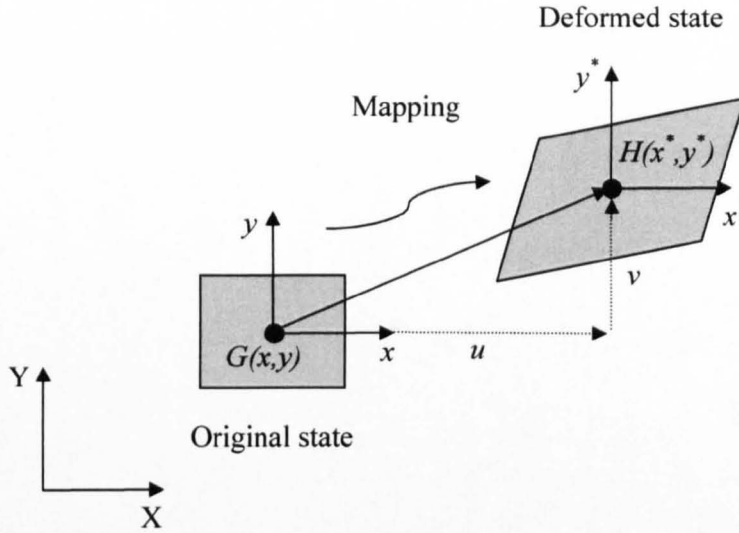


Figure 5-2 Concept of digital image correlation

Depending on the use of a first or second order approximation, six or twelve unknowns are available and can be found by correlation between the two images. This can be done by minimizing the so called correlation factor,  $C$ , defined as [128],

$$C = \frac{\sum_S [G(x, y) - H(x^*, y^*)]^2}{\sum_S G^2(x, y)}
 \tag{5-3}$$

where  $G$  and  $H$  are the grey scale light intensities corresponding to all the points in the subset,  $S$ . Since the intensity of light obtained from a digital image is a digital quantity, it needs to be smoothed first and then be used in the cross correlation algorithm. This can be done using B-Splines [129], Bi-cubic splines [128] or any other interpolation technique. As an alternative, a Fast Fourier Transform (FFT) cross correlation can be used to compare the subsets [127]. The

latter technique has been implemented in the DaVis software [130] which was used in this current work.

## 5.2 Methodology

There are two different approaches to tackle any elasticity problem using experimental data. The first approach is to guess an analytical stress function (it can be complex or not) satisfying the boundary conditions and determining the displacement and stress field analytically. Then these analytical fields can be fitted to the experimental data and the required parameters (for example, T-stress and SIF) can be determined. One such analytical solution is Williams' solution [120].

The second approach is to guess a general form of analytical function and fit this general form to the experimental data and then determine the displacement field and stress field. Muskhelishvili's [83] approach belongs to the second group in which two complex analytical functions need to be used.

Both these approaches were used with respect to the sum of principal stresses in previous chapters on TSA. Here both these approaches are used to explore their performance in a displacement field.

### 5.2.1 Williams' approach

Based on Williams' approach the stress field ahead of a crack can be expressed as an infinite series. In a plane mixed mode I and II condition this stress field is expressed as equations 5-4 and 5-5.

$$\text{Mode I} \left\{ \begin{array}{l} u_I = \sum_{n=1}^{\infty} \frac{r^{\frac{n}{2}}}{2\mu} a_n \left\{ \left[ \kappa + \frac{n}{2} + (-1)^n \right] \cos \frac{n\theta}{2} - \frac{n}{2} \cos \frac{(n-4)\theta}{2} \right\} \\ v_I = \sum_{n=1}^{\infty} \frac{r^{\frac{n}{2}}}{2\mu} a_n \left\{ \left[ \kappa - \frac{n}{2} - (-1)^n \right] \sin \frac{n\theta}{2} + \frac{n}{2} \sin \frac{(n-4)\theta}{2} \right\} \end{array} \right. \quad 5-4$$

and,

$$\text{Mode II} \begin{cases} u_{II} = -\sum_{n=1}^{\infty} \frac{r^{\frac{n}{2}}}{2\mu} b_n \left\{ \left[ \kappa + \frac{n}{2} - (-1)^n \right] \sin \frac{n\theta}{2} - \frac{n}{2} \cos \frac{(n-4)\theta}{2} \right\} \\ v_{II} = \sum_{n=1}^{\infty} \frac{r^{\frac{n}{2}}}{2\mu} b_n \left\{ \left[ \kappa - \frac{n}{2} + (-1)^n \right] \cos \frac{n\theta}{2} + \frac{n}{2} \cos \frac{(n-4)\theta}{2} \right\} \end{cases} \quad 5-5$$

where,  $u$  and  $v$  are horizontal ( $x$  direction) and vertical ( $y$  direction) displacements in mode  $I$  and  $II$ .  $\mu$  is the shear modulus and  $\kappa = (3 - \nu)/(1 + \nu)$  for plane stress and  $\kappa = 3 - 4\nu$  for plane strain conditions, where  $\nu$  is the Poisson's ratio.  $a$  and  $b$  are constants and  $r$  and  $\theta$  are defined as in Figure 5-3.

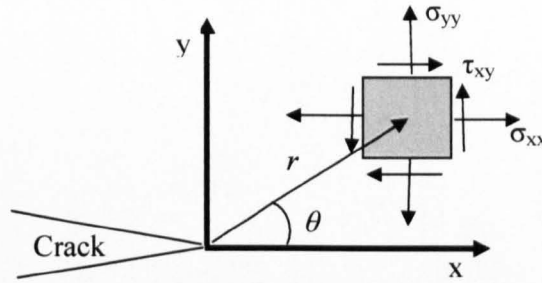


Figure 5-3 Stress state ahead of a crack tip

So, the mixed mode displacement fields ( $u$  and  $v$ ) which are obtained from DIC, can be derived by superimposing the mode  $I$  and  $II$  displacement field. By defining  $f_{n,m}(r, \theta)$ ,  $g_{n,m}(r, \theta)$ ,  $h_{n,m}(r, \theta)$  and  $l_{n,m}(r, \theta)$  as follows (5-6); the displacement field (equations 5-4 and 5-5) can be written in a matrix form (equation 5-7).

$$\begin{aligned} f_{n,m} &= \frac{r_m^{\frac{n}{2}}}{2\mu} \left\{ \left[ \kappa + \frac{n}{2} + (-1)^n \right] \cos \frac{n\theta_m}{2} - \frac{n}{2} \cos \frac{(n-4\theta_m)}{2} \right\} \\ g_{n,m} &= \frac{-r_m^{\frac{n}{2}}}{2\mu} \left\{ \left[ \kappa + \frac{n}{2} - (-1)^n \right] \sin \frac{n\theta_m}{2} - \frac{n}{2} \sin \frac{(n-4\theta_m)}{2} \right\} \\ h_{n,m} &= \frac{r_m^{\frac{n}{2}}}{2\mu} \left\{ \left[ \kappa - \frac{n}{2} - (-1)^n \right] \sin \frac{n\theta_m}{2} + \frac{n}{2} \sin \frac{(n-4\theta_m)}{2} \right\} \\ l_{n,m} &= \frac{r_m^{\frac{n}{2}}}{2\mu} \left\{ \left[ \kappa - \frac{n}{2} + (-1)^n \right] \cos \frac{n\theta_m}{2} + \frac{n}{2} \cos \frac{(n-4\theta_m)}{2} \right\} \end{aligned} \quad 5-6$$

$$\begin{Bmatrix} u_1 \\ \vdots \\ u_m \\ v_1 \\ \vdots \\ v_m \end{Bmatrix} = \begin{bmatrix} f_{1,1} \cdots f_{n,1} & g_{1,1} \cdots g_{n,1} \\ \vdots & \vdots \\ f_{1,m} \cdots f_{n,m} & g_{1,m} \cdots g_{n,m} \\ h_{1,1} \cdots h_{n,1} & l_{1,1} \cdots l_{n,1} \\ \vdots & \vdots \\ h_{1,1} \cdots h_{n,1} & l_{1,1} \cdots l_{n,1} \end{bmatrix} \begin{Bmatrix} a_1 \\ \vdots \\ a_n \\ b_1 \\ \vdots \\ b_n \end{Bmatrix} \quad 5-7$$

where  $m$  is the data point index.

By expanding equations 5-4 and 5-5, keeping the terms up to order  $r^{3/2}$  and comparing with the more common notation, i.e. using stress intensity factors and T-stress, it can be shown that

$$\begin{aligned} K_I &= a_1 \sqrt{2\pi} \\ K_{II} &= -b_1 \sqrt{2\pi} \\ T &= 4a_2 \end{aligned} \quad 5-8$$

in which  $K_I$  is the mode I stress intensity factor,  $K_{II}$  is mode II stress intensity factor and  $T$  is the T-stress.

## 5.2.2 Muskhelishvili's approach

In a general two dimensional elasticity problem the displacement field can be expressed by two analytical complex functions  $\varphi(z)$  and  $\psi(z)$  as [131].

$$2\mu(u + iv) = \kappa\varphi(z) - z\overline{\varphi'(z)} - \overline{\psi(z)} \quad 5-9$$

where  $z$  is a complex variable,  $u$  and  $v$  are horizontal (x direction) and vertical (y direction) displacements;  $\mu$  is the shear modulus and  $\kappa = (3 - \nu)/(1 + \nu)$  for plane stress and  $\kappa = 3 - 4\nu$  for plane strain conditions, where  $\nu$  is the Poisson's ratio.

By considering,  $\varphi(\zeta) = \sum_{k=-\infty}^{+\infty} a_k \zeta^k$ ,  $\psi(\zeta) = \sum_{k=-\infty}^{+\infty} b_k \zeta^k$ ,  $z = \omega(\zeta)$ , and

$$\Omega(\zeta) = \frac{\omega(\zeta)}{\omega'(\zeta)} = \sum_{l=-\infty}^{+\infty} c_l \zeta^l \quad \text{in which } \omega(\zeta) \text{ is a function which maps the } z\text{-plane to}$$

$\zeta$ -plane, and satisfying the boundary conditions, it can be shown that for a plate containing a crack the displacement field can be written as [99],

$$\begin{aligned}\sum_{k=-N}^N C_{j,k} \alpha_k + \sum_{k=-N}^N D_{j,k} \beta_k &= 2\mu u_j \\ \sum_{k=-N}^N E_{j,k} \alpha_k + \sum_{k=-N}^N F_{j,k} \beta_k &= 2\mu v_j\end{aligned}\quad 5-10$$

$\alpha$  and  $\beta$  are the real part and imaginary part of  $a$ , the complex unknown, respectively. In equations 5-10,  $C$ ,  $D$ ,  $E$  and  $F$  are defined as follows,

$$C_{j,k} = \kappa \operatorname{Re} \zeta_j^k - k \operatorname{Re} \Omega \operatorname{Re} \zeta_j^{k-1} - k \operatorname{Im} \Omega \operatorname{Im} \zeta_j^{k-1} + \operatorname{Re} \zeta_j^{-k} + k \sum_{l=-k}^M c_{l+k-1} \operatorname{Re} \zeta_j^{-l} \quad 5-11$$

$$D_{j,k} = -\kappa \operatorname{Im} \zeta_j^k + k \operatorname{Re} \Omega \operatorname{Im} \zeta_j^{k-1} - k \operatorname{Im} \Omega \operatorname{Re} \zeta_j^{k-1} + \operatorname{Im} \zeta_j^{-k} - k \sum_{l=-k}^M c_{l+k-1} \operatorname{Im} \zeta_j^{-l} \quad 5-12$$

$$E_{j,k} = \kappa \operatorname{Im} \zeta_j^k + k \operatorname{Re} \Omega \operatorname{Im} \zeta_j^{k-1} - k \operatorname{Im} \Omega \operatorname{Re} \zeta_j^{k-1} - \operatorname{Im} \zeta_j^{-k} - k \sum_{l=-k}^M c_{l+k-1} \operatorname{Im} \zeta_j^{-l} \quad 5-13$$

$$F_{j,k} = \kappa \operatorname{Re} \zeta_j^k + k \operatorname{Re} \Omega \operatorname{Re} \zeta_j^{k-1} + k \operatorname{Im} \Omega \operatorname{Im} \zeta_j^{k-1} + \operatorname{Re} \zeta_j^{-k} - k \sum_{l=-k}^M c_{l+k-1} \operatorname{Re} \zeta_j^{-l} \quad 5-14$$

In matrix format equation 5-10 can be written as,

$$Ax = b \quad 5-15$$

where

$$A = \begin{pmatrix} C_{1,-N} & \cdots & C_{1,N} & D_{1,-N} & \cdots & D_{1,N} \\ \vdots & \vdots & \vdots & \vdots & \vdots & \vdots \\ C_{p,-N} & \cdots & C_{p,N} & D_{p,-N} & \cdots & D_{p,N} \\ E_{1,-N} & \cdots & E_{1,N} & F_{1,-N} & \cdots & F_{1,N} \\ \vdots & \vdots & \vdots & \vdots & \vdots & \vdots \\ E_{p,-N} & \cdots & E_{p,N} & F_{p,-N} & \cdots & F_{p,N} \end{pmatrix}, \quad x = \begin{pmatrix} \alpha_{-N} \\ \vdots \\ \alpha_N \\ \beta_{-N} \\ \vdots \\ \beta_N \end{pmatrix} \quad \text{and} \quad b = 2\mu \begin{pmatrix} u_1 \\ \vdots \\ u_p \\ v_1 \\ \vdots \\ v_p \end{pmatrix} \quad 5-16$$

By solving equation 5-10 and finding  $\alpha$  and  $\beta$ , stress intensity factors can be determined as follows [99],

$$\begin{aligned}K_I &= 2\sqrt{\frac{\pi}{a}} \sum_{k=-N}^N k \alpha_k \\ K_{II} &= -2\sqrt{\frac{\pi}{a}} \sum_{k=-N}^N k \beta_k\end{aligned}\quad 5-17$$

It is worth noting that the T-stress can not be determined using the Muskhelishvili's approach explained in section 5.2.2.

### 5.3 Methodology assessment using artificial data

To explore the reliability of both methodologies, another subroutine was developed to produce an artificial displacement field based on equation 5-18 in a DIC file format legible for Digital Image Correlation Intensity factor and T-stress Analyser Code (DICITAC).

$$\begin{aligned}
 u = & \frac{K_I}{2\mu} \sqrt{\frac{r}{2\pi}} \cos \frac{\theta}{2} \left( \kappa - 1 + 2 \sin^2 \frac{\theta}{2} \right) & v = & \frac{K_I}{2\mu} \sqrt{\frac{r}{2\pi}} \sin \frac{\theta}{2} \left( \kappa + 1 - 2 \cos^2 \frac{\theta}{2} \right) \\
 & + \frac{K_{II}}{2\mu} \sqrt{\frac{r}{2\pi}} \sin \frac{\theta}{2} \left( \kappa + 1 + 2 \cos^2 \frac{\theta}{2} \right), & & - \frac{K_{II}}{2\mu} \sqrt{\frac{r}{2\pi}} \cos \frac{\theta}{2} \left( \kappa - 1 - 2 \cos^2 \frac{\theta}{2} \right) \\
 & + \frac{T}{8\mu} r (\kappa + 1) \cos \theta & & + \frac{T}{8\mu} r (\kappa - 3) \sin \theta
 \end{aligned} \quad 5-18$$

where,  $u$  and  $v$  are horizontal (x direction) and vertical (y direction) displacements.  $\mu$  is the shear modulus and  $\kappa = (3 - \nu)/(1 + \nu)$  for plane stress and  $\kappa = 3 - 4\nu$  for plane strain conditions, where  $\nu$  is the Poisson's ratio.  $a$  and  $b$  are constants and  $r$  and  $\theta$  are defined as in Figure 5-3.

To consider different situations three different conditions were investigated using the artificial data. First, a pure mode I case was examined then a mixed mode condition was created by introducing mode II contributions to the artificial data. At the end T-stress was also included in the data. Table 5-1 shows the SIF and T-stress used in each case.

In contrast to the stress field generated in the TSA chapter, the displacement field depends on material properties. To generate the fields, elastic modulus and Poisson's ratio are considered as 70GPa and 0.3, respectively. Moreover, 20 data points per mm have been used in the field generation procedure.

**Table 5-1 The SIF and the T-stress used in each case**

Case No.	Description	$K_I$ [MPa m <sup>0.5</sup> ]	$K_{II}$ [MPa m <sup>0.5</sup> ]	$T$ [MPa]
1	Pure mode I	6	0	0
2	Mixed mode I & II	6	2	0
3	General plane stress	6	2	10

Figure 5-4 shows the displacement distribution using equation 5-18 for the three cases in Table 5-1. Based on the generated displacement fields, stress intensity factors were determined using Muskhelishvili's approach as described in section 5.2.2. The results are shown in Table 5-2. It can be observed that Muskhelishvili's approach underestimates the SIF values by more than 30% for the mode I stress intensity factor in all the cases. This error is less (15% approximately) for mode II values.

**Table 5-2 SIF using Muskhelishvili's approach**

Case No.	Description	$K_I$ [MPa m <sup>0.5</sup> ]	$K_{II}$ [MPa m <sup>0.5</sup> ]
1	Pure mode I	4.088	-0.109
2	Mixed mode I & II	4.111	1.709
3	General plane stress	4.043	1.710

The same case studies were used to determine stress intensity factors using Williams' approach. To explore the effect of the number of terms used on the calculated T-stress and SIF, up to 25 terms of Williams' expansion were considered in the calculations. The convergence curves are shown in Figure 5-5.

As it is observed from Figure 5-5, unlike the stress solution found in the previous chapter for the sum of the principal stresses data, the displacement solution is less sensitive to the number of terms. It was observed in the previous chapter that the stress solution was numerically unstable even for mode I stress intensity factor for more than 9 terms of the Williams' expansion. However, for noise free artificial displacement data the results are stable for more than 25 terms.

In real experiments noise infects the data. Therefore, before starting experiments the feasibility of this approach was assessed using artificially generated displacement fields which were disturbed by different levels of noise.

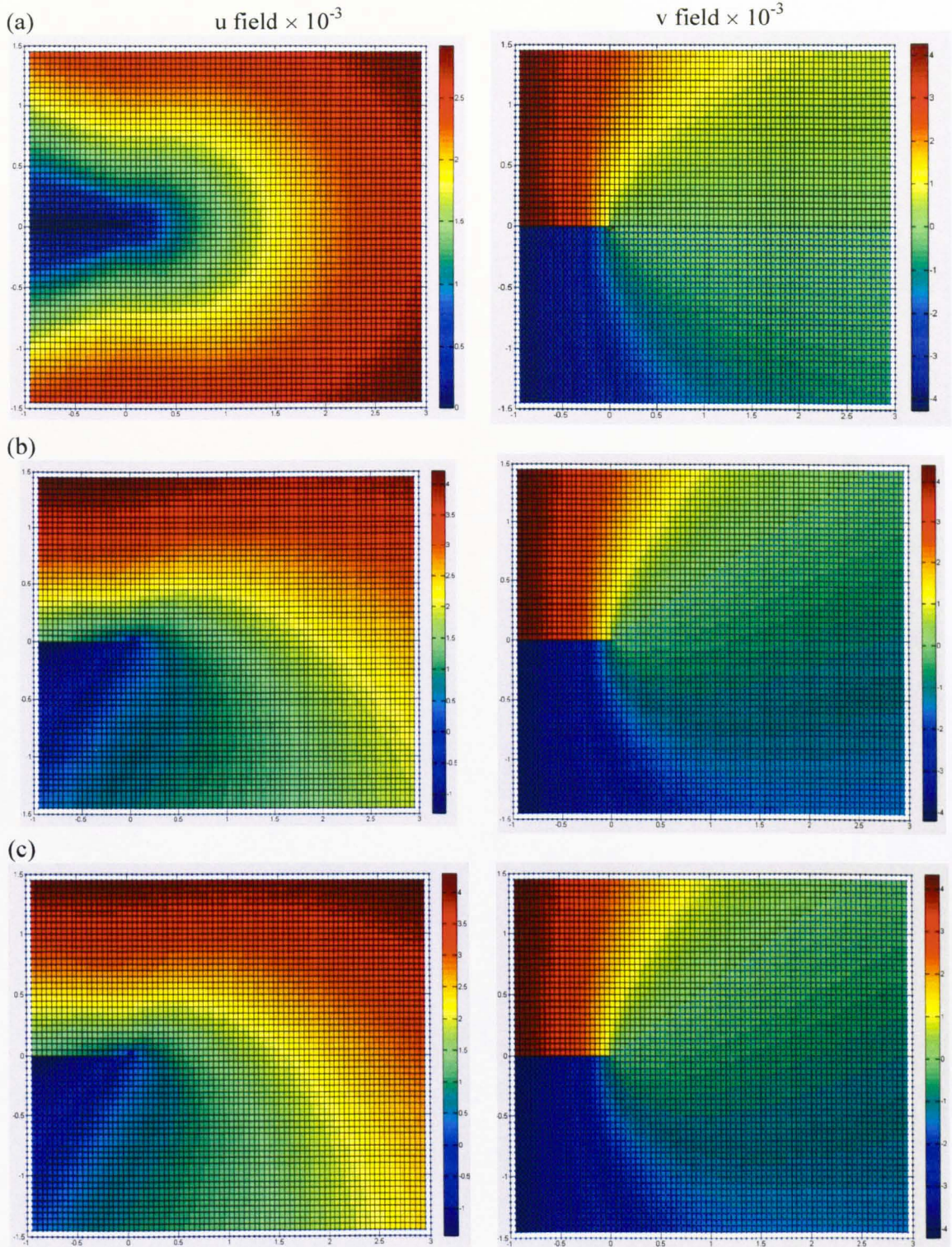


**Figure 5-4** Displacement field  $u$  (left) and  $v$  (right) for (a) case 1, (b) case 2 and (c) case 3 defined in Table 5-1 (all in mm)

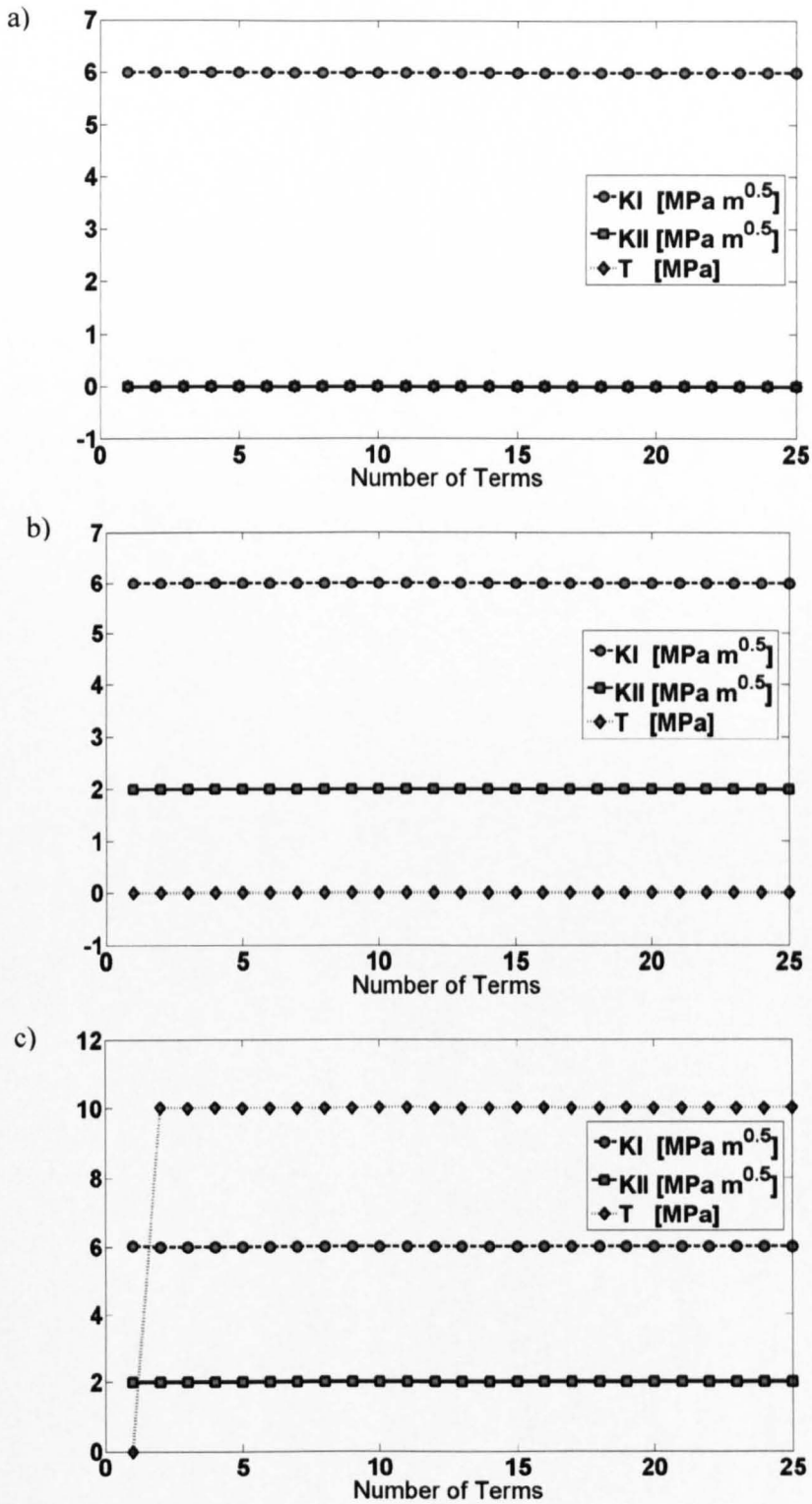


Figure 5-5 Convergence curves for a) case 1, b) case 2 and c) case 3 (see also Table 5-1 and Figure 5-3)

### 5.3.1 Williams' field with noise

To explore the effect of noise on the determined T-stress and SIF, different levels (10% and 30%) of Gaussian noise were uniformly introduced into the artificial data. Different cases have been outlined in Table 5-3.

**Table 5-3 Description of the noise introduced into the different cases**

Case No.	Description	$K_I$ [MPa m <sup>0.5</sup> ]	$K_{II}$ [MPa m <sup>0.5</sup> ]	$T$ [MPa]
1b	Pure mode I 10% noise	6	0	0
1c	Pure mode I 30% noise	6	0	0
2b	Mixed mode I & II 10% noise	6	2	0
2c	Mixed mode I & II 30% noise	6	2	0
3b	General plane stress 10% noise	6	2	10
3c	General plane stress 30% noise	6	2	10

Figure 5-6 shows the displacement distribution for these cases, and Figure 5-7 shows the stress intensity factors and T-stress determined using an increasing number of terms.

From Figure 5-7 both stress intensity factors are not neither sensitive to the number of terms nor to the level of noise introduced. The difference due to the noise introduced is about 1% for the 10% noise case and about 2% for the 30% noise case for mode I stress intensity factors. However, this is different for the T-stress. In the pure mode I case (Figure 5-7 a) and b)), where there is neither a mode II stress intensity factor nor a T-stress, the noise in the data introduces a significant difference in T-stress when the number of terms is increased. However, when a mode II stress intensity factor exists (Figure 5-7 c) and d)) the effect of noise on T-stress is reduced. This might be because of the fact that the parameters close to zero are more sensitive to the noise when they are determined. As it is observed in cases where the T-stress has non-zero value (Figure 5-7 e) and

f)), the calculated T-stress first diverges from the expected value but by increasing the number of terms they almost converge to the expected results (the difference is 3.9% for 10% noise case and 4.5% for 30% noise case).

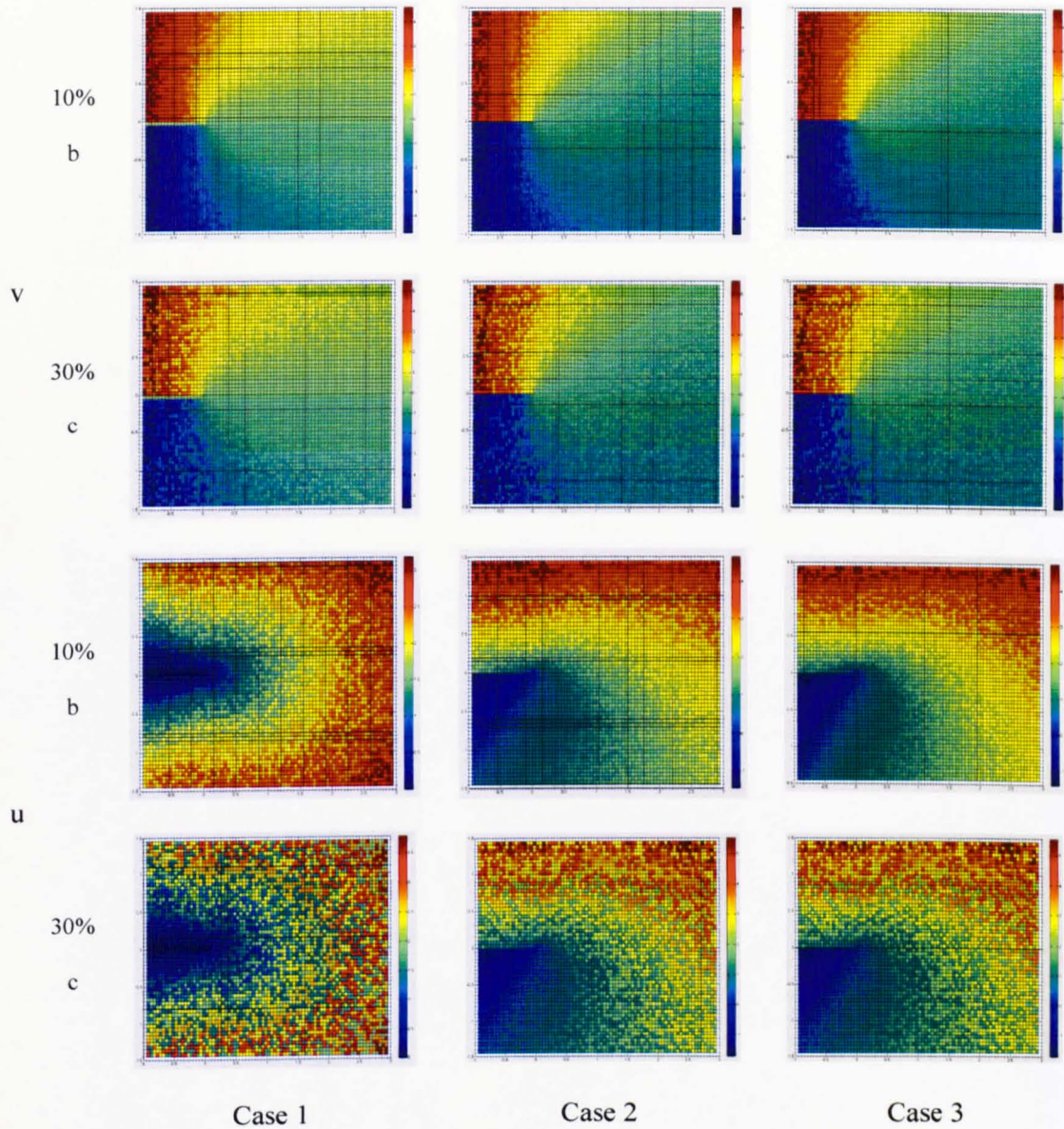


**Figure 5-6** Different levels of noise introduced in vertical displacement field (v) and horizontal displacement field (u) for different cases as mentioned in Table 5-3

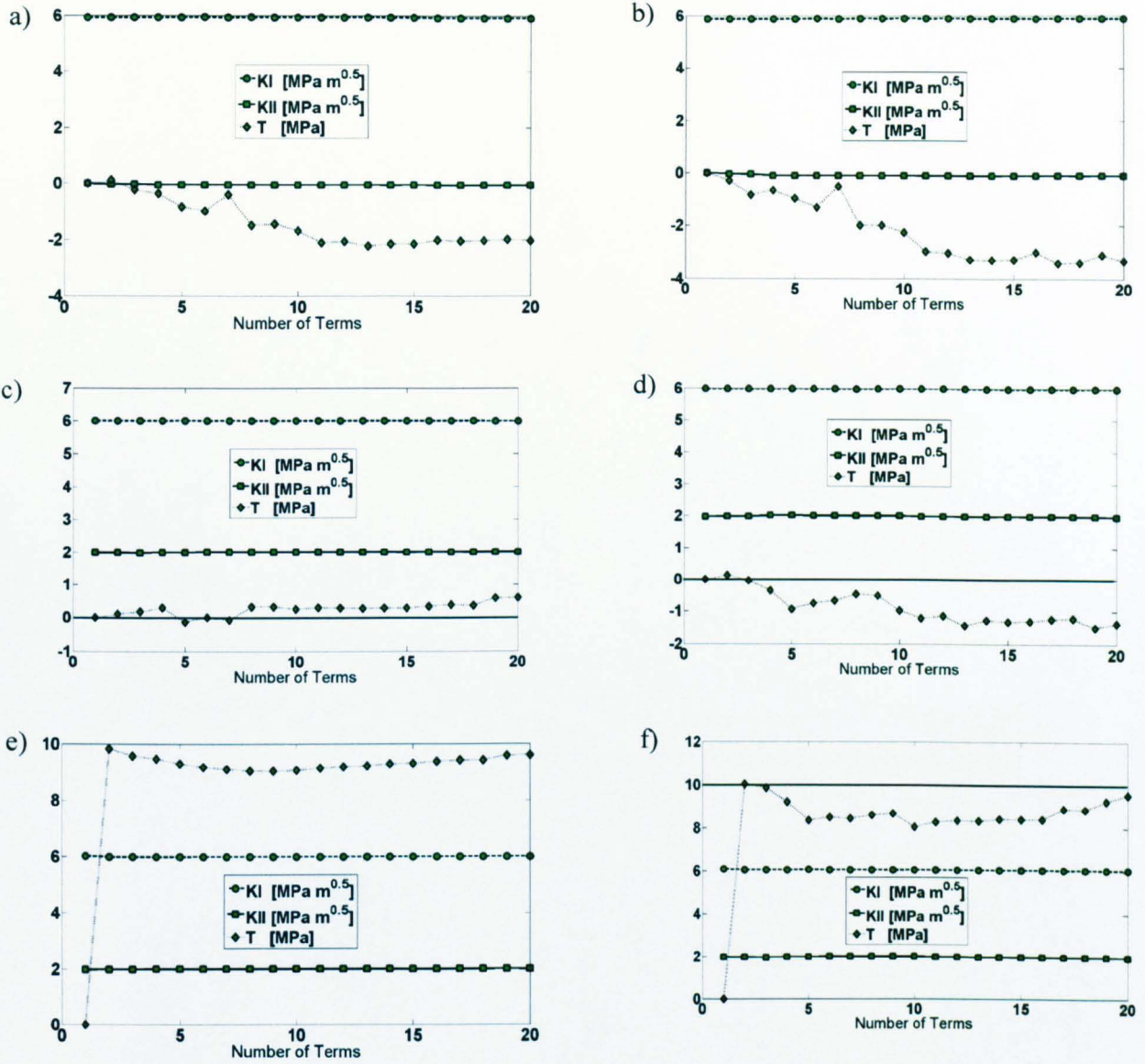


**Figure 5-7** Convergence curve for a) case 1b, b) case 1c, c) case 2b, d) case 2c, e) case 3b and f) case 3c (see Table 5-3 and Figure 5-6 for the data)

By looking at all the artificial cases with or without noise it is revealed that using only two terms of the Williams’ solution is the most accurate and quickest way to determine the T-stress and the SIF. However, this might be only because of the fact that the artificial field is based on only two terms of the Williams’ solution. So, to investigate this matter, a more realistic model for producing the artificial data is needed. This is explored in the next section using a finite element model.

### 5.3.2 Finite element displacement field

To create more realistic artificial data a DCB model was created in ABAQUS as shown in Figure 5-8. The values of  $K_I$ ,  $K_{II}$  and  $T$  gained from the simulation in ABAQUS are shown in Table 5-4. ABAQUS uses the J integral method for stress intensity factor determinations and an interaction integral method to determine the T-stress as discussed in sections 3.4.1.3 and 2.3, respectively. A code was developed to transfer the nodal displacement data from ABAQUS to the Williams' solver.  $K_I$ ,  $K_{II}$  and  $T$  were determined as in the previous 3 case studies and the output of the Williams' solver is shown in Figure 5-9.

**Table 5-4 Values of T-stress and SIF in FE model**

$K_I$ [MPa m <sup>0.5</sup> ]	$K_{II}$ [MPa m <sup>0.5</sup> ]	$T$ [MPa]
6.85	0	27.77

As it is observed from the convergence curve (Figure 5-9) the results are far away from expected results gained from ABAQUS. The  $K_I$ ,  $K_{II}$  and T-stress are about 12.65, 1.392 MPa.m<sup>0.5</sup> and 33.87 MPa, respectively. This is about 85% difference for  $K_I$  and 21% difference for T-stress. Why?

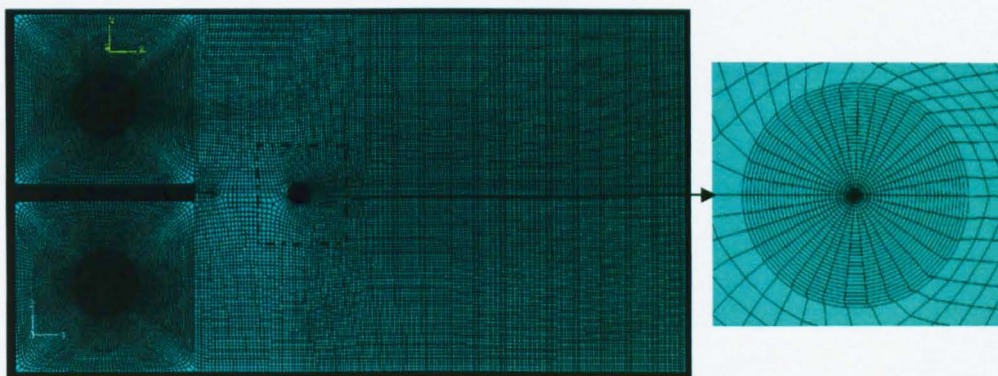


**Figure 5-8 FE model created in ABAQUS**

Since the stress intensity factor determination was accurate for the artificial data, there must be something that happens in ABAQUS but when generating the artificial data generation. The artificial data do not contain any rigid body motion.

However, rigid body motion occurs in FE models as well as in experiments. Looking at equation 5-7 it is evident that no rigid body motion term has been considered in that equation.

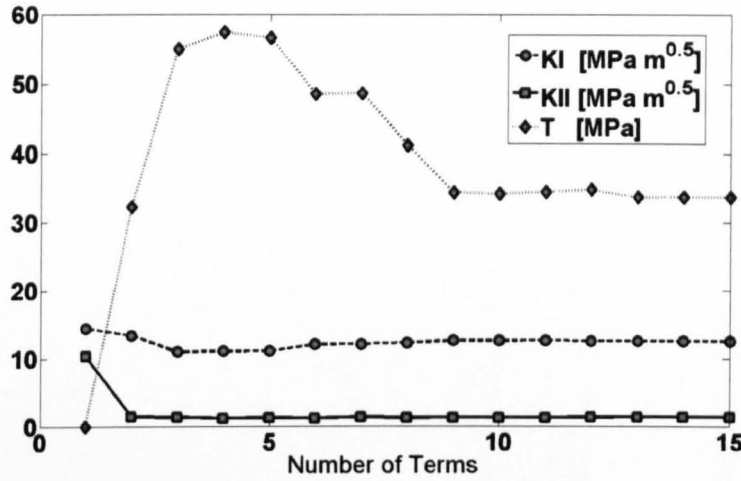


Figure 5-9 Convergence curve from FE data

This can be compensated for by adding constant terms in equation 5-7 to compensate for the rigid body translations and another term to compensate for the rigid body rotation as follows,

$$\begin{Bmatrix} u_1 \\ \vdots \\ u_m \\ v_1 \\ \vdots \\ v_m \end{Bmatrix} = \begin{bmatrix} 1 & f_{1,1} \cdots f_{n,1} & 0 & g_{1,1} \cdots g_{n,1} & -r_1 \sin \theta_1 \\ \vdots & \vdots & \vdots & \vdots & \vdots \\ 1 & f_{1,m} \cdots f_{n,m} & 0 & g_{1,m} \cdots g_{n,m} & -r_m \sin \theta_m \\ 0 & h_{1,1} \cdots h_{n,1} & 1 & l_{1,1} \cdots l_{n,1} & r_1 \sin \theta_1 \\ \vdots & \vdots & \vdots & \vdots & \vdots \\ 0 & h_{1,1} \cdots h_{n,1} & 1 & l_{1,1} \cdots l_{n,1} & r_m \cos \theta_m \end{bmatrix} \begin{Bmatrix} a_0 \\ a_1 \\ \vdots \\ a_n \\ b_0 \\ b_1 \\ \vdots \\ b_n \\ R \end{Bmatrix} \quad 5-19$$

where  $a_o$  and  $b_o$  are used to compensate for the rigid body motion and  $R$  compensates for the rigid body rotation. Solving the modified equation (equation 5-19) for ABAQUS data yields Figure 5-10 for the solution of the stress intensity factors and T-stress using Williams' approach.

Compensating for the rigid body motion improves the results significantly.  $K_I$ ,  $K_{II}$  and T-stress were found as 6.72, 0.09 MPa.m<sup>0.5</sup> and 27.49 MPa, respectively,

which is less than 2% difference for  $K_I$  and 1% difference for the determined T-stress. It is worth mentioning that rigid body rotation does not significantly affect the results specifically for the T-stress and the mode I stress intensity factor. Since in some pure mode I cases, the mode II results became more sensitive when the rigid body rotation was used, it is recommended that in pure mode I cases the rigid body rotation term is ignored.

Another point which is evident from Figure 5-10 is that using only two terms of the Williams expansion can make 21% difference in the determined  $K_I$  and 67% difference in the determined T-stress. Therefore, it is concluded that although the two terms approach works in artificial data but it is not sufficient for more realistic artificial data (FE data) and perhaps experimental data. So, using more terms of the Williams' expansion is recommended. Like the TSA data, another alternative is using three terms of the Williams' solution. By looking at all the previous analyses, the values of both T-stress and stress intensity factors obtained based on a 3 terms solution look promising. Although they are less accurate for T-stress in FEM data (Figure 5-10), they are less sensitive to the noise (see Figure 5-7) and more economical in processing time.

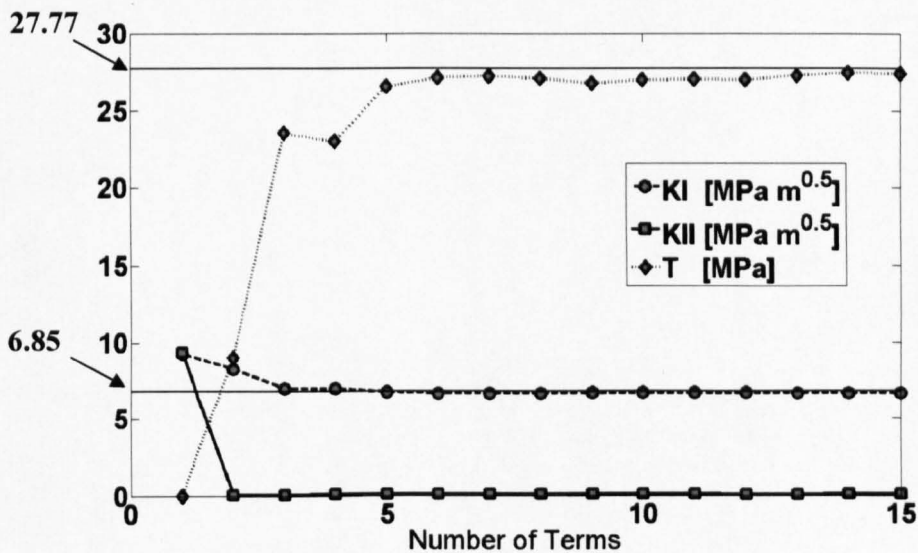


Figure 5-10 Convergence curves for FE data; compensated for rigid body motion

So far the location of the crack tip was given. However, in experiments there might be some differences between the real crack tip position and the crack tip that we assume in the algorithm. This matter is explored in the next section.

### 5.3.3 Sensitivity to the crack tip position

When locating the crack tip position in the experiments, a few pixels error may occur. To study the effect of crack tip position on T-stress and SIF results, the FE model used in section 5.3.2 (a DCB model with the stress intensity factors and the T-stress as mentioned in Table 5-4) was used as the case study. The crack tip was moved  $\pm 1$  mm in both vertical and horizontal directions and the T-stress and the stress intensity factors were calculated using the 3 terms of Williams' solution described previously ( $W_3$  as in Figure 5-11 and Figure 5-12) and the converged value ( $W_{conv}$  as in Figure 5-11 and Figure 5-12). Results are shown in Figure 5-11 and Figure 5-12.

It is observed that underestimation of the crack tip slightly increases the mode I stress intensity factor but decreases the T-stress. However, overestimation has an inverse effect. It is also observed that the mode I stress intensity factor and T-stress are more sensitive to horizontal uncertainties but mode II stress intensity factor is more affected by vertical uncertainties.  $\pm 1$  mm can introduce approximately 18% and 16% difference in  $K_I$  values and 30% and 11% difference in T-stress using converged values and 3 terms solution, respectively. However, it should be mentioned that the minimum resolution of images used in the experiments is 18.75 microns per pixel. Therefore,  $\pm 1$  mm is at least  $\pm 50$  pixel. Such an error in locating the crack tip in this resolution is unlikely to happen and can be considered as an extreme case.

Although the error in the stress intensity factors will be small if the crack tip location is mis-estimated by a few pixels, it is obviously best practise to determine the location as accurately as possible.

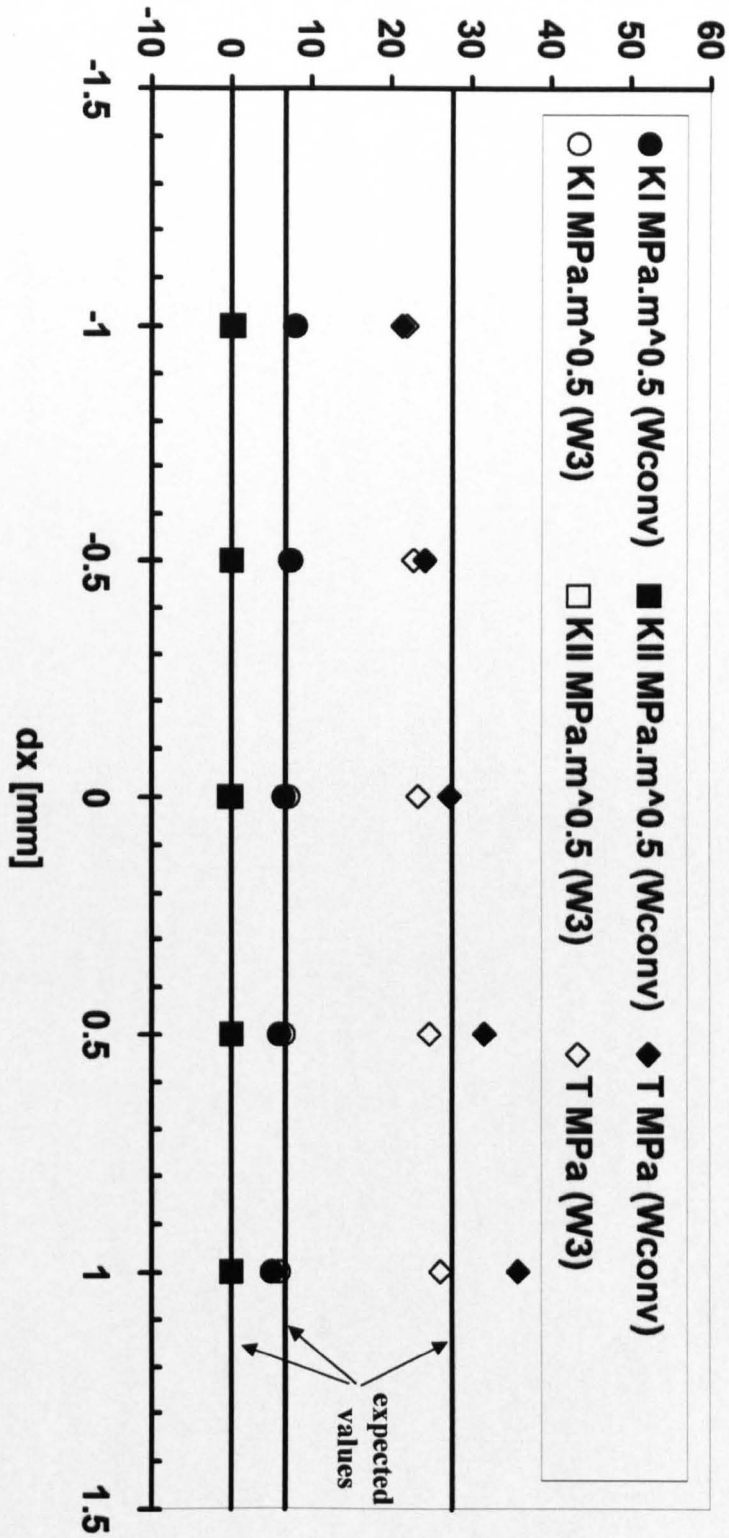


Figure 5-11 Effect of uncertainty in the horizontal crack tip position

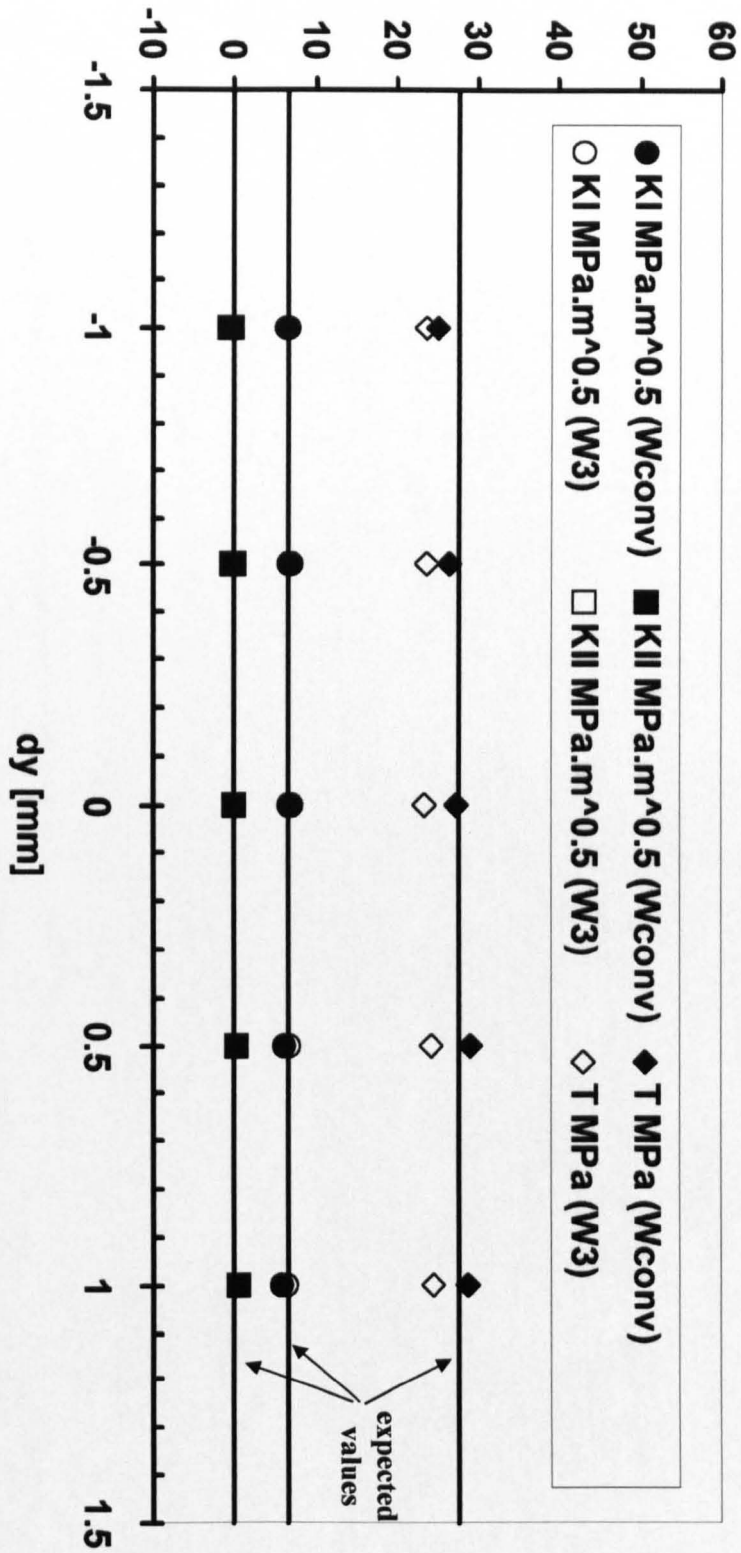


Figure 5-12 Effect of uncertainty in the vertical crack tip position

There are a few techniques to estimate the crack tip position. Edge finding algorithms such as those of Sobel, Prewitt & Robert [122] which are usually used in photography and image processing applications, are an option which have also been used in image correlation and crack finding problems [99, 130]. Since on the edges of an object the gradient of change in light intensity (or displacement in image correlation applications) is high, these techniques are based on finding the maximum gradient of intensity of the studied field. Due to the fact that finding the gradient of a field process is always affected by the noise available in the field, these techniques need filtering and smoothing which in return affects the accuracy of the results. Figure 5-13 is an example of using the Sobel algorithm. As it is observed from Figure 5-13 when a filter (for example median filter) is used the output of the algorithm is totally different from the image where no filtering has been applied. It is evident from Figure 5-13(a) that the crack is not distinct from the other part of the image. This makes using the filtering essential in this algorithm. The threshold value is another parameter in the Sobel technique that can affect the length of the crack found. As it is observed in Figure 5-13(c) and (d) different threshold values can result in different crack lengths (as surrounded by an oval in the figures).

It has also been reported that the edge finding algorithms can yield different results if horizontal or vertical displacement fields are used to find the edge [99]. Moreover, these techniques are not applicable to stress intensity factor ranges of less than  $3 \text{ MPa}\sqrt{\text{m}}$  [99].

An alternative to edge finding algorithms, is to consider the crack tip coordinates as two unknowns in the equations. However, using this approach makes the governing equations (equations 5-4 and 5-5) non-linear and a non-linear solution algorithm must be used to solve the equations. Therefore the non-linear iterative Newton-Raphson technique was implemented to solve the equations making the crack tip coordinates unknown as will be explained in the next section.



**Figure 5-13** Effects of filtering and threshold value on crack length a) no filter b) Median filter c) Median filter and 0.003 as the threshold value d) Median filter and 0.15 as the threshold value

## 5.4 Crack tip positioning and the Newton-Raphson method

The objective of this section is to introducing the crack tip coordinates as two unknowns ( $x_0$  and  $y_0$ ) into the Williams' equations (equations 5-4 and 5-5) and find these coordinates as well as the T-stress and the stress intensity factors using the DIC displacement data.

Let us define  $p_x$  and  $p_y$  as the residual of determined displacement field using rigid body motion compensated Williams' solution ( $u_d$  and  $v_d$ ) and the experimental displacement field gained from DIC ( $u_e$  and  $v_e$ ) as,

$$\begin{aligned} p_x &= u_d - u_e \\ p_y &= v_d - v_e \end{aligned} \quad 5-20$$

where the determined displacement fields are defined as follows.

$$\begin{aligned} u_d &= \sum_{n=1}^{\infty} \frac{r^{\frac{n}{2}}}{2\mu} a_n \left\{ \left[ \kappa + \frac{n}{2} + (-1)^n \right] \cos \frac{n\theta}{2} - \frac{n}{2} \cos \frac{(n-4)\theta}{2} \right\} \\ &\quad - \sum_{n=1}^{\infty} \frac{r^{\frac{n}{2}}}{2\mu} b_n \left\{ \left[ \kappa + \frac{n}{2} - (-1)^n \right] \sin \frac{n\theta}{2} - \frac{n}{2} \sin \frac{(n-4)\theta}{2} \right\} \\ &\quad + a_0 - Ry \end{aligned} \quad 5-21$$

$$\begin{aligned} v_d &= \sum_{n=1}^{\infty} \frac{r^{\frac{n}{2}}}{2\mu} a_n \left\{ \left[ \kappa - \frac{n}{2} - (-1)^n \right] \sin \frac{n\theta}{2} + \frac{n}{2} \sin \frac{(n-4)\theta}{2} \right\} \\ &\quad + \sum_{n=1}^{\infty} \frac{r^{\frac{n}{2}}}{2\mu} b_n \left\{ \left[ \kappa - \frac{n}{2} + (-1)^n \right] \cos \frac{n\theta}{2} + \frac{n}{2} \cos \frac{(n-4)\theta}{2} \right\} \\ &\quad + b_0 + Rx \end{aligned} \quad 5-22$$

in which

$$r = \sqrt{(x - x_0)^2 + (y - y_0)^2} \quad \text{and} \quad \theta = \tan^{-1} \frac{y - y_0}{x - x_0} \quad 5-23$$

where  $x_0$  and  $y_0$  are the crack tip positions. Therefore,  $p_x$  and  $p_y$  are functions of a series of unknowns consisting of crack tip position, rigid body motion and Williams' coefficients. Applying the Taylor expansion to  $p_x$  and  $p_y$  yields,

$$\begin{aligned} (p_x)_{i+1} &= (p_x)_i \\ &\quad + \sum_{k=0}^n \left[ \left( \frac{\partial p_x}{\partial a_k} \right)_i \Delta a_k + \left( \frac{\partial p_x}{\partial b_k} \right)_i \Delta b_k \right] + \left( \frac{\partial p_x}{\partial x_0} \right)_i \Delta x_0 + \left( \frac{\partial p_x}{\partial y_0} \right)_i \Delta y_0 + \left( \frac{\partial p_x}{\partial R} \right)_i \Delta R \end{aligned} \quad 5-24$$

$$\begin{aligned} (p_y)_{i+1} &= (p_y)_i \\ &\quad + \sum_{k=0}^n \left[ \left( \frac{\partial p_y}{\partial a_k} \right)_i \Delta a_k + \left( \frac{\partial p_y}{\partial b_k} \right)_i \Delta b_k \right] + \left( \frac{\partial p_y}{\partial x_0} \right)_i \Delta x_0 + \left( \frac{\partial p_y}{\partial y_0} \right)_i \Delta y_0 + \left( \frac{\partial p_y}{\partial R} \right)_i \Delta R \end{aligned} \quad 5-25$$

where  $i$  represents the iteration number. Ideally we should have  $(p_x)_{i+1} = 0$  and  $(p_y)_{i+1} = 0$ . Therefore, we will have,

$$-p = q\Delta \quad 5-26$$

where,

$$q = \begin{bmatrix} \frac{\partial p_{x,1}}{\partial a_0} & \dots & \frac{\partial p_{x,1}}{\partial a_n} & \frac{\partial p_{x,1}}{\partial b_0} & \dots & \frac{\partial p_{x,1}}{\partial b_n} & \frac{\partial p_{x,1}}{\partial R} & \frac{\partial p_{x,1}}{\partial x_0} & \frac{\partial p_{x,1}}{\partial y_0} \\ \vdots & & \vdots & \vdots & & \vdots & \vdots & \vdots & \vdots \\ \frac{\partial p_{x,m}}{\partial a_0} & \dots & \frac{\partial p_{x,m}}{\partial a_n} & \frac{\partial p_{x,m}}{\partial b_0} & \dots & \frac{\partial p_{x,m}}{\partial b_n} & \frac{\partial p_{x,m}}{\partial R} & \frac{\partial p_{x,m}}{\partial x_0} & \frac{\partial p_{x,m}}{\partial y_0} \\ \frac{\partial p_{y,1}}{\partial a_0} & \dots & \frac{\partial p_{y,1}}{\partial a_n} & \frac{\partial p_{y,1}}{\partial b_0} & \dots & \frac{\partial p_{y,1}}{\partial b_n} & \frac{\partial p_{y,1}}{\partial R} & \frac{\partial p_{y,1}}{\partial x_0} & \frac{\partial p_{y,1}}{\partial y_0} \\ \vdots & & \vdots & \vdots & & \vdots & \vdots & \vdots & \vdots \\ \frac{\partial p_{y,m}}{\partial a_0} & \dots & \frac{\partial p_{y,m}}{\partial a_n} & \frac{\partial p_{y,m}}{\partial b_0} & \dots & \frac{\partial p_{y,m}}{\partial b_n} & \frac{\partial p_{y,m}}{\partial R} & \frac{\partial p_{y,m}}{\partial x_0} & \frac{\partial p_{y,m}}{\partial y_0} \end{bmatrix} \quad 5-27$$

and,

$$\frac{\partial p_x}{\partial a_0} = 1, \quad \frac{\partial p_x}{\partial b_0} = 0, \quad \frac{\partial p_x}{\partial R} = -r \sin \theta, \quad \frac{\partial p_y}{\partial a_0} = 0, \quad \frac{\partial p_y}{\partial b_0} = 1, \quad \frac{\partial p_y}{\partial R} = r \cos \theta \quad 5-28$$

$$\frac{\partial p_x}{\partial a_{n \neq 0}} = f_n, \quad \frac{\partial p_x}{\partial b_{n \neq 0}} = g_n, \quad \frac{\partial p_y}{\partial a_{n \neq 0}} = h_n, \quad \frac{\partial p_y}{\partial b_{n \neq 0}} = l_n$$

$$\begin{aligned} \frac{\partial p_x}{\partial x_0} &= \sum_{n=1}^{\infty} \frac{a_n}{2r^2} n(x_0 - x) \left( \frac{\partial p_x}{\partial a_n} + \frac{\partial p_x}{\partial b_n} \right) \\ &+ \sum_{n=1}^{\infty} \frac{a_n}{4\mu} r^{\frac{n-4}{2}} n(y - y_0) \left\{ - \left[ \kappa + \frac{n}{2} + (-1)^n \right] \sin \frac{n\theta}{2} + \left( \frac{n-4}{2} \right) \sin \frac{(n-4)\theta}{2} \right\} \\ &- \sum_{n=1}^{\infty} \frac{b_n}{4\mu} r^{\frac{n-4}{2}} n(y - y_0) \left\{ + \left[ \kappa + \frac{n}{2} - (-1)^n \right] \cos \frac{n\theta}{2} - \left( \frac{n-4}{2} \right) \cos \frac{(n-4)\theta}{2} \right\} \quad 5-29 \\ \frac{\partial p_x}{\partial y_0} &= \sum_{n=1}^{\infty} \frac{a_n}{2r^2} n(y_0 - y) \left( \frac{\partial p_x}{\partial a_n} + \frac{\partial p_x}{\partial b_n} \right) \\ &+ \sum_{n=1}^{\infty} \frac{a_n}{4\mu} r^{\frac{n-4}{2}} n \left\{ + \left[ \kappa + \frac{n}{2} + (-1)^n \right] \sin \frac{n\theta}{2} - \left( \frac{n-4}{2} \right) \sin \frac{(n-4)\theta}{2} \right\} \\ &- \sum_{n=1}^{\infty} \frac{b_n}{4\mu} r^{\frac{n-4}{2}} n \left\{ - \left[ \kappa + \frac{n}{2} - (-1)^n \right] \cos \frac{n\theta}{2} + \left( \frac{n-4}{2} \right) \cos \frac{(n-4)\theta}{2} \right\} + R \end{aligned}$$

$$\begin{aligned}
\frac{\partial p_y}{\partial x_0} &= \sum_{n=1}^{\infty} \frac{a_n}{2r^2} n(x_0 - x) \left( \frac{\partial p_y}{\partial a_n} + \frac{\partial p_y}{\partial b_n} \right) \\
&+ \sum_{n=1}^{\infty} \frac{a_n}{4\mu} r^{\frac{n-4}{2}} n(y - y_0) \left\{ + \left[ \kappa - \frac{n}{2} - (-1)^n \right] \cos \frac{n\theta}{2} + \left( \frac{n-4}{2} \right) \cos \frac{(n-4)\theta}{2} \right\} \\
&+ \sum_{n=1}^{\infty} \frac{b_n}{4\mu} r^{\frac{n-4}{2}} n(y - y_0) \left\{ - \left[ \kappa - \frac{n}{2} + (-1)^n \right] \sin \frac{n\theta}{2} - \left( \frac{n-4}{2} \right) \sin \frac{(n-4)\theta}{2} \right\} - R \\
\frac{\partial p_y}{\partial y_0} &= \sum_{n=1}^{\infty} \frac{a_n}{2r^2} n(y_0 - y) \left( \frac{\partial p_y}{\partial a_n} + \frac{\partial p_y}{\partial b_n} \right) \\
&+ \sum_{n=1}^{\infty} \frac{a_n}{4\mu} r^{\frac{n-4}{2}} n \left\{ - \left[ \kappa - \frac{n}{2} - (-1)^n \right] \cos \frac{n\theta}{2} - \left( \frac{n-4}{2} \right) \cos \frac{(n-4)\theta}{2} \right\} \\
&+ \sum_{n=1}^{\infty} \frac{b_n}{4\mu} r^{\frac{n-4}{2}} n \left\{ + \left[ \kappa - \frac{n}{2} + (-1)^n \right] \sin \frac{n\theta}{2} + \left( \frac{n-4}{2} \right) \sin \frac{(n-4)\theta}{2} \right\}
\end{aligned} \tag{5-30}$$

where  $f$ ,  $g$ ,  $h$ , and,  $l$  are defined in equation 5-6.

In the next section a series of experiments have been conducted to assess the feasibility of these methodologies to determine the T-stress and stress intensity factor from experimental DIC data.

## 5.5 Interface

All the previously mentioned approaches were implemented in a MATLAB based interface (DICITAC) as shown in Figure 5-14. This interface consists of a graphical panel on the right hand side and a control panel on the left hand side to set various parameters needed to determine the stress intensity factors and the T-stress. The control panel is shown in detail in Figure 5-15.

The control panel consists of different sections which will briefly be explained here. By pressing the 'Browse...' button the output the DIC is imported to the interface. The recognisable format for this interface is the ASCII format. It should be noted that the output of DIC (using DaVis software) is in millimetres and this also has been considered in the interface and there is no need to convert the DIC files to metres. The Graphical Control Panel controls the imported file graphically. Both vertical and horizontal displacements can be zoomed, rotated and panned. The next step is selecting the data points. This can be done by selecting and removing the data using the 'Data point selection' panel. Material

properties can be defined in the 'Material properties' section and the crack tip position can be set in the 'Crack tip position' section by entering the crack tip position manually or using the gradient of the displacement fields. As a complement the Newton-Raphson method (described in section 5.4) can also be used to determine the crack tip coordinates.

In the 'Muskhelishvili Approach' section, the mapping parameters and the solution parameters as explained in section 5.2.2 can be adjusted and by pressing the 'Solve' button the corresponding stress intensity factors are determined. In the 'Williams Approach' section, by setting the number of terms, the stress intensity factors and the T-stress are determined and displayed in the listbox. A convergence curve and two other graphs are also shown to check the fitness quality of the data. It should be noted that the fitness quality graphs are only shown if both vertical and horizontal displacements are chosen.

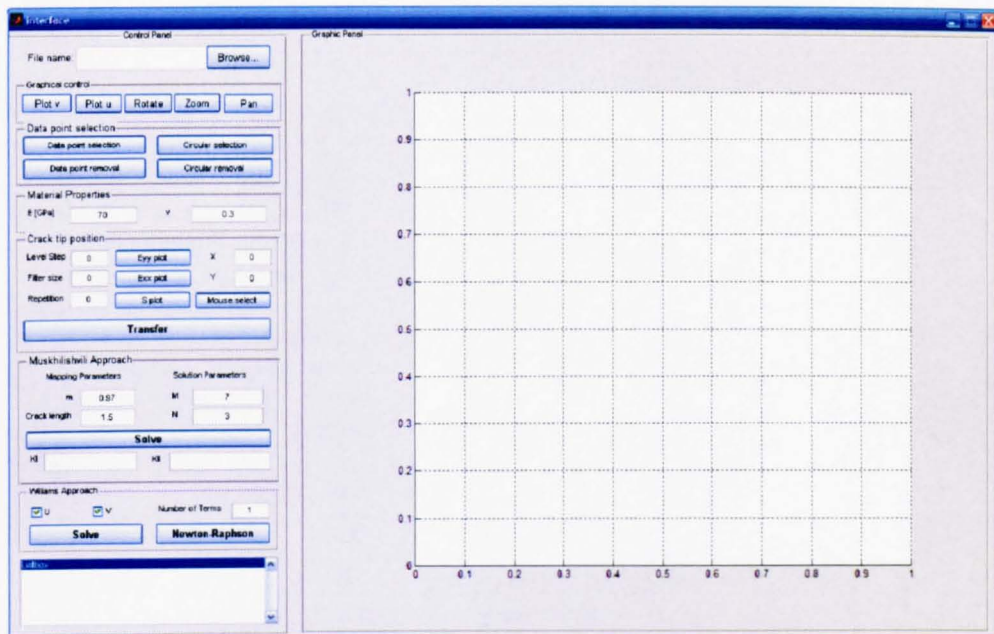


Figure 5-14 Graphical interface (see Figure 5-15 for details)

Control Panel

File name:

Graphical control

Data point selection

Material Properties

E [GPa]   $\nu$

Crack tip position

Level Step   X

Filter size   Y

Repetition

Muskhilishvili Approach

Mapping Parameters		Solution Parameters	
m	<input type="text" value="0.97"/>	M	<input type="text" value="7"/>
Crack length	<input type="text" value="1.5"/>	N	<input type="text" value="3"/>

KI  KII

Williams Approach

U  V Number of Terms

Listbox

Figure 5-15 Control panel of the graphical interface

## 5.6 Experimental results and discussion

Experiments were undertaken on both sharp notches and fatigue cracks emanating from notches. In the first stage, pure mode I loading conditions were created ahead of a 4mm notch in a 5mm thick DCB specimen with the dimensions shown in Figure 5-16.

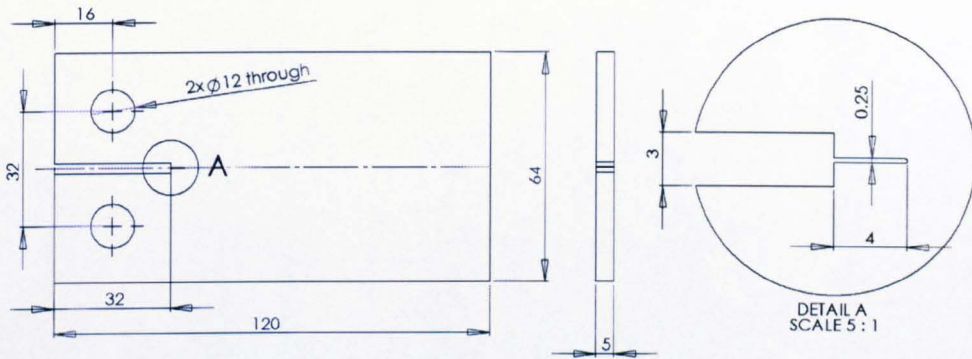
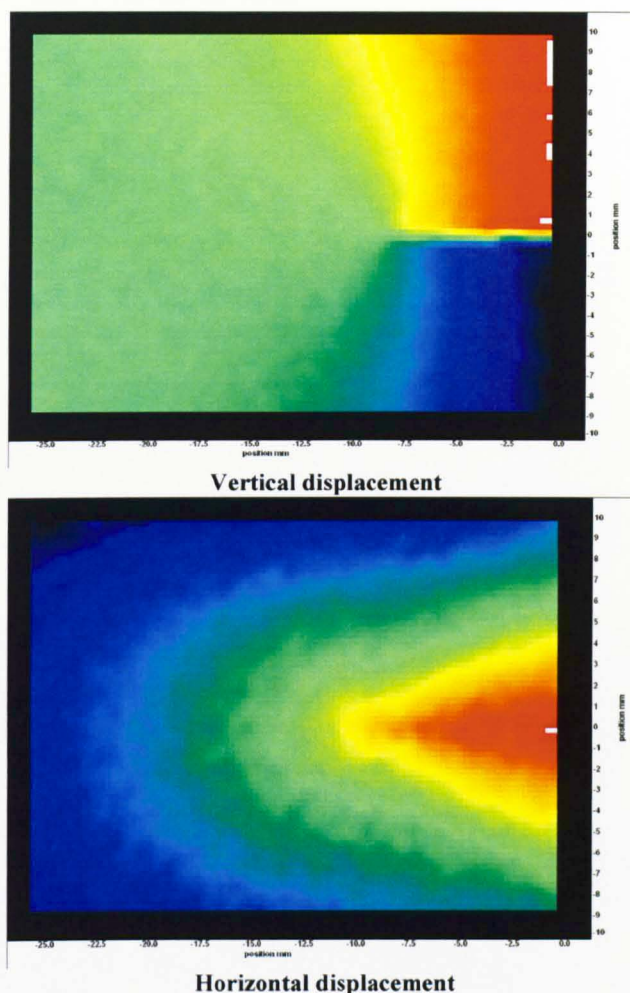


Figure 5-16 DCB specimen dimensions in mm

The specimen was machined from a plate of 7010 T7651 aluminium alloy and spark eroded to introduce the notch into the specimen. The required speckles for DIC were produced on the surface of specimen using a fine spray of black paint. A 100kN MAND hydraulic test machine was used to load the specimen. Two load ranges of 0.5kN to 1.5kN and 0.5kN to 3kN were applied to the specimen. A 14 bit, 1600x1200 CCD camera and a Nikon lens with a resolution of 18.75 microns per pixel was used to record the images. DaVis software [130] was employed to correlate the images. The software was set up to use a 64x64 pixels interrogation window, followed by two iterations using a 32x32 pixels interrogation window with 50% overlap. Figure 5-17 shows a typical correlated displacement field obtained around a crack.

The experiments were continued by growing a fatigue crack from the notch tip, using a 0.5kN to 2kN load range with 15Hz loading frequency. The crack growth was paused when the fatigue crack length was approximately 1mm, 4mm, 8mm and 15mm. For each increment of crack growth load ranges of 0.5kN to 1.5kN

and 0.5kN to 3kN were applied, images were recorded at each load and processed to determine the stress intensity factors and T-stress.



**Figure 5-17** Typical correlated displacement fields obtained around a crack using DIC

The displacement field obtained from DIC was imported to the DICITAC software to determine the stress intensity factors and the T-stress using equations 5-19 and 5-8 under plane stress conditions. In the solution process of equation 5-19, the number of terms was increased until the stress intensity factors and the T-stress converged as shown in Figure 5-18 to Figure 5-21. No change in the first decimal place of the results was usually used as the convergence criterion. These figures also show the quality of the fitted data to the experimental displacement fields. As it was mentioned before (section 5.2) to extract the stress intensity

factors, T-stress or any other parameter from experimental data a mathematical description of the field is needed. This mathematical description should be fitted to the experimental data and the required parameters are determined. The fitted data shown in Figure 5-18(a) and (b) to Figure 5-21(a) and (b) are based on the recreation of the displacement fields using the coefficients of 15 terms of Williams' solution.

Looking at Figure 5-18(c) to Figure 5-21(c) it is observed that the stress intensity factors for both mode I and mode II (which is practically zero in this type of specimen) are almost converged at the 3<sup>rd</sup> term and using more terms of the Williams' solution does not significantly improve the results. However, the T-stress does not always converge in the 3<sup>rd</sup> term. When the fatigue crack length is shorter, as shown in Figure 5-18(c) and Figure 5-19(c), there is a considerable difference between the 3<sup>rd</sup> term and final converged T-stresses. However, as the fatigue crack grows (see Figure 5-20(c) and Figure 5-21(c)) the difference between the T-stress at the 3<sup>rd</sup> term and the converged value decreases. For example in case of 8mm fatigue crack (Figure 5-20(c)) and 15mm fatigue crack (Figure 5-21(c)) the T-stress values are almost converged by the 3<sup>rd</sup> term. This is because of the fact that theoretically the displacement field ahead of a notch is slightly different from a crack and apparently three terms of Williams' solution are not capable of describing the correct form of the displacement field. However, a solution with more terms can better describe the displacement field.

The Newton-Raphson method was also used to determine the crack tip position, T-stress and stress intensity factors. In such a way that the results of the Williams' solution were used as the initial values for the Newton-Raphson algorithm as described before in section 5.4 and the position of the crack tip, the stress intensity factors and the T-stress were considered as unknowns in the algorithm. Therefore the change in the crack tip position (as shown in Table 5-5) and the stress intensity factors and the T-stress were determined as the output of the Newton-Raphson algorithm. Results are compared with other results gained from Williams' solution and ABAQUS simulations in Figure 5-22 and Figure 5-23.

As it is observed from Figure 5-22 and Figure 5-23, although the values found for the mode II stress intensity factors using the 3 terms solution are slightly better than the others, using any of the solutions yields practically zero values for mode II stress intensity factors in both the 0.5 to 1.5 kN and 0.5 to 3 kN load ranges.

**Table 5-5 Change in crack tip position using Newton-Raphson method**

Fatigue Crack Length [mm]	0.5 to 1.5 kN case		0.5 to 3 kN case	
	$\Delta x_o$	$\Delta y_o$	$\Delta x_o$	$\Delta y_o$
0	0.3362	-0.0004	0.0511	0
1	-0.6455	-0.0001	0.0852	-0.0001
4	0.3996	0	-	-
8	0.1162	0.0003	0.713	-0.001
15	0.6988	0.0003	0.1894	0.0002

In 0.5 to 1.5 kN load range, Figure 5-22(a), the mode I stress intensity factors determined using any of the aforementioned solutions are in a reasonable agreement with the numerically simulated cases. The average differences found are 12.6% (with standard deviation of 8.8%) using the 3 terms solution, 12.9% (with standard deviation of 11.5%) using the converged term solution (15 terms solution) and 7.4% (with standard deviation of 4.4%) using Newton-Raphson method. This shows that a slight improvement may be obtained using the Newton-Raphson method compared to the other two solutions. It should also be mentioned that the more the fatigue crack grows the better is the agreement, which shows that the mathematical model is more appropriate in the fatigue crack cases studied.

Part of the difference in the experimental results compared to FE results is due to the errors introduced into the correlated displacement field because of a low signal to noise ratio. Looking at Figure 5-23(a) in which the load range has increased from 0.5 to 3 kN the average difference decreased to 12.1% (with standard deviation of 6.2%) using the 3 terms solution, 12.9% (with standard deviation of 6.9%) using the converged term solution and 4.4% (with standard deviation of 4.5%) using Newton-Raphson method. In all the above solutions both vertical and horizontal displacement fields were used simultaneously as mentioned in section 5.2.

Since some other authors [90, 93], as mentioned in the literature review, have only used the vertical displacement field in a pure mode I case, this matter was also investigated. For the 0.5 to 1.5 kN load range case, a comparison has been made

(Figure 5-24(a)) between the results obtained using only vertical displacement field ( $v$ ) and using both horizontal and vertical displacement fields ( $u$  and  $v$ ). It was found that the determined mode I stress intensity factors are less accurate compared to the cases where both vertical and horizontal displacement fields are used especially when more terms in Williams' solution are used.

Almost the same trend as the mode I stress intensity factors is observed for the determined T-stresses when compared to the FE results. The average differences percentage of 24.9% (with standard deviation of 2.2%), 35.4% (with standard deviation of 14.9%) and 24.6% (with standard deviation of 22.1%) were found using 3 terms, converged term and Newton-Raphson solutions, respectively for 0.5 to 1.5 kN load range. Both 3 terms solution and Newton-Raphson results show smaller differences than the 15 terms solution when compared with FE results. Although the 3 terms solutions average differences are slightly higher than the Newton-Raphson, it seems more consistent (lower standard deviation) in different cases. In 0.5 to 3 kN load range case, the average differences were found as to be 14.4% (with standard deviation of 8.9%), 36.0% (with standard deviation of 27.4%) and 24.9% (with standard deviation of 23.2%) using the 3 terms, converged term and Newton-Raphson solutions, respectively. In the same way as mode I stress intensity factors, increasing the load range to 0.5 to 3 kN (reducing the signal to noise ratio) improves the results for the 3 terms solution but it does not change the 15 terms and Newton-Raphson results significantly. That is true that the results obtained for the T-stress are not as accurate as the stress intensity factor results. This is basically due to the nature of the T-stress. Compared to the stress intensity factor the T-stress is one order higher and this makes the T-stress relatively a more difficult parameter to measure experimentally. However, the accuracy obtained from the aforementioned methodology seems very promising when it is compared with for example 100% errors reported by other authors [102].

It is worth mentioning that unlike mode I stress intensity factors, using only the vertical displacement field as shown in Figure 5-24(b) introduces significant error (average difference of 75% with 121% standard deviation using the 3 terms solution for instance) in T-stress calculations for the 0.5 to 1.5 kN load range.

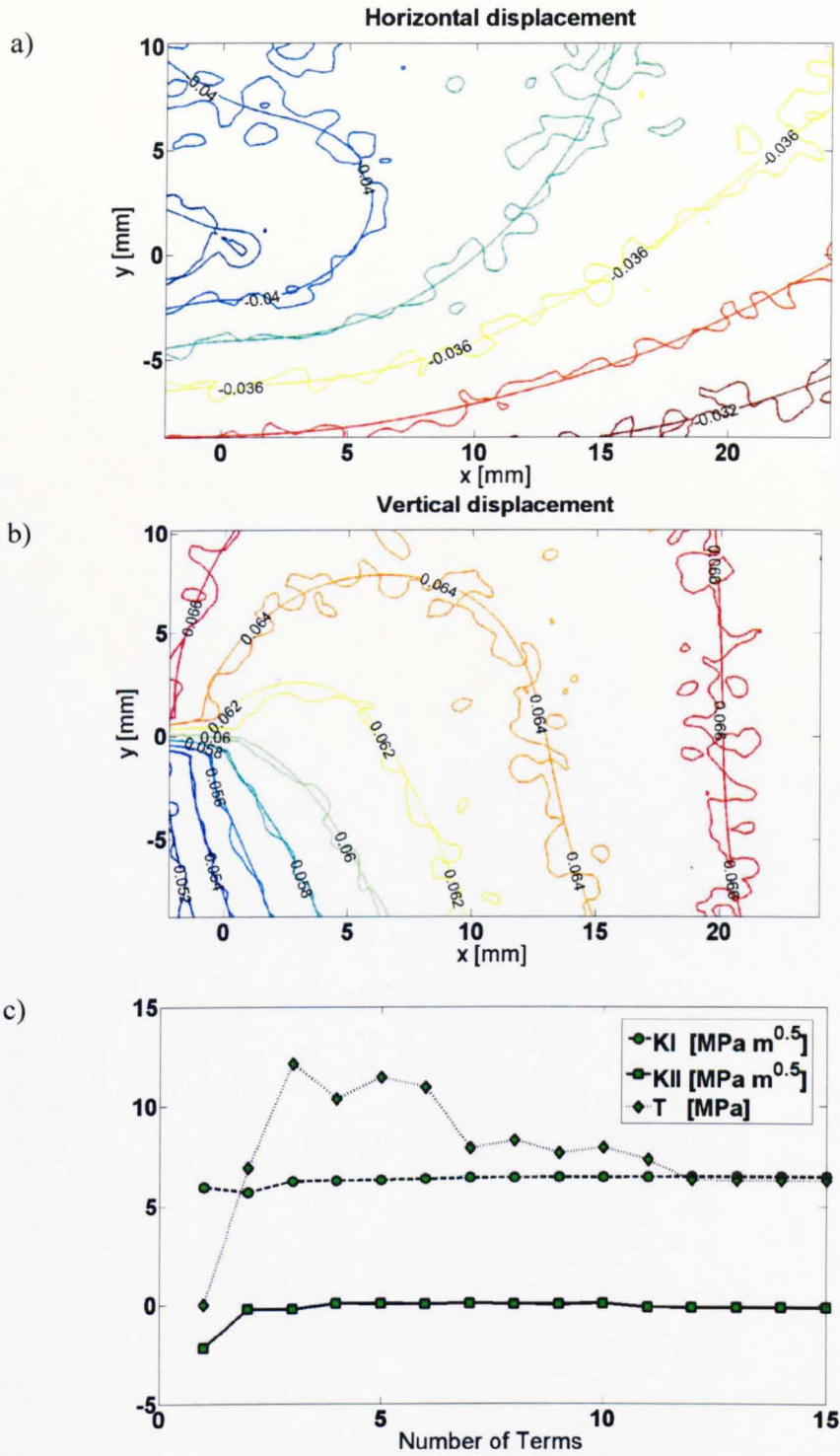


Figure 5-18 Quality of fitted displacement field a) Horizontal and b) Vertical and c) variation of T-stress and SIF versus number of Williams' solution terms for the 1mm fatigue crack under 0.5 to 1.5 kN loading condition

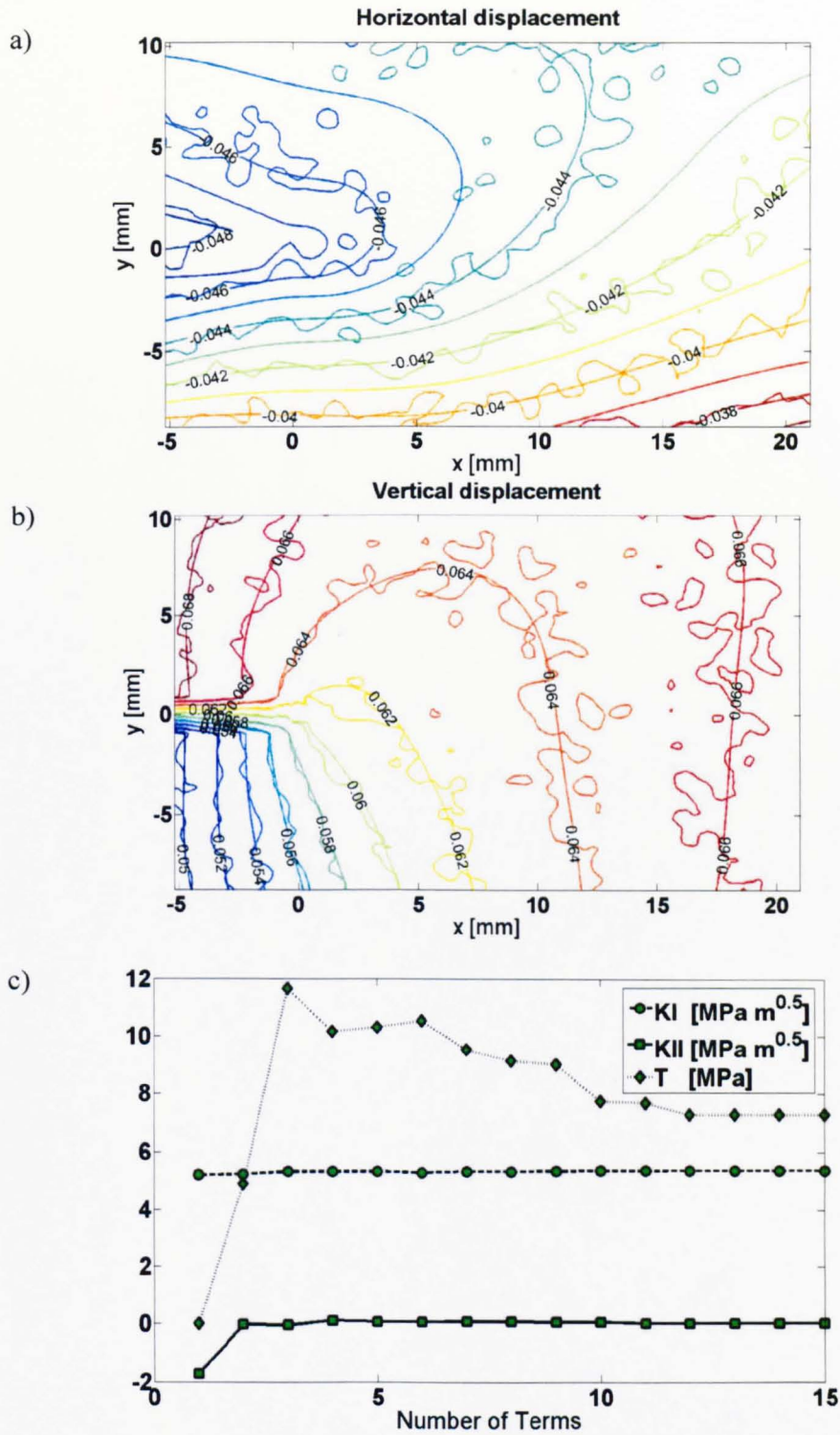


Figure 5-19 Quality of fitted displacement field a) Horizontal and b) Vertical and c) variation of T-stress and SIF versus number of Williams' solution terms for the 4mm fatigue crack under 0.5 to 1.5 kN loading condition

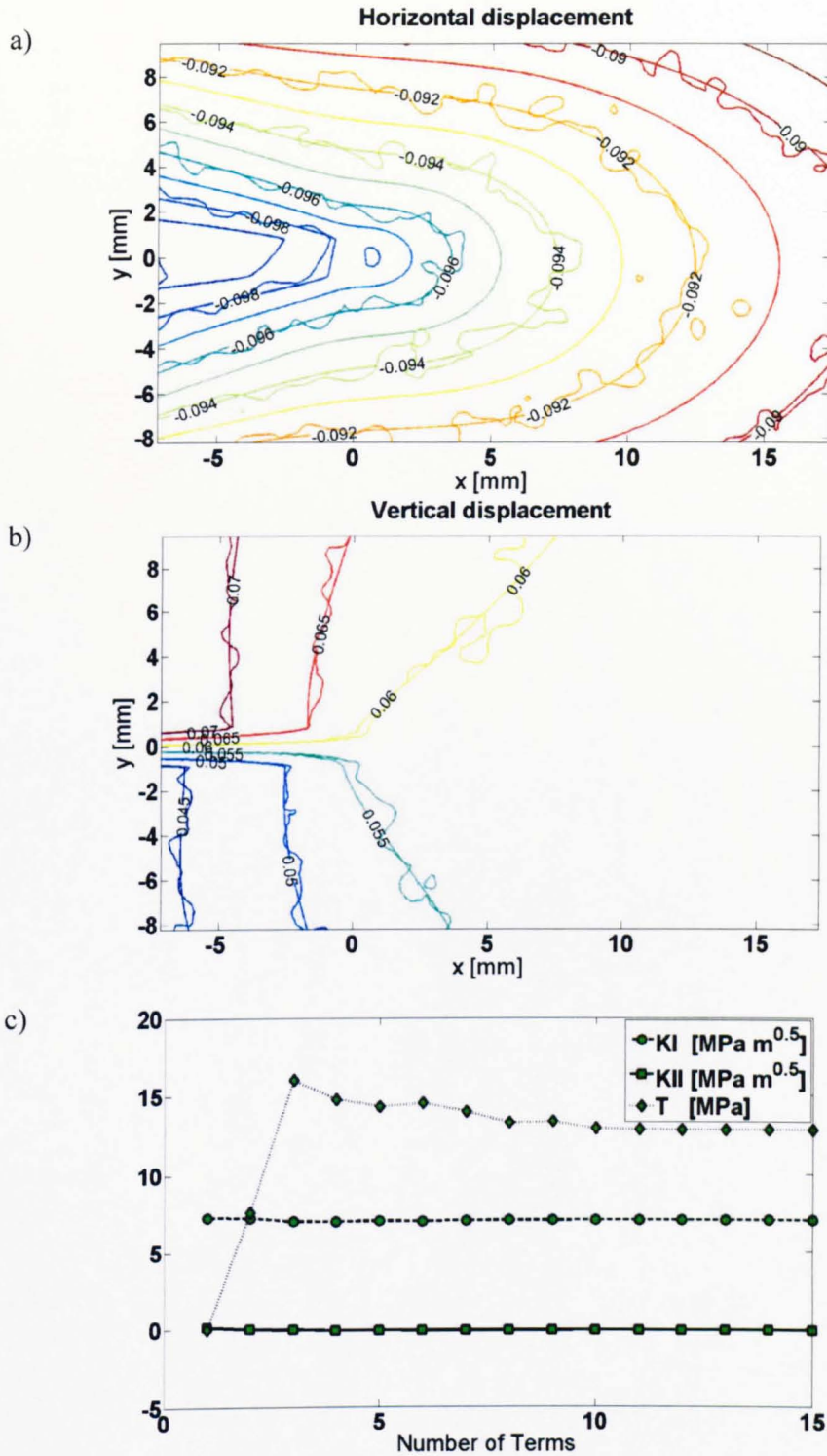


Figure 5-20 Quality of fitted displacement field a) Horizontal and b) Vertical and c) variation of T-stress and SIF versus number of Williams' solution terms for the 8mm fatigue crack under 0.5 to 1.5 kN loading condition

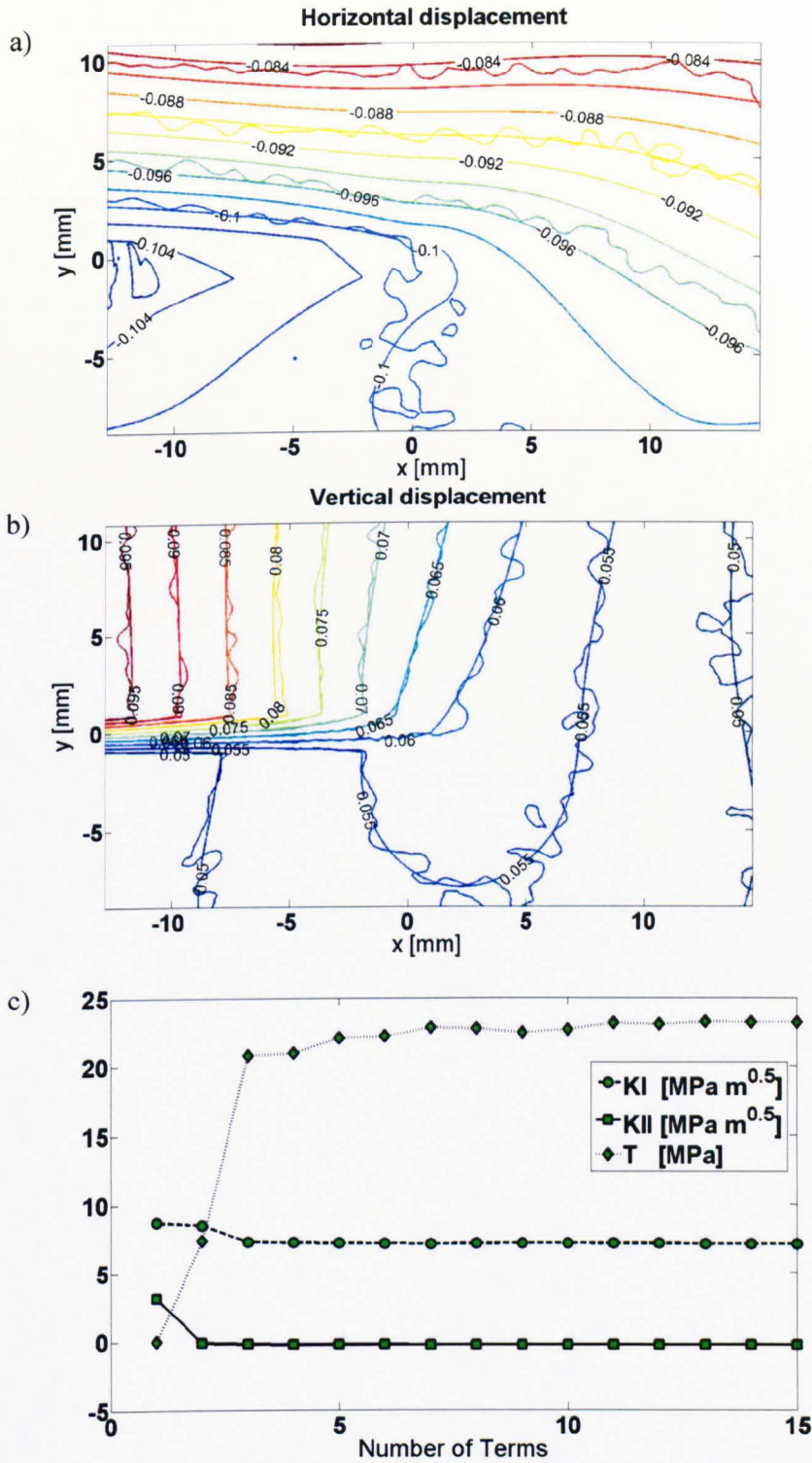


Figure 5-21 Quality of fitted displacement field a) Horizontal and b) Vertical and c) variation of T-stress and SIF versus number of Williams' solution terms for the 15mm fatigue crack under 0.5 to 1.5 kN loading condition

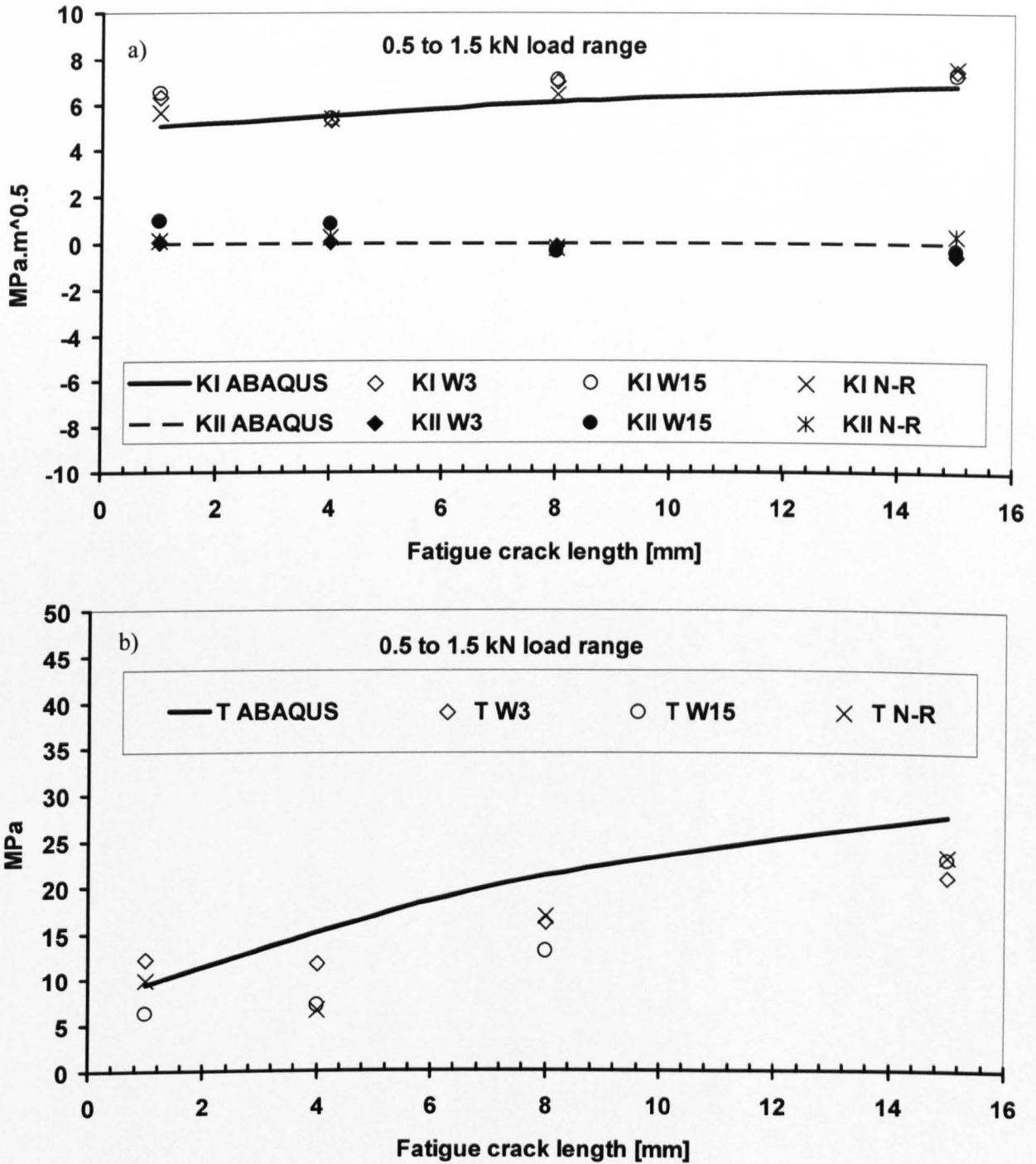


Figure 5-22 Comparison of a) stress intensity factors and b) T-stresses determined using ABAQUS, 3 terms Williams (W3), 15 terms Williams (W15) and Newton-Raphson method for 0.5 to 1.5 kN load range

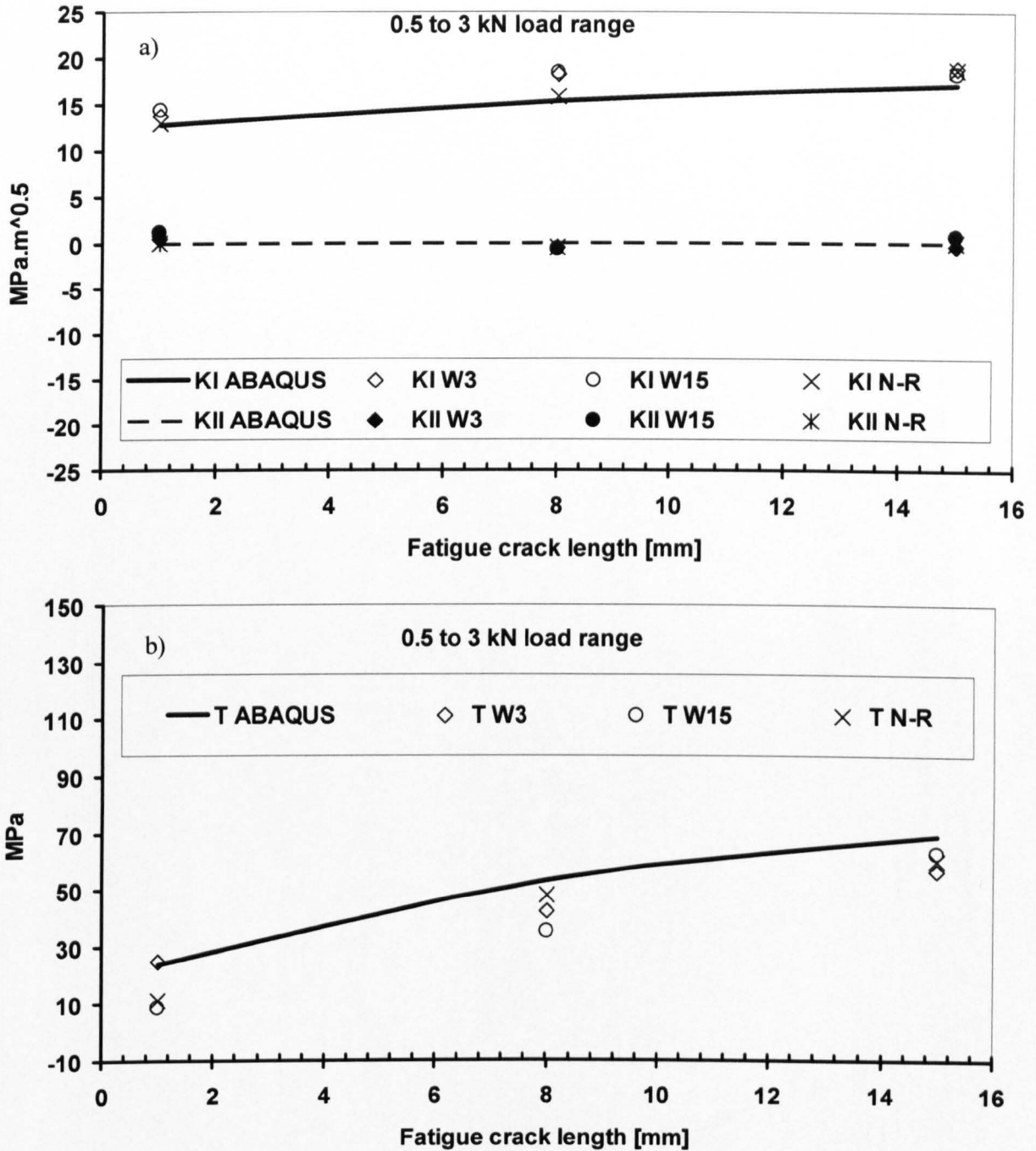


Figure 5-23 Comparison of a) stress intensity factors and b) T-stresses determined using ABAQUS, 3 terms Williams (W3), 15 terms Williams (W15) and Newton-Raphson method for 0.5 to 3 kN load range

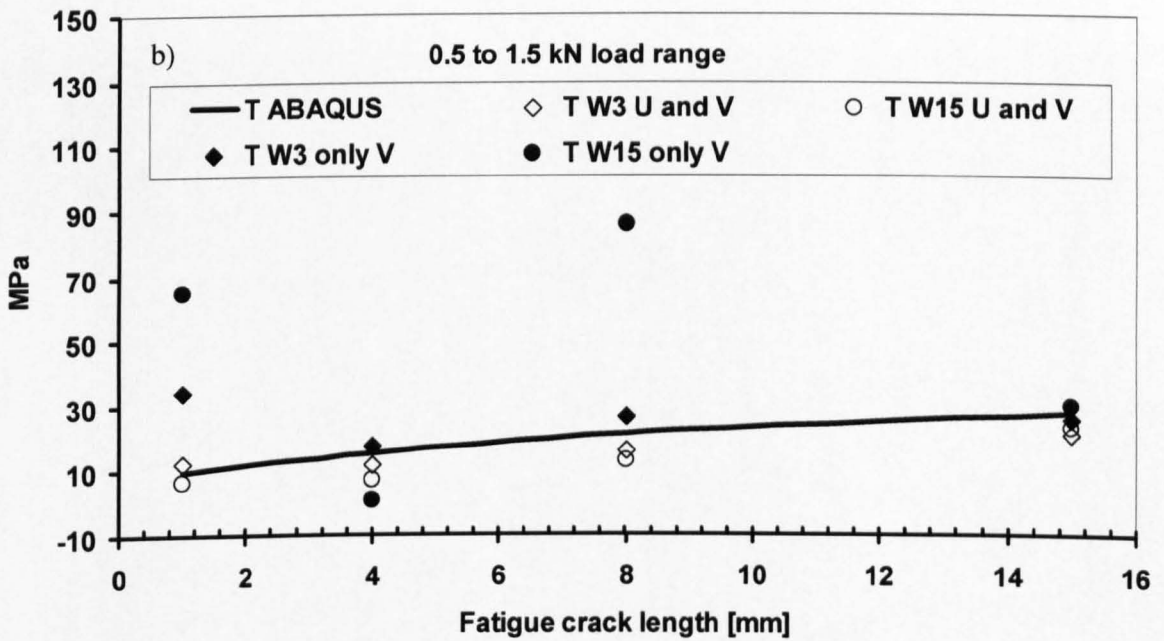
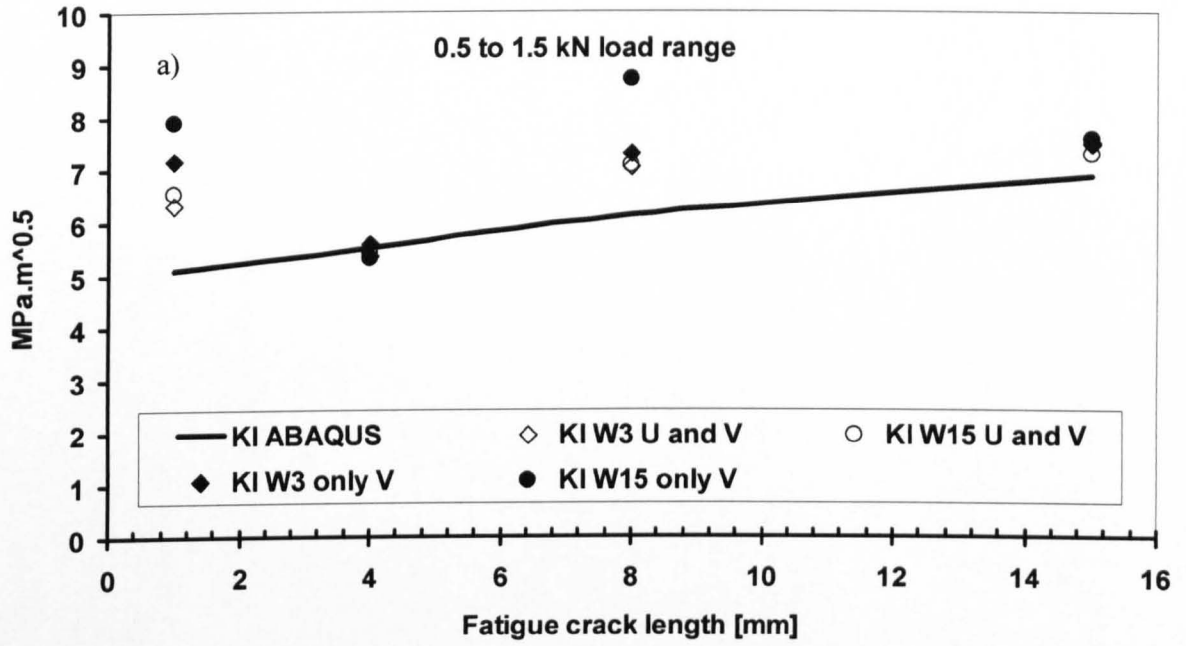


Figure 5-24 Comparison between a) stress intensity factors and b) T-stress obtained using only vertical displacement field (v) and using both horizontal and vertical displacement fields (u and v)

### 5.6.1 Mixed mode experiments

In order to investigate the applicability of the DIC method to mixed mode cracks, a centrally notched specimen with the dimensions shown in Figure 5-25(a) was loaded under different loading angles ranging from  $0^\circ$  (pure mode I) to  $90^\circ$  (pure mode II) using the mixed mode grips shown in Figure 5-25(b). It was previously experienced by Pinna [132] that these grips make the specimen over constrained. To overcome this problem it was suggested that [132] the grips holes are modified from a circular shape to a slot shape as shown in Figure 5-26. Thus the modified grips were used for the experiments. First, only pins were used to connect the specimen to the grips. However, during the experiments it was observed that the load does not evenly distributed through the pins and even under loading conditions some of the pins were not under any load. So, rather than only using pins the specimen was bolted to the grips as shown in Figure 5-27.

The same surface preparation and resolution as the previous DCB specimen were used. For each loading angle, first the camera was focused on the left hand side crack tip, a 0.5kN to 5kN load range was applied and the images were recorded during the loading. Then the camera was moved to the right hand side crack and the loading and recording steps were repeated. After doing the experiments for all the angles the same procedure as in the previous mode I experiments was performed to determine the stress intensity factors and the T-stress.

In order to numerically simulate the problem, an elastic model as shown in Figure 5-28 was used in ABAQUS. Quarter point singular elements used to model the elastic singularity ahead of the crack tip and the stress intensity factors were determined using the J integral method. The T-stress was also determined using an interaction integral technique. A comparison between the FE and experimental results is shown in Figure 5-29.

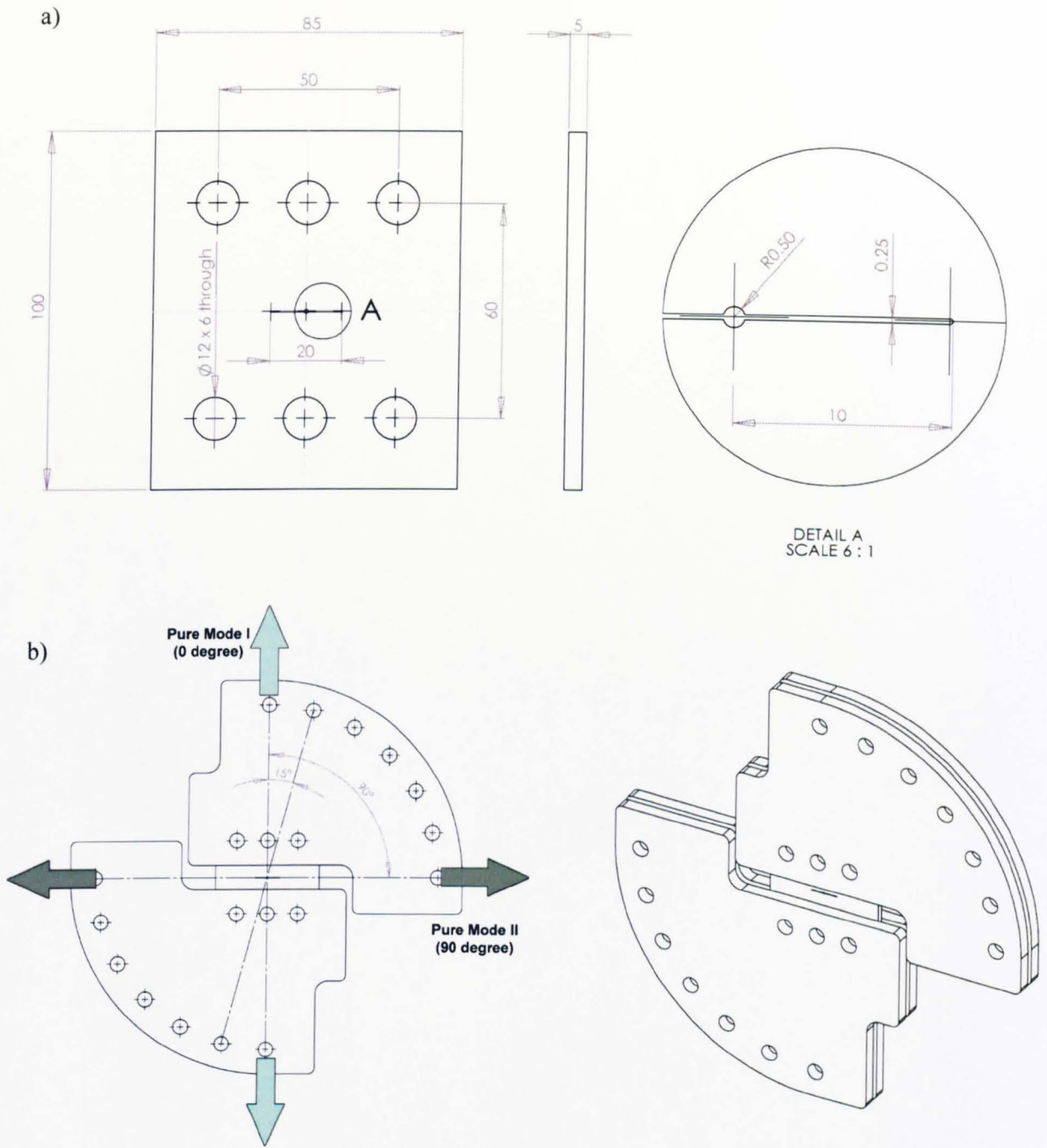


Figure 5-25 Centrally cracked specimen and mixed mode grips

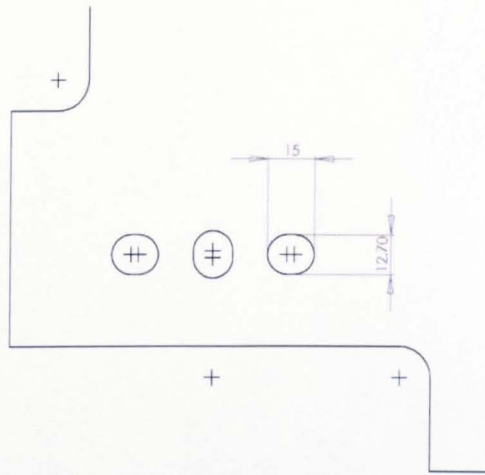


Figure 5-26 Modifications in the holes of the grips

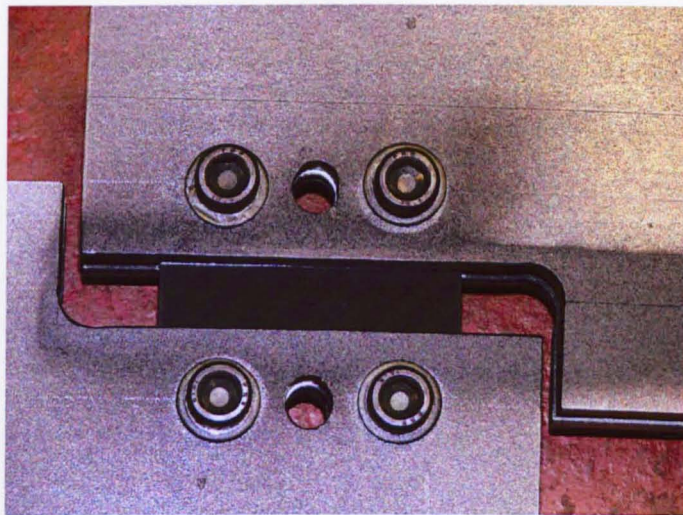


Figure 5-27 Bolted specimen

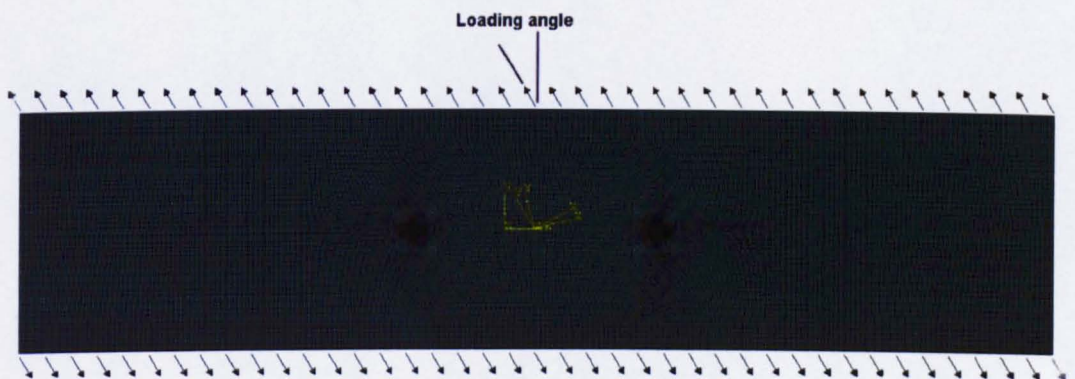


Figure 5-28 FEM model used in simulations

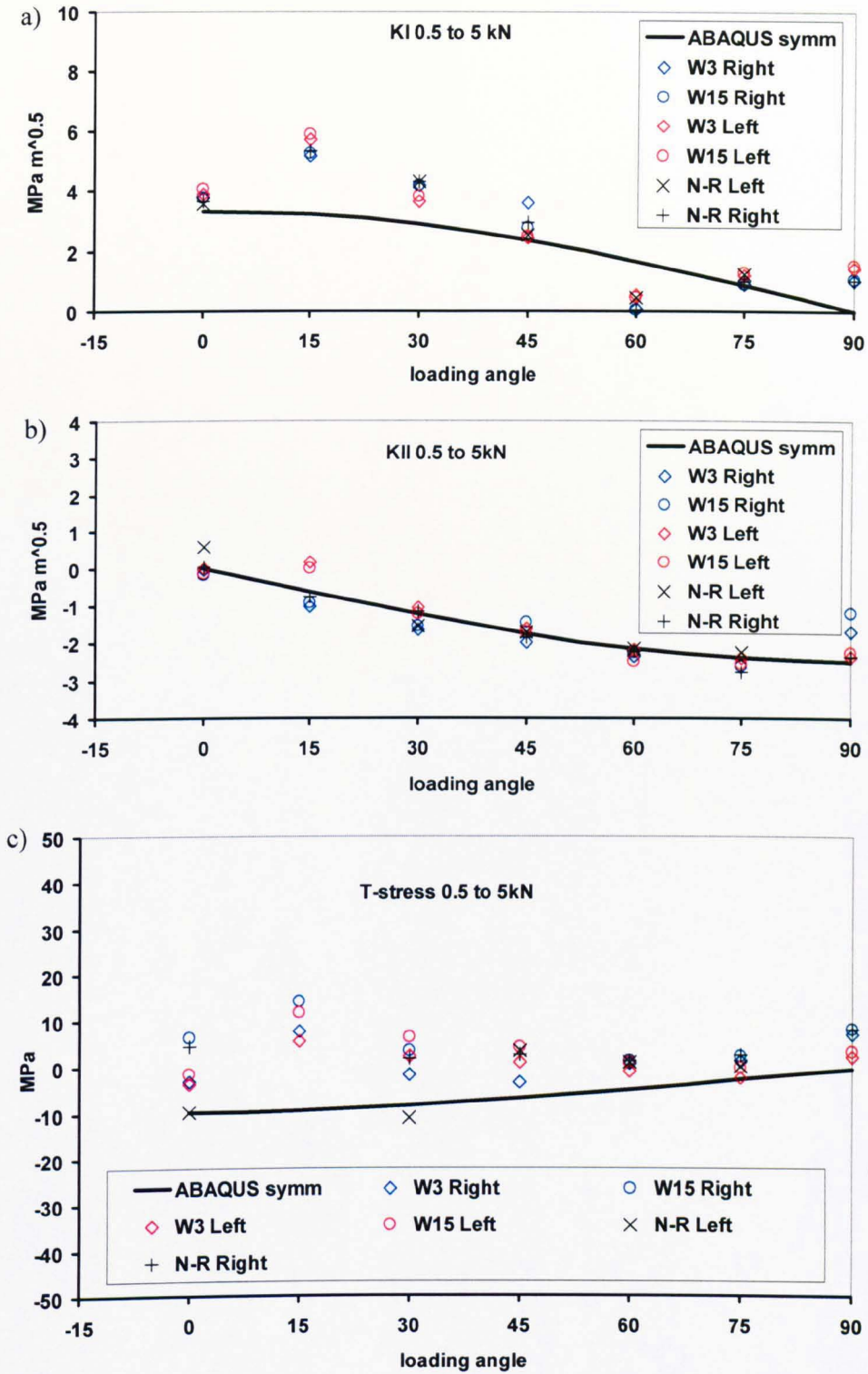


Figure 5-29 a) Mode I, b) mode II and c) T-stress found in a centrally crack specimen under mixed mode loading conditions

It is observed from Figure 5-29(b) that there is a good agreement between the determined mode II stress intensity factors and the numerically calculated ones for almost all the cases. All three solutions (3 terms, converged term and Newton-Raphson) yield almost the same values. This is the same for both left and right hand side crack tips. A similar trend for the three different solutions is observed for the mode I stress intensity factors but the stress intensity factors are slightly different in left and right hand side cracks. Moreover, for mode I stress intensity factor, a higher discrepancy is observed between the numerical and experimentally determined results. Regarding the T-stress, it is observed that the T-stress in the left and right hand side cracks are different especially at small loading angles. It can also be seen that the 3 terms solution is slightly closer to the numerical results. Although the T-stresses found in higher loading angles (mode I dominant) are close to numerical results, in lower loading angles (mode II dominant) the difference is higher.

These disagreements are mainly due to the following reasons. First of all the grips are not perfect. In other words the holes in the grips are not completely aligned and this caused misalignment and consequently non-symmetrical stress distribution in specimen thus causing differences between the left and right crack results. To see the effect of non-symmetrical loading conditions on the stress intensity factors and the T-stresses a new model (see Figure 5-30) was created using finite element analysis. In this model (Figure 5-30) one edge of the specimen was constrained in both the vertical and horizontal directions and load was applied at different angles. This model gives a symmetrical stress distribution when the loading angle is zero

However, the stress distribution on the specimen becomes asymmetrical as the loading angle increases. Basically, since the actual misalignment in the grips is unknown it is not possible to accurately model the asymmetry in the loading. However, such a simple model can be helpful in studying how a little asymmetry in loading or specimen can affect the stress intensity factors and the T-stresses as shown in Figure 5-31.

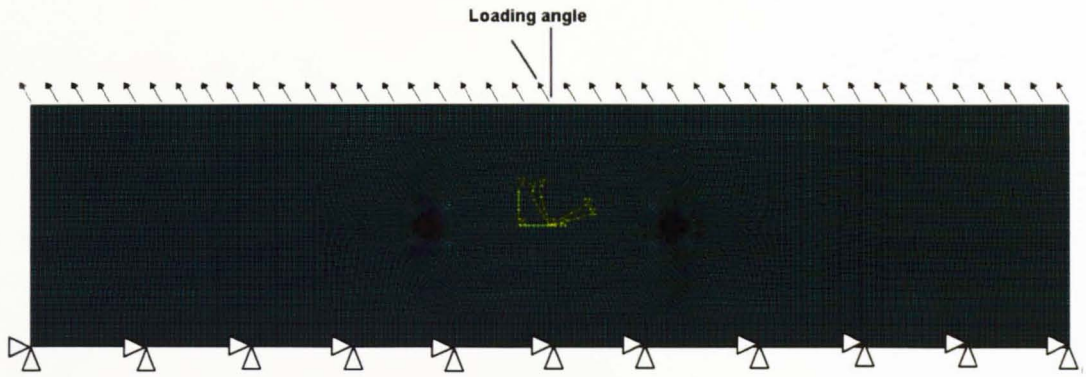


Figure 5-30 Non-symmetric boundary condition

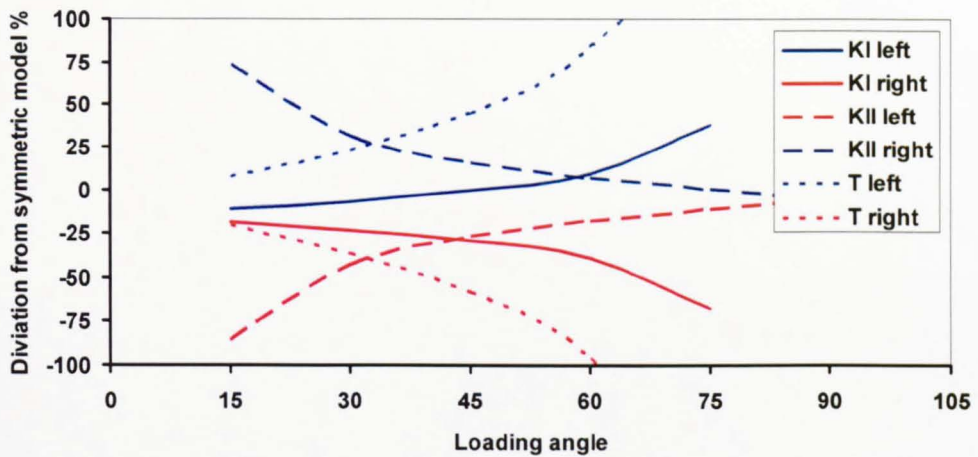


Figure 5-31 Effect of asymmetric boundary conditions on T-stress and SIF

As it is observed from Figure 5-31, such a simple asymmetric condition can significantly affect the stress distribution on the specimen. As it was mentioned before, the misalignment in the holes can make the specimen over constrained. This makes the stress distribution obtained by finite element an unreliable comparator in some cases.

The quality of fitting and the region where the data points are selected can also affect the results. In case of pure mode I as shown in Figure 5-18(a) and (b) to Figure 5-21(a) and (b), all data points obtained from the experiments were selected and only the area around the edges of the specimen and the notches/cracks were excluded. Such a data point selection resulted in a good

fitness quality as observed previously. The same procedure was used for the mixed mode case as well.

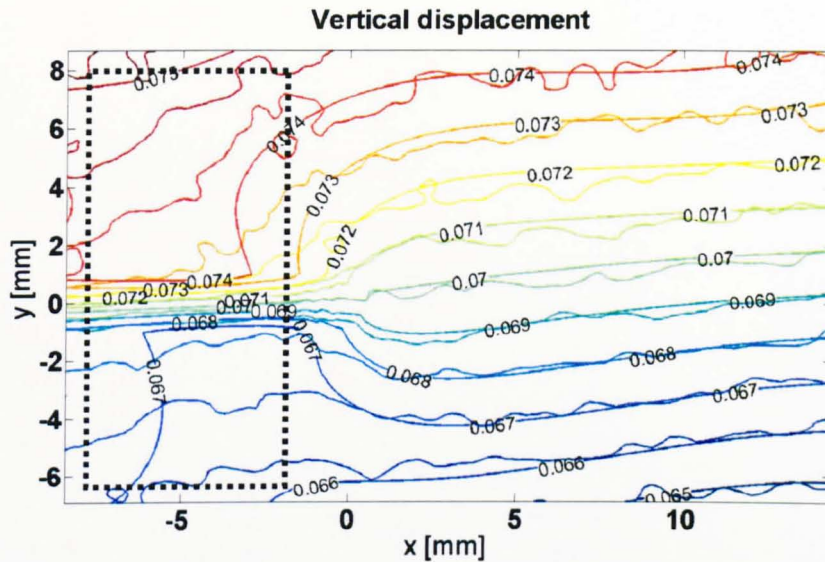


Figure 5-32 Fitness quality for 30° loading angle

As it is observed from Figure 5-32 compared to pure mode I case the determined displacement field is poorly fitted to the experimental results especially in the highlighted region. This region is around the crack flanks and close to the centre of the specimen. This might show that the load had been transmitted less to the specimen through the central pin. Such a distribution was more critical in the lower loading angles. Excluding these data points and re-performing the calculations slightly improves the results as shown in Figure 5-33.

## 5.7 Conclusions

Digital image correlation was used to determine the T-stress and stress intensity factors from displacement fields. Both Muskhelishvili's and Williams' approaches were examined. It was found that Muskhelishvili's approach underestimates the stress intensity factor in artificial data and obviously is not capable of determining the T-stress. Williams' approach however showed excellent evaluation of both T-stress and stress intensity factors in artificially produced data, either with or

without noise and also for finite element data. Good agreements were also found in the case of fatigue cracked specimens. It was shown that rigid body translations can significantly affect the results. However, rigid body rotations are more influential in mode II stress intensity factors.

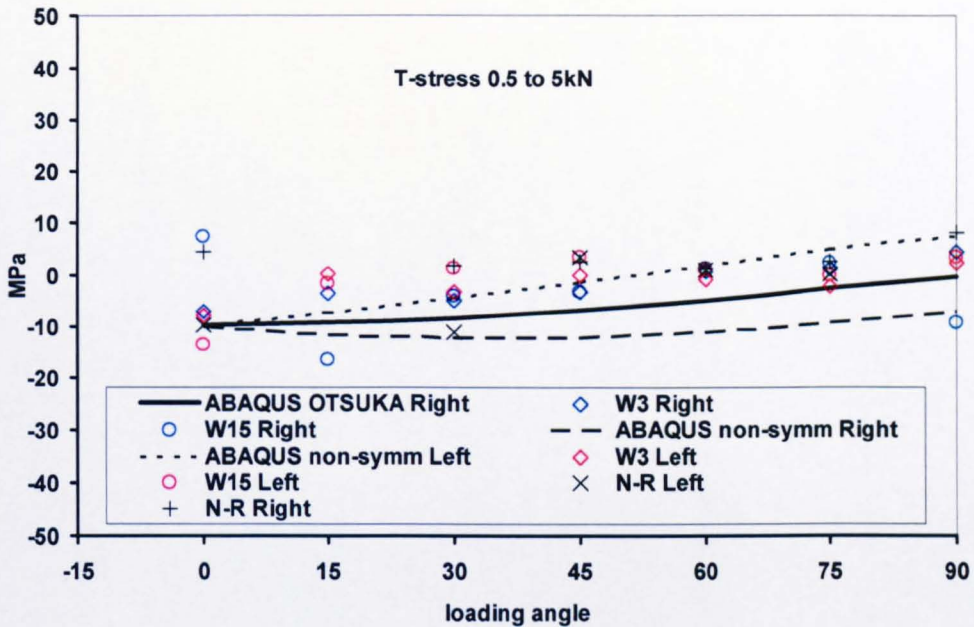


Figure 5-33 T-stress determined by excluding the poorly fitted regions surrounding the crack flanks

As it was mentioned in the literature review chapter, it is common in the literature to use only the vertical displacement field to extract the stress intensity factors. It was shown that even in pure mode I cases, this might lead to significant errors in T-stress calculations and therefore it is recommended that both vertical and horizontal displacement fields are used in the calculations.

Different numbers of terms of Williams' expansion were used and their effect was investigated on the results. It was shown that the 3 terms solution seems sufficient in T-stress and stress intensity factors determination and less affected by uncertainties involve in the experiments particularly in longer fatigue crack cases. The Newton-Raphson technique was also implemented in the calculations and it

was shown that by considering the crack tip coordinates as two more unknowns in the system of equations, the uncertainties regarding the crack tip position can be reduced and the results are slightly improved.

# **Chapter 6**

## **Conclusions and Future Work**

### **6.1 Overall conclusions**

- The interaction of cracks with different offsets was investigated experimentally and numerically. It was shown that the crack paths are not always repeatable as expected in FE models. It was found that the crack path criteria are capable of an acceptable prediction only in the early stages of the crack growth. Furthermore, the stress intensity factors only partially control the crack path and it can be affected by the T-stress as well.
- Both Muskhelishvili's approach and Williams' approach were used to determine the stress intensity factors from the sum of principal stress field as the output of experimental data from thermoelastic stress analysis (TSA). It was shown that the Muskhelishvili's approach yields exactly the same results of the Williams' approach if only two terms of the Williams' solution is used.

- It is not possible to determine the T-stress using Muskhelishvili's approach. It was shown that using only two terms of Williams' solution is not enough to determine the T-stress and, three or more terms are needed.
- Using artificially generated data and finite element data, it was shown that the Williams' solution is not numerically stable when more than four terms of Williams' solution is being used. In real experimental data using more than three terms of the Williams' expansion make the solution unstable. However, results obtained using three terms solution looked promising.
- Due to instability observed in T-stress and stress intensity factor determination using the stress field, the usefulness of the displacement field was also examined using the data obtained from digital image correlation (DIC). Again both Muskhelishvili's and Williams' approach were used. It was shown that the Muskhelishvili's approach, underdetermines the stress intensity factors.
- The Williams' approach was used to determine the T-stress and stress intensity factors. In contrary to the results obtained from stress field, the results obtained from displacements were more robust and a convergent trend was observed for the T-stress and the stress intensity factors when the number of terms of Williams' solution was increased.
- Although the converged values obtained were within an acceptable range, results obtained from the three terms Williams' solution looked less sensitive to the uncertainties in the experiment and more economical in time and computer resources.

## 6.2 Suggestions for future work

- The crack path simulations can be improved by developing subroutines in commercial software such ANSYS or ABAQUS to consider the effects of the T-stress in crack path finite element simulations.
- To improve the reliability of the TSA results it is recommended that rather than circular selection of data points, all the data points are used and the

areas (such as crack tip and flanks) which are not representative of the sum of the principal stress are excluded. The fitted data can be compared to the experimental results and the quality of the fitting can be used to check the validity of the model in the selected areas.

- During performing the experiments it was observed that if rather than fully painting the surface of the specimen a random pattern is produced, due to different emissivity on the surface, a random *thermal* pattern is observed. A thermal camera can be used to capture these thermal images and a similar correlation algorithms as the one which is normally used in digital image correlation applications can be used to determine the displacement field. This was done on a DCB specimen in two different resolutions. The qualitative results are shown in Figure 6-1 to Figure 6-6.

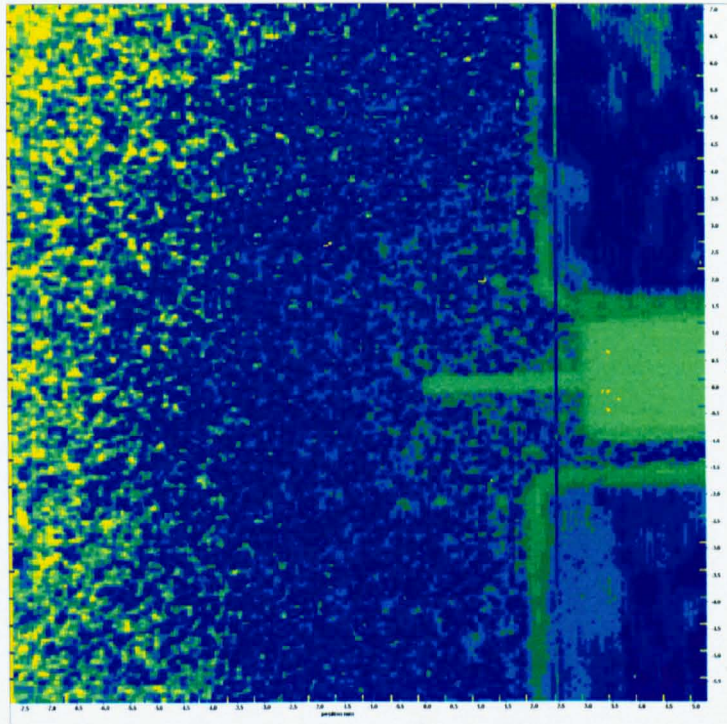


**Figure 6-1 Thermal speckles**

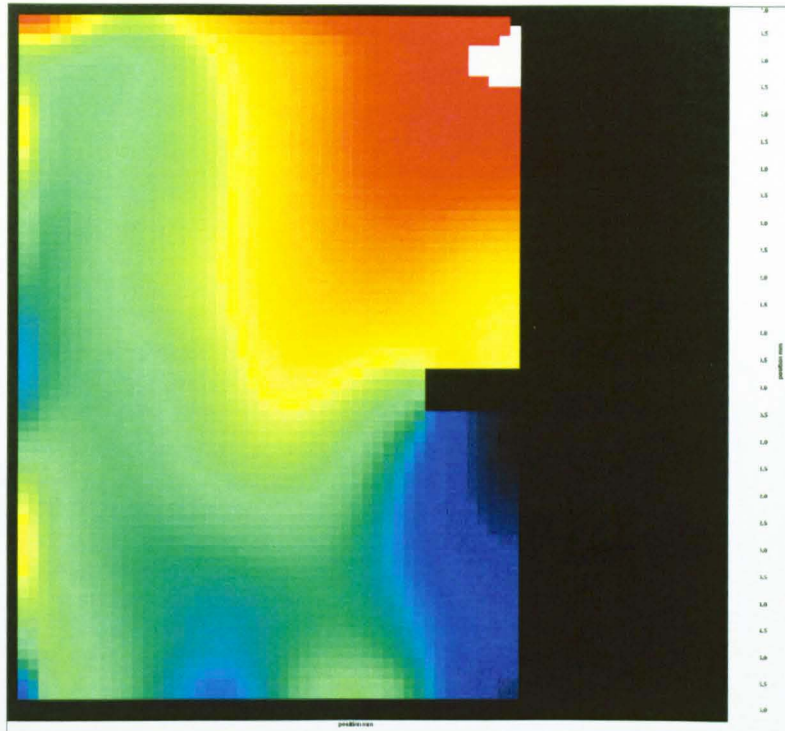


Figure 6-2 Correlated vertical displacement field

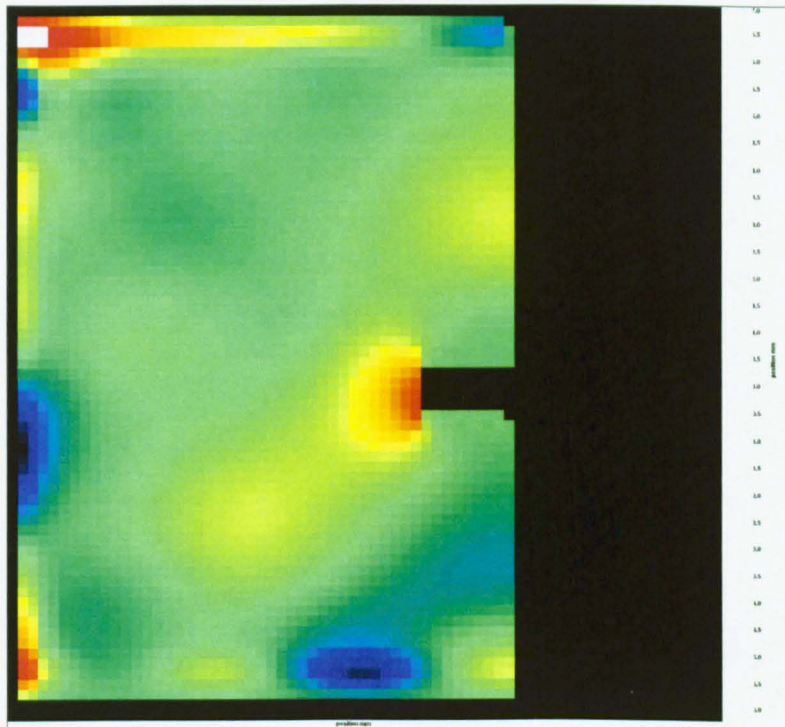


Figure 6-3 Correlated vertical strain field

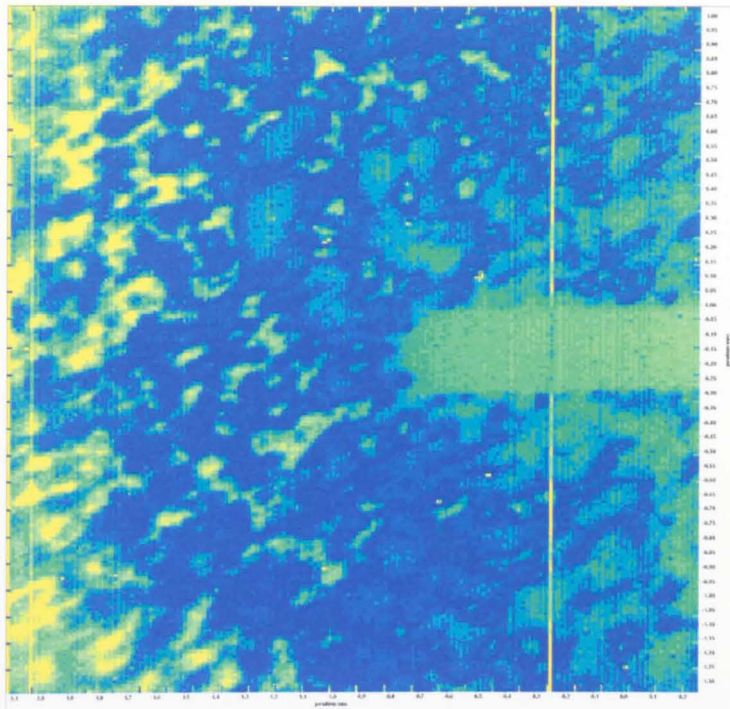


Figure 6-4 Thermal speckles in a higher resolution

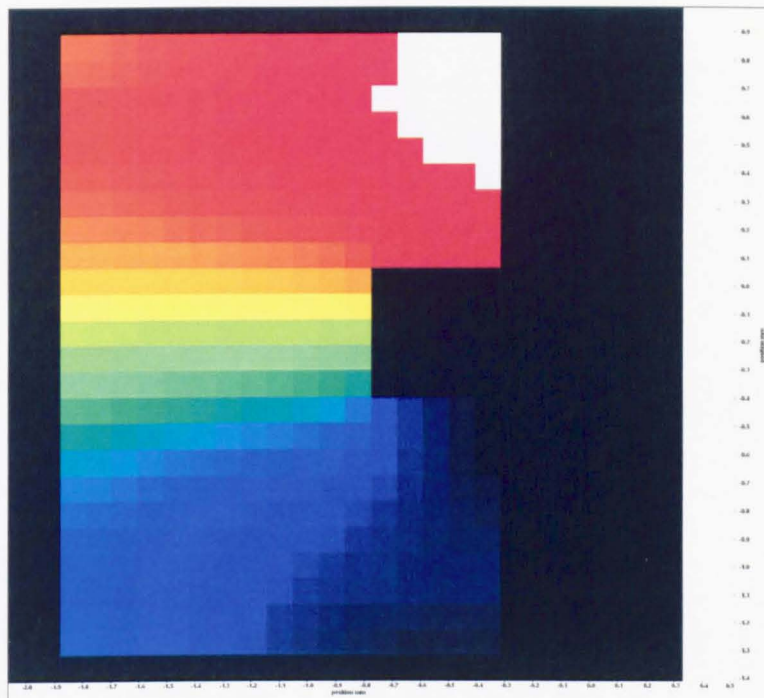
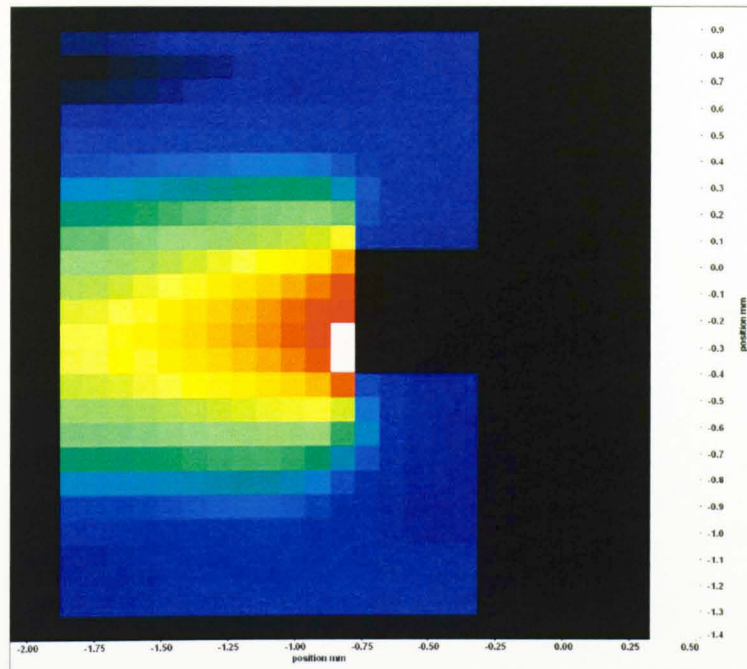


Figure 6-5 Correlated vertical displacement in a higher resolution



**Figure 6-6 Correlated vertical strain field in a higher resolution**

It is an interesting research area which can make it possible to measure both displacement field and the stress field at the same time. However, more research is required to develop a reliable method.

- A 2D image correlation system was used in this current work. Using a 3D system makes it possible to measure the out of plane displacement field as well as the in-plane displacement fields. This can potentially decrease inaccuracies involved in the experiments and leads to more reliable correlation and eventually more reliable results.
- In this work the crack tips were visually located from digital image correlation images. A Newton-Raphson algorithm was also used to find the crack tip coordinates as two unknowns from displacement data. To be able to achieve more accurately determined crack tip position and lowering the corresponding uncertainties in the experiments, the optimization algorithms such as Genetic Algorithm can be used.

## References

- [1] **Pettit RG.** Crack turning in integrally stiffened aircraft structures. Faculty of Graduate School: Cornell University; 2000.
- [2] **Rankin CC, Brogan FA, and Riks E.** *Some computational tools for the analysis of through cracks in stiffened fuselage shells.* Comp Mech. 1993;13:143-156.
- [3] **Broberg KB.** *On crack paths.* Eng Fract Mech. 1987;28(5/6):663-679.
- [4] **Cotterell B.** *On brittle fracture paths.* Int J Fracture. 1965;1(2):96-103.
- [5] **Barenblatt GI, and Cherepanov GP.** *On brittle cracks of longitudinal shear (in Russian).* PMM. 1961;25(6).
- [6] **Cherepanov GP.** *One problem of indenter testing with formation of cracks (in Russian).* PMM. 1963;27(1).
- [7] **Gol'dstein RV, and Salganik RL.** *Brittle fracture of solids with arbitrary cracks.* Int J Fracture. 1974;10(4):507-523.
- [8] **Erdogan F, and Sih GC.** *On the crack extension in plates under plane loading and transverse shear.* J Bas Engng. 1963;85:519-525.
- [9] **Sih GC.** *Strain-energy-density factor applied to mixed mode crack problems.* Int J Fracture. 1974;10(3):305-321.
- [10] **Cotterell B, and Rice JR.** *Slightly curved or kinked cracks.* Int J Fracture. 1980;16(2):155-169.
- [11] **Melin S.** *When does a crack grow under mode II conditions?* Int J Fracture. 1986;30:103-114.
- [12] **Shirmohammadi M.** *Stable crack growth trajectories and fracture due to interacting cracks.* USA: University of California at Berkeley; 1995.

- [13] **Pook LP.** *On fatigue crack paths.* Int J Fatigue. 1995;17(1):5-13.
- [14] **Ritchie RO, Knott JF, and Rice JR.** *On the relationship between critical tensile stress and fracture toughness in mild steel.* J Mech Phys Solids. 1973;21:395-410.
- [15] **Streit RD, and Finnie I.** *The directional stability of crack propagation.* Mech behav mater. 1979;3:469-478.
- [16] **Pineau A, and Besson J.** In: Besson J, editor. Local approach to fracture: Ecole des Mines de Paris, 2004.
- [17] **Qian J, and Fatemi A.** *Mixed mode fatigue crack growth: A literature survey.* Eng Fract Mech. 1996;55:969-990.
- [18] **Cotterell B.** *Notes on the paths and stability of cracks.* Int J Fracture. 1966;2(3):526-533.
- [19] **Radon JC, Leever PS, and Culver LE.** Fracture toughness of PMMA under biaxial stress. University of Waterloo Press; 1977. p. 1113-1118.
- [20] **Melin S.** *Why do cracks avoid each other.* Int J Fracture. 1983;23:37-45.
- [21] **Melin S.** *Directional stability of an originally straight crack.* Int J Fracture. 1992;53:121-128.
- [22] **Melin S.** *The influence of the T-stress on the directional stability of cracks.* Int J Fracture. 2002;114:259-265.
- [23] **Larsson SG, and Carlsson AJ.** *Influence of non-singular stress terms and specimen geometry on small scale yielding at crack tips in elastic-plastic materials.* J Mech Phys Solids. 1973;21:263-277.
- [24] **Kim M, and Pan J.** *Effects of non-singular stresses on crack-tip fields for pressure-sensitive materials, Part 1: Plane strain case.* Int J Fracture. 1994;68:1-34.

- [25] **Broek D.** Elementary engineering fracture mechanics. Springer, 1986.
- [26] **Tong J.** *T-stress and its implications for crack growth.* Eng Fract Mech. 2002;**69**(12):1325-1337.
- [27] **Rice JR.** *Limitations to the small scale yielding approximation for crack tip plasticity.* J Mech Phys Solids. 1974;**22**:17-26.
- [28] **Betegon C, and Hancock JW.** *Two-parameter characterization of elastic-plastic crack-tip fields.* J Appl Mech. 1991;**58**:104-110.
- [29] **O'Dowd NP, and Shih CF.** *Family of crack tip fields characterized by a triaxiality parameter - I - Structure of fields.* J Mech Phys Solids. 1991;**39**(8):989-1015.
- [30] **Ayatollahi MR, Smith DJ, and Pavier MJ.** *Crack-tip constraints in mode II deformation.* Int J Fracture. 2002;**113**:153-173.
- [31] **Miannay DP.** Fracture mechanics. Springer-Verlag, 1998.
- [32] **Shih CF, and German MD.** *Requirements for a one parameter characterization of crack tip fields by the HRR singularity.* Int J Fracture. 1981;**17**(1):27-43.
- [33] **Hancock JW, Reuter WG, and Parks DM.** Constraint and toughness parameterized by T. In: Hackett EM, Schwalbe KH, and Dodds RH, editors. Constraint effects in fracture: ASTM STP 1171, 1993.
- [34] **Shah PD.** Determination of T-stress solutions for cracked 2D anisotropic elastic bodies using the boundary element method. Mechanical and Aerospace Engineering Department. Ottawa, Canada: Carleton University; 2007.
- [35] **Dowling AR, and Townley CHA.** *The effect of defects on structural failure: A two-criteria approach.* Int J Pres Ves & Piping. 1975;**3**:77-107.

- [36] **Janssen M, Zuidema J, and Wanhill R.** Fracture mechanics. Spon Press, 2004.
- [37] **Ainsworth RA, and O'Dowd NP.** *Constraint in the failure assessment diagram approach for fracture assessment.* J Pres Ves Tech. 1995;117:260-267.
- [38] **Bilby BA, Howard IC, and Li ZH.** *The use of constraint-modified failure assessment lines in failure assessment diagrams.* Int J Fracture. 1996;75:323-334.
- [39] **Ainsworth RA, Sattari-Far I, Sherry AH, Hooton DG, and Hadley I.** *Methods for including constraint effects within the SINTAP procedures.* Eng Fract Mech. 2000;67:563-571.
- [40] **Zhao LG, Tong J, and Byrne J.** *Stress intensity factor K and the elastic T-stress for corner cracks.* Int J Fracture. 2001;109:209-225.
- [41] **Brown CW, and Hicks MA.** *Fatigue growth of surface cracks in nickel-based superalloys.* int J Fatigue. 1982;4:73-81.
- [42] **Sherry AH, France CC, and Goldthor MR.** *Compendium of T-stress solutions for two and three dimensional cracked geometries.* Fatigue Fract Engng Mater Struct. 1995;18(1):141-155.
- [43] **Leevers PS, and Radon JC.** *Inherent stress biaxiality in various fracture specimen geometries.* Int J Fracture. 1982;19:311-325.
- [44] **Kfoury AP.** *Some evaluations of the elastic T-term using Eshelby's method.* Int J Fracture. 1986;30:301-315.
- [45] **Sham TL.** *The determination of the elastic T-term using higher order weight functions.* Int J Fracture. 1991;48:81-102.
- [46] **Nakamura T, and Parks DM.** *Determination of elastic T-stress along three-dimensional crack fronts.* Int J Solid Struct. 1992;29:1597-1611.

- [47] **Wang YY, and Parks DM.** *Evaluation of the elastic T-stress in surface-cracked plates using the line-spring method.* Int J Fracture. 1992;**56**:25-40.
- [48] **Fett T.** *A green's function for T-stresses in an edge cracked rectangular plate.* Eng Fract Mech. 1997;**97**:365-373.
- [49] **Ayatollahi MR, Pavier MJ, and Smith DJ.** *Determination of T-stress from finite element analysis for mode I and mixed mode I/II loading.* Int J Fracture. 1998;**91**:283-298.
- [50] **Yang B, and Ravi-Chandar K.** *Evaluation of elastic T-stress by the stress difference method.* Eng Fract Mech. 1999;**64**:589-605.
- [51] **Shih CF, and Asaro RJ.** *Elastic-plastic analysis of cracks on bimaterial interfaces: Part I - small scale yielding.* J Appl Mech. 1988;**55**:299-316.
- [52] **Patterson EA, and Olden EJ.** *Optical analysis of crack tip stress fields: a comparative study.* Fatigue Fract Engng Mater Struct. 2004;**27**:623-635.
- [53] **Post D.** *Photoelastic stress analysis for an edge crack in a tensile field.* Proceedings SESA. 1954;**12**(1):99-116.
- [54] **Wells A, and Post D.** *The dynamic stress distribution surrounding a running crack - a photoelastic analysis.* Proceedings SESA. 1958;**16**(1):69-92.
- [55] **Irwin GR.** *Discussion of previous reference.* Proceedings SESA. 1958;**16**(1):93-96.
- [56] **Bradley WB, and Kobayashi AS.** *An investigation of propagating cracks by dynamic photoelasticity.* Exp Mech. 1970;**10**:106-113.
- [57] **Sanford RJ, and Dally JW.** *A general method for determining mixed-mode stress intensity factors from isochromatic fringe patterns.* Eng Fract Mech. 1979;**11**:621-633.

- [58] **Nurse AD, and Patteson EA.** *Determination of predominantly mode II stress intensity factors from isochromatic data.* Fatigue Fract Engng Mater Struct. 1993;16(12):1339-1354.
- [59] **Christopher CJ, James MN, Patteson EA, and Tee KF.** *A quantitative evaluation of fatigue crack shielding forces using photoelasticity.* Eng Fract Mech. 2008;75.
- [60] **Christopher CJ, James MN, Patteson EA, and Tee KF.** *Towards a new model of crack tip stress fields.* Int J Fracture. 2008;148(4):361-371.
- [61] **James MN, Pacey MN, Wei LW, And Patterson EA.** *Characterisation of plasticity-induced closure—crack flank contact force versus plastic enclave.* Eng Fract Mech. 2003;70:2473-2487.
- [62] **Pacey MN, James MN, And Patterson EA.** *A new photoelastic model for studying fatigue crack closure.* Exp Mech. 2005;45(1):42-52.
- [63] **Nurse AD, and Patteson EA.** Photoelastic determination of fatigue crack stress intensity factors. in Proceedings of SPIE, Annual Symposium on Optical Engineering, San Diego; 1993.
- [64] **Baker DB, Sanford RJ, and Chona R.** *Determining K and related stress-field parameters from displacement field.* Exp Mech. 1985;25(4):399-407.
- [65] **Moore AJ, and Tyrer JR.** *Phase-stepped ESPI and moiré interferometry for measuring stress-intensity factor and J integral.* Exp Mech. 1995;35(4):306-314.
- [66] **Han MK, Carlsen CA, and Ramulu M.** *Mixed mode fatigue crack propagation in 7075 T6 aluminum sheet material.* In: Advances in fracture and strength Parts 1-4 Key Eng Mater. 2005;297-300:1565-1571.
- [67] **Kokaly MT, Lee J, and Kobayashi AS.** *Moiré interferometry for dynamic fracture study.* Opt Lasers Eng. 2003;40:231-247.

- [68] **Gray TGF, and MacKenzie PM.** *Fatigue crack closure investigation using Moire interferometry.* Int J Fatigue. 1990;**12**(5):417-423.
- [69] **Fellows LJ, and Nowell D.** *Crack closure measurements using moire' interferometry with photoresist gratings.* Int J Fatigue. 2004;**26**:1075-1082.
- [70] **Moore AJ, and Tyrer JR.** *Evaluation of fracture mechanics parameters using electronic speckle pattern interferometry.* J Strain Anal. 1994;**29**(4):257-262.
- [71] **Shterenlikht A, Diaz FA, Lopez-Crespo P, Withers PJ, and Patterson EA.** *Mixed mode (KI + KII) stress intensity factor measurement by electronic speckle pattern interferometry and image correlation.* Appl Mech Mater. 2004;**1-2**:107-112.
- [72] **Patteson EA, and Olden EJ.** *Optical analysis of crack tip stress fields: a comparative study.* Fatigue Fract Engng Mater Struct. 2004;**27**:623-635.
- [73] **Harwood N, and Cummings WM.** *Thermoelastic stress analysis.* IOP Publishing Ltd., 1991.
- [74] **Stanley P, And Chan WK.** in Internaional conference on Experimental Mechanics. Las Vegas, Bethel, CT: SEM; 1985. p. 747-757.
- [75] **Stanley P, And Chan WK.** The determination of stress intensity factors via thermoelastic stress analysis. in Proc of International conference of fatigue of engineering materials and structures, C262, IMechE. Sheffield, UK; 1986. p. 105-114.
- [76] **Stanley P, and Chan WK.** Mode II crack studies using the SPATE technique. in Proceedings of SEM spring conference on experimental mechanics. New Orleans, USA; 1986. p. 916-923.
- [77] **Stanley P, and Dulieu-Smith JM.** *The determination of crack-tip parameters from thermoelastic data.* Exp Tech. 1996;**20**(2):21-23.

- [78] **Dulieu-Barton JM, Fulton MC, and Stanley P.** *The analysis of thermoelastic isopachic data from crack tip stress fields.* Fatigue Fract Engng Mater Struct. 2000;**23**(301-313).
- [79] **Dulieu-Barton JM, and Worden K.** *Genetic identification of crack-tip parameters using thermoelastic isopachics.* Meas Sci Tech. 2003;**14**:176-183.
- [80] **Worden K, Spencer AB, and Dulieu-Barton JM.** *The effect of crack-tip interactions on the curve-fitting of isopachics.* Appl Mech Mater. 2004;**1-2**:121-126.
- [81] **Lesniak JR, and Boyce BR.** Differential thermography for extreme environment structural integrity measurement. 565 Sience Dr. Madison WI, 53711: Stress Photonics; 1994.
- [82] **Ju SH, Lesniak JR, and Sandor BI.** *Numerical simulation of stress intensity factors via the thermoelastic technique.* Exp Mech. 1997;**37**(3):278-284.
- [83] **Muskheishvili NI.** Some basic problems of the mathematical theory of elasticity. P. NOORDHOFF Ltd, 1963.
- [84] **Tomlinson RA, Nurse AD, And Patterson EA.** *On determining stress intensity factors for mixed mode cracks from thermoelastic data.* Fatigue Fract Engng Mater Struct. 1997;**20**(2):217-226.
- [85] **Diaz FA.** Development of a methodology for thermoelastic investigation of the effective stress intensity factor. UK: The University of Sheffield; 2004.
- [86] **Lin ST, Feng Z, and Rowlands RE.** *Thermoelastic determination of stress intensity factors in orthotropic composites using the J-integral.* Eng Fract Mech. 1997;**56**(4):579-592.

- [87] **Diaz FA, Yates JR, and Patterson EA.** *Some improvements in the analysis of fatigue cracks using thermoelasticity.* Int J Fatigue. 2004;**26**:365-376.
- [88] **Diaz FA, Patterson EA, Tomlinson RA, and Yates JR.** *Measuring stress intensity factors during fatigue crack growth using thermoelasticity.* Fatigue Fract Engng Mater Struct. 2004;**27**:571-583.
- [89] **Evans WT, and Luxmoore A.** *Measurement of in-plane displacement around crack tips by a laser speckle method.* Eng Fract Mech. 1974;**6**:735-743.
- [90] **McNeill SR, Peters WH, and Sutton MA.** *Estimation of stress intensity factor by digital image correlation.* Eng Fract Mech. 1987;**28**(1):101-112.
- [91] **Durig B, Zhang F, McNeill SR, Chao YJ, and Peters III WH.** *A study of mixed mode fracture by photoelasticity and digital image analysis.* Opt Lasers Eng. 1991;**14**:203-215.
- [92] **Hild F, and Roux S.** *Measuring stress intensity factors with a camera: Integrated digital image correlation (I-DIC).* CR Mecanique. 2006;**334**:8-12.
- [93] **Yoneyama S, Morimoto Y, and Takashi M.** *Automatic Evaluation of Mixed-mode Stress Intensity Factors Utilizing Digital Image Correlation.* Strain. 2006;**42**:21-29.
- [94] **Yoneyama S, Ogawa T, and Kobayashi AS.** *Evaluating mixed-mode stress intensity factors from full-field displacement fields obtained by optical methods.* Eng Fract Mech. 2007;**74**:1399-1412.
- [95] **Huntley JM, and Field JE.** *Measurement of crack tip displacement field using laser speckle photography.* Eng Fract Mech. 1988;**30**(6):779-790.

- [96] **Rethore J, Gravouil A, Morestin F, and Combescure A.** *Estimation of mixed-mode stress intensity factors using digital image correlation and an interaction integral.* Int J Fracture. 2005;132:65-79.
- [97] **Fujikawa M, and Takashi M.** *An experimental and numerical hybrid technique for reconstructing boundary conditions in elastic analysis.* J Strain Anal. 2007;42:47-54.
- [98] **Machida K, and Yamada H.** *Evaluation of mixed-mode stress intensity factor by digital image correlation and intelligent hybrid method.* Int J Appl Sci Eng Tech. 2004;1(4):188-193.
- [99] **Lopez-Crespo.** *Fatigue crack characterization by image correlation.* Department of Mechanical Engineering. Sheffield, UK: Sheffield; 2007.
- [100] **Abanto-Bueno J, and Lambros J.** *Experimental determination of cohesive failure properties of a photodegradable copolymer.* Exp Mech. 2005;45(2):144-152.
- [101] **Abanto-Bueno J, and Lambros J.** *An experimental study of mixed mode crack Initiation and growth in functionally graded materials.* Exp Mech. 2006;46:179-196.
- [102] **Carroll J, Efstathiou C, Lambros J, Sehitoglu H, Hauber B, Spottswood SM, and Chona R.** *Multiscale analysis of fatigue crack growth using digital image correlation.* In: Proceedings of the XIth international congress and exposition, June 2-5. Orlando, Florida USA; 2008.
- [103] **Anderson TL.** *Fracture Mechanics: Fundamentals and Applications.* CRC Press, 1995.
- [104] **Maleski MJ, Kirugulige MS, and Tippur HV.** *A method for measuring mode I crack tip constraint under static and dynamic loading conditions.* Exp Mech. 2004;44(5):522-532.

- [105] **G. P, and Patterson EA.** *A review of the general theory of thermoelastic stress analysis.* J Strain Anal. 2003;**38**(5):405-417.
- [106] **Diulieu-Smith JM.** *Alternative calibration techniques for quantitative thermoelastic stress analysis.* Strain. 1995;**31**:9-16.
- [107] DeltaTherm User Manual, Stress Photonics.
- [108] **Boldetti C.** Multi-scale measurement and modelling of large deformation of structural metals during thermomechanical processing. Mechanical Engineering Department. Sheffield, UK: University of Sheffield; 2006.
- [109] ANSYS 5.4 User's Manual.
- [110] **Sih GC.** *Crack tip, stress-intensity factors for plane extension and plate bending problems.* J Appl Mech. 1962;**29**:306-312.
- [111] **Nelder JA, and Mead R.** *A simplex method for function minimization.* Comp J. 1965;**7**:308-313.
- [112] **Press WH.** Numerical recipes in C: The art of scientific computing. Cambridge: Cambridge University Press, 1988.
- [113] **Stanley P, and Chan WK.** The determination of stress intensity factors and crack tip velocities from thermoelastic infra-red emissions. In: Proceedings of International Conference of Fatigue of Engineering Materials and Structures. Sheffield, UK: c262, IMechE; 1986. p. 105-114.
- [114] **Swenson D, and James M.** FRANC2D/L: A crack propagation simulator for plane layered structures, Version 1.4 User's Guide. Kansas State University; 1997.
- [115] **Sutton MA, Deng X, Ma F, Newman Jr JC, and James M.** *Development and application of a crack tip opening displacement-based mixed mode fracture criterion.* Int J Solid Struct. 2000;**37**:3591-3618.
- [116] CEE 770, Enigeering Fracture Mechanics Meetings. 2002.

- [117] **Rybicki EF, and Kanninen MF.** *A finite element calculation of stress intensity factors by a modified crack closure integral.* Eng Fract Mech. 1977;9:931-938.
- [118] **Hussain MA, Pu SL, and Underwood J.** *Strain energy release rate for a crack under combined mode I and II.* Fracture Analysis, ASTM STP 560. 1974:2-28.
- [119] **Bittencourt TN, Wawrzynek PA, Ingraffea AR, and Sousa JL.** *Quasi-automatic simulation of crack propagation for 2D LEFM problems.* Eng Fract Mech. 1996;55(2):321-334.
- [120] **Williams ML.** *On the stress distribution at the base of a stationary crack.* J App Mech. 1957;24:109-114.
- [121] **Haefele PM, and Lee JD.** *The constant stress term.* Eng Fract Mech. 1995;50(5/6):869-882.
- [122] **MATLAB 7.1 users manual.**
- [123] **Tomlinson RA, and Marsavina L.** *Thermoelastic investigations for fatigue life assessment.* Exp Mech. 2004;44(5):487-494.
- [124] **Fett T.** *T-stresses in rectangular plates and circular disks.* Eng Fract Mech. 1998;60(5-6):631-652.
- [125] **Dulieu-Barton JM, and Worden K.** *Identification of Crack-tip parameters using thermoelastic isopachics and differential evolution.* Key Eng Mater. 2003;245-246:77-86.
- [126] **Patteson EA, Diaz FA, and Yates JR.** *Observations on photo-emission and the process zone of a fatigue crack.* J ASTM int. 2006;3(6):225-233.
- [127] **Quinta da Fonseca J, Mummery PM, and Withers PJ.** *Full-field strain mapping by optical correlation of micrographs acquired during deformation.* J Microscopy. 2005;218:9-21.

- [128] **Lu H, and Cary PD.** *Deformation measurements by digital image correlation: Implementation of a second-order displacement gradient.* Exp Mech. 2000;40(4):393-400.
- [129] **Cheng P, Sutton MA, Schreier HW, and McNeill R.** *Full-field speckle pattern image correlation with B-Spline deformation function.* Exp Mech. 2002;42(3):344-352.
- [130] LaVision GmbH. [www.lavision.de](http://www.lavision.de).
- [131] **Dugdale DS, and Ruiz C.** *Elasticity for engineers.* London: McGRAW-HILL, 1971.
- [132] Private communication with Dr C. Pinna. 2007.